Outcrop/Behind Outcrop (O/BO) Characterization and Modelling of Highly Heterogeneous Reservoir Analogues
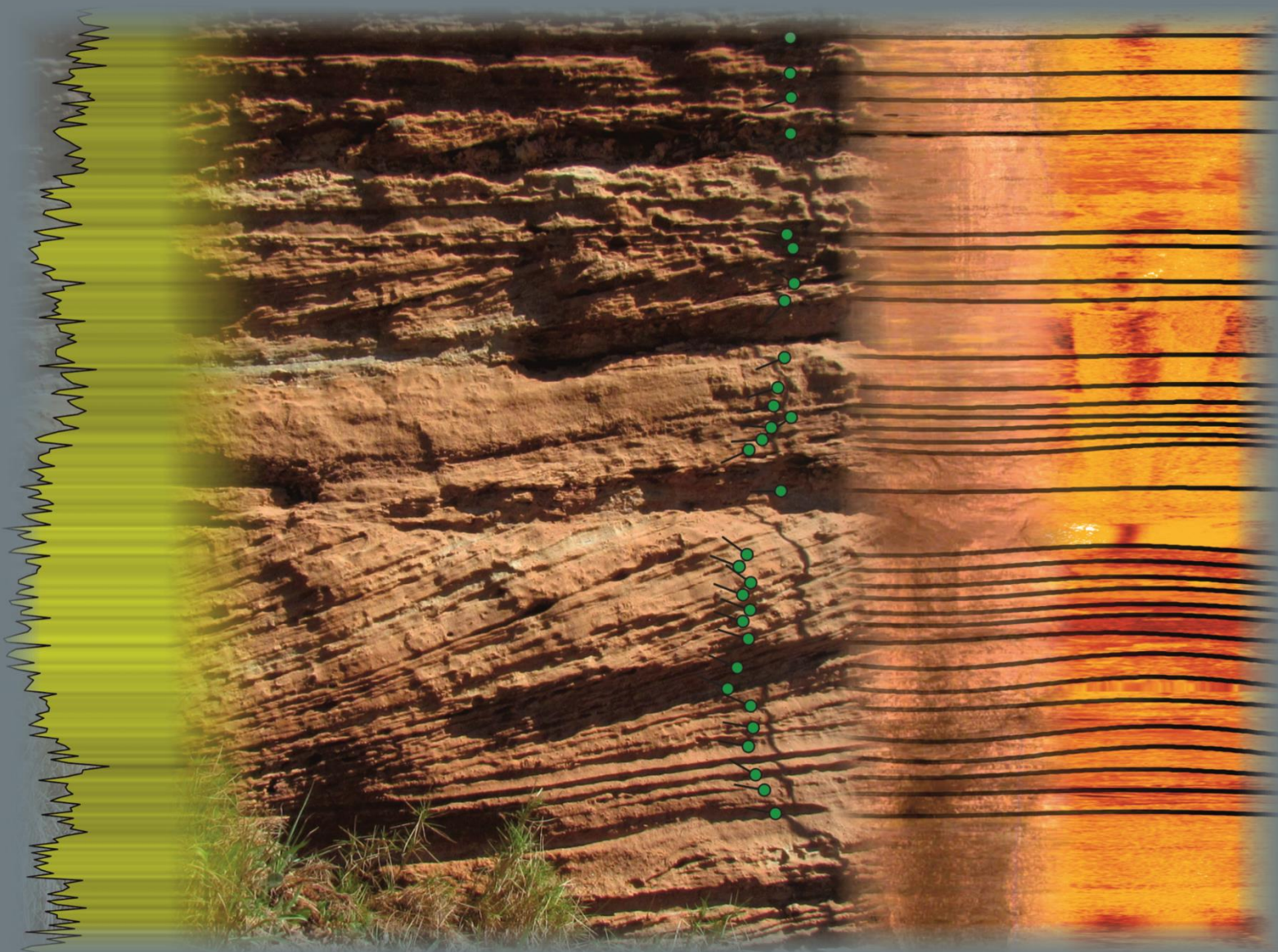
PhD Thesis

Luis Miguel Yeste Pérez

UNIVERSIDAD DE GRANADA

Outcrop Behind Outcrop (O/BO) Characterization and Modelling of Highly Heterogeneous Reservoir Analogues

Tesis Doctoral – PhD Thesis

Luis Miguel Yeste Pérez

Septiembre/September 2020

Directores / Supervisors:

César Viseras Alarcón

Neil David McDougall

UNIVERSIDAD DE GRANADA

Programa Doctorado
Ciencias de la Tierra

La presente Tesis doctoral se enmarca dentro del convenio específico de colaboración entre la Universidad de Granada y Repsol Exploración S.A.

/

This doctoral thesis is part of the specific collaboration agreement between the University of Granada and Repsol Exploración S.A.

Agradecimientos / Acknowledgments

Quisiera mostrar, en primer lugar, mi más sincero agradecimiento a mis directores de tesis, el Dr. César Viseras y el Dr. Neil McDougall por haberme dado esta oportunidad profesional. Gracias, César, por depositar tu confianza en mí desde el primer momento para llevar a cabo este proyecto, por tu dedicación, por tus consejos, por tu apoyo y por guiarme en todas las decisiones que he tomado. Gracias, Neil, por confiar en mí y guiarme a lo largo de este proyecto, por tu paciencia y dedicación y por depositar toda tu experiencia profesional e investigadora en esta tesis. Gracias a ambos por vuestro ánimo y vuestro compromiso. Dicen que los primeros jefes son los que marcan la trayectoria profesional de una persona y, para mí, ha sido una suerte y un honor haber disfrutado de vosotros como mis directores de tesis. Sin lugar a dudas, gracias a vosotros este trabajo ha salido adelante, me habéis permitido crecer tanto en el terreno profesional como personal y estar donde hoy me encuentro os lo debo en gran parte a vosotros.

Agradecer a la Dra. María Luisa Calvache por prestarse amablemente a tutorizar esta tesis y estar siempre disponible, así como por guiarme en mi proceso de formación.

Quisiera mostrar mi especial gratitud a una serie de personas que han contribuido significativamente al desarrollo de esta tesis:

Al Dr. Fernando García-García por transmitirme toda su sabiduría y guiarme en muchas interpretaciones. Sin su ayuda aún podría estar decidiendo en algún que otro afloramiento si es fluvial o tiene influencia mareal.

Al Dr. Augusto Varela por su gran acogimiento en mi paso por Argentina, por darme la oportunidad de disfrutar de esa inolvidable campaña de campo y los buenos momentos vividos por la Patagonia argentina, y por su compañía durante esas incalculables horas de campo y de descripción de testigos en su paso por la Universidad de Granada, transmitiéndome su gran conocimiento sedimentológico y en paleosuelos.

A D. Ricardo Palomino por todo su tiempo, esfuerzo y dedicación, desde el primer momento, con este proyecto, así como por su acogimiento durante mi paso por las oficinas de

Repsol en Noruega. Todo un maestro en modelado geoestadístico gracias al cual he adquirido los conocimientos que hoy poseo en esta materia.

A la Dra. Saturnina Henares por transmitirme sus conocimientos en petrología y diagénesis, su apoyo y su gran colaboración en esta tesis.

A D. Javier Jáimez, un gran profesional y un gran compañero, siempre disponible, y gracias al cual se han obtenido unos datos de sondeos y modelos digitales de afloramiento de invaluable calidad, que han sido el sustento de esta tesis.

Todos ellos grandes personas, grandes profesionales y ha sido todo un lujo haber podido disfrutar de su compañía, experiencia y conocimientos a lo largo de este proyecto.

Agradecer también al Departamento de Estratigrafía y Paleontología por acogerme como uno más desde el primer momento y, en particular, a Dña. Socorro Aranda sin la orientación de la cual aún estaría elaborando dietas y justificantes de gastos.

Al Programa de Doctorado de Ciencias de la Tierra, en especial a su coordinador, el Dr. José Benavente, por su permanente disposición y su dedicación a los estudiantes de doctorado.

A Repsol Exploración S.A. por brindarme la oportunidad de llevar a cabo este proyecto y conceder la financiación necesaria, así como a la Escuela Internacional de Posgrado, en especial al Director de la Escuela de Doctorado de Ciencias, Tecnologías e Ingenierías, el Dr. Antonio García Casco, por su constante disponibilidad con todos los asuntos relacionados con el convenio específico entre la Universidad de Granada y Repsol Exploración S.A. en el que se ha enmarcado esta tesis, así como a D. José Balderas Cejuno, Jefe de Servicio de la Escuela Internacional de Posgrado y a D. Sergio González, de la Unidad de Asuntos Económicos de la Escuela Internacional de Posgrado, por todas sus labores relacionadas con la gestión administrativa de este convenio.

Agradecer al Proyecto de Investigación CGL2017-89618-R de la Agencia Estatal de Investigación (AEI) y Fondo Europeo de Desarrollo Regional (FEDER) otorgado por el Ministerio de Ciencia e Innovación, que ha financiado parte de la investigación de esta Tesis, así como al Grupo RNM 369 del Plan Andaluz de Investigación.

Agradecer a todas las empresas e instituciones que han concedido licencias académicas de softwares específicos a este proyecto de investigación. Especialmente a Schlumberger por la concesión de la licencia académica del software Petrel; a Advanced Logic Technology (ALT) por la concesión de la licencia académica del software WellCAD y, particularmente, a Mariano Rodríguez por estar siempre disponible para solventar todas las dudas que han ido surgiendo

con la adquisición y tratamiento de los datos de diagrafías; y por último, a la Universidad de Manchester, en especial a David Hodgetts, por la creación y desarrollo, así como la concesión de la licencia académica del software VRGS (Virtual Reality Geological Studio). Sin estas licencias académicas para los softwares específicos no hubiera sido posible adquirir los resultados de esta tesis.

Agradecer también a la empresa CEPSA S.A. por su interés mostrado en los resultados de esta Tesis.

Por último, pero no menos importante, y aunque no encuentre las palabras que reflejen mi gratitud, deseo mostrar mis agradecimientos de todo corazón a mis padres, María del Carmen y Antonio, gracias a su apoyo y confianza incondicional que han depositado en mi en todos los aspectos de mi vida, han hecho que esté hoy donde me encuentro; y, por supuesto a ti, Inmaculada, mi compañera de viaje, gracias por creer en mí, por tu apoyo absoluto día tras día y por haber estado a mi lado contra viento y marea en esta etapa de mi vida.

Contents

Extended Abstract

Since the beginning of the 20th century, oil and gas have been the most important energy sources for global economic development. As the most geologically simple reservoirs are progressively produced to depletion, and whilst hydrocarbon consumption continues to increase, it becomes increasingly necessary to identify, evaluate and develop more complex, heterogeneous reservoirs. More than 90% of these reservoirs are located in sedimentary rocks and, as such, research on reservoir sedimentology is both a necessary element in the exploration and discovery of additional hydrocarbons, as well as helping to solve problems related to the appraisal and efficient development of existing sedimentary reservoirs. In addition, the new energy policy paradigm and the growing interest in the development of techniques for CO_2 capture, utilization and geological storage, give a new impulse to the need to understand and manage sedimentary reservoirs.

In order to correctly interpret the evolution of a reservoir, whether from the perspective of hydrocarbon recovery, for underground capture of CO_2 or groundwater exploitation, a detailed three-dimensional knowledge of the heterogeneities characterizing reservoirs, is becoming increasingly necessary. Establishing reservoir heterogeneity is an especially complex problem when analysing non-outcropping formations, as it depends on a number of geological variables, such as geological structure, stratigraphy, lithology and facies, all of which condition the distribution of the petrophysical variables (porosity and permeability). All these variables contribute to reservoir heterogeneity at different scales and, consequently, condition fluid storage and flow in a reservoir.

The description and quantification of geometries, architecture and heterogeneities are fundamental in determining the storage and fluid flow in sedimentary reservoirs. However, in terms of the three-dimensional characteristics of a reservoir and its heterogeneities, the level of precision in our knowledge will greatly depend on the quantity and quality of the available data. In this sense, studies of outcrop analogues have proven to be a valuable tool, complementing

the typically scarce and/or scattered data, characteristic of the subsurface, with direct observations on outcrop.

Traditional data collection in the study of outcrop analogues (e.g. sedimentological logs, geological maps and cross-sections) provides invaluable knowledge with which to characterize subsurface reservoirs. However, it is often difficult to extract reliable quantitative data on the geometries and spatial heterogeneities of sedimentary geobodies. In this sense, new advances in digital techniques and data capture for outcrop analysis, such as digital outcrop models (DOM), are filling this gap, allowing the acquisition and analysis of reliable measurements and interpretations of geological features within their correct geographical context.

Furthermore, when the outcrop-based study is complemented by subsurface information (e.g. core and well logs data), a complete dataset is obtained resulting in an accurate control of the distribution of the heterogeneities in outcrop analogues by direct validation of 1D data (core) with 3D data (outcrop-based data). This methodology is known as Outcrop/Behind Outcrop (OBO) characterization. OBO characterization is a multi-approach set of methodologies aimed at the study of outcrop analogues, integrating outcrop-based and subsurface data from wells drilled immediately behind the outcrop, principally recovering cores and acquiring wireline log data. This integrated approach, contributes significantly to a better understanding of reservoir characteristics and the interpretation of well data from reservoirs typically located at depths of several thousand metres.

In the subsurface, sedimentological characterization of reservoirs based on facies maps and correlations between wells is a common practice and an often successful approach relatively homogeneous reservoirs. However, this methodology cannot accurately represent the distribution of heterogeneities in complex reservoirs. In this sense, and considering recent advances in computational capabilities, this problem can be addressed by three-dimensional geostatistical reservoir modelling.

Geostatistical reservoir modelling is a process of building a digital representation of the three-dimensional architecture of a reservoir and its rock properties, through the integration of geological and engineering data, both descriptive and quantitative. As a rapidly growing discipline in recent years, geostatistical reservoir modelling has become an essential component in the process of reservoir evaluation and development, both for large-scale development projects and for small and medium-scale reservoir projects. Reservoir modelling and simulation can help reservoir development more efficiently, both to plan depletion and improve

hydrocarbon recovery or to evaluate storage and control the injection of CO_2 into the subsurface.

Sedimentary reservoir characterization has always been a key factor in reservoir modelling, effectively acting as the main driver in controlling the prediction of reservoir characteristics. In this sense, outcrop analogues play a valuable role in guiding modellers towards the appropriate levels of geological detail that a reservoir model should reproduce, providing for both 'hard' (geometry and dimensions of geobodies) and 'soft' (knowledge and understanding of sedimentary depositional systems) inputs that control the principal characteristics of a reservoir.

In this context, this thesis project aims to provide datasets from outcrop analogues, in order to significantly improve our knowledge of the sedimentary variables which condition the optimal exploration and development of highly heterogeneous reservoirs. These datasets include outcrop analogue examples of both high and low-sinuosity fluvial systems and a mixed tidal and wave-influenced shoreline system. The project integrates both outcrop and subsurface data, ultimately providing reservoir modelling workflows to reproduce the distribution of heterogeneities in these types of reservoirs.

The outcrops selected for study correspond to the Triassic Red Beds succession of the Iberian Meseta, located in south-central Spain (the Triassic Red Beds of the Iberian Meseta or TIBEM. The TIBEM succession in the study area, located to the east of Alcaraz village (Albacete Province), comprises fluvial to coastal deposits within a linked stratigraphic framework. The ca. 160 m-thick sedimentary succession in this area is divided into four informal member-rank lithostratigraphic units. From base to top, they are: (i) a mudstone-sandstone unit (M-S Unit), composed of high-sinuosity fluvial systems and their associated overbank sandstone deposits embedded in floodplain mudstones; (ii) a sandstone unit (S Unit) corresponding to a low-sinuosity fluvial system; (iii) a heterolithic unit (H Unit) comprising alternating sandstone and mudstone layers deposited in a fluvio-marine transition; and (iv) a mudstone-evaporitic unit (M-E Unit) composed of silt-rich coastal plain facies and intertidal sabkha evaporites. The selected TIBEM succession is not the most complete of this formation, although it is considered as an excellent outcrop analogue for several currently productive subsurface reservoirs, such as the TAGI (*Trias Argilo-Gréseux Inférieur*) reservoir in Algeria. Both formations result from the erosion of Paleozoic granitic and metamorphic terrains during the Tethyan rifting (Middle-Upper Triassic) and were deposited in a peri-intracratonic basin under similar climatic, base level and tectonic conditions. Basin architectures, in both cases, show similar fluvial facies stacking

patterns, varying from high-sinuosity fluvial systems, to low-sinuosity fluvial systems evolving up-section to shallow marine deposits (tidal bars and foreshore deposits).

The workflow designed for this thesis comprises two key elements: (1) Outcrop/Behind Outcrop (OBO) methodology for data acquisition and (2) geostatistical reservoir modelling based on this combined outcrop and subsurface dataset. Through the application of the OBO methodology, "classical" field work was undertaken, based on identification and description of the main sedimentary geobodies in terms of geometry, facies analysis and vertical relationship with other geobodies. In addition, new technical advances, based on photogrammetry with RPAS (Remotely Piloted Aircraft System), were used in the construction of digital outcrop models (DOM), a useful tool for completing field information as well as georeferencing of all key outcrop data.

The complementary subsurface-based study consisted, principally, of the acquisition of both cores and well logs by drilling boreholes directly behind the selected outcrops. Additionally, geophysical techniques such as GPR (Ground Penetrating Radar) were also utilized in order to provide a complete subsurface dataset. Through the integration of data, from both outcrop and subsurface (OBO characterization), key characteristics, that help in the identification of the geobodies, as well as the spatial distribution of the heterogeneities that delimit these geobodies were established. In addition, quantitative conceptual models and paleogeographic maps, that represent the distribution of the identified geobodies, were also generated. OBO characterization provided the necessary input data for the second key element of the study; geostatistical reservoir modelling. This modelling process included the construction of a 3D stratigraphic model and determining the spatial distributions of facies in the 3D model with geostatistical techniques. Two stochastic simulation algorithms for facies modelling were used in this work: (1) object-based modelling and (2) multi-point statistics-based modelling.

The first part of this research has focused on the OBO characterization of the studied succession with the aim of extracting the geometrical and dimensional properties of the sedimentary geobodies that comprise the Mudstone-Sandstone (M-S Unit), Sandstone (S Unit) and Heterolithic (H Unit) Units, to recognize the lateral and vertical variability of heterogeneities at lithofacies scale, and to generate quantitative conceptual models and paleogeographic reconstructions for these units.

Results of the OBO characterization of the M-S Unit show a lateral and vertical stacking of four types of geobodies: (i) channelized sandstone bodies; (ii) asymmetrical sigmoidal-shaped sandstone bodies; (iii) lobe-shaped to sheet-like sandstone bodies; and (iv) sheet-like

mudstones. These geobodies represent, respectively, meandering channel, point bar, crevasse-channel-splay and floodplain sub-environments, all comprising a distal, low-gradient meandering fluvial system. The full integration of outcrop and subsurface datasets has enabled generation of a robust conceptual model with predictive potential when establishing the three-dimensional stacking of facies, distribution of heterogeneities, and the connectivity between reservoir rock geobodies of both primary (channel) and secondary (crevasse complex) interest in this type of fluvial reservoir.

In the S Unit, two types of geobodies were identified: (i) channel and (ii) compound bar. These geobodies represent a perennial deep braided fluvial system. By integrating both surface and subsurface data, a detailed paleogeographic reconstruction is proposed, including the dimensions and spatial distribution of the main architectural elements, as well as key features in core, Gamma Ray log and dip tadpole patterns, that help identify and characterize this type of reservoir.

Finally, the H Unit is characterized by the deposits of a mixed tidal and wave-influenced shoreline system comprising three main types of reservoir geobody: (i) elongate geobodies, associated with subtidal sandbar facies and intertidal sandbar facies; (ii) asymmetric-sigmoidal geobodies formed by tidal-dominated point-bar facies; and (iii) a tabular geobody associated with a hyperpycnite sandbody facies and open-coast, linear shoreface facies. The full integration of outcrop and subsurface datasets has enabled the generation of a predictive conceptual model, based on facies analysis, which through integration with a sequence stratigraphic framework has allowed us to characterise the development through time of the system, in response to the changing balance between shoreline processes, all of which impacts on both geobody geometries and reservoir potential.

The second part of this research has focused on reservoir modelling of the M-S Unit, characterized by high-sinuosity fluvial systems. A critical element in this chapter was the design of appropriate modelling workflows with Petrel$_{TM}$ which would best reproduce with a high detail the distribution of heterogeneities, both at the scale of geobodies and at the finer scale of lithofacies by using both object-based modelling technique and logical statement calculations. The workflow at geobody scale was used to construct a 3D training image (TI) of a fluvial reservoir, comprising both a meandering channel system and its associated overbank sandstone deposits. This TI was subsequently used as mathematical pattern in MPS (Multi-Point Statistical) simulations, in order to establish whether it was able to assist in the prediction of the reservoir geobodies, as well as confirming to what extent this prediction matched the outcrop. MPS

simulations generated good predictions for geobodies throughout the model framework with mean match values ranging from 15% to 44%. The workflow at the scale of lithofacies was then used to estimate the static connectivity of the reservoir in the M-S Unit. The results of this exercise reveal the importance of considering both point bar and, especially, crevasse-splay geobodies, besides channel geobody, in enhancing static reservoir connectivity in this type of reservoirs.

The multidisciplinary workflow developed in this thesis highlights the importance of studies focused on the sedimentological characterization of outcrop analogues, as an effective approach to significantly improving our knowledge of sedimentary reservoirs. The integrated study of outcrop-derived and subsurface data, has allowed the generation of quantitative conceptual models useful in geostatistical modelling. This is especially so when planning modelling strategies as well as producing exportable 3D training images that can be used as input in the facies modelling process in real reservoirs using the MPS technique. In addition, recent technical advances in digital outcrop model characterization and data capture have proven to be effective tools, that not only allow us to extract valuable information from outcrops, but also leads to accurate uncertainty analysis of reservoir modelling results.

Resumen Extendido

Desde principios del siglo XX el petróleo y el gas han sido las fuentes de energía más importantes para el desarrollo económico mundial. A medida que los yacimientos de hidrocarburos geológicamente más simples han estado produciendo progresivamente hasta su agotamiento, la demanda de hidrocarburos ha continuado en aumento, por lo que se hace cada vez más necesario identificar, evaluar y desarrollar yacimientos más complejos y heterogéneos. Más del 90% de estos yacimientos se encuentran en rocas sedimentarias, lo que contribuye al hecho de que la investigación focalizada en la caracterización sedimentológica de rocas almacén sea cada vez más importante, tanto para la exploración de nuevos yacimientos como para la ejecución de planes de desarrollo eficiente y gestión de los yacimientos ya conocidos. Por otro lado, el nuevo paradigma de política energética y el creciente interés por el desarrollo de técnicas de captura y almacenamiento geológico de CO_2 imprime un nuevo impulso a la necesidad de comprensión y control de las rocas almacén.

Para interpretar correctamente la evolución de un yacimiento, ya sea desde la perspectiva de la recuperación de hidrocarburos, para el secuestro subterráneo de CO_2 o para la explotación de aguas subterráneas, se hace cada vez más necesario el conocimiento detallado, en 3 dimensiones, de las heterogeneidades que presenta la roca almacén. Establecer la heterogeneidad de un yacimiento se convierte en uno de los problemas más complejos a la hora de analizar formaciones no aflorantes, ya que ésta depende de un elenco de condiciones geológicas, tales como estructura, estratigrafía, litología y facies, que condicionan la distribución de las variables petrofísicas (porosidad y permeabilidad) en el reservorio. Todas estas variables contribuyen a la heterogeneidad de la roca almacén a diferentes escalas y, por tanto, condicionan el almacenamiento y el flujo de fluidos en un yacimiento.

La descripción y cuantificación de geometrías, arquitectura y heterogeneidades son fundamentales para determinar el almacenamiento y el flujo de fluidos en los yacimientos ligados a rocas sedimentarias. Sin embargo, el nivel de precisión de nuestro conocimiento, en

relación con las características tridimensionales de un yacimiento y sus heterogeneidades, dependerá en gran medida de la cantidad y calidad de los datos disponibles. En este sentido, los estudios de análogos aflorantes han demostrado ser una herramienta valiosa complementando los datos del subsuelo, que a menudo son escasos y/o dispersos, con observaciones directas sobre afloramientos.

Las técnicas tradicionales de recopilación de datos en el estudio de análogos aflorantes (como son, por ejemplo, el levantamiento de columnas sedimentológicas, la elaboración de mapas de facies y el establecimiento de correlaciones estratigráficas) proporcionan un invaluable conocimiento con el que caracterizar las rocas almacén en el subsuelo. Sin embargo, a menudo es difícil extraer datos cuantitativos fiables sobre las geometrías y heterogeneidades de los cuerpos sedimentarios. En este sentido, los nuevos avances en las técnicas digitales y la captura de datos para el análisis de afloramientos, como son los modelos digitales de afloramiento (DOM), están cubriendo esta brecha permitiendo la adquisición y el análisis cuantitativo, perfectamente georreferenciado, de mediciones e interpretaciones de las características geológicas de los afloramientos.

Adicionalmente, cuando el estudio de análogos aflorantes se completa con información del subsuelo (como, por ejemplo, testigos de roca y diagrafías), se obtiene un conjunto de datos completo que proporciona un control preciso de la distribución de las heterogeneidades en los análogos aflorantes mediante la validación directa de datos unidimensionales (testigo de roca y diagrafías) con datos tridimensionales (datos geométricos a partir de afloramientos). Esta metodología se conoce como caracterización *Outcrop/Behind Outcrop* (OBO). La caracterización OBO engloba un conjunto de metodologías con un enfoque multidisciplinar, integrando datos obtenidos en afloramiento con datos procedentes de información de subsuelo, obtenida mediante la perforación de pozos y adquisición de datos geofísicos en una posición inmediatamente trasera al afloramiento seleccionado. Este enfoque integrado, que combina información de afloramiento y subsuelo, contribuye significativamente a una mejor comprensión de las características de las rocas almacén y a la interpretación de los datos de subsuelo obtenidos en yacimientos reales, normalmente ubicados a miles de metros bajo la superficie.

Por otro lado, la caracterización sedimentológica de yacimientos basada en mapas de facies y las correlaciones sedimentológicas entre pozos puede ser fiable en reservorios relativamente homogéneos, pero no consiguen representar con precisión la distribución de heterogeneidades en formaciones altamente heterogéneas. En este sentido, con los avances en

las capacidades computacionales que existen hoy día, este problema puede ser abordado mediante la modelización geoestadística tridimensional de yacimientos. El modelado geoestadístico de yacimientos es un proceso de construcción de una representación digital de la arquitectura tridimensional de un yacimiento y sus propiedades, mediante la integración de datos geológicos e ingenieriles, tanto descriptivos como cuantitativos. Como disciplina de rápido crecimiento en los últimos años, el modelado geoestadístico de yacimientos se ha convertido en una parte esencial en la evaluación y desarrollo de un yacimiento, tanto en proyectos de desarrollo de gran envergadura como para proyectos de yacimientos de pequeña y mediana escala, ya que el modelado y simulación de yacimientos pueden ayudar a un desarrollo más eficiente de los mismos, tanto para planificar el agotamiento y mejorar la recuperación de hidrocarburos como para estimar el almacenamiento y controlar la inyección de CO_2 en el subsuelo.

La caracterización sedimentológica de rocas almacén siempre ha sido clave en el modelado de yacimientos, actuando de manera efectiva en el control de la predicción de las características de la roca almacén. En este sentido, los análogos aflorantes desempeñan un papel valioso para orientar a los modeladores hacia los niveles apropiados de detalle geológico que debe representar un modelo de yacimiento, proporcionando tanto datos geométricos y dimensionales de las rocas almacén como el conocimiento y comprensión de la dinámica de los ambientes sedimentarios que dieron lugar a la roca que alberga el yacimiento.

En este contexto, este proyecto de Tesis tiene como objetivo proporcionar los conjuntos de datos necesarios a partir del estudio de análogos aflorantes para mejorar significativamente el conocimiento de las variables sedimentarias que condicionan la exploración y el desarrollo óptimo de reservorios altamente heterogéneos. Estos conjuntos de datos incluyen ejemplos análogos aflorantes de sistemas fluviales, de alta y baja sinuosidad, y un sistema costero mixto influenciado por las mareas y el oleaje. Este proyecto integra tanto datos de afloramiento como de subsuelo, proporcionando en última instancia flujos de trabajo de modelado de yacimientos para reproducir la distribución de heterogeneidades en este tipo de yacimientos.

Los afloramientos seleccionados para este estudio corresponden a una sucesión Triásica expuesta en el sureste de España (el Triásico de Capas Rojas de la Cobertera Tabular de la Meseta Ibérica o TIBEM). La sucesión del TIBEM estudiada, ubicada en las inmediaciones del pueblo de Alcaraz (provincia de Albacete), comprende tanto depósitos sedimentarios fluviales como costeros. La sucesión sedimentaria, de casi 160 m de espesor en el área de estudio, se divide en cuatro unidades litoestratigráficas informales que, de base a techo, son: (i) unidad lutítico-

arenosa (Unidad M-S), formada por sistemas fluviales de alta sinuosidad y sus depósitos de desbordamiento asociados embebidos en lutitas de llanura de inundación; (ii) unidad arenosa (Unidad S), caracterizada por un sistema fluvial de baja sinuosidad; unidad heterolítica (Unidad H), que comprende capas alternas de areniscas y lutitas depositadas en una zona de transición fluvio-marina; y (iv) unidad lutítico-evaporítica (Unidad M-E), caracterizada por depósitos de llanura costera rica en lutitas y evaporitas típicas de ambientes de *sabkha* intermareal. La sucesión del TIBEM seleccionada no es la más completa de esta formación, sin embargo, corresponde al que puede considerarse como un afloramiento análogo para varios reservorios subterráneos actualmente productivos, como es el caso del almacén TAGI (*Trias Argilo-Gréseux Inférieur*) en Argelia. Ambas formaciones resultan de la erosión de terrenos Paleozoicos graníticos y metamórficos durante el Triásico Medio-Superior y son depositados bajo unas condiciones climáticas, de nivel de base y tectónica similares. La arquitectura de cuenca, en ambos casos, muestra patrones de apilamiento de facies fluviales muy parecidos, que varían desde sistemas fluviales de alta sinuosidad hasta sistemas fluviales trenzados, evolucionando hacia el techo a depósitos marinos poco profundos (barras de mareas y depósitos costeros).

El flujo de trabajo diseñado para el desarrollo de esta investigación comprende dos elementos clave: (1) la metodología *Outcrop/Behind Outcrop* (OBO) para la adquisición de datos y (2) el modelado geoestadístico de yacimientos a partir de estos datos que suman información de afloramiento y de subsuelo. A través de la aplicación de la metodología OBO se llevó a cabo un trabajo de campo clásico sobre los afloramientos seleccionados, basado en la identificación y descripción de los principales geocuerpos sedimentarios en términos de geometría, análisis de facies y relación vertical con otros geocuerpos. Además, se realizó la construcción de modelos digitales de los afloramientos (DOMs) a través de fotogrametría con RPAS (*Remote Piloted Aircraft System,* normalmente conocido como dron), con el objetivo de completar la información de campo, así como para poder georreferenciar todos los datos clave de los afloramientos estudiados. El estudio complementario del subsuelo consistió, principalmente, en la adquisición tanto de testigos de roca como de diagrafías (rayos gamma natural y espectral e imágenes óptica y acústica de las paredes del pozo) mediante la perforación de un total de 15 pozos ubicados directamente detrás de los afloramientos seleccionados. Adicionalmente, también se utilizaron técnicas geofísicas como GPR (*Ground Penetrating Radar,* Georradar) para proporcionar un conjunto de datos subterráneo más completo. A través de la integración de datos, tanto de afloramiento como del subsuelo (caracterización OBO), se establecieron las características clave, que ayudan a la identificación de los geocuerpos sedimentarios, así como a la distribución espacial de sus heterogeneidades, generando modelos conceptuales cuantitativos y mapas

paleogeográficos que representan la distribución de los geocuerpos identificados. La caracterización OBO proporcionó los datos de entrada necesarios para el segundo elemento clave del estudio: el modelado geoestadístico de yacimientos. Este proceso de modelado incluyó la construcción de un modelo estratigráfico y la determinación de las distribuciones espaciales de facies mediante técnicas geoestadísticas. En este trabajo se utilizaron dos algoritmos de simulación estocástica para el modelado de facies: (1) modelado basado en objetos y (2) modelado basado en estadísticas multipunto.

La primera parte de esta investigación se ha centrado en la caracterización OBO de la sucesión estudiada para tratar de extraer las propiedades geométricas y dimensionales de los geocuerpos sedimentarios que comprenden las Unidades lutítico-arenosa (Unidad M-S), arenosa (Unidad S) y heterolítica (Unidad H), reconocer la variabilidad lateral y vertical de las heterogeneidades a escala de litofacies, y generar modelos conceptuales cuantitativos y reconstrucciones paleogeográficas que representen la variabilidad lateral y vertical de las heterogeneidades que componen los geocuerpos sedimentarios identificados.

Los resultados obtenidos a través de la caracterización OBO en la Unidad M-S muestran que esta unidad está compuesta por el apilamiento lateral y vertical de cuatro tipos de geocuerpos: (i) geocuerpos arenosos canalizados; (ii) geocuerpos arenosos sigmoidales; (iii) geocuerpos arenosos lobulares y (iv) geocuerpos lutíticos tabulares. Estos geocuerpos representan, respectivamente, los subambientes de canal meandriforme, *point bar*, *crevasse-splay* y llanura de inundación; dentro de un sistema fluvial de alta sinuosidad distal de bajo gradiente. La integración de los conjuntos de datos de afloramiento y subsuelo ha permitido la generación de un modelo conceptual robusto y con potencial predictivo ya que establece patrones de apilamiento tridimensional de facies, de distribución de heterogeneidades y de conectividad entre los geocuerpos de roca almacén, tanto los que son de interés primario (canal) como secundario (crevasse-splay) en este tipo de almacén de origen fluvial.

En la Unidad S se identificaron dos tipos de geocuerpos: (i) canal y (ii) barra compuesta. Estos geocuerpos representan un sistema fluvial de baja sinuosidad (trenzado). A través de la integración de datos de afloramiento y subsuelo de esta unidad se propone una reconstrucción paleogeográfica detallada, que incluye las dimensiones y distribución espacial de los principales geocuerpos identificados, así como las características clave en testigo de roca, registro de rayos gamma y patrones de paleocorrientes que ayudan a identificar este tipo de yacimientos.

Por último, la Unidad H está caracterizada por depósitos de un sistema costero mixto, influenciado por las mareas y el oleaje. En esta unidad se identificaron 3 tipos de geocuerpos

almacén: (i) geocuerpos elongados, asociados con barras intermareales y submareales; (ii) geocuerpos sigmoidales, caracterizados por facies típicas de *point bars* mareales; y (iii) geocuerpos tabulares asociados con depósitos hiperpícnicos o con depósitos de *shoreface*. La integración de datos de afloramiento y subsuelo en esta unidad ha posibilitado la generación de un modelo conceptual predictivo, basado en el análisis de facies, que a través de su integración en un marco secuencial estratigráfico nos ha permitido determinar el desarrollo temporal del sistema, en respuesta al equilibrio cambiante entre los procesos de la costa y su impacto tanto en las geometrías de los geocuerpos resultantes de la dinámica litoral como en el potencial de la roca almacén a la que dan lugar.

La segunda parte de esta investigación se ha centrado en el modelado geoestadístico de la Unidad M-S, caracterizada por un sistema fluvial de alta sinuosidad. Un elemento crítico en esta parte de la investigación fue el diseño de flujos de trabajo de modelado apropiados con el *software* específico Petrel$_{TM}$ capaces de reproducir con un alto grado de detalle, la distribución de heterogeneidades, tanto a escala de geocuerpos sedimentarios como a escala de litofacies, mediante el uso de técnicas de modelado basadas en objetos y cálculos de declaraciones lógicas. El flujo de trabajo a escala de geocuerpos sedimentarios diseñado se utilizó para la construcción de una imagen de entrenamiento tridimensional (*Training Image – TI*) de un yacimiento fluvial de alta sinuosidad, compuesto por un sistema de canales meandriformes y sus depósitos de desbordamiento asociados. Esta TI fue utilizada como patrón matemático para realizar la simulación mediante estadísticas multipunto (MPS), con el fin de establecer cómo esta TI puede ayudar en la predicción de los geocuerpos almacén, así como confirmar en qué medida esta predicción coincide con el afloramiento. Los resultados obtenidos a partir de las simulaciones MPS muestran unas buenas predicciones para los geocuerpos en todo el marco del modelo, con valores medios de coincidencia con el afloramiento que oscilan entre el 15% y el 44%. El flujo de trabajo de modelado a escala de litofacies fue utilizado para estimar la conectividad estática del yacimiento que representa la Unidad M-S. Los resultados revelan la importancia de considerar tanto los geocuerpos de *point bar* como los geocuerpos de *crevasse-splay*, adicionalmente al geocuerpo de canal, en la evaluación de la conectividad estática de un yacimiento de este tipo.

El flujo de trabajo multidisciplinar desarrollado en esta Tesis pone de manifiesto la importancia de los estudios focalizados en la caracterización sedimentológica de análogos aflorantes para profundizar en el conocimiento de los yacimientos de hidrocarburos en rocas sedimentarias. Mediante el estudio integrado de datos derivados de afloramiento y subsuelo se han podido elaborar modelos conceptuales cuantitativos que han demostrado ser de gran utilidad en el modelado geoestadístico de yacimientos, especialmente a la hora de diseñar

estrategias de modelado y de producir imágenes de entrenamiento exportables y que sirvan de entrada en el modelado de facies en yacimientos reales mediante la técnica MPS. Además, los avances técnicos recientes en la caracterización digital de afloramientos y la captura de datos han demostrado ser una herramienta eficaz que no solo permite extraer una información valiosa de los afloramientos, sino que también conduce a un análisis preciso de la incertidumbre de los resultados del modelado.

CHAPTER 1:

Introduction

1.1. Introduction

The description and quantification of geometries, architecture and heterogeneities are fundamental to constraining the connectivity of facies and distribution of permeability in sedimentary reservoirs. This has important implications for establishing approaches to hydrocarbon exploration and recovery, underground CO_2 storage and groundwater exploitation. Relationships between depositional environments, sedimentary facies patterns, diagenesis, and petrophysical properties have been widely described from a range of different settings, demonstrating the value of sedimentology in reservoir characterization. Datasets acquired from outcrop and cores can provide information on how sedimentary facies stack spatially and aid in development of predictive models for subsurface analogues. Thus, the multi-scale characterization of sediment body geometries, heterogeneities, architecture and connectivity will be of vital importance for the evaluation and modelling of siliciclastic reservoirs.

Reservoir heterogeneity conditions flow circulation in reservoirs (Akaku, 2008; Ambrose *et al*., 2008; Sifuentes *et al*., 2009; Deng *et al*., 2012) and influences the reservoir quality of potential reservoirs (Henares *et al*., 2016). The goal of building geological models for flow simulation studies is the integration, at different scales, of the heterogeneities and relevant petrophysical characteristics that control fluid flow in a reservoir (Corbett & Potter, 2004). The outcrop-scale represents an intermediate scale between seismic and well data, and has the advantage of direct access to different observation scales, from the macro-scale, represented by the stacking patterns of geobodies (Hubbard *et al*., 2009), to the mesoscale, as represented by the distribution and type of geobodies in the depositional system, down to the microscale in

which the composition, texture of the sediment and diagenetic evolution constrain the quality, fluid flow, and recovery or storage efficiency of a reservoir (Yoshida *et al.*, 2001).

To understand the evolution of a reservoir, whether from the perspective of hydrocarbon recovery, or for underground carbon sequestration or groundwater exploitation, a detailed 3D knowledge of the formation is necessary. However, the level of precision in our knowledge of the 3D characteristics will depend very much on the quantity and quality of the available data. In this sense, studies of outcrop analogues have proven to be a valuable tool, complementing the typically scarce and/or scattered data, characteristic of the subsurface, with direct observations on outcrop.

For realistic 3D reservoir modelling, detailed data on the geometry, dimensions and spatial distribution of geobodies, as well as of variables which contribute to internal heterogeneities, such as grain size, sand:mud ratio, facies, lithology, potential flow barriers, porosity and permeability, is essential (Falivene *et al.*, 2007). Integrated studies of both outcrop and subsurface data, known as outcrop/behind outcrop characterization (hereinafter OBO characterization; Slatt *et al.*, 2012; Viseras *et al.*, 2018; Yeste *et al.*, 2019, 2020) has been revealed as the most effective technique in the study of outcrop analogues, providing useful datasets for the evaluation and prediction of reservoir heterogeneities (Rarity *et al.*, 2014; Henares *et al.,* 2016; Viseras *et al.*, 2018; Yeste *et al.*, 2019, 2020).

Triassic rift basins located along the northern Atlantic margins are well-known oil and gas exploration targets. Some examples of currently productive Triassic reservoirs are: the TAGI/TAGS reservoir (Trias Argilo-Gréseux Inférieur & Superior) in the Ghadames petroleum province (Algeria, Tunisia); Triassic levels from the Essaouira Basin (Morocco); the Wolfville Formation of the Fundy basin (Nova Scotia, Canada); the Sherwood Sandstone Group in the Slyne Basin of offshore West Ireland, Dorset Coast (SW UK) and Irish Sea Basin (NW UK), and the Skagerrak Formation (Central North Sea, UK and Norway), amongst others.

During the Triassic, deposition in these basins developed in response to similar tectonic and climatic conditions, most notably during the Carnian interval (Arche & López-Gómez, 2014). Such semi-arid climates and extensional tectonic frameworks favoured the development of similar reservoirs in fluvio-deltaic deposits found throughout the (paleo-) Atlantic margins.

There is accordingly a double interest from both the oil industry and academia in the thorough characterization of such Triassic deposits. This has promoted a multi-scale approach to building a comprehensive picture of the three-dimensional distribution of rocks-pores-fluids in the reservoir by using all available data sources, such as outcrop analogues studies (Arche *et*

al., 2002; Fabuel-Perez *et al.,* 2010; Arche & López-Gómez, 2014; Henares *et al.*, 2014, 2016; Viseras *et al.,* 2018; Yeste *et al.,* 2019, 2020).

In this sense, this thesis has as its general objective the characterization of Triassic outcrop analogues with highly heterogeneous properties to broaden our knowledge of the sedimentary variables conditioning the optimal exploration and exploitation of this type of reservoir.

The outcrops selected for study correspond to the Triassic Red Beds succession of the Iberian Meseta, located in south-central Spain (the TIBEM of Viseras *et al.*, 2011; Henares *et al.*, 2014, 2016; Viseras *et al.*, 2019; Yeste *et al.*, 2019). The TIBEM succession in the study area (Fig. 1.1), located to the east of Alcaraz village (Albacete Province), comprises fluvial to coastal deposits within a linked stratigraphic framework. The ca. 160 m-thick sedimentary succession in this area is divided into four informal member-rank lithostratigraphic units (Fig. 1.1; Yeste *et al.*, 2019; 2020). From base to top, they are: (i) a mudstone-sandstone unit (M-S Unit), composed of high-sinuosity fluvial systems and their associated overbank sandstone deposits embedded in floodplain mudstones (Yeste *et al.* 2020); (ii) a sandstone unit (S Unit) corresponding to a low-sinuosity fluvial system (Yeste *et al.* 2019); (iii) a heterolithic unit (H Unit) comprising alternating sandstone and mudstone layers deposited in a fluvio-marine transition zone (Yeste *et al.*, 2017; García-García *et al.*, 2017); and (iv) a mudstone-evaporitic unit (M-E Unit) composed of silt-rich coastal plain facies and intertidal sabkha evaporites.

1.2. The importance of reservoir characterization

Since the beginning of the 20th century, oil and gas have been the most important energy sources for global industries and national economic development (Yu *et al.,* 2018). However, over 90% of the world's hydrocarbon reserves are located in sedimentary rocks and, as such, research on reservoir sedimentology is both a necessary element in the exploration and discovery of additional hydrocarbons, as well as helping to solve problems related the appraisal and development of sedimentary reservoirs (Yu *et al.,* 2018). In addition, despite the challenges of the new energy policy paradigm and the role of new technologies, which facilitate a switch from carbon intensive fossil fuels to low carbon energy carriers (e.g. natural gas) via CO_2 capture, utilization and storage (CCUS), it is still necessary to continue broadening our knowledge of reservoir sedimentology (Surdam, 2013).
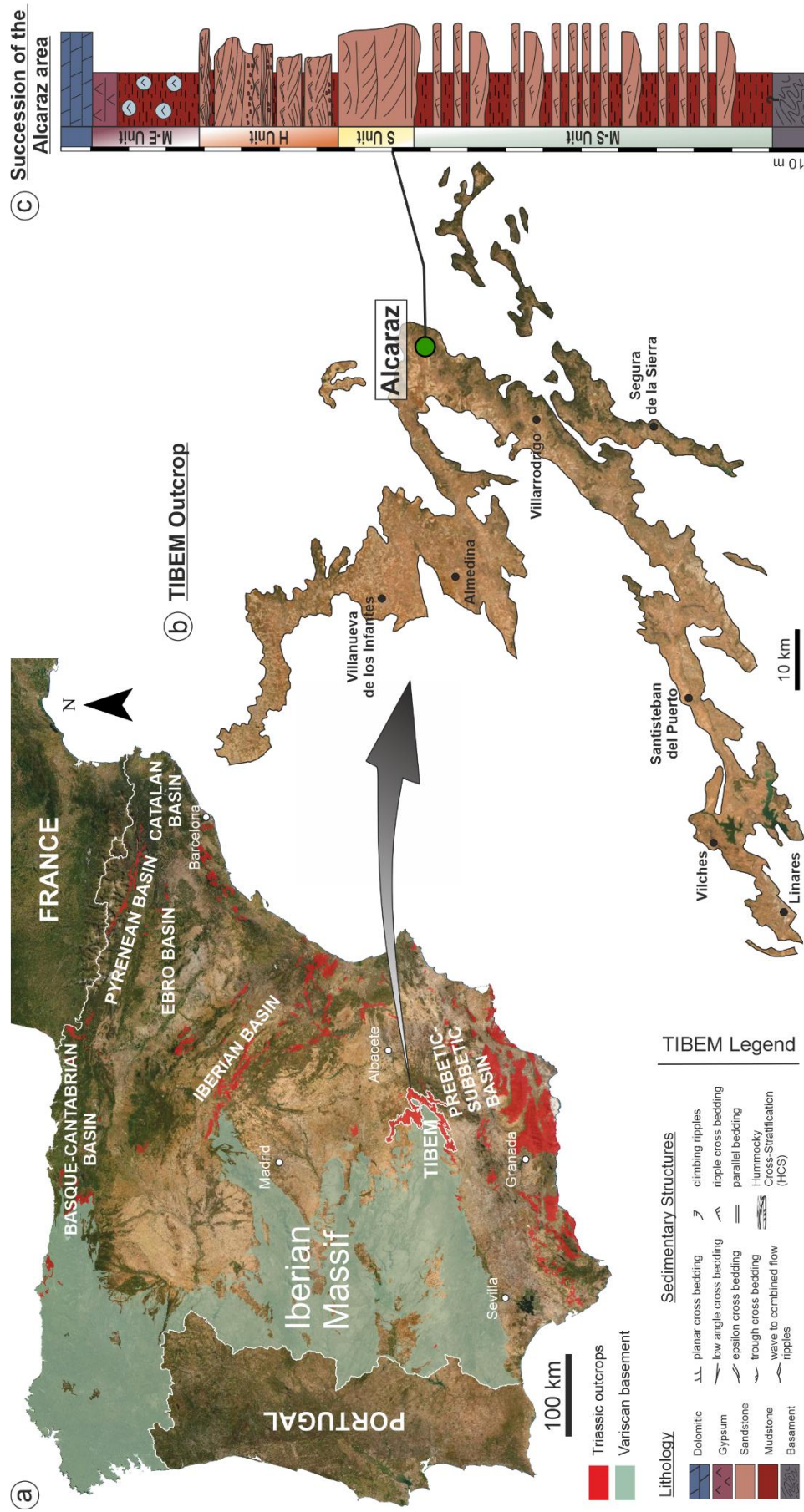
Fig. 1.1. Location of study area. **(a)** Distribution of Triassic basins in eastern Iberia (modified from GEODE, 2020 and López-Gómez *et al.*, 2019). **(b)** Detailed view of the TIBEM outcrop area, and **(c)** a synthetic stratigraphic succession of the selected study area (eastern of Alcaraz village). M-S Unit: Mudstone-Sandstone Unit; S Unit: Sandstone Unit; H Unit: Heterolithic Unit; M-E Unit: Mudstone-Evaporitic Unit.

Reservoir sedimentology is a an applied discipline that generates diverse data types which are used in the study and interpretation of depositional environments, diagenesis, and the formation mechanisms of reservoirs, with the objective of both analysing and determining the necessary geological knowledge required to improve the exploration and development of reservoirs (Yu *et al.,* 2018). It focuses on the analysis and prediction of reservoir heterogeneity at different scales through the integration of geological, seismic, well logging, and core data.

The description and characterization of reservoirs are the main objectives in the exploration and development of reservoirs. Within this context, significant interest is focused on the concept of reservoir heterogeneity. This is simply because heterogeneity in reservoir characteristics strongly impacts the reserves, yield and productivity of the reservoir. In other words, the study of reservoir heterogeneities constitutes the basis for appraisal and development schemes, providing an important geological basis for the evaluation of reservoirs, discovering productivity potential, and predicting the final recovery ratio (Yu *et al.,* 2018).

Reservoir heterogeneity is one of the most complex problems in subsurface formations (Ma, 2019). Fluid storage and flow in porous media depend on a variety of geological and petrophysical variables, such as, geological structure, stratigraphy, facies, lithology, porosity and permeability (Ma, 2019). All these variables contribute to reservoir heterogeneity and can be identified at different scales.

Reservoir heterogeneity is mainly classified on the basis of research scale or scope, reservoir genesis or sedimentary boundary, and influence on fluids (Yu *et al.,* 2018). Weber (1986) defined the scales of reservoir heterogeneity, based on size, genetic origin and influence on fluid flow; in macro-, meso-, and micro-scale heterogeneities (Fig. 1.2). At mega-scale (1-10km) reservoir heterogeneity is typically associated with geobody stacking. At meso-scale (1-100m), characteristic patterns of permeability zonation and permeability baffles, with characteristic shapes and distributions related to depositional environments and lithofacies variability, commonly occur within certain types of geobody. At micro-scale (<1mm), the heterogeneity is related to the grain-size, sorting, detrital composition, pore types, pore network and diagenetic processes.

The term 'geobody', as used in this study, refers to the geological elements in a reservoir. These elements are defined on the basis of their specific geometry (including width, thickness and orientation), bounding surfaces, internal sedimentary features (lithofacies and/or facies associations) and the location within the depositional environment. This is a term commonly used in geological modelling. Geobody is also equivalent to 'architectural element' as defined

by Miall (1985), 'depositional elements' defined by Kostic & Aigner (2007) or the storeys of Ford & Pyles (2014).

Research focussed on the classification, description and analysis of reservoir heterogeneity is therefore of vital importance for the exploration, appraisal and development of reservoirs, which, in the case of the latter specifically requires reservoir modelling.
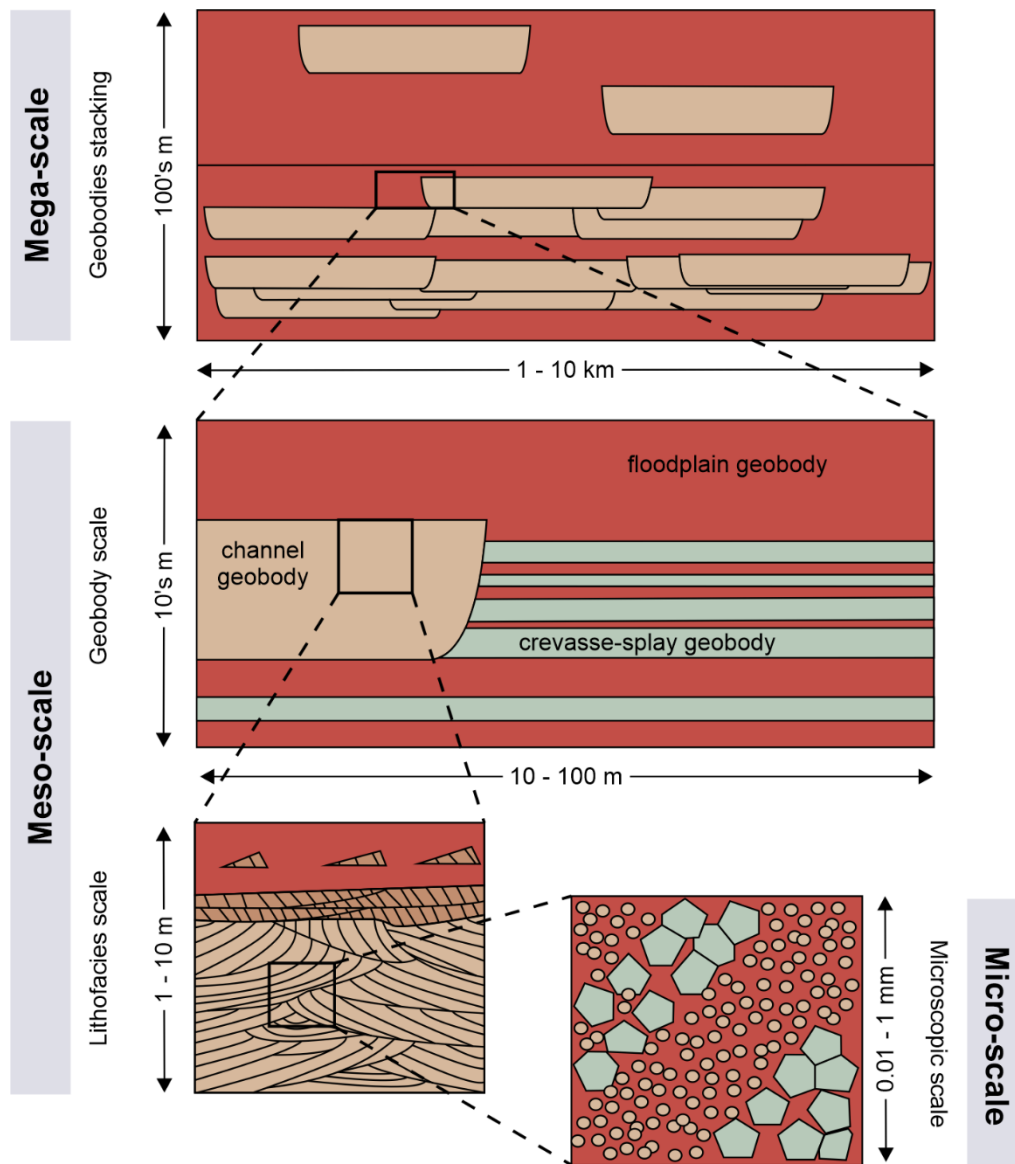
Fig. 1.2. Scales of reservoir heterogeneity (modified from Weber, 1986).

1.3. The value of outcrop studies in reducing subsurface uncertainty and prediction of heterogeneity

Outcrop-based studies provide an important primary source of knowledge on basic principles in geology. They are extensively used within both academia and industry for research and training, as well as for the development of conceptual and predictive geological models (Rarity *et al*., 2014; Bowman & Smyth, 2016; Viseras *et al.*, 2018; Yeste *et al.,* 2019, 2020).

Seismic reflection data can image large-scale reservoir architectures, both in 2D and especially in 3D where line spacing is sufficiently dense, although vertical and horizontal resolution is typically limited to tens of metres (Fig. 1.3). Core and wireline logs, in contrast, can provide a higher resolution image of the reservoir albeit sampling only a very small percentage of the rock volume with an effective one-dimensional character when compared to seismic. Outcrops, however, offer direct two- and often three-dimensional observations of rock bodies, their geometries, architecture and lithological heterogeneities ranging over scales from less than 1 cm to several tens of kilometres, in well exposed areas (Fig. 1.3). Thus, outcrop-based studies provide information at a scale ideally located between seismic and well data, and are commonly used as analogues for subsurface reservoir characterization and modelling (e.g. Alexander 1993; Bryant & Flint 1993; Tinker 1996; Grammer *et al.* 2004; Cabello *et al*., 2010; Viseras *et al.*, 2018; Cabello *et al.,* 2018; Puig *et al.,* 2019; Yeste *et al.,* 2019, 2020).
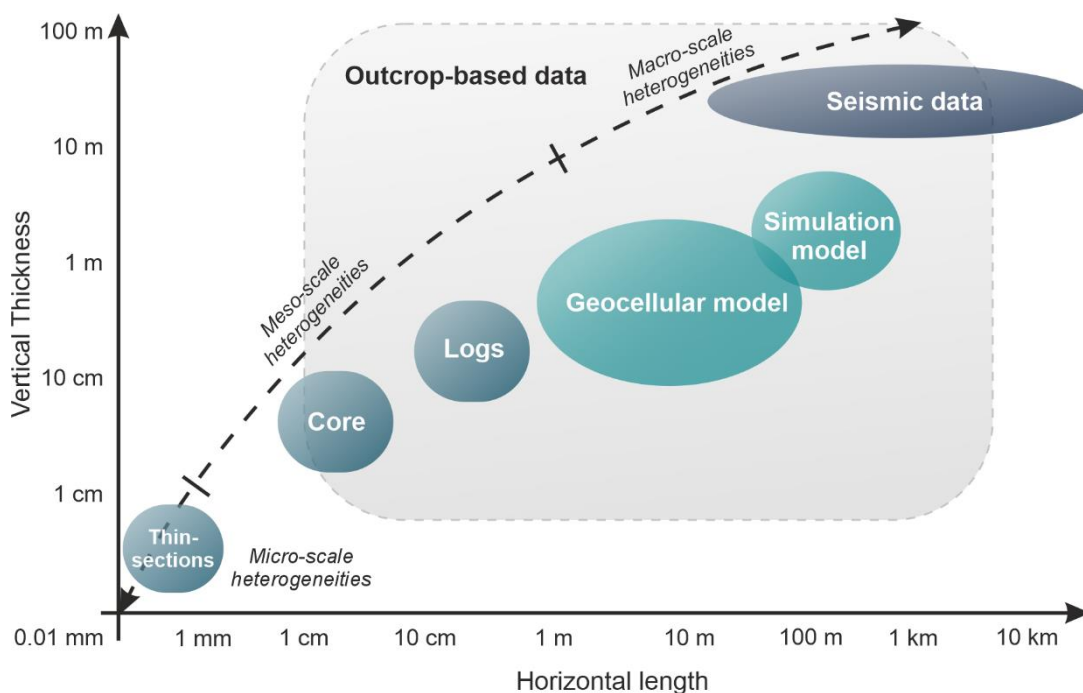
Fig. 1.3. Typical length and width scales of reservoir heterogeneities in relation to the sampling scale of subsurface seismic, wells and core (after Pickup and Hern 2002; Enge *et al.,* 2007; Rarity *et al*., 2014).

"Traditional" field data collection in outcrop analogues (e.g. sedimentological logs, geological maps and cross-sections) provides invaluable knowledge with which to characterize subsurface reservoirs (e.g. depositional systems, stratigraphic and paleogeographical syntheses). However, it is often difficult to extract reliable quantitative data on the geometries and spatial heterogeneities of sedimentary geobodies, data which are essential for 3D geostatistical reservoir modelling (e.g. Krum & Johnson, 1993; Bryant *et al.,* 2000; Deutsch, 2002; Rarity *et al*., 2014). New advances in digital techniques and data capture for outcrop analysis, such as digital outcrop models (DOM), are covering this gap allowing for the acquisition and analysis of reliable measurements and interpretations of geological features in their correct geographical positions (e.g. Enge *et* al., 2007; Howell *et al.,* 2014; Rarity *et al*., 2014; Cabello *et al*., 2018; Yeste *et al*., 2020).

As a key additional tool in field data acquisition, digital outcrop models provide several advantages (McCaffrey *et al.*, 2005; Pringle *et al*., 2006; Hodgetts, 2013). Some of these are: (1) data collection from otherwise inaccessible areas; (2) data visualization from many different angles, as well as the ability to switch rapidly between different scales; (3) with digital datasets, the areas from which we can make measurements are massively increased, meaning more statistical information can be collected, increasing sample size and therefore reducing the errors in statistical analysis; (4) new attributes can be generated to highlight subtle features, assist with interpretation and provide the basis for automated mapping approaches; (5) new aerial platforms (RPAS) have lower costs compared to other techniques such as LiDAR and allow higher flexibility in data acquisition data; (6) digital outcrop models can make remaining field time more efficient by offsetting some data interpretation back into the lab; and (7) digital outcrop models are a useful tool for teaching, although they are a long way from being a replacement for traditional field classes, but used correctly can greatly enhance the field experience.

Additionally, when the outcrop-based study is completed with subsurface information (e.g. core and well logs data), a complete dataset is obtained providing an accurate control of the distribution of the heterogeneities in outcrop analogues by direct validation of 1D data (core) with 3D data (outcrop-based data). This methodology is known as Outcrop/Behind Outcrop (OBO) characterization (Donselaar and Schmidt, 2005; Slatt *et al*., 2012; Henares *et al.,* 2016; Viseras *et al.,* 2018; Yeste *et al.,* 2019, 2020).

OBO characterization is a multi-approach set of methodologies aimed at the study of outcrop analogues integrating outcrop-based data and subsurface data from wells drilled immediately behind the outcrop, principally recovering cores and acquiring wireline log data.

This integrated approach contributes significantly to a better understanding of the reservoir characteristics and the interpretation of well data in actual reservoirs. The stratigraphic context, location and extent of potential reservoir geobodies in wells can be better constrained with this dataset in outcrop analogues. Thus, this methodology, integrating subsurface data with the outcrop data, will lead to better reservoir models and a higher success rates in appraisal and development drilling, as well as better estimates of reservoir volumes connected to the borehole (Rarity *et al*., 2014; Viseras *et al.,* 2018; Yeste *et al.,* 2020).

Given that no two systems are identical, the perfect analogue does not exist. The key issue is to first understand the aims of the reservoir model in order to select an appropriate analogue (Howell *et al*., 2014). Outcrop analogues are selected based on four criteria (Enge *et al.,* 2007): relevance and applicability to the problem, the level of three dimensionality, outcrop quality, and accessibility. In some cases, it is possible that no single outcrop analogue exists and it may be necessary to combine information from several different outcrop analogues (Howell *et al.*, 2014). The choice of the correct outcrop analogue is critical since an incorrect selection can lead to the wrong data being used to populate reservoir models (Howell *et al.*, 2014).

In this context, the selected study area can be considered as an outcrop analogue for several currently productive subsurface reservoirs. Of most relevance is that the Triassic red beds of the Tabular Cover (TIBEM; Iberian Meseta, Central SE Spain) resemble the TAGI reservoirs in Algeria. Both formations result from the erosion of Paleozoic granitic and metamorphic terrains during the Tethyan rifting (Middle-Upper Triassic) and were deposited in a peri-intracratonic basin under similar climatic, base level and tectonic conditions. Basin architectures, in both cases, show similar fluvial facies stacking patterns, varying from high-sinuosity fluvial systems, to low-sinuosity fluvial systems (Fernández & Dabrio, 1985; Turner *et al.*, 2001; Rossi *et al.*, 2002; Ratcliffe *et al.*, 2006; Henares *et al.,* 2014, 2016; Baouche *et al.,* 2020) evolving up-section to shallow marine deposits (tidal bars and foreshore deposits; Baouche *et al*., 2020).

1.4. The application of outcrop analogues in reservoir modelling

Sedimentology has always been a key factor in reservoir modelling, effectively acting as the main driver in controlling the prediction of reservoir *versus* non-reservoir facies characteristics and relationships, as well as porosity and permeability distributions.

Recent improvements in reservoir modelling capabilities and computational capacity provide an opportunity to input reservoir models with more accurate sedimentological data and to obtain more geologically consistent representations. This leads to different modelling opportunities, such as building large geocellular models, unlocking the possibility of representing reservoir heterogeneity in greater detail; or the realization of a high number (tens to hundreds) of equiprobable and alternative scenarios in an attempt to capture the reservoir uncertainties (Yeste *et al.,* 2019). However, independently of the modelling approach, accurate sedimentological models derived from outcrop analogues assume an even greater importance given that their characteristics can now be extracted with high precision.

Outcrop analogues provide both 'hard' (geometry and dimensions of geobodies) and 'soft' (knowledge and understanding of sedimentary depositional systems) data that are routinely used to improve our understanding of the subsurface, which is heavily under-sampled (Howell *et al.*, 2014). In this context, outcrop analogues play a valuable role in steering geomodellers towards appropriate levels of geological detail. Due to new advances in outcrop data acquisition, digital outcrop models now offer an extremely useful tool for reservoir characterization, allowing for a precise and quantitative analysis of the geological exposure. The use of high-resolution digital outcrop models in the reservoir characterization of outcrop analogues permits the extraction of datasets of geostatistical parameters, such as facies proportions, geometrical and dimensional measurements of geobodies and the spatial distribution of heterogeneities; which are the basis for current stochastic reservoir modelling approaches such as Sequential Indicator Simulations (SIS), object-based modelling and multipoint statistics techniques (Hodgetts, 2013; Howell *et al.*, 2014).

1.5. Objectives

As the most geologically simple reservoirs are progressively produced to depletion, and whilst hydrocarbon consumption continues to increase, it becomes increasingly necessary to identify, evaluate and develop more complex, heterogeneous reservoirs. In such cases development plans and reservoir management become increasingly important. Furthermore, with the challenge of new energy policies and the rise in CO_2 capture, utilization and storage techniques, it is also necessary to improve our understanding and control of reservoirs. As such, the successful integration between reservoir characterization and reservoir modelling is becoming ever more essential. In this integration, data should not only be quantitative in format, such as cores, well logs and seismic data, but also geological concepts and descriptive

interpretations are of key importance. In this sense, a multi-scale characterization of the geometry, distribution of heterogeneities, architecture and connectivity from outcrop analogues is crucial in the broadening of our knowledge of sedimentary reservoirs, providing datasets of vital importance for the evaluation and modelling of sedimentary reservoirs.

This thesis project aims to provide datasets from outcrop analogues to significantly improve our knowledge of the sedimentary variables which condition the optimal exploration and development of highly heterogeneous reservoirs. These datasets include outcrop analogue examples of both high and low-sinuosity fluvial systems and a mixed tidal and wave-influenced shoreline system from a Triassic succession exposed in Central SE Spain. The project integrates both outcrop and subsurface data, ultimately providing reservoir modelling workflows to reproduce the distribution of heterogeneities in these types of reservoirs. To reach these goals, the following objectives have been defined:

1. Application of an Outcrop/Behind Outcrop characterization workflow at meso-scale in a selected section of the Triassic deposits of Central SE Spain by comparison and validation of sedimentary characteristics in outcrop and behind-outcrop data.

2. Characterization of architectural elements from both "classical" outcrop and digital outcrop data, in order to extract the geometrical data (shape and dimensions) of the geobodies which comprise the selected outcrops, as well as the spatial relationships between them.

3. Recognition of lateral and vertical variability of heterogeneities, at lithofacies scale, by characterizing the selected outcrop analogues through the description and interpretation of cores, in terms of sedimentary processes and depositional sub-environments, and integration with the analysis of architectural elements in outcrop.

4. Generation of quantitative conceptual models and paleogeographic reconstructions representing both the lateral and vertical variability of heterogeneities, as well as the geometric parameters of the geobodies.

5. Planning hypothetical reservoir modelling strategies from OBO characterization datasets, reproducing the distribution of heterogeneities in the interpreted geobodies.

6. Compilation of a dataset of the most characteristic geobodies representing highly heterogeneous reservoirs. It will also include their diagnostic features and the spatial distribution of heterogeneities that condition modelling.

1.6. Research outline

The structure of the Thesis is organised according to the previously outlined objectives:

Chapter 2 provides a **geological framework** for the studied Triassic deposits from Central SE Spain. The Triassic break-up of Pangea triggered the formation of rift basins, on the margins of Tethys, where thick continental red bed successions accumulated. The stratigraphy and the depositional facies, as summarised, highlight the suitability of these deposits as outcrop analogues for highly heterogeneous, fluvial and marginal marine reservoirs.

Chapter 3 includes a **detailed description of the workflow designed** for the development and completion of this PhD project. This workflow comprises two key elements: (1) Outcrop/Behind Outcrop (OBO) characterization and (2) reservoir modelling. OBO methodology integrates outcrop-based and subsurface-based data. The results obtained from this methodology (OBO characterization) provide the necessary input data for the second key element; geostatistical reservoir modelling. Methodological procedures as well as the technical specifications adopted for both OBO methodology and reservoir modelling are detailed in this chapter.

Results and Discussion are presented in two parts (I and II) according to the applied methodology and the obtained results:

Part I presents the results generated by the OBO characterization of the studied succession. This section of the thesis is accordingly divided into four chapters:

> **Chapter 4** presents the results of the **OBO characterization of the Mudstone-Sandstone or M-S Unit.** This unit is characterized by high-sinuosity fluvial systems comprising the lateral and vertical stacking of four geobodies (or architectural elements): (i) channelized sandstone bodies; (ii) asymmetrical sigmoidal-shaped sandstone bodies; (iii) lobe-shaped to sheet-like sandstone bodies; and (iv) sheet-like mudstones. These geobodies represent, respectively, meandering channel, point bar, crevasse-channel-splay and floodplain sub-environments, all comprising a distal, low-gradient meandering fluvial system. The full integration of outcrop and subsurface datasets has enabled generation of a robust conceptual model with predictive potential when establishing the three-

dimensional stacking of facies, distribution of heterogeneities, and the connectivity between reservoir rock geobodies of both primary (channel) and secondary (crevasse complex) interest in this type of fluvial reservoir. The results of this chapter have been published in the journal *Sedimentology*:

Yeste, L.M., Varela, A.N., Viseras, C., McDougall, N.D. and García-García, F. (2020). Reservoir architecture and heterogeneity distribution in floodplain sandstones: Key features in outcrop, core and wireline logs. Sedimentology. DOI: 10.1111/sed.12747.

Chapter 5 presents the results of the **OBO characterization of the Sandstone or S Unit.** This is characterized by a low-sinuosity fluvial system composed of two geobodies (or architectural elements): (i) channel and (ii) compound bar. These geobodies represent a perennial deep braided fluvial system. By integrating both surface and subsurface data, a detailed paleogeographic reconstruction is proposed, including the dimensions and spatial distribution of the main architectural elements, as well as key features in core, gamma ray log and tadpole patterns that help identify this type of reservoir. The results of this chapter have been published in the Special Publication volume *"River to Reservoir: Geoscience to Engineering"* of the Geological Society of London:

Yeste, L.M., Henares, S., McDougall, N., García-García, F. and Viseras, C. (2018). Towards the multi-scale characterization of braided fluvial geobodies from outcrop, core, georradar and well logs data. In: River to Reservoir: Geoscience to Engineering (Eds Corbett, P., Owen, A., Hartley, A., Pla-Pueyo, S., Barreto, D., Hackney, C. and Kape, S.), GSL Special Publication, 488. https://doi.org/10.1144/sp488.3

Chapter 6 presents the results of the **OBO characterization for the Heterolithic or H Unit.** This is characterized by the deposits of a mixed tidal and wave-influenced shoreline system comprising three main types of reservoir geobody: (i) elongate geobodies, associated with subtidal sandbar facies and intertidal sandbar facies; (ii) asymmetric-sigmoidal geobodies formed by tidal-dominated point-bar facies; and (iii) a tabular geobody associated with a hyperpycnite sandbody facies and open-coast, linear shoreface facies. A new outcrop analogue dataset for shoreline reservoirs, specifically for both a tide-dominated delta and estuarine system, including key geometric and sediment body dimension data, is presented in this chapter.

Chapter 7 attempts to assign appropriate geometries and dimensions to the various geobodies identified in the whole study section, summarizing their internal heterogeneities for reservoir modelling purposes. These are then upscaled to describe

the gross scale reservoir architecture of the three TIBEM Units (M-S, S and H Units) and the key bounding surfaces (or correlation surfaces) between the units.

Part II, comprising **Chapter 8**, presents the results obtained from the reservoir modelling of the M-S Unit, characterized by high-sinuosity fluvial systems. A critical element in this chapter was the design of appropriate modelling workflows with Petrel$_{TM}$ which would best reproduce the distribution of heterogeneities, both at the scale of geobodies and at the finer scale of lithofacies by using both object-based modelling technique and logical statement calculations. The workflow at geobody scale was used to construct a 3D training image (TI) of a fluvial reservoir, comprising both a meandering channel system and its associated overbank sandstone deposits. This TI was subsequently used in MPS (Multi-Point Statistical) simulations, in order to establish whether it was able to assist in the prediction of the reservoir geobodies, as well as confirming to what extent this prediction matched the outcrop. The workflow at the scale of lithofacies was then used to estimate the static connectivity of the reservoir in the M-S Unit.

Chapter 9 summarises the key general conclusions drawn from this PhD project.

CHAPTER 2:

Geological Setting of the Study Area

Abstract   The extensive Triassic Red Beds succession of the Iberian Meseta, south-central Spain (the TIBEM of Viseras *et al.*, 2011, 2018; Henares *et al.*, 2014, 2016; Yeste *et al.*, 2019a) are continental deposits which accumulated during the Tethyan rifting process (Late Permian-Upper Triassic; López-Gómez *et al.*, 2019). The study area, located to the east of Alcaraz village (Albacete Province), corresponds to the most distal part of the outcropping TIBEM, as suggested by paleocurrent data. The TIBEM succession in the study area thus comprises fluvial to coastal deposits within a linked stratigraphic framework. In the study area, the ca. 160 m-thick sedimentary succession (Ladinian-Norian) is divided into four informal member-rank lithostratigraphic units (Yeste *et al.*, 2019a; 2020). From base to top, they are: (i) a mudstone-sandstone unit (M-S Unit), that includes both a meandering channel system and overbank sandstone deposits embedded in distal floodplain mudstones (Yeste *et al.* 2020); (ii) a sandstone unit (S Unit) corresponding to a braided system (Yeste *et al.* 2019a); (iii) a heterolithic unit (H Unit) comprising alternating sandstone and mudstone layers deposited in a fluvio-marine transition zone (Yeste *et al.*, 2017; García-García *et al.*, 2017); and (iv) a mudstone-evaporitic unit (M-E Unit) composed of silt-rich coastal plain facies and intertidal sabkha evaporites. Pre-existing, interpretations of the Triassic Red Beds by both Fernández (1977), which divided the succession into Sequences I to IV, and Arche & López-Gómez (2014), which divided the succession on the basis of the classic Germanic Trias Units (Keuper; K1 to K5), are here avoided in order to focus the chosen stratigraphy on the purely descriptive basis of lithology and sedimentological features.

2.1. The Permian-Triassic break-up of Pangea

Permian-Triassic rifting represents the first of the two Mesozoic rifting stages identified in the Iberian Peninsula. The initial phases of development began during the Early Permian, and were linked to the beginning of the break-up of the Pangea supercontinent (López-Gómez *et al*., 2019). During these initial phases, a new geodynamic configuration was developed in which the compressional tectonics of the Hercynian-Variscan phase gave way to a large-scale transtensional and extensional regime, leading to the formation of many basins in different microplates, including Iberia. These new conditions eventually resulted in continental break-up, the northwards-directed subduction of the Paleotethys oceanic ridge under Eurasia and the opening and westward expansion of the Neotethyan ocean (Fig. 2.1; Stampfli & Borel, 2002; Angiolini *et al.,* 2013; Stampfli *et al.,* 2013; Druguet *et al.,* 2014, López-Gómez *et al.,* 2019).
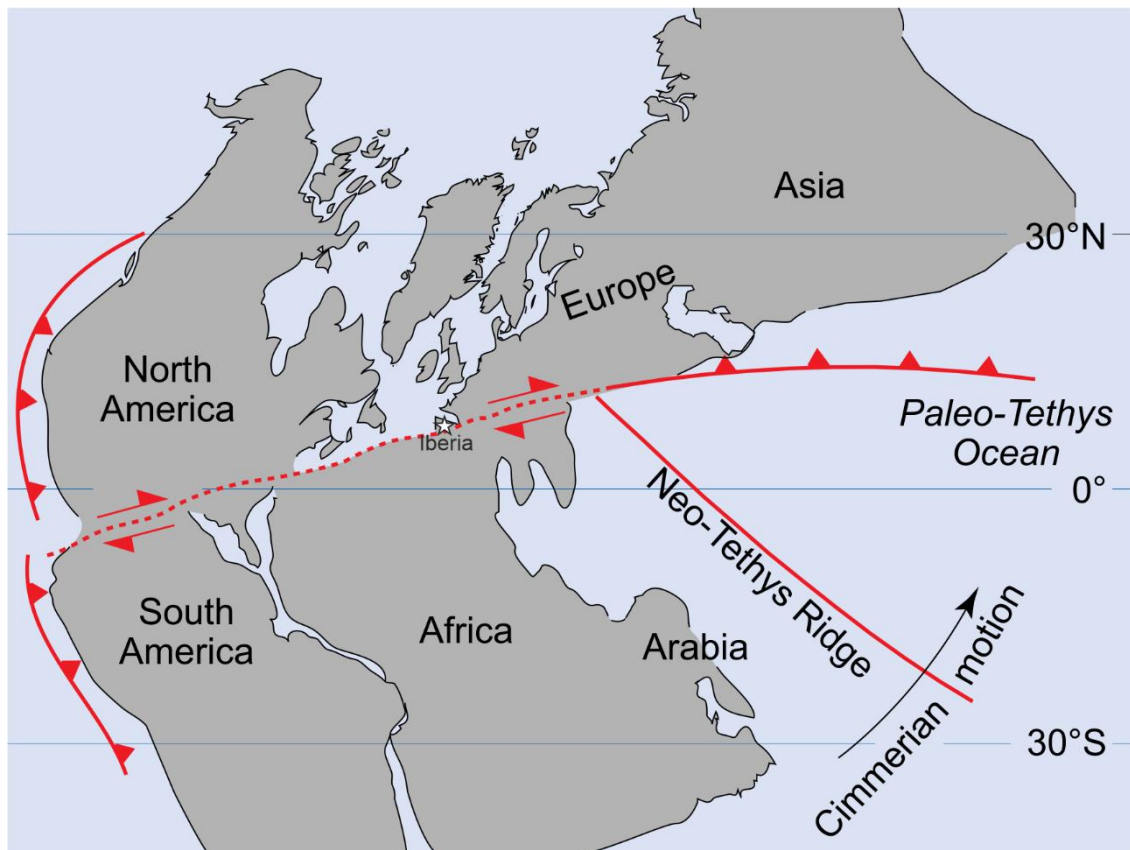

Fig. 2.1. Plate tectonic framework during the Late Permian – Early Triassic showing subduction of the Paleotethys oceanic ridge under Eurasia and the opening and westward expansion of the Neotethyan ocean (modified from Muttoni *et al*., 2009).

During the Permian, the evolution and development of rifting phases produced several small extensional sub-basins in Iberia, filled by terrestrial sediments, a local response to the progressive collapse and dismantling of the Variscan belt, through late to post-orogenic extension, wrenching and thinning of the orogenic lithosphere (Fig. 2.2a; Faure & Pons 1991; Faure *et al.* 2002; Von Raumer *et al.* 2013; López-Gómez *et al.,* 2019). This tectonic activity controlled both subsidence and the post-orogenic magmatism affecting much of SW Europe (Arche & López-Gómez 1996; Cortesogno *et al.*, 1998; Fernández-Suárez et al. 2000; Bruguier *et al.,* 2003; Cassinis *et al.,* 2003; Valle Aguado *et al.,* 2005; Ronchi *et al.,* 2008; Dallagiovanna *et al.*, 2009; Gutiérrez-Alonso *et al.,* 2011; Maino *et al.,* 2012; Decarlis *et al.,* 2013; Pereira *et al.,* 2014).

These rifts were characterized by an initial phase of generalized subsidence, albeit with continuing tectonic influence which continued during the Early Triassic. This would suggest a transitional stage from tectonic to thermal subsidence and the beginning of the mature phase in the rifting evolution of these basins. This transitional stage was associated with the first marine incursions, although these were limited in areal extent, none completely flooding the new basins (Fig. 2.2b, Ziegler & Stampfli 2001).

Subsequently, generalized thermal subsidence promoted the development of extensive marine platforms within the basins, representing the post-rift or passive margin stage, which extended from Late Triassic to Middle Jurassic times (López-Gómez *et al*., 2019).

The Permo-Triassic break-up of Pangea conditioned, as outlined above, the onset of numerous rift systems in the southern Iberian Peninsula and northern Africa (Tethyan and Atlantic branches, respectively, Fig. 2.2b) and, consequently, the formation of several depocentres. The Triassic sediments related of the South-Iberian paleomargin, known as the "South iberian Triassic" according to Pérez-López & Pérez-Valera (2007), consists of two main facies belts, proximal and distal (Fig. 2.2b). The proximal facies belt is exclusively characterized by continental red beds, defined as the "Hesperian Triassic" by Sopeña *et al.* (1983). The distal facies belt, in contrast, consists of the epicontinental or "Germanic facies". These are present in the External Zones (Prebetic and Subbetic Domains; Fig. 2.3), with the three-fold classic division of: Buntsandstein, Muschelkalk and Keuper (Pérez-López, 1991). Buntsandstein represents the initial or tectonic rifting phase during the Early Triassic, while Muschelkalk and Keuper represent the mature rifting phase during the Middle Triassic (Pérez-Valera *et al*., 2000; López-Gómez *et al*., 2019).

Fig. 2.2. Paleogeographic maps of Central Eastern Pangea in **(a)** Middle Triassic and **(b)** Late Triassic times. The study area (TIBEM) is indicated by the red boxes. Paleocurrent data for the Triassic fluvial deposits around the Iberian Massif also are shown (from Fernández & Dabrio, 1985; Arche & López-Gómez, 2014; Henares *et al.,* 2014; Viseras *et al*., 2019; Yeste *et al*., 2019; 2020). The paleogeographic maps are modified from Critelli *et al.*, 2008, Arche & López-Gómez (2014) and Escudero-Mozo *et al.* (2015).

The "Hesperian Triassic" is characterized by Buntsandstein and Keuper facies, completely lacking Muschelkalk facies (Fernández *et al.* 1994). The "Hesperian Triassic" outcrops widely north of the central sector of the Betic Cordillera along the south eastern edge of the Variscan Iberian Massif. These Triassic deposits form the sedimentary cover of the Variscan Iberian Massif, the so-called "Tabular Cover" or, more recently, the TIBEM ("Triassic red beds of the Iberian Meseta; Viseras *et al.,* 2011; Henares *et al.,* 2014, 2016; Yeste *et al.,* 2019, 2020).

Fernández *et al.* (1994), Pérez-López & Pérez-Valera (2007) and Arche & López-Gómez (2014) presented a correlation between the TIBEM and the Germanic facies units in the Prebetic Domain (Fig. 2.3). These authors reported an important lateral increase in thickness from the TIBEM into the Prebetic. This was also reported by Ortíz *et al.* (1996) through the study of two deep wells (Carcelén and Salobral) which have cores of more than 1000 m length through almost undisturbed Keuper facies. Towards the south, the Subbetic Triassic outcrops reveal enormous original stratigraphic thickness, especially in the Keuper facies (Pérez-López & Pérez-Valera, 2007; López-Gómez *et al*., 2019).

Pérez-López (1991, 2000), Pérez-Valera (2005) and Pérez-Valera & Pérez-López (2008) synthesized the Triassic stratigraphy of the Prebetic and Subbetic tectonostratigraphic units. These authors distinguished one package of Muschelkalk carbonates, five detrital and evaporitic formations constituting the Keuper Group (K1 to K5); and finally, one upper carbonate formation of Norian age (Zamoranos Fm). According to these authors, this general stratigraphic framework can be maintained with only few variations up to the front of the Internal Zones of the Betic Cordillera. However, there exist important lateral changes in sediment thickness, and a general trend of facies change towards more open marine environments, towards the south and east in the Triassic Betic basin (López-Gómez *et al.*, 2019).
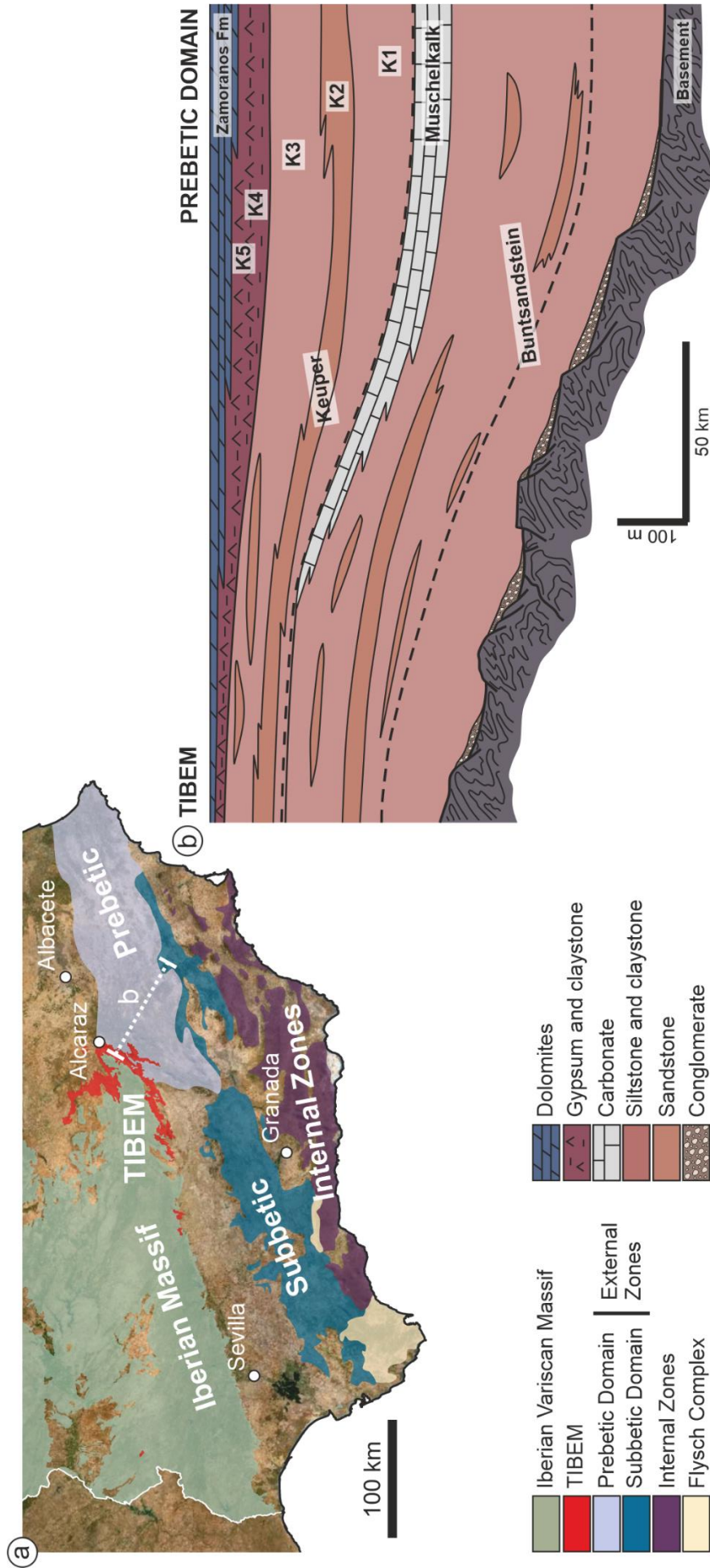
Fig. 2.3. (a) Geological sketch map of the different tectonic units in the Betic Cordillera (S Spain). Modified from Pérez-López & Pérez-Valera (2007). **(b)** Correlation between the TIBEM and Prebetic domain highlighting the major thickness change in the Keuper facies unit. Modified from Fernández et al., 1994; Pérez-Valera & Pérez-López (2008).

51

2.2. Triassic red beds of the Tabular Cover of the Iberian Meseta (south-central Spain)

The Triassic red beds of the Tabular Cover of the Iberian Meseta (south-central Spain (Fig. 1.1); herein referred as TIBEM; Henares *et al*., 2011; Viseras *et al*., 2011; Viseras *et al.,* 2019; Yeste *et al.,* 2019a, 2020), were originally defined as the Chiclana de Segura Formation (López-Garrido, 1971) or as the "Hesperian Triassic" by Sopeña et al. (1983). The TIBEM outcrop covers an area of approximately 4000 km^2 ranging in thickness from 50 m to 400 m (Fig. 2.4 and Fig. 2.5; Fernández, 1977). It corresponds to the weakly deformed lower part of the assemblage that covers the south eastern margin of the Iberian Massif and constitutes an extensive continental sedimentary package dominated by red beds.
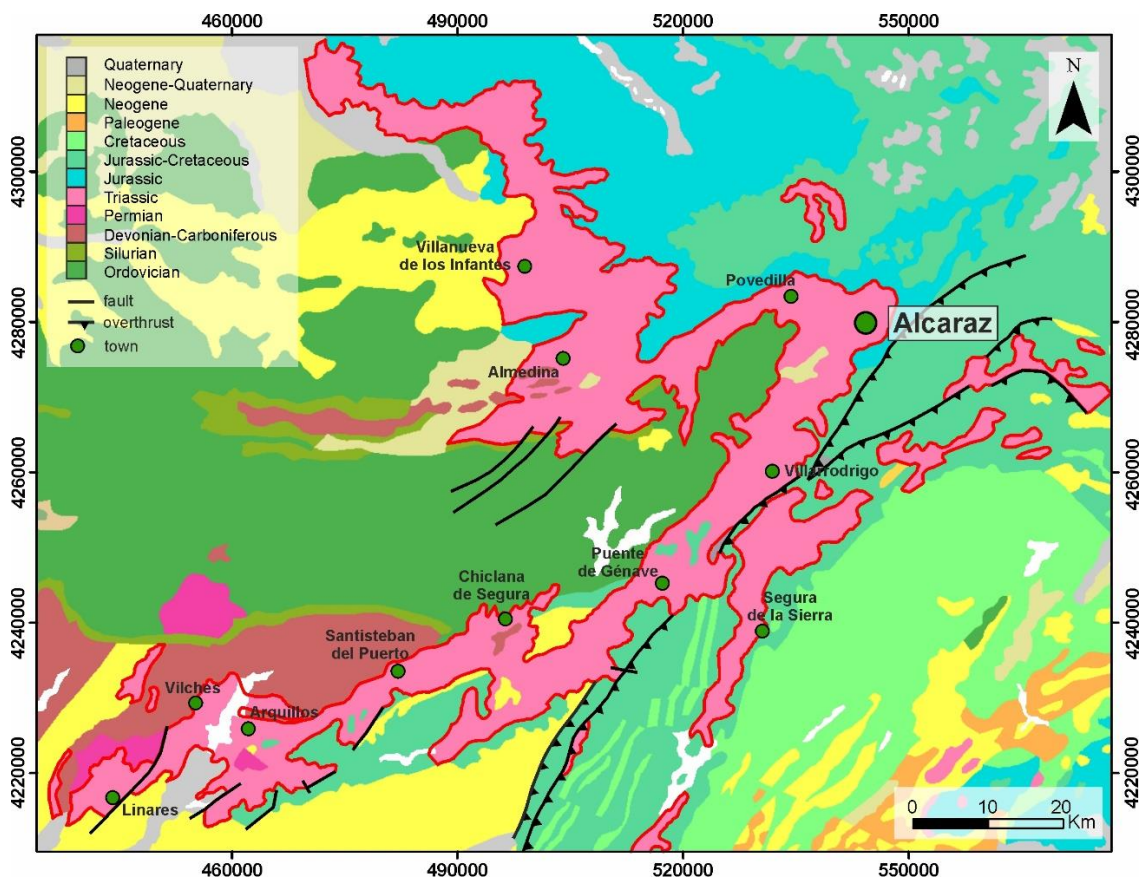
Fig. 2.4. Distribution of chronostratigraphic units in the region (SE Castilla-La Mancha and NE Andalucia) of the study area. The pink-red colour corresponds to the Triassic and specifically to the TIBEM outcrop (from GEODE, 2020). The study area is located near Alcaraz village. See Figure 1.1 for a general location of the TIBEM in the Iberian Peninsula.
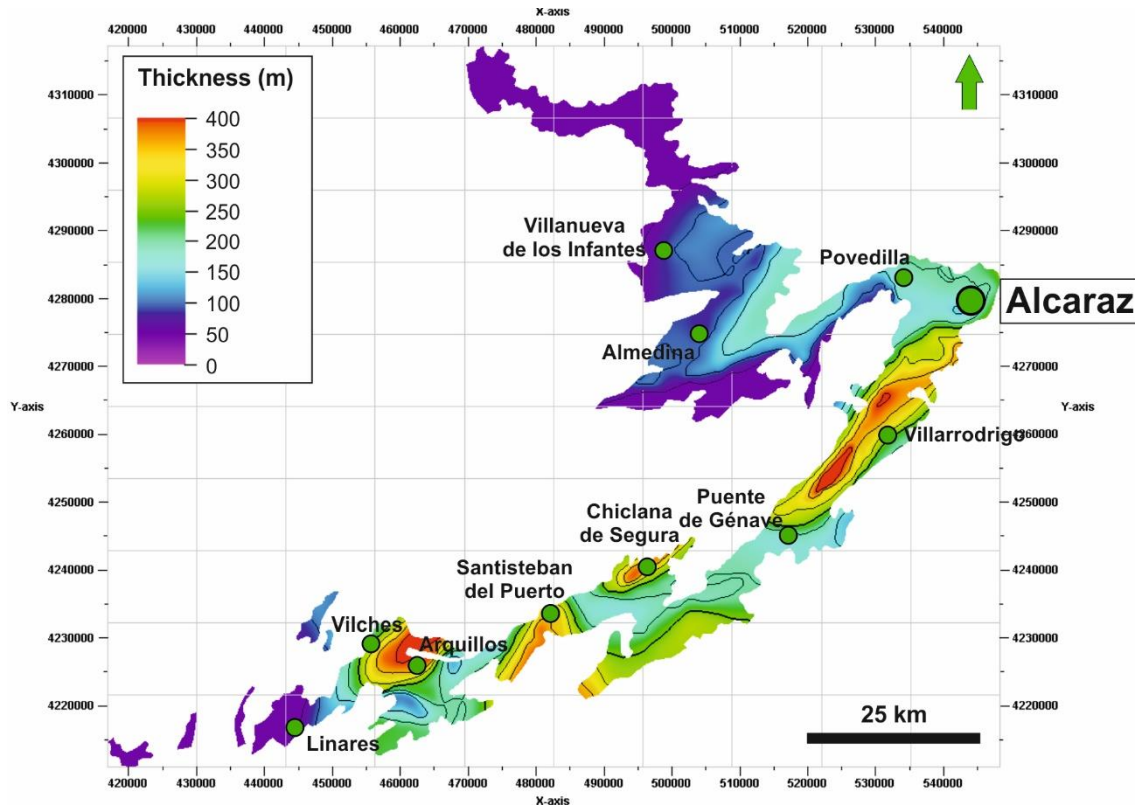
Fig. 2.5. Thickness distribution map of the TIBEM (modified from Fernández *et al.,* 2005). The study area is located near Alcaraz village.

Age dating of continental red beds is always problematic due to limited recovery of age-diagnostic fauna. Available data for the TIBEM allows the identification of the Ladinian at the base of the succession and the Norian in the upper evaporitic Keuper. Thus, the upper and lower boundaries are well constrained, but a more precise internal age zonation is not possible, especially for Carnian age sediments (Besems, 1981, Márquez-Aliaga, 2003, Critelli *et al.*, 2008; Arche & López-Gómez, 2014). This problem could be overcome by correlation between the TIBEM and the Prebetic Domain of the External zones (Fig. 2.3). The upper dolomitic unit has been assigned a Rhaetian age by regional correlation between the Imón Fm of the study area (Goy & Yébenes, 1977) and the Zamoranos Fm (Pérez-López, 1991; Pérez-López *et al.,* 1992).

Fernández (1977) interpreted four Triassic sequences (Sequences I to IV) in the TIBEM. These must be considered as an attempt to place the Triassic sections of the Prebetic and TIBEM into a sequence stratigraphic framework. These units belong only to the emergent portion of transgressive system tract and are not true depositional sequences corresponding to a complete sea level rise-fall cycle. The following is a description of four Triassic sequences described by Fernández (1977):

- Sequence I (Lower Ladinian) is fining-upward and characterised by an angular unconformity as a lower boundary overlying the Paleozoic basement. The upper boundary, in contrast, corresponds to a sharp, apparently non-erosional change in sedimentary character. This sequence is also characterized by a basal conglomeratic unit, interpreted as the deposits of small alluvial fans or braided streams grading into sand-flat and playa-lake depositional environments. This sequence was interpreted by Fernández (1977) as deposited during the middle Triassic, in subsiding rift basins with no marine connection.

- Sequence II (Ladinian) comprises both the Buntsandstein and Muschelkalk facies in the Prebetic Domain and most of the Buntsandstein in the TIBEM (Fig. 2.7). Conversely, Arche & López-Gómez (2014), in correlation with the Iberian basin, interpreted this sequence as Keuper facies. Sequence II includes a complex group of lithologies and sedimentary environments, deposited during a period of rising relative sea level, which resulted in a lack of channel incision and relatively high vertical accretion rates in floodplain settings. Sandstone bodies accumulated in high-sinuosity fluvial systems and their associated overbank deposits (crevasse-splays). Floodplain deposits include micritic carbonate paleosols, displacive gypsum nodules, and locally the presence of coal layers, typical of swamp deposits (Yeste *et al.,* 2020).

- Sequence III (Ladinian-Carnian?) of Fernandéz (1977) corresponds approximately to the K1 unit (Arche *et al.,* 2002; Pérez-Valera & Pérez-López, 2008; Arche & López-Gómez, 2014; Fig. 2.7). The upper boundary is clear in the Prebetic Domain, where it coincides with the base of the K2 Unit, which can also be traced through most of the southern TIBEM. The lower boundary is a karstified surface at the top of the Muschelkalk carbonates in the Prebetic Domain, where it consists of a series of silt-gypsum-carbonate sequences, whereas, in the TIBEM, it includes sandstone levels embedded in silty sediments with calcrete paleosols. This sequence represents the deposits of a fluvial system connected with an evaporitic coastal plain. Sequence III was deposited during a phase of stable or slightly falling relative sea level which favoured the development of paleosols on floodplains characterised by a low sedimentation rate (Fernández *et al.*, 1994).

- Sequence IV (Carnian-Rhaetian) is also equivalent to Keuper Units K2, K3, K4, K5 and the dolomitic Zamoranos Formation (Upper Triassic-Lower Jurassic; Pérez-López, 1991) in the Prebetic Domain. A 20-m-thick and hundred-kilometre-long continuous sandstone unit (the K2 unit) formed as a braidplain depositional system. The base of the K2 unit corresponds to a regional erosional surface that is interpreted as a major discontinuity (López-Gómez *et al.*, 2019). The deposition of K2 was certainly related to a major sequence boundary which was probably associated with a combination of eustatic and climatic phenomena related to the Carnian Pluvial Event (Arche & López-Gómez, 2014). This allowed widespread deposition of fluvial sandstone in and around the Iberian continent, also at its southern margin. The deposition of the overlying K3 Unit occurred due to an increase in accommodation space associated with a relatively rapid rise in the base level (Pérez-López, 1996). The K3 Unit, constituted mainly by red clay and heterolithic-sandstone deposits, grades upwards into K4 Unit, composed mainly of claystones with nodular gypsum, and the K5 Unit, constituted by claystones and laminated gypsum levels. Facies within Units K3 to K5 suggest a coastal alluvial system passing into an evaporitic tidal flat under rising base level conditions. Subsequently, a rapid base level rise marked the backstepping of the former coastal plain which was then converted into a coastal environment in which sabkha evaporites were overlain by marine carbonates (Zamoranos Fm; Pérez-López, 1991; Fig. 2.7).

Previous publications focussed on the TIBEM (Fernández & Dabrio, 1985; Henares *et al.,* 2014; Viseras *et al.,* 2019; Yeste *et al.,* 2018 and Yeste *et al.,* 2020), show that paleocurrent data indicate that the main drainage direction was to the E and NE. As such, the study area (Alcaraz sector) corresponds to the most distal part of the outcropping TIBEM (Fig. 2.6).

2.3. Stratigraphic framework of the study area

The Triassic succession in the study area, located to the east of Alcaraz village (Albacete Province), is about 160 m thick and includes only, from base to top, Sequences II, III and IV (Fernandez; 1977 and Fernández & Gil; 1989; Fig. 2.7).
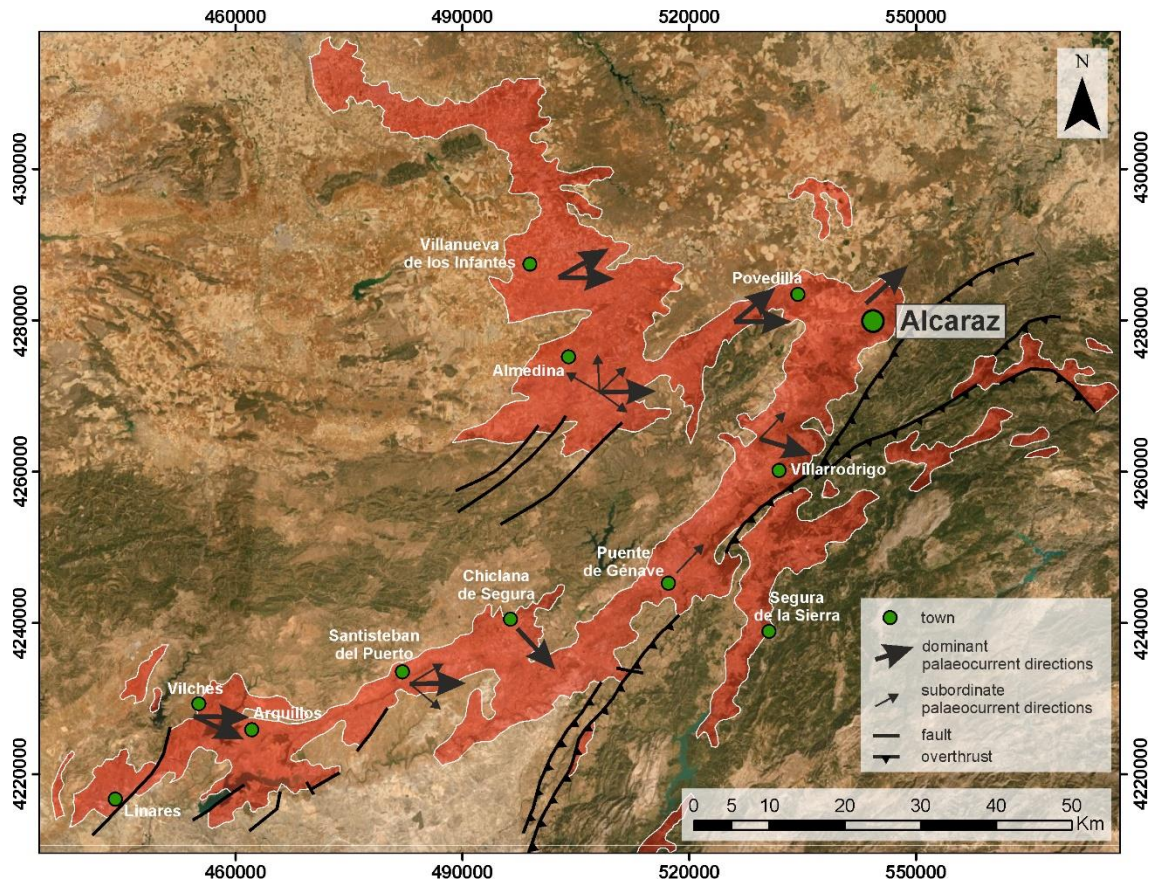
Fig. 2.6. Simplified summary of paleocurrent distribution in the TIBEM outcrop (modified from Henares *et al.,* 2014 and Viseras *et al.,* 2019).

Within this broad framework, and on the basis of the predominant lithology, depositional environments and subsurface expression, Yeste *et al.* (2019a) divided the Triassic section in the studied area into four sub-horizontal lithostratigraphic units: Mudstone-Sandstone Unit (M-S Unit), which includes high-sinuosity fluvial systems; Sandstone Unit (S Unit), corresponding to a low-sinuosity fluvial system; Heterolithic Unit (H Unit), comprising alternating sandstone and mudstone layers deposited in a fluvial-tidal transition zone; and, finally the Mudstone-Evaporitic unit (M-E Unit) consisting of silt-rich coastal plain facies and intertidal sabkha evaporites (Fig 2.7 and Fig. 2.8).

The Mudstone-Sandstone Unit (M-S Unit), which is at least 90 m thick, occurs at the base of the studied stratigraphic succession. The lower boundary was not observed in either outcrop or subsurface data in the study area, although its onlap across Palaeozoic paleorelief is observed in nearby outcrops. This unit is characterized by a low net-to-gross, effectively a sand:mud ratio of 10:90. It comprises lenticular, sand-prone packages up to 4 m thick, as well as thin, tabular, sand-prone packages, up to 2 m thick, encased within mud-prone sediments (Fig. 2.8). The main depositional environment is interpreted as a high-sinuosity fluvial system, characterized by

meandering channels and associated overbank deposits (crevasse-splays) encased within argillaceous floodplain deposits (Yeste *et al*, 2020). Paleocurrent data show a dominant flow direction toward the north (Yeste *et al*, 2020). The M-S Unit shows a serrated gamma-ray profile characterised by both bell and funnel shapes. API values average 150 API, but range from 48 to 250 (Fig. 2.7).

The Sandstone Unit (S Unit) is distinguished by an irregular base, eroding the M-S Unit, and an undulatory top. In marked contrast to the M-S Unit, this Unit is characterized by a high net-to-gross (sand:mud ratio of 95:5) and consists of a laterally extensive (hundreds of metres along strike and/or along depositional dip) tabular sand package up to 20 m thick (Fig. 2.8). The main depositional environment is interpreted as a low-sinuosity fluvial system, characterized by a perennial deep braided system (Yeste *et al*., 2019). Palaeocurrent data show a dominant flow direction toward the north-east (Yeste *et al*, 2020). The S Unit is characterized by a smooth, cylindrical gamma-ray profile showing mean values of 59 API, but ranging from 33 to 175 API (Fig. 2.7).

The Heterolithic Unit (H Unit) is 40 m thick, characterised by medium net-to-gross, (sand:mud ratio of 60:40) comprising metre-scale heterolithic sandstone-dominated packages encased in mudstones (Fig. 2.8). Sediments were deposited in a fluvio-marine transition zone interpreted as a mixed tidal and wave-influenced shoreline system (García-García *et al*., 2017; Yeste *et al.,* 2017). Paleocurrent data, in marked contrast to Units M-S and S, show a general paleoflow toward the south-east (Yeste *et al.,* 2017). The gamma-ray profile is serrated and characterised by API values ranging from 87 to 236 with a mean value of 135 (Fig. 2.7).

The H Unit gradually transitions into the Mudstone-Evaporitic Unit (M-E Unit), characterized by mudstone horizons comprising nodular red gypsums interpreted as the deposits of sabkha depositional environments. Toward the top, this unit shows mudstones with laminated gypsum and limestones, deposited in a lagoonal environment. The M-E Unit is characterised by a cylindrical gamma-ray profile, with a mean API value of 98 (Fig. 2.7). This Unit is overlain by marine carbonates (dolostones) known as the Imón Formation, in the outcrops of the Iberian Cordillera, located to the north (Goy and Yébenes, 1977), and which is interpreted as equivalent to the Zamoranos Fm, described by Pérez-López *et al.* (1991) in the nearby Sub-Betic domain.
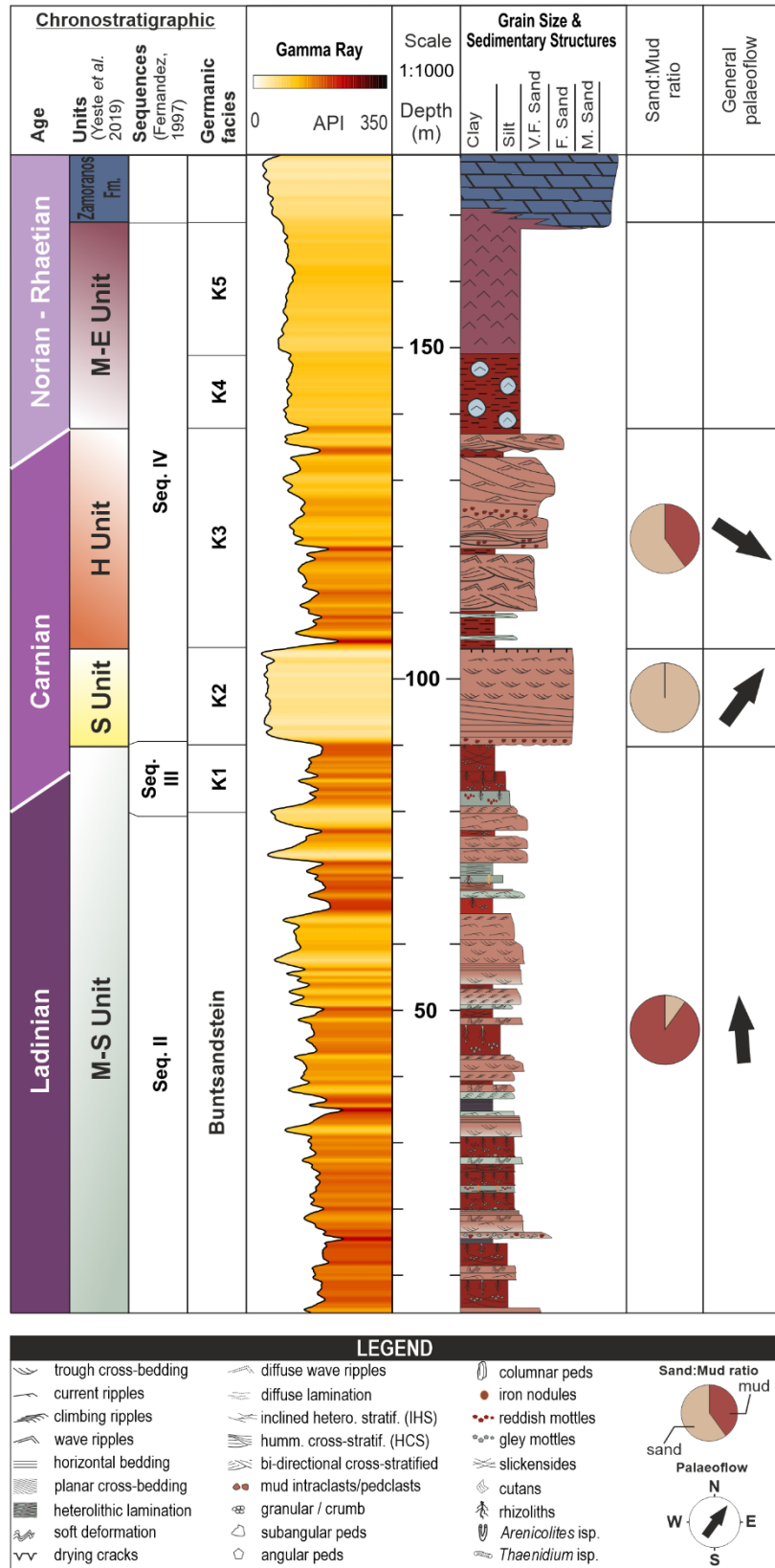
Fig. 2.7. Simplified Triassic Red Beds of Iberian Meseta (TIBEM) stratigraphic and lithological succession in the Alcaraz area based on the Gamma Ray log. The relationship of the current study lithostratigraphy to key pre-existing stratigraphic schemes is also shown. M-S Unit: Mudstone–Sandstone Unit; S Unit: Sandstone Unit; H Unit: Heterolithic Unit; M-E Unit: Mudstone–Evaporitic Unit.
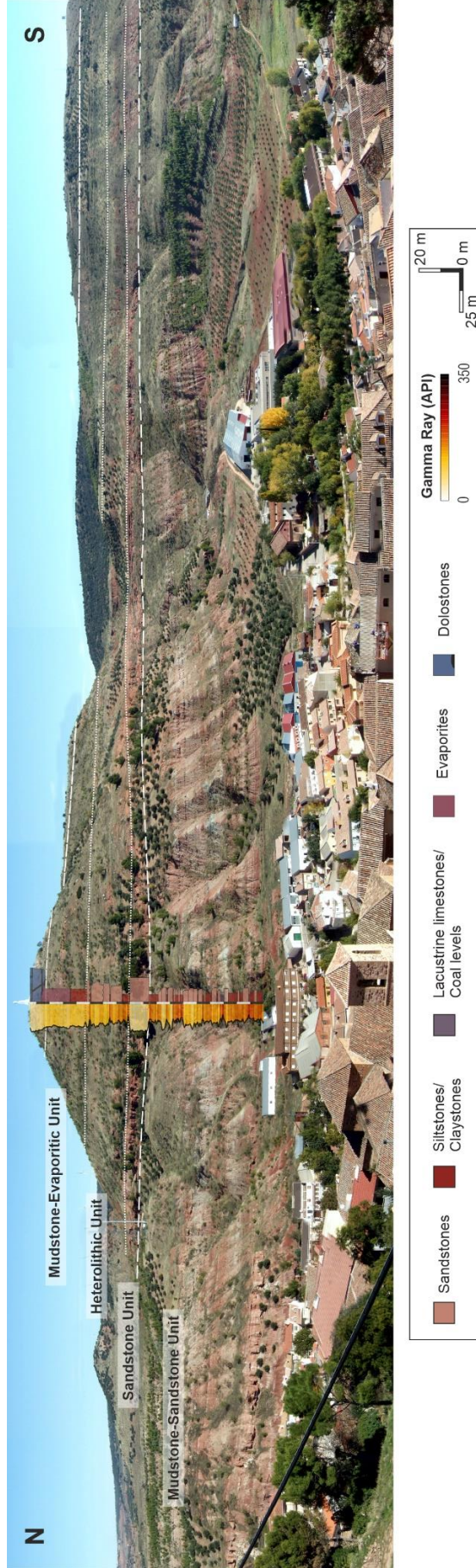
Fig. 2.8. North-south panoramic view of TIBEM succession in the Alcaraz area (village in the foreground). White lines show the surface boundary of each described stratigraphic unit. Synthetic gamma ray and lithological logs are also included.

CHAPTER 3:

Methodology and Data

Abstract   The workflow designed for this thesis comprises two key elements: (1) Outcrop/Behind Outcrop (OBO) methodology and (2) reservoir modelling.

OBO is a multi-approach methodology, integrating both outcrop- and subsurface-derived data. After an initial selection of outcrops best suited to this approach, classical field work was undertaken, based on identification and description of the main sedimentary geobodies in terms of geometry, facies analysis and vertical relationship with other geobodies. In addition, new technical advances, based on photogrammetry with RPAS (Remotely Piloted Aircraft System), were used in the construction of digital outcrop models (DOM), a useful tool for completing field information as well as georeferencing of all key outcrop data. The complementary subsurface-based study consisted, principally, of the acquisition of both cores and well logs by drilling boreholes directly behind the selected outcrops. Additionally, geophysical techniques such as GPR (Ground Penetrating Radar) were also utilized in order to provide a complete subsurface dataset. Through the integration of data, from both outcrop and subsurface (OBO characterization), key characteristics, that help in the identification of the geobodies, as well as the spatial distribution of the heterogeneities that delimit these geobodies were established. In addition, quantitative conceptual models and paleogeographic maps, that represent the distribution of the identified geobodies, were also generated.

OBO characterization provided the necessary input data for the second key element of the study; geostatistical reservoir modelling. A 3D reservoir model is a computer-based digital representation, discretized into 3D cells, of the subsurface and its rock and petrophysical properties. Building a 3D reservoir model includes the construction of a stratigraphic model and determining the spatial distributions of facies in the 3D model with geostatistical techniques. Two stochastic simulation algorithms for facies modelling were used in this work: (1) object-based modelling and (2) multi-point statistics-based modelling.

A total of 2.5 km^2 of outcrop area, were studied. 22 high-resolution sedimentological logs were constructed in order to characterize lateral and vertical facies variability in the studied stratigraphic section. In addition, 15 wells were drilled behind the outcrop, with a total drilled section of 274.4 m. Three GPR profiles were also acquired, covered across a total of 443 m of outcrop length.

3.1. Introduction

Guided by the general objectives of the present thesis, established in Chapter 1, a study methodology with two key elements was applied: (1) Outcrop/Behind Outcrop (OBO) methodology and (2) reservoir modelling. The first is a multi-approach technique, integrating both outcrop and subsurface data, in order to best characterize the outcrops. The results of this were the input data for the second phase of the study; reservoir modelling. Figure 3.1 details the workflow designed for this thesis, from acquiring outcrop and subsurface data required for OBO characterization to obtaining the results of geostatistical modelling of selected outcrop analogues.

3.2. Outcrop/Behind Outcrop (OBO) Methodology

Outcrop/Behind Outcrop methodology is a multi-approach technique that consists of data collection in both the outcrop and subsurface of a selected location (Fig. 3.2). This technique includes, in turn, different methodologies at different study scales (macro-, meso and micro-scale). Two large groups of data are acquired with this methodology: outcrop- and subsurface-derived data.

Firstly, an outcrop-based study was undertaken with the aim of describing the sedimentological characteristics of the selected outcrops, aimed principally at the identification and description of the main architectural elements or geobodies, in terms of geometry, internal structure, facies analysis and both the vertical and lateral relationship with other geobodies. In addition, this phase also included the 3D reconstruction of outcrops (digital outcrop models or DOM), a task made possible by new technical advances in photogrammetry with RPAS (Remotely Piloted Aircraft System) designed to complement the outcrop-based observations.

In a second phase, subsurface data was acquired directly behind the selected outcrops. These data include continuous core recovery and well log data (See Sections 3.13 to 3.15).

The final phase of this part of the study workflow was the integration of both outcrop and subsurface data (OBO characterization; Fig. 3.1), in order to establish those key characteristics that: (a) assist in the identification of the geobodies and determine the spatial distribution of the heterogeneities that delimit these geobodies for a specific depositional environment; and (b) the generation of quantitative conceptual models and paleogeographic maps which summarise the spatial distribution of the identified geobodies.
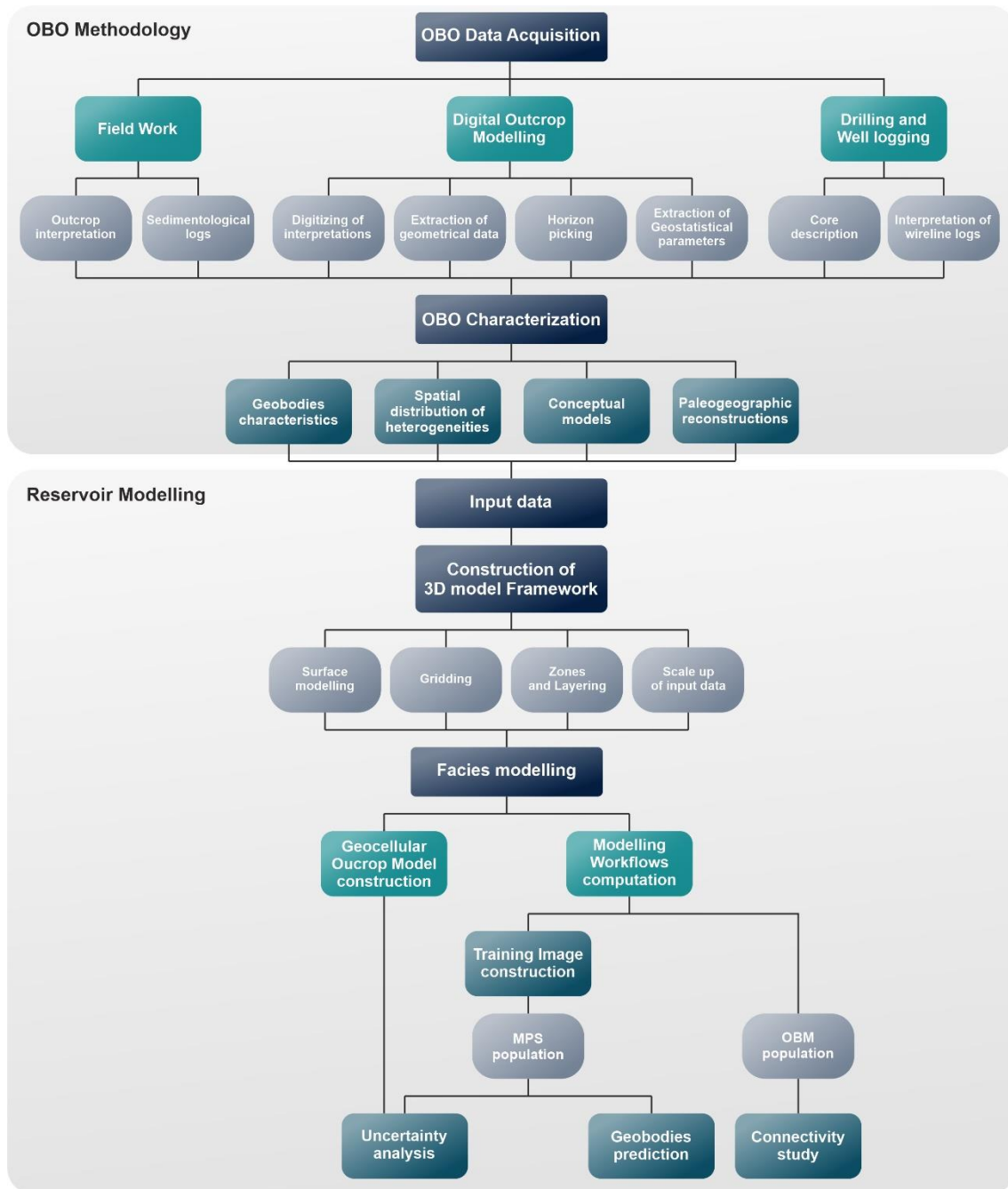
Fig. 3.1. Generalised workflow applied in this study to both outcrop/behind outcrop characterization and geostatistical reservoir modelling of outcrop analogues. OBO (Outcrop/Behind Outcrop); MPS (Multi-Point Statistics); OBM (Object-based modelling).
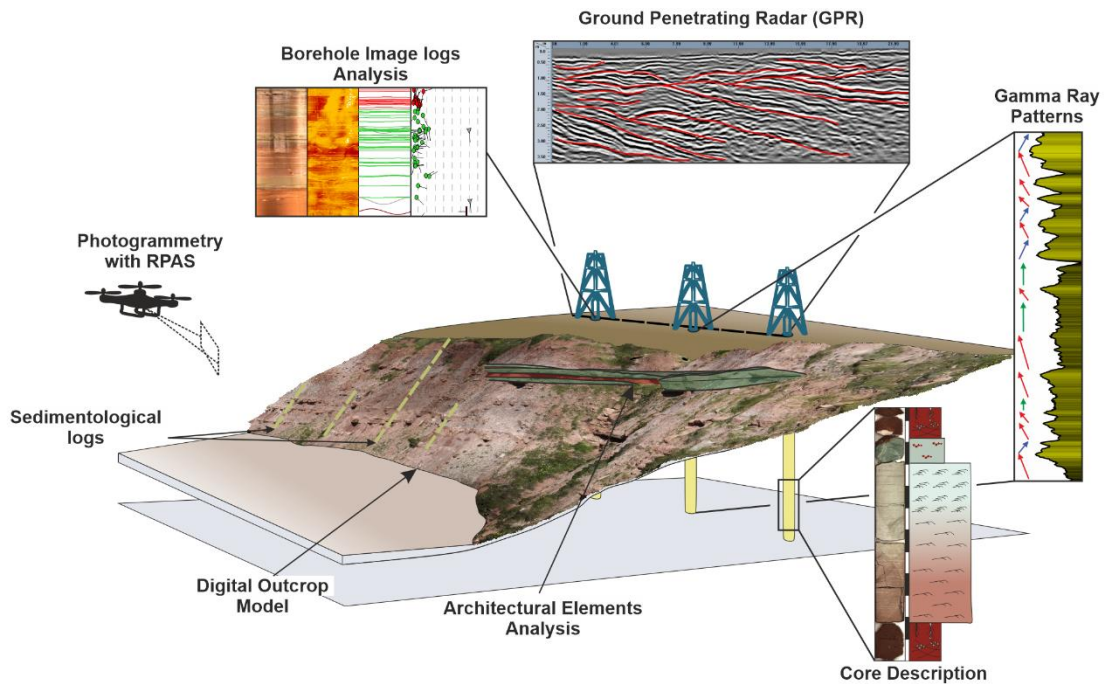
Fig. 3.2. Outcrop/Below Outcrop (OBO) characterization workflow designed and applied in this study including outcrop-derived and digital outcrop-derived observations and measurements, core description, Gamma Ray logging, borehole imaging and ground-penetrating radar profiles. RPAS: Remotely Piloted Aircraft System.

The following sections present a detailed description of the techniques and equipment used to carry out the OBO characterization.

3.1.1. Fieldwork

In the first phase of data acquisition, traditional field data collection was carried out. This consisted of: (1) definition of the area selected for this study; (2) selection of those outcrops best suited for integration of both surface and subsurface data, (3) photointerpretation of the selected outcrops; (4) geometric analysis of the architectural elements (geobodies) on the selected outcrops; and (5) construction of high-resolution sedimentological logs along the outcrop.

3.1.2. Digital Outcrop Model: Acquisition, Model Building and Interpretation

Digital outcrop models (DOMs), also called virtual outcrop models (VOMs), are a 3D digital representation of the outcrop surface, in the form of a textured polygonal mesh generated from a three-dimensional dense point cloud (Bellian *et al.*, 2005; Buckley *et al.*, 2010).

DOMs allow for the interpretation and reproducible measurement of different geological characteristics (e.g. geological surface orientation or width and thickness of the layers; Bellian *et al.*, 2005). The number of identifiable and measurable geological features depends, to a large extent, on the outcrop model resolution (Buckley *et al.*, 2008).

Two techniques are available to obtain the necessary data to build a DOM: LiDAR and Structure-from-Motion photogrammetry (SfM photogrammetry). The latter, SfM photogrammetry, was selected to build the DOMs for this study as this technique has both a lower cost and higher flexibility in terms of data acquisition as compared to the LiDAR technique.

Photogrammetry is a technique that captures 3D characteristics from two or more images of the same object, obtained from different angles (Donovan & Lebaron, 2009, Haneberg, 2008, Wilkinson *et al.*, 2016). In particular, Structure-from-Motion (SfM), is a photogrammetric technique, where the positions and orientation of the camera are resolved automatically (Ullman, 1979; Snavely *et al.*, 2007). SfM uses superimposed images to generate 3D point clouds, from which a textured polygonal mesh is calculated, generating the DOMs (Vasuki *et al.*, 2014; Wilkinson *et al.*, 2016). For this study, the images were acquired with a Remotely Piloted Aircraft System (RPAS).

Although the process of data acquisition with RPAS, in order to generate a DOM, with SfM photogrammetry, is relatively fast and flexible; the subsequent data processing leading to the finished digital outcrop model is, at present, very labour intensive. The time needed for data acquisition and building a DOM depends both on outcrop area and the resolution of the DOM. Figure 3.3 summarises the workflow applied in this study for both the data acquisition and the processing to build a DOM. In addition, the approximate time needed to complete each stage of the workflow to build a DOM is also shown.

Equipment

A Remotely Piloted Aircraft System (RPAS) was used to acquire the images. Two high-precision GPS devices were used for the acquisition of the Ground Control Points (GCPs). The RPAS was a multi-rotor octocopter FV-8 manufactured by Atyges, equipped with a Sony ILCE-5000 camera with a resolution of 20.1 megapixels (Fig. 3.4). The images were acquired with an exposure time of 1/800s and an ISO speed of 100. The focal length used was 16 mm. The two GPS devices used were the GEOMAX Zenith 20, with a cm-scale accuracy. One device was used as base and the other was used as a Rover, obtaining measurements from a Differential GPS system (DGPS) with errors on a scale of centimetres (horizontal accuracy 10 mm ± 1 ppm and

vertical accuracy 20 mm ± 1 ppm; Fig. 3.4). The WGS84 UTM Zone 30 N coordinate system was used in the georeferencing of all acquired data.
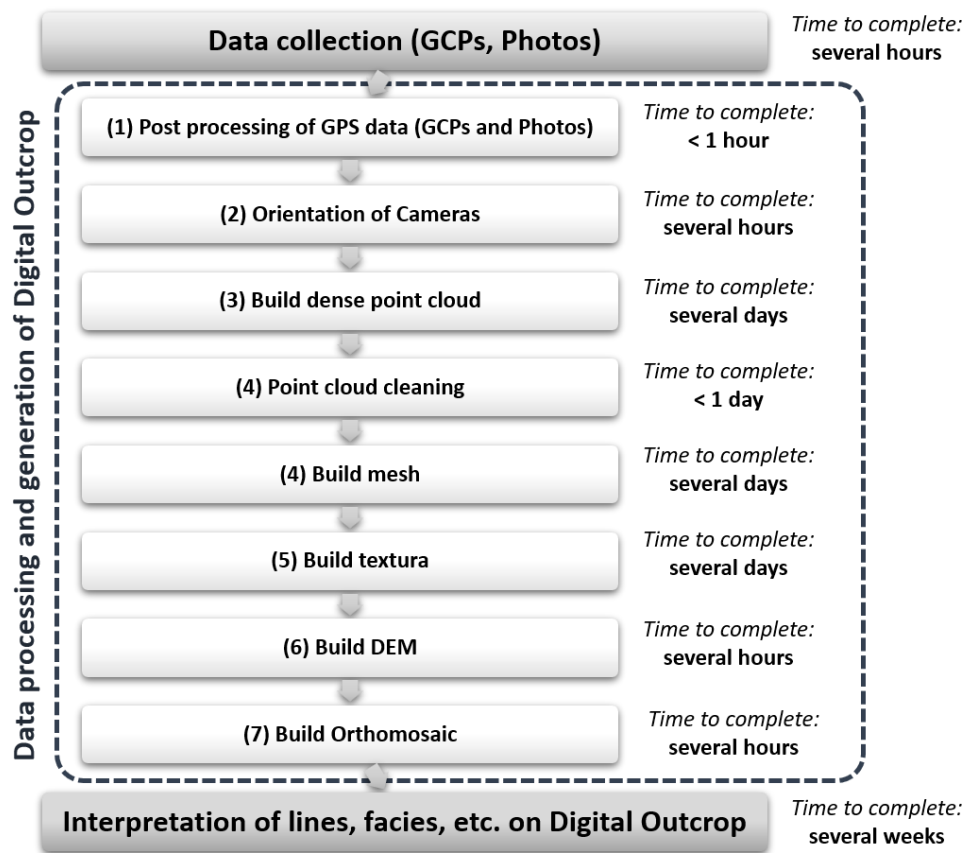
Fig. 3.3. Data collection and processing to build a digital outcrop model; workflow and approximate time needed to complete each stage of the workflow. GPS: Global Positioning System; GCP: Ground Control Point; DEM: Digital Elevation Model**.**

Specific markers were designed in order to obtain an easy and precise recognition of the GCPs in the images taken from different angles. These markers are metallic and have an inverted T shape, with a flat base and another surface perpendicular to the base (Fig. 3.4).

Two specific software applications were used: MiKroKopter-Tool$_{TM}$ v2.20 software, used for flight planning; and Agisoft Metashape Professional$_{TM}$ v1.5.1 software, used in building the DOMs from SfM photogrammetry.
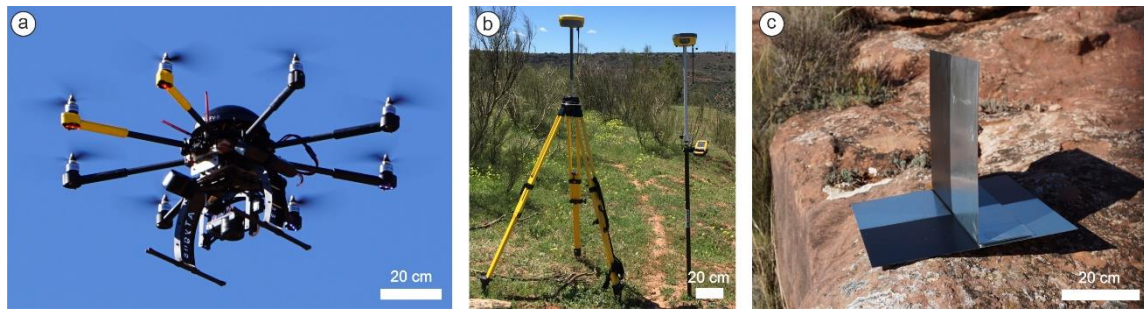
Fig. 3.4. Equipment used in this study: (a) Multi-rotor Octocopter FV-8 from Atyges, equipped with a Sony ILCE-5000 camera of 20.1 megapixels resolution; (b) GPS GEOMAX Zenith 20; (c) Metallic marker with inverted T-shape used for the acquisition of ground control points.

Data acquisition

A typical SfM photogrammetry survey with RAPS platform requires flight planning and measurement of ground control points (GCPs) for georeferencing purposes. The flight plans are typically generated in the laboratory with dedicated software. In this case the MiKroKopter-Tool$_{TM}$ v2.20 application was used for the flight planning. The parameters to be considered in the flight planning are: flight height, flight trajectory and camera pitch. The flight height is set based on the desired ground sampling distance (GSD). Fight trajectory is calculated based on the outcrop orientation and the longitudinal and transversal image overlap. The camera pitch is set based on the outcrop slope angle in order to obtain images from different perspectives. All these parameters vary according to the goal of each flight. For this study, generation of a high-resolution 3D model was required. Accordingly, high image overlaps and low-altitude flights were preferred in order to achieve small GSDs.

In the field, before executing the flight plans, a systematic acquisition of the GCPs, covering the entire surface of the model, was carried out. The final step was to execute the previously generated RPAS flight plans, in order to obtain the necessary images (Fig. 3.5).
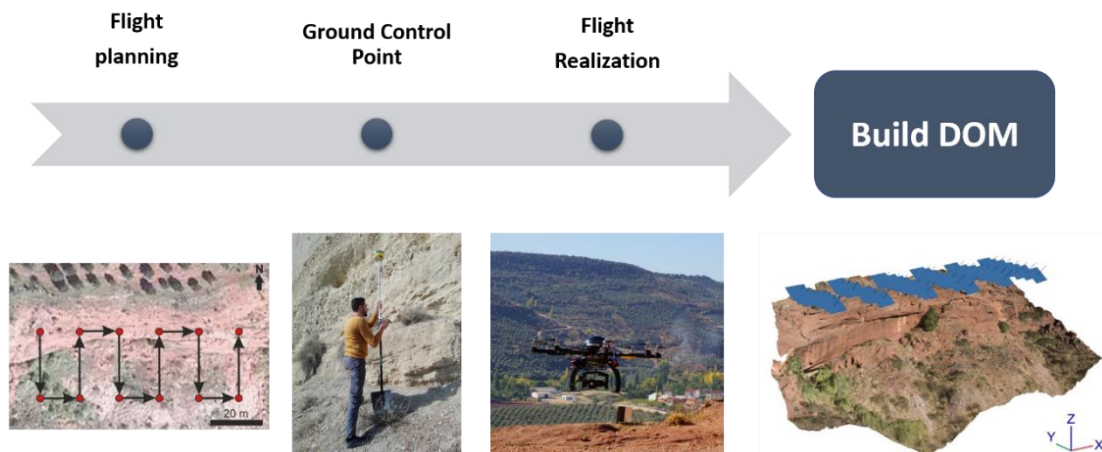
Fig. 3.5. The data acquisition workflow for building a DOM used in this study.

Data processing and generation of Digital Outcrop Models

Before starting any operation, it is necessary to load the images in the photogrammetric software (Agisoft Metashape_{TM}), check that the images are correctly georeferenced, apply a mask to the areas that are not of interest for the modelling (e.g. sky and/or background terrain) and introduce and identify the GCPs in each image.

Once a set of images is loaded into the software, they must be aligned. In this stage the software finds the camera position and orientation for each photo and builds a disperse point cloud model (Fig. 3.6a). The next step is building a dense points cloud model. Based on the estimated camera positions the program calculates depth information for each camera to be combined into a single dense point cloud (Fig. 3.6b). This dense points cloud is connected by triangles in a triangulation operation to from a mesh surface (Fig. 3.6c). The final step is rendering the triangular mesh, building a texture map from the high-resolution images captured with the RPAS (Fig. 3.6d).

Additionally, high-resolution digital elevation models and high-resolution orthomosaics can be generated with SfM photogrammetric technique.
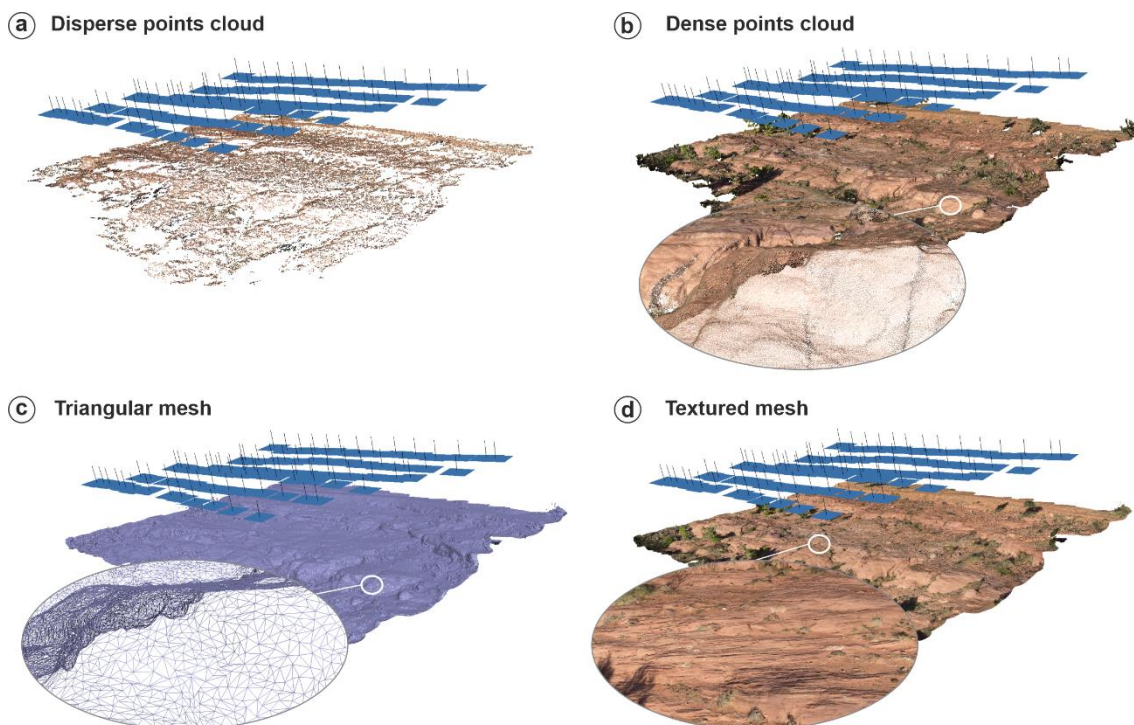
Fig. 3.6. The workflow for building a digital outcrop model in this study

Interpretation of Digital Outcrop Models

Once the DOM is built, it is imported into the specific DOM interpretation software. For this study the Virtual Reality Geological Studio (VRRGS) software application was used.

In this step, the outcrop interpretations developed during the fieldwork stage were digitized; specifically, geobody mapping, facies and facies associations mapping, as well as the bounding surfaces of the geobodies and any key stratigraphic surfaces**.** The geometric parameters (shape, thickness and width) of the identified geobodies were also extracted, as well as measurements of paleocurrents to complete the field observations (Fig. 3.7). In this way, all the interpretations that characterize the outcrop are perfectly georeferenced.
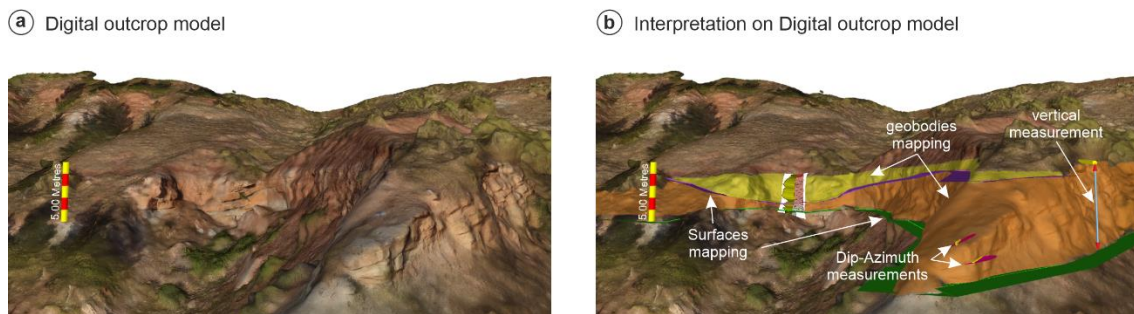
Fig. 3.7. Digitization of interpretations and extracting georeferenced outcrop information from the DOM. (a) Results of high-resolution DOM imported into VRGS software. (b) Example of DOM interpretation.

3.1.3. Drilling and Well logging

The equipment for core recovery and well log acquisition used in this study were provided by the Drilling and Well logging Unit of the Scientific Instrumentation Centre (CIC) of the University of Granada. It consists of a rotary drill, geophysical well logging equipment and a high-resolution core scanner.

Drilling

The objective of this process was to obtain high quality cores behind the previously selected outcrops. For this, the Rolatec RL 48 rotary drill (Fig. 3.8a) of CIC is ideal due to its compact design and the ease with which it was able to access areas characterised by difficult topography. During drilling, continuous rock cores with a diameter of 85 mm were recovered (Fig. 3.8b). Once the cores were acquired, they were scanned with the Smartcube CIS 1000L scanner (Fig. 3.8c), slabbed parallel to maximum dip and placed in a core tray by the CIC technician for later description (Fig. 3.8d).

Fig. 3.8. (a) CIC Rolatec RL-48 rotary drill used in this study. **(b)** Example of recovered cores. **(c)** CIC core scanner Smartcube CIS 1000L used in this study. **(d)** Example of core tray displaying 1m of slabbed core.

Well logging

Well logging, also referred to as wireline logging, is an important tool in the acquisition of data from the subsurface. In general, each logging method or tool is based on a certain physical property of rocks (electrical conductivity, natural or induced radiation, propagation of

mechanical energy, etc.) and from both measurements of these properties and subsequent data processing an image of one or more aspects of the subsurface is obtained.

Well logging acquires continuous data on the rock properties along the borehole wall and for some limited distance into the surrounding rock. Through integration of the different well logs, we are able to generate an interpretation of many aspects of the relevant rock horizons in the subsurface. Well logging is therefore a major tool with which to complement the data acquired from the outcrop.

The well logging equipment used for this study was again provided by the Drilling and Well Logging Unit of the Scientific Instrumentation Centre of the University of Granada. This equipment, supplied by ALT (Advanced Logic Technology S.A.), is composed of (Fig. 3.9):

(1) *Winch*: is the component which winds the wireline up the borehole. The motor regulates the speed of ascent and descent of the downhole probe.

(2) *Wireline*: the aim of this cable is to support the downhole probe, supply power, and send the measurement signal through the downhole probe to the borehole logging system.

(3) *Borehole logging system (MATRIX)*. This includes the communication control elements of the downhole probe as well as the recording of data for subsequent processing.

(4) *Tripod*: is a purely mechanical component designed is to support and guide the cable.

(5) *Downhole Probe*: this is a cylindrical metal tube that consists of an active or passive sensor (generator and/or receiver) of a physical property (electrical, radioactive, etc.) and a converter of the captured signal. The equipment used in this study consists of four probes (natural gamma ray, spectral gamma ray, acoustic borehole imager and optical borehole imager probes).

The following is a description of the different downhole probes used in this study:

Natural Gamma Ray probe (GR)

The Natural Gamma Ray (GR) probe measures the amount of gamma radiation occurring naturally within the formations crossed by a borehole (Fig. 3.10). The GR tool is equipped with a scintillation Thallium-doped Sodium Iodide crystal, which, when hit by gamma rays, emits pulses of light. These pulses of light are amplified by a photo multiplier tube and are then converted into electrical pulses. The pulses are counted, digitized and transmitted up the wireline to the surface acquisition system. Gamma rays are produced mainly by isotopes of Potassium, Thorium, Uranium and their decay products.
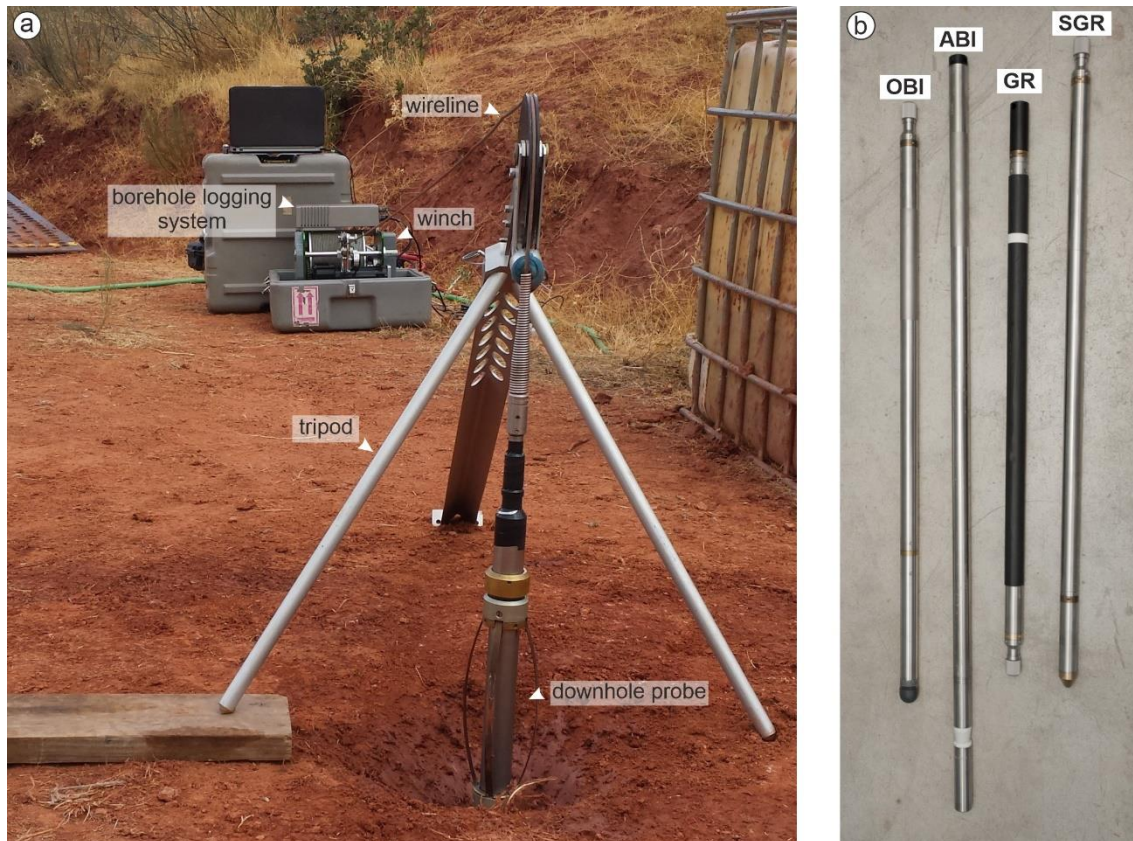
Fig. 3.9. Well logging equipment provided by the Drilling and Well logging unit of the Scientific Instrumentation Centre of the University of Granada, as used in this study. GR: Natural Gamma Ray probe; SGR: Spectral Gamma Ray probe; ABI: Acoustic borehole imager probe; OBI: Optical borehole imager probe.

The parameters assigned to the acquisition of GR logs were a sampling rate of 3 cm and a logging speed of 2 m/min.

Qualitatively, and in its simplest form, the GR can be used to help identify lithologies based on the API values (often in conjunction with other logs), to suggest facies and sequences on the basis of repeatable patterns in the GR curve validated by comparison with core analogues, to identify key stratigraphic surfaces and to correlate. In addition, quantitatively, the most important use of the gamma ray is in petrophysics, as a shale indicator (VShale or VClay), although this relationship is not always straightforward, if we assume that the entire GR response is associated with detrital clay. However, the presence of associated radioactive detrital minerals in sandstones, such as K-feldspars, micas and/or heavy minerals, generates GR responses characterized by high to moderate API values.

Spectral Gamma Ray probe (SGR)

The Spectral Gamma Ray (SGR) probe has the similar measurement principle to the natural gamma ray tool. This tool is also equipped with a scintillation Thallium-doped Sodium Iodide crystal, which, when hit by natural gamma rays, emits pulses of light. However, it differs from the natural gamma ray tool as it records the energy spectrum of the gamma radiation emitted by the formations. A real time processing is applied to the energy spectrum and computes the concentration of the three main radioisotopes ^{40}K, ^{232}Th and ^{238}U (Fig. 3.10).

The parameters assigned to the acquisition of SGR logs were a sampling spacing of 3 cm and a logging speed of 1 m/min.

The spectral gamma ray can be used to derive a quantitative radioactive mineral volume and thus a more accurate shale volume. Qualitatively it can also indicate dominant clay mineral types, provenance, suggest broad depositional environments help to localise source rocks, and major sequence stratigraphic surfaces (Bataller *et al.,* 2020), and occasionally to indicate fractures.

Acoustic Borehole Imager probe (ABI)

The acoustic borehole scanner tool generates an image of the borehole wall by transmitting ultrasound pulses from a fixed transducer with a rotating mirror and recording the amplitude (travel time) of the signals reflected at the interface between borehole fluid and the borehole wall (Fig. 3.10).

The ultrasonic energy wave is generated by a specially designed piezoelectric ceramic crystal and has a frequency of around 1.2MHz. On triggering, an acoustic energy wave is emitted by the transducer and travels through the acoustic head and borehole fluid until it reaches the interface between the borehole fluid and the borehole wall. Here a part of the beam energy is reflected back to the sensor, the remainder continuing on into the formation at a changed velocity. By careful time sequencing the piezoelectric transducer acts as both transmitter of the ultrasonic pulse and receiver of the reflected wave. The travel time for the energy wave is the period between transmission of the source energy pulse and the return of the reflected wave measured at the point of maximum wave amplitude. The results of this tool are two unwrapped 360° oriented image representing the travel time for the energy wave and the wave amplitude (Fig. 3.10).

The parameters assigned to the acquisition of ABI logs were a sampling spacing of 3 mm and a logging speed of 2 m/min.

The main application of this probe is the identification of sedimentary structures and fractures. With the image data displayed on screen, in the unwrapped borehole format, dipping surfaces appear as a sine wave, the amplitude of the wave indicating the dip, and the position of the low point of the wave indicating the dip azimuth.

Optical Borehole Imager probe (OBI)

The Optical Borehole Imager (OBI) is an advanced logging tool designed for the optical imaging of the borehole wall in both open and cased wells, whether drilled with air or clear water. The OBI incorporates a high resolution, high sensitivity CCD digital camera with matching Pentax optics. The CCD camera, located above a conical mirror, captures the reflection of the borehole wall. The light source is provided by a light ring assembly located in the optical head. The camera CCD sensor consists of an array of light sensors, each representing one pixel of the complete image. Due to manufacturing limitations individual sensors have a slightly different response and calibration factor. To produce a coherent image the camera processing system checks all the pixels and compensates for variations (white balance). The displayed log image is derived from a single annulus extracted from the total pixel array. Azimuthal resolutions available are 720, 360, 180 and 90 points per recorded circle. By using processed camera data in combination with deviation sensor data, the tool can generate an unwrapped 360° oriented image (Fig. 3.10).

The parameters assigned to the acquisition of OBI logs were a 3 mm sample spacing and a logging speed of 2 m/min.

As the result of the OBI probe is a real and oriented unwrapped image from the borehole wall, its primary applicability is the identification of sedimentary structures and fractures, similar in many respects to the ABI tool, with the additional benefit of acquiring visual lithological information from well intervals with no core recovery. In addition, given the high resolution and visual component, it is an extremely useful tool for depth matching core and wireline logs.
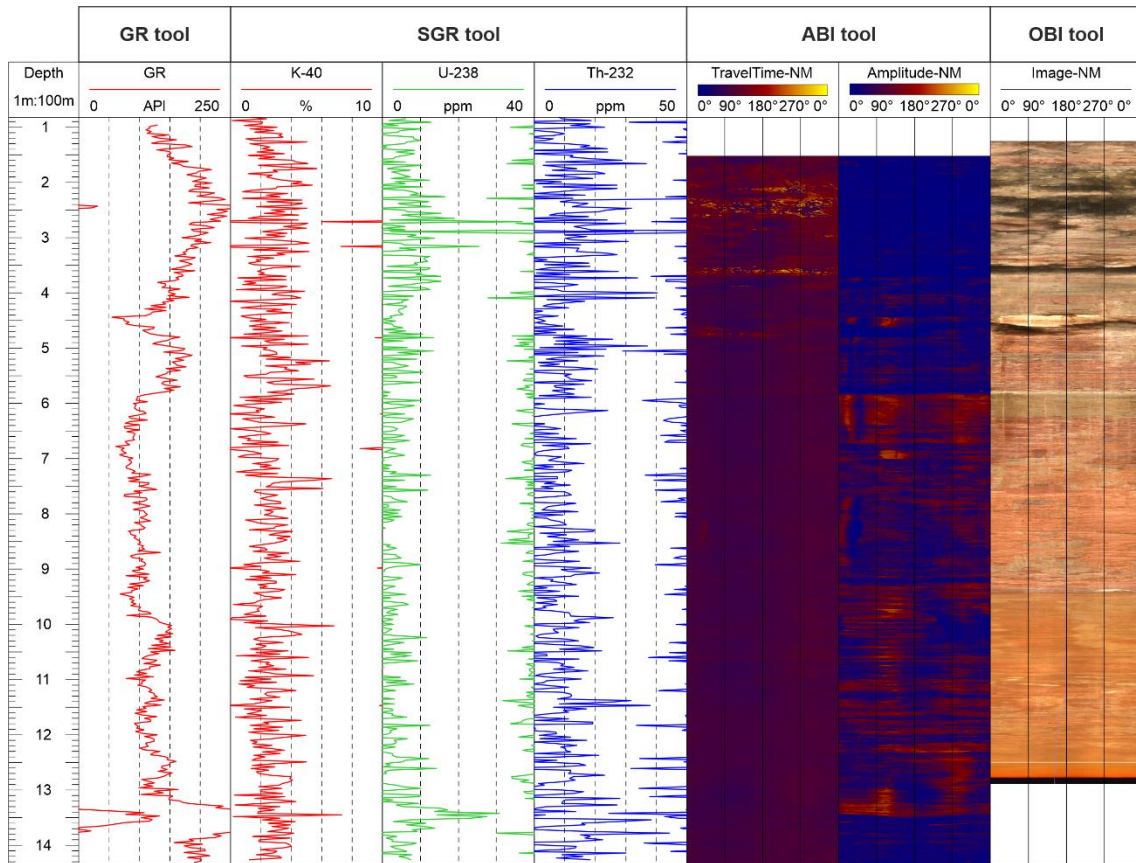
Fig. 3.10. Sample of pre-processed wireline log data acquired from the natural gamma ray (GR), spectral gamma ray (SGR), acoustic borehole imager (ABI) and optical borehole imager (OBI) tools.

3.1.4. Processing of Well logs

The response of the electrical logs acquired by logging tools is typically affected by numerous factors, some inherent in the drilling of a well and both its dimensions and rugosity, whilst others are due to the formation fluids or mechanical failures. Almost all of these factors impact the final response of the tool and accordingly they should be minimized, as far as possible, during logging.

For the processing and interpretation of well logs in this study, WellCAD$_{TM}$ software from ALT (Advanced Logic Technology S.A.) was used.

Corrections applied during well log processing were as follows (Fig. 3.11):

Depth corrections

Sometimes, the depth reference of a log is altered by circumstances, purely mechanical in origin or operator error, which arise during data acquisition. In this case, it is necessary to

readjust the depth with respect to a reference log. In this work, the OBI log was used as a reference log, as it shows the real image of the borehole wall.

Data filtering

The filter process aims to remove spikes from the data set and thereby reduce the effect of erroneous data recordings. This process was applied to all logs (GR, SGR, ABI and OBI logs). In addition, the filter process was also applied when data density was high and impeding correct visualization of the data trend. This process was especially applied to the GR and SGR logs.

Interpolation of Bad Traces

Sometimes, ABI and OBI logs show No Data or Null traces which can be removed. The algorithm scans the image from bottom to top for traces consisting entirely of Null values. If such a trace has been detected it will be replaced with the last trace found containing valid data points. This process was applied to both ABI and OBI logs.

Data display corrections

This process consists of applying different visual modifications to the hard data to facilitate its visualization. For example, in the GR logs, a shading was applied with a vertical gradient to the right of the log. In the case of ABI logs, the colour palette used to represent the amplitude data was adjusted to improve its visualization.

Image quality corrections

These corrections are applied to the OBI log. Image quality correction is based on modifying the brightness and contrast parameters of the image to optimize the quality of the resulting image.

Centralization corrections

The process of centralizing corrections was applied to the ABI logs. A correct measurement of the acoustic signal travel time depends on the degree of decentralization of the probe within the borehole. Centralizing corrections is a process to correct travel time for decentralization effects. Assuming that the decentralization effect on the data can be approximately described through a sinusoid the centralization process removes this trend and corrects the input data according to a best-fit sinusoid.

Image normalization

The goal of the normalization process is to improve the contrast in an image using a histogram normalization technique. A histogram of the data is computed and the total range is

partitioned into several classes, each having the same number of data points. This process is applicable to ABI logs.

In general, two normalization types can be distinguished, static and dynamic. Static normalization computes the histogram and cumulative distribution taking the entire data set into account. This means the value range is between the total minimum and maximum of the log. Dynamic normalization improves the local contrast in an image. Histogram and cumulative distribution are computed from a sliding data window and the normalization result is applied to a distinct part of the window only. The window size is determined from the extension of the largest event for which we wish to improve the contrast.

WellCAD$_{TM}$ offers both Dynamic 1- and 2-dimensional options. The only difference is the option to additionally define the extension of the data window in a radial direction when choosing the Dynamic 2-dimensional option. The radial extension of the data window always covers an entire trace (360°) when using the Dynamic 1-dimensional algorithm, whereas the Dynamic 2-dimensional algorithm replaces only the centre value of the data window. In addition, a High Pass normalization mode is also available. This combines Dynamic 2-dimensional normalization with a high pass filter. It can be used to remove radial low frequency trends such as those effects caused by a decentralized tool.
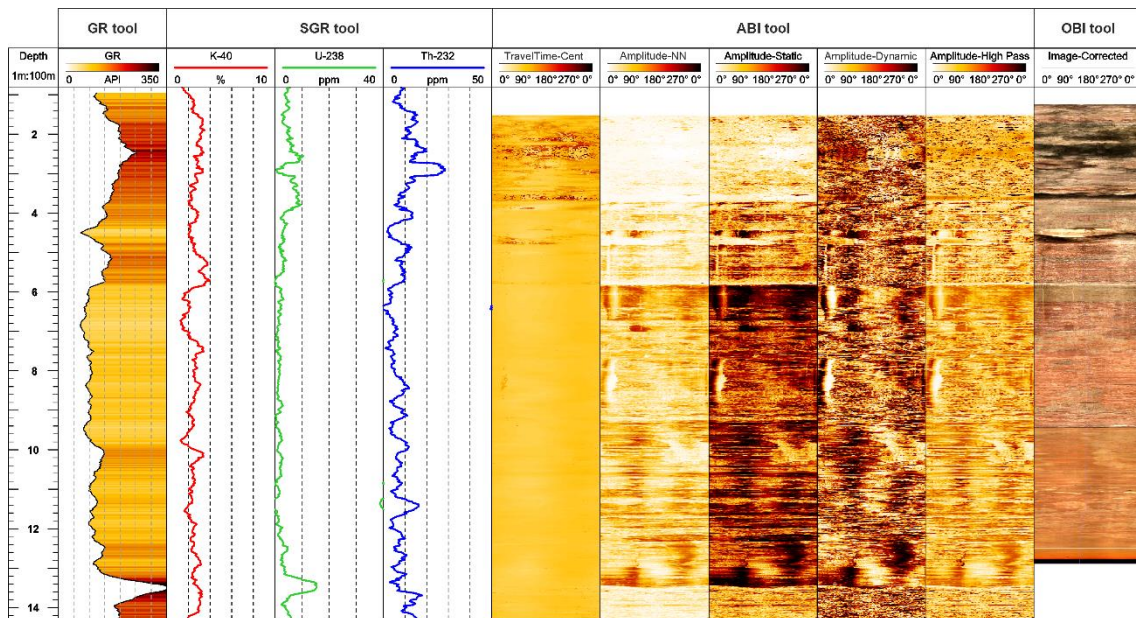
Fig. 3.11. Sample of processed data obtained from the GR, SGR, ABI and OBI tools. For the GR and SGR logs a filter was applied. For the ABI; static, 1-dimensional dynamic and High Pass normalization were applied. For the OBI log, image quality corrections were applied. See Figure 3.10 for a comparison between the pre-processing and post-processing data results. Header key: GR: Gamma Ray log; Travel Time-Cent: centralized Travel time log; Amplitude-NN: non-normalized amplitude log; Amplitude-Static: amplitude log with static normalization; Amplitude-Dynamic: amplitude log with 1-dimensional dynamic normalization; Amplitude-High Pass: amplitude log with high pass normalization.

3.1.5. Core Description

This phase of the OBO workflow consisted of a high-resolution description of the slabbed cores recovered during the drilling phase. A 1:10 scale core description, was carried-out using a template, designed for this study, which includes columns for: driller's depth, modal grain-size, principal and subordinate sedimentary structures, rock colour (based on the Munsell colour chart), bed contacts, sequence trends (fining- or coarsening upward), fractures and lithofacies codes as well as other remarks and environmental interpretations.

Fig. 3.12. Core description template used in this study. Depth: driller's depth; Nº core: number of core; Nº box: number of core box; Fm/Mb: Geological Formation or Member; Grain Size: VF (very-fine sandstone), F (fine sandstone), M (medium sandstone), C (coarse sandstone), VC (very-coarse sandstone), G (granule conglomerate); P (pebble conglomerate); C (cobble conglomerate); Mud cont.: visual estimate of detrital mud content; Color: rock colour based on the Munsell colour chart; Surfaces: bed contacts (e.g. sharp, erosive, etc.); Trend: sequence trends (fining- or coarsening upward); Cem. abun. & distrib.: cement abundance and distribution; Sed. struct.: principal and subordinate sedimentary structures; Dep. Env.: depositional environment.

3.1.6. Ground Penetrating Radar (GPR)

Ground Penetrating Radar (GPR) is a high frequency electromagnetic sounding technique that has been developed to investigate the shallow subsurface using the contrast of dielectric properties (Casas *et al.,* 2000). The principles and theory of this technique are based on the wave equation, itself derived from Maxwell's equations for electromagnetic wave propagation. The GPR technique operates on the simple principle that electromagnetic waves, emitted from a transmitter antenna, are reflected from subsurface materials and detected at another antenna, acting as receiver. The results of GPR data are presented in the form of time-distance plots that are analogous to conventional reflection seismic records, and in fact the

method has many similarities to the seismic reflection method with a pulse of electromagnetic energy substituting for the elastic (seismic) energy (Fig. 3.13; Casas *et al.,* 2000).

GPR has been demonstrated to be a valuable tool in the study of outcrop analogues (e.g. Corbenau *et al.*, 2001; Zeng *et al.*, 2004; Van Den Bril *et al.*, 2007; Kostic & Aigner, 2007; Hugenholtz *et al.*, 2007; Rice *et al.*, 2009; Pascucci *et al.*, 2009; Nielsen *et al.*, 2009; Szerbiak *et al.*, 2010; Abatan *et al.*, 2013; Franke *et al*., 2015). Several GPR campaigns were designed in this case, to image the subsurface in the outcrops of the study area. The campaigns were conducted in collaboration with Dr. Teresa Teixidó and Dr. José Antonio Peña (Instituto Andaluz de Geofísica, University of Granada).

Keeping in mind the guiding principle, that there is a clear relationship between increasing frequencies, increased resolution but decreasing depths of penetration, the GPR profiles, for this study, were acquired using both a shielded 200 MHz antenna, penetrating to only about 7 m below the surface, and a 40 MHz antenna, which increased the penetration depth to 20 m below the surface but with lower resolution.
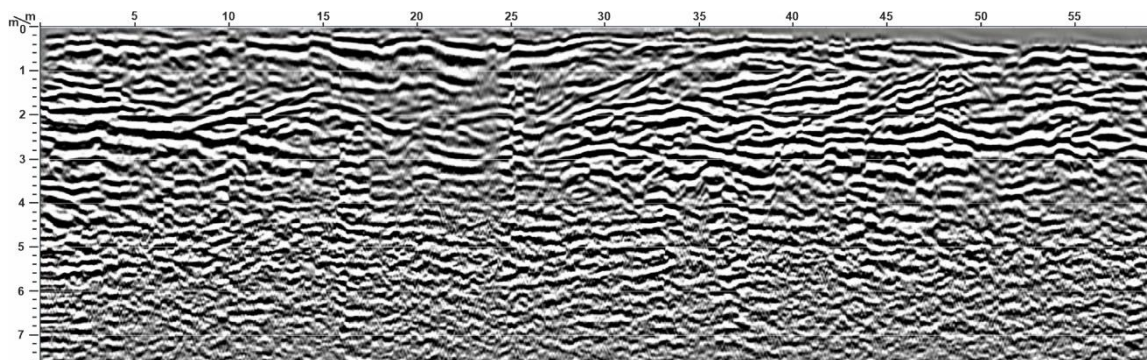
Fig. 3.13. Example of GRP profile obtained with a 200 MHz antenna.

3.2. Reservoir Modelling

Typically, geoscientists will use a series of 2D maps and cross sections, derived from well and/or seismic data, in order to characterize the reservoir. These methods may often be sufficient for homogeneous, structurally and/or sedimentologically simple reservoirs. However, for highly heterogeneous reservoirs, these methods can not accurately represent the distribution of heterogeneities through the full volume of the reservoir, given the significant lateral and vertical variability in many parameters. In this sense, reservoir modelling is the

technique which can best describe the distribution of reservoir heterogeneities in sufficient detail, by integrating both descriptive and quantitative analyses, as well as mitigating the sampling bias that is often present in reservoir exploration and production.

Reservoir modelling is the broad term for a set of processes which typically aim to integrate all available geoscience data and interpretations, into a 3D volume, discretized into 3D cells, with the aim of modelling or predicting rock heterogeneities and petrophysical properties within the framework of necessarily incomplete data typical of subsurface contexts (Ma, 2019). This process, known as static reservoir modelling, consists of assigning facies types and petrophysical property values using statistically-based methods and workflows which require input data to geometrically define the reservoir and condition modelling of key properties. The result is a 3D model that describes the main characteristics of the reservoir in terms of its facies distribution, petrophysical properties and volumetrics. This static reservoir model is then used as input into reservoir simulation (dynamic reservoir modelling), during which reservoir engineers add other reservoir characteristics, such as pressures, temperatures, and fluid and gas compositions to simulate the flow of fluids within the reservoir over its production lifetime. In this study, the reservoir modelling process has focused only on the geostatistical modelling of facies.

A software application, known as Petrel$_{TM}$, was used in this study for the reservoir modelling process. Petrel$_{TM}$ is a powerful software platform, commonly used in the exploration and production sector of the petroleum industry. This software platform allows the user to interpret seismic data, perform well correlations, build reservoir models, visualize reservoir simulation results, calculate volumes, produce maps and design development strategies to maximize reservoir exploitation (https://www.software.slb.com/products/petrel). Risk and uncertainty can also be assessed throughout the life of the reservoir. Petrel$_{TM}$ is developed and commercialized by Schlumberger.

This section presents the reservoir modelling workflow designed for this study, including the input data used, the process of constructing both a 3D reservoir model and a geocellular outcrop model and the modelling methods applied in order to obtain the geostatistical reservoir modelling results.

3.2.1. Input Data

Two types of hard data were used in the reservoir modelling process: (1) data required to define the geometry of the reservoir model and (2) data required to define the 3D distribution of rock properties.

Data required to define the geometry of the reservoir model include a polygon that delineates the lateral extension of the reservoir model. In addition, the top and base surfaces of the reservoir model are required in order to define the vertical boundaries and thickness of the model. Also, intermediate surfaces were added to define the internal stratigraphic architecture of the reservoir model. These data, both boundary polygon and surfaces, were obtained from the DOM (see Section 3.1.2).

The 3D distribution of rock properties mainly uses data acquired from the shallow wells to condition the model. These data are derived from the sedimentological logs, core description and well logs. As $Petrel_{TM}$ software is designed for subsurface modelling, the sedimentological logs generated at outcrop were also added as "pseudowells". This type of data includes lithology, lithofacies, facies associations, gamma ray logs and paleocurrent data. Additionally, digitized outcrop interpretations from DOM were added in order to build the geocellular outcrop model.

3.2.2. Construction of 3D Reservoir Model

A 3D reservoir model is a computer-generated digital representation of the subsurface, including rock (facies) and petrophysical properties (Ma, 2019). This digital representation is discretized into 3D cells for modelling the properties (facies and petrophysical properties). Building a reservoir model includes the construction of a structural and/or stratigraphic model as well as determining the spatial distributions of facies and petrophysical properties in the model (Ma, 2019). A reservoir model requires input data to geometrically define the reservoir and condition the property modelling.

The first step is modelling of those surfaces previously interpreted in the digital outcrop model (Fig. 3.14). In this study, these surfaces correspond to stratigraphic boundaries. Surface modelling is a process that consists of generating grid surfaces based on point and/or line data.

Because a reservoir model is a digital representation of the reservoir, discretized into 3D cells, a grid is a necessary requirement (Fig. 3.14). The gridding process consists of dividing the

reservoir into small cells. The size of the grid cells should be determined as a function of the desired resolution and heterogeneities of the properties to be modelled.

In order to establish the vertical resolution of the 3D grid, the reservoir model is divided into zones and layers (Fig. 3.14). Each zone is defined by two surfaces, at its base and top, reflecting the stratigraphic zones of the model. Layering process defines the cell thickness for each zone of the model, reflecting the depositional patterns of a specific stratigraphic zone of the model. Thus, the layering process enables us to define the final vertical resolution of the grid by setting the cell thickness (Fig. 3.14).

The last step is to assign log values to those cells in the 3D grid that are penetrated by the input data (wells and/or sedimentological logs). Each grid cell should have a single value for each property. As the grid cells are often much larger than the sample density for well logs, data must be upscaled before it can be entered into the grid. This process is known as upscale (Fig. 3.14). Through the upscale process, for each grid cell, all of the log values that fall within the cell will be averaged to produce one log value for that cell. The upscaled value will then correspond to the value that is most representative of the log data for that particular cell. Thus, upscaling of well logs is the process of sampling values from well logs or well log attributes into the grid, ready for use as input for both facies and petrophysical modelling.
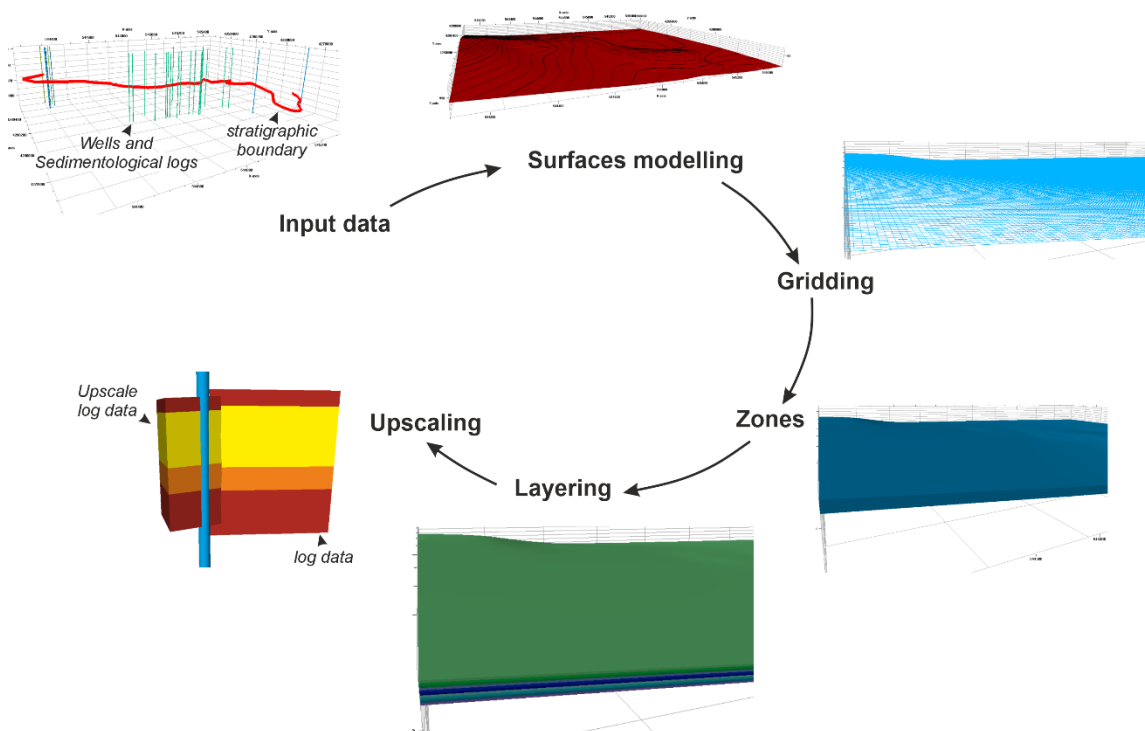
Fig. 3.14. Workflow applied to the construction of a 3D reservoir model framework.

3.2.3. Construction of Geocellular Outcrop Model

A Geocellular Outcrop Model (GOM) is a digital representation of the outcrop interpretation discretized into 3D cells (Fig. 3.15). This digital representation includes the spatial distributions of geobodies, facies associations and/or facies, depending of resolution of outcrop interpretation.

The first step in building a GOM is to digitize the outcrop interpretation in the digital outcrop model (DOM). This digitized outcrop interpretation is converted to a georeferenced point cloud. Each point in this cloud stores interpretation information (geobody, facies association, facies) as an attribute, in addition to its spatial position. This point cloud with attributes is imported into Petrel$_{TM}$ (Fig. 3.15). The last step is to assign the attribute values of the points to the cells in the 3D grid (upscaling process).

The digitizing of outcrop interpretations as well as the creation of a point cloud with attributes was carried out with Virtual Reality Geological Studio (VRGS) software. The GOM is a useful tool with which to contrast the results obtained from geostatistical simulations, as well as to quantify the uncertainty associated with the results.
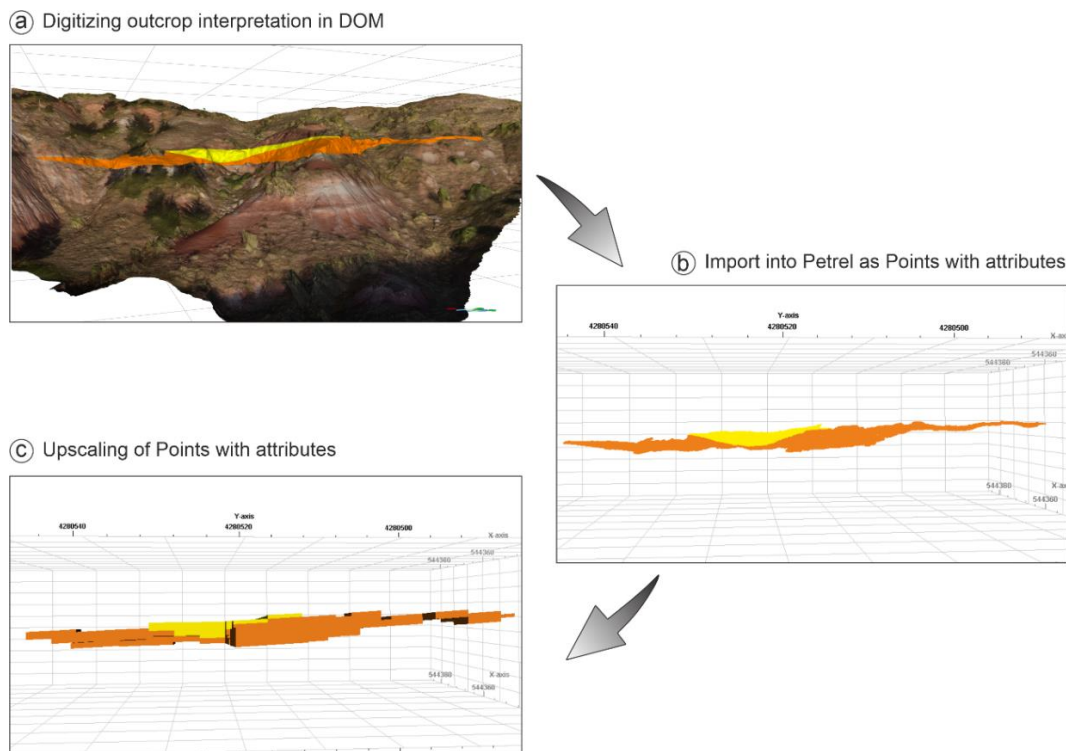
Fig. 3.15. Workflow applied to the construction a Geocellular Outcrop Model. **(a)** the first step is digitizing the outcrop interpretation in the Digital Outcrop Model (DOM); **(b)** import of this interpretation into Petrel$_{TM}$ as points with attributes, and finally; **(c)** assigning point-attributes values to the cells in the 3D grid (upscaling).

3.2.4. Designing a Modelling Workflow

The "Modelling workflow" is a tool of Petrel$_{TM}$ that allows the generation of multiple models to test uncertainty associated with specific parameters. This tool may execute a large number of steps without interruption. Using workflows allows us to document what each process and/or calculation is doing and, if necessary, rerun the steps when data or parameters change. In this study, two modelling workflows were designed, and will be described in Chapter 8, using facies modelling process and logical statement calculations, mainly conditional "If" and "And" statements (Fig. 3.16).

Working with logical statement calculations, new 3D properties can be created and/or operations performed between properties that have already been created. Thus, from a specific property of an object (e.g. object depth, object curvature, distance to the object), using a logical statement we can assign, for example, the insertion point of another object or populate a specific facies in a concrete position within an object.
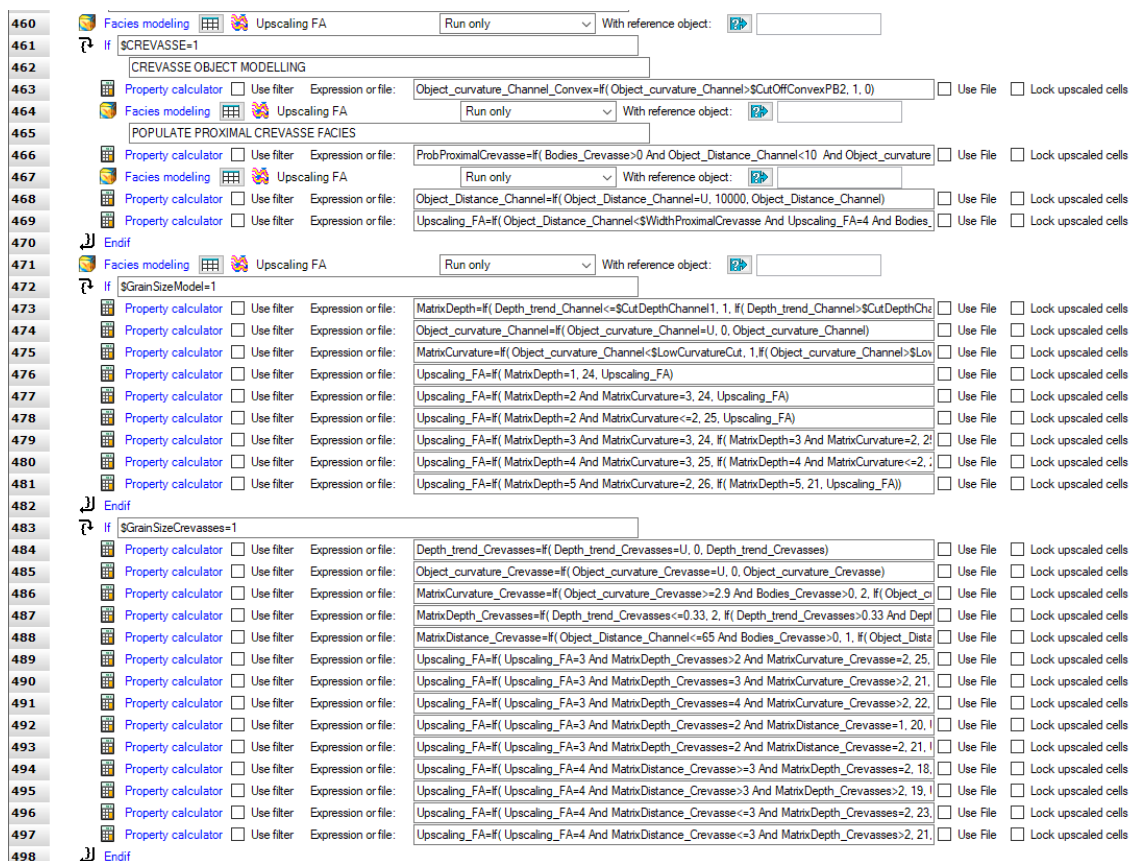
Fig. 3.16. Sample of the modelling workflow designed for this study.

3.2.5. Key geostatistical concepts

The reservoir modelling process is based on the spatial interpolation of values or properties, such as facies, porosity, or permeability; between available data. Two techniques can be used for the modelling process: deterministic or stochastic techniques. Using deterministic techniques, a mathematical model which contains no random components is created; consequently, each component and input is determined exactly by the user. The deterministic methods yield a single estimated result. Using stochastic techniques, a mathematical model which are specified by a random outcome from a probabilistic algorithm is created. These methods produce a possible result and can be used to produce multiple equally probable realizations.

Using stochastic techniques, the original data distribution should be honoured during the interpolation process. In this sense, geostatistical analyses help to identify trends in the spatial distribution of the data, as well as in the results. The typical statistical concepts used to calculate the spatial distribution of variable values are variance, standard deviation, correlation coefficients and variogram.

The ***Variance*** (σ^2) is a measure of the average difference between individual values and the mean of the dataset they come from. It is a measure of the spread of the dataset (Ringrose & Bentley, 2015):

$$\sigma^2 = \sum (x_i - \mu)^2 / N \qquad (1)$$

where x_i represents the individual value for the variable in question, N is the number of values in the data set, and μ is the mean of the data set.

The ***Standard deviation*** (Std) is simply the square root of the variance and indicates how dispersed the data is relative to the mean.

The ***correlation coefficient*** measures the strength of the dependency between two parameters by comparing how far pairs of values (x, y) deviate from a straight-line function. Correlation between datasets is typically entered into reservoir modelling as a value between 0 and 1, in which values of 0.7 or higher generally indicate a strong relationship (Ringrose & Bentley, 2015). The correlation coefficient is given by the function:

$$\rho = \frac{1/N \ \sum_{n=1}^{n=N} (x_i - \mu_x)(y_i - \mu_y)}{\sigma_x \sigma_y} \qquad (2)$$

where N is the number of points in the data set; x_i, y_i are the values of point in the two data sets; μ_x, μ_y are the mean values of the two data sets; and $\sigma_x \sigma_y$ is the standard deviations of the two data sets.

Correlation coefficients reflect the variation of values within a dataset, but they do not offer any information as to how these values vary spatially. In this sense, the spatial variation of the data can be described by a ***variogram*** (Isaaks & Srivastava, 1989). The half of the variogram is known as the semi-variance function. The semi-variogram associated with this function captures the relationship between the difference in value between pairs of data points, and the distance separating those two points (Ringrose & Bentley, 2015). Numerically, this is expressed as the averaged squared differences between the pairs of data in the data set; given by the experimental semi-variogram function:

$$\gamma(h) = \frac{1}{2} E \sum [Z(x+h) - Z(x)]^2 \qquad (3)$$

where $\gamma(h)$ is the semi-variance at a specific distance; E is the calculated average mean difference or the expected mean difference between two samples; Z represents the value of the variable; x is the position of one sample in the pair; h is generally referred to as the lag distance.

Commonly, γ increases as a function of separation distance. Where there is a relationship between the values in a spatial dataset, γ shows smaller values for points which are closer together in space, and therefore more likely to have similar values. As the separation distance increases the difference between the paired samples tends to increase (Ringrose & Bentley, 2015).

The results of semi-variogram calculations are represented graphically to establish the relationship between the separation distance and the average γ value for pairs of points which are that distance apart (Fig. 3.17a; Ringrose & Bentley, 2015). The result of fitting a trend line through the points on the plot is a semi-variogram model (Fig. 3.17a; Ringrose & Bentley, 2015) and this semi-variogram model is used as input to stochastic algorithms during parameter modelling. The most common semi-variogram models are spherical, gaussian, exponential, potential and linear.

A semi-variogram model has three defining features (Fig. 3.17a; Isaaks & Srivastava, 1989; Ringrose & Bentley, 2015; Ma, 2019):

• *Sill*, which is a constant γ value that may be approached for widely-spaced pairs and approximates the variance, where the data become uncorrelated;

• *Range*, which is the distance at which the sill is reached, thus, the distance at which samples became independent of one another; and

• *Nugget*, which represents the variability at distances smaller than the sample spacing.
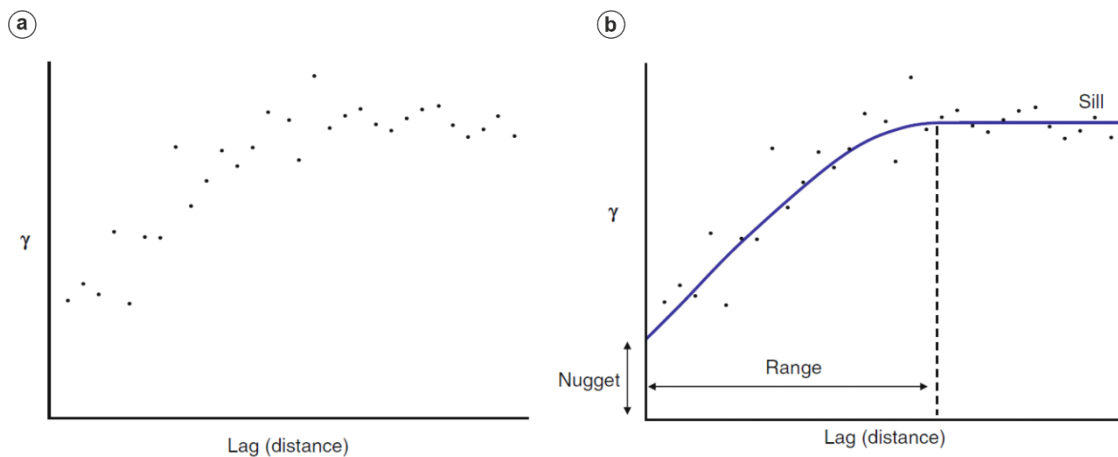
Fig. 3.17. Example of an experimental semi-variogram and its elements (from Ringrose & Bentley, 2015). **(a)** Shows the raw data for a semi-variogram model. Note the systematic change in semivariance between data points with increasing distance between those points. **(b)** Shows the fitting of a trend line through the points and the key elements of a semi-variogram model.

3.2.6. Facies modelling: Stochastic simulation algorithms

Facies modelling can be challenging due to the complexity and peculiarities of different sedimentary environments, notably in terms of the distribution patterns of facies. There are three major conventional stochastic techniques currently used in the reservoir modelling of fluvial deposits: object-based modelling (OBM), sequential-indicator simulation (SIS) and multi-point statistics-based modelling (MPS). Many papers have been published on each of these methods and the comparison between them (e.g. Bastante *et* al., 2008; Barboza *et* al., 2009; dell'Arciprete *et al.,* 2011; Deveugle *et al.*, 2014; Mitten *et al.,* 2020). However, all these methods have strengths and weaknesses, and they may or may not be suitable for a specific modelling project. In this work, OBM and MPS were the selected modelling methods. The characteristics of each method are summarised below.

Object-Based modelling (OBM) is a facies modelling technique aimed principally at the geometry of geological objects. This technique uses a stochastic simulation algorithm, termed marked point process, to generate facies models (Holden *et al.*, 1998). OBM provides the capability for modelling complex, well-defined facies objects as discrete bodies. OBM can readily incorporate geological concepts identified or interpreted from subsurface formations.

Typically, the geometry of facies bodies is analysed using sedimentary principles, field data, depositional analogues, regional geological studies and seismic attribute analysis; and is characterized by probabilistic distributions (e.g., normal, triangular or uniform). Depending on the shapes of facies bodies, such as channels, bars, and various ellipsoidal deposits, OBM uses predefined mathematical functions to approximate the facies body shapes.

In the marked point process for facies modelling, the probability density function for a target facies can be defined as the product of several terms according to the following equation (Holden *et al.,* 1998):

$$P(u) = c\, h_M(u) h_I(u) h_W(u) h_S(s|u) I(u) \qquad (1)$$

where c is a coefficient, $h_M(u)$ describes the facies body geometry, $h_I(u)$ describes the interaction between different facies bodies, $h_W(u)$ describes the well contacts, $h_S(s|u)$ is the secondary conditioning term, and $I(u)$ describes the well and volume constraints.

The object-based simulation algorithm works by randomly selecting a reference point and creating a facies body based on different criteria, such as facies fractions and rules of erosion. Whereas individual facies objects are predefined geometrically with statistical parameters, the distribution of different facies objects may be random, clustered, uniform, or repulsive in character. These distributions of facies objects describe the spatial relationships of different facies objects. One of the most commonly used OBM methods is fluvial object-based modelling, which generates channels with defined ranges in width, thickness, and sinuosity (Clement *et al*. 1990; Holden *et al*. 1998; Colombera *et al*., 2019).

Multi-Point Statistics (MPS)-based modelling is a facies modelling technique that uses conceptual geological models as 3D training images (TI) to generate geologically realistic reservoir models conditioned to well data. It combines the ability to reproduce geological 'shapes', similar to object-based methods, with the speed and exact data-conditioning provided by variogram-based techniques. MPS extracts facies patterns from a conceptual TI that displays the type of facies elements believed to be present in the reservoir, and then reproduces in the model the patterns that fit the reservoir well data.

Traditionally, the variogram (see Section 3.2.5) has been used as the key geostatistical tool used to describe the spatial continuity of a reservoir property. However, the variogram describes only two-point spatial relationships and may not be effective in characterizing complex spatial relationships, such as curvilinear features (Guardiano & Srivastava 1993; Mustapha & Dimitrakopoulos, 2010). One way to achieve such a goal is to borrow complex spatial geometries

through a TI which conveys the relevant spatial relationships between many points (Strebelle, 2002; Daly & Caers, 2010; Mariethoz & Caers, 2015).

Thus, MPS is a stochastic modelling method that generates a reservoir model on the basis of a given TI. Multiple points also imply exploring the relationships between one-to-many points at the same time. The local conditional probability at the cell is calculated by scanning the TI. The probability of a facies code is calculated from the matched patterns based on its relative occurrences.

The TI is the main geological concept introduced in this approach. This conveys some complex spatial features in facies that are not carried by others statistical tools, such as the variogram, but are, nonetheless, key geometrical complexities. The relationships between the different facies are assumed to be conveyed by the TI. Therefore, a TI can be considered as an idealized representation of the geology. The main goal of the TI is to describe geometries (shapes and dimensions) and the neighborhood relationships of facies bodies, i.e., the relative position of the facies bodies to each other.

The TI can be a conceptual geological model, a pre-existing facies model generated by another modeling method (such as a model by OBM or process-based modelling), hand drawn images, aerial images or analogues. For constructing a 3D facies model, a 3D TI is commonly recommended because it conveys both lateral geometries and vertical sequence patterns of the facies. A 2D TI will guide the MPS in the lateral distribution of facies shapes, but the vertical distribution cannot be borrowed from the training image. The TI should be large enough to cover multiple examples of facies shapes and interactions between facies bodies. The facies proportions of the TI should be close to the estimate of relative facies proportions (target fractions), not attempt to model an excessive number of lithofacies codes (fewer than eight is preferable), and have repeatability; that is it should be large enough to cover several replications of facies shapes and interactions between facies bodies (Ma, 2019).

MPS facies simulation enables the generation of models with considerably more geological complexity than other techniques (e.g. sequential indicator simulation). As its algorithm is cell-based, it has the advantage over the object modeling method in that it can condition to data more easily than an object-based model.

The two facies modelling methods presented here have both pros and cons (Ma, 2019). OBM, for example, can be used with defined objects, when the shapes of facies bodies are clearly definable, as it provides the flexibility of modelling a combination of facies with different geometries. As such OBM is suitable for modelling river deposits with both simple and complex

geometries. It is also relatively straightforward to model curvilinear features, including meandering channels. Furthermore, OBM can generally model reservoir connectivity better than the other methods, which can be important in characterizing flow (Pranter & Sommer, 2011). However, it has difficulties in honouring abundant hard data. Honouring soft data may also present difficulties, depending on the consistency between the soft data and facies objects (Ma, 2019). In contrast, MPS trades off the honouring of conditioning data and geometrical complexity. It can model moderately curvilinear spatial features, and it can also model connectivity quite well. Preparation of a reliable 3D training image is also a major element in building a reasonable MPS facies model, but this is often difficult due to the limited data available for a reservoir (Ma, 2019).

In this study, a combination of these two methods was used to model a high-sinuosity fluvial system (M-S Unit). As outlined above, OBM is the most suitable method for modelling river deposits with complex geometries, such as high-sinuosity fluvial systems. In addition, this method is best for estimating reservoir connectivity. Thus, the OBM methodology was used to generate both a 3D TI and, the complete reservoir model in order to estimate the reservoir connectivity. MPS was subsequently used to predict the distribution of the geobodies from the OBM-generated TI, as well as to estimate the influence of the input data on the prediction of geobody distribution. This approach was chosen as the MPS method better trades off the honouring of conditioning data and geometrical complexity in comparison with the OBM method.

3.3. Data

A total of 2.5 km^2 of outcrop area were studied, of which 1.5 km^2 were incorporated into a Digital Outcrop Model. In the studied outcrop area, a total of 20 high-resolution sedimentological logs were constructed for the characterization of lateral facies variability in the M-S Unit. In addition, and also in the M-S Unit, one high-resolution sedimentological log (PNV 1), through a section of 72 m, were constructed in order to fully characterize the vertical facies variability in the M-S Unit. Another high-resolution sedimentological log (HU1), through a section of 40 m, was constructed in order to fully characterize the vertical facies variability in the H Unit (Fig. 3.17).

In the studied area, a total of 15 wells were drilled with a total drilled section of 274.4 m (Fig. 3.17). In all wells, core recovery and well log data were acquired. In the M-S Unit, Wells

MB1 to MB4, with, respectively, 3.6, 2.9, 4.8 and 8 m of drilled section; and Well S2P4, with a section of 70 m, were drilled. In addition, Well K2P1 was drilled to a depth of 42 m; of which the uppermost 22 m correspond to the S Unit and the remaining 20 m to the M-S Unit. Also, Wells K2L1 to K2L4 and Well K2P2 penetrated the S Unit with, respectively, 16, 17, 15, 7 and 20 m of drilled section. Wells HU 1 to HU 4, which reached total depths of 14.7, 15, 34.5 and 3.9 m, respectively; drilled the H Unit.

Fig. 3.17. Satellite image of the study area showing the location of the wells, sedimentological logs and GPR profiles. In addition, the area incorporated into the digital outcrop model is also shown. Acronyms correspond to the names attributed to the sedimentological logs, well data and/or GPR profiles.

A total of Three GPR profiles, covering a total of 443 m of outcrop length, were acquired. GPR-N and GPR-S2 profiles, 70 and 248 m long, respectively, were acquired with a shielded 200 MHz antenna which limited the penetration to a depth of 10 m. GPR-S1, with a 125 m long profile, was acquired with a shielded 40 MHz antenna which increased the penetration depth to 30 m below the surface.

PART I:

OUTCROP/BEHIND OUTCROP CHARACTERIZATION
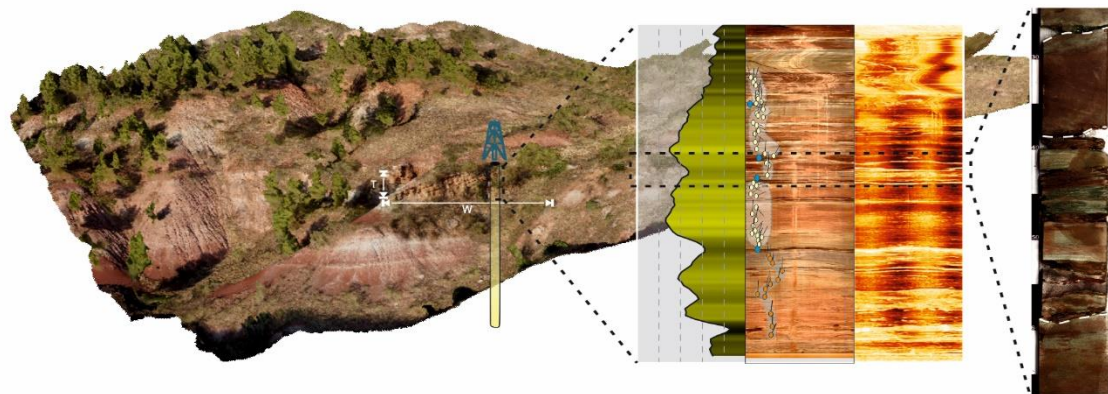
CHAPTER 4:

Mudstone-Sandstone Unit: High-sinuosity fluvial system

Abstract   Exploration and production from formations deposited in low-gradient fluvial systems is typically associated with a high degree of uncertainty; a reflection of the inherent characteristics of these environments, notably the dominance of non-reservoir floodplain fines, rapid lateral facies variations and associated heterogeneities at different scales. However, for a field development to be successful it becomes crucial to know the location, geometry, dimensions and connectivity of the most permeable facies, related to the main channel and the associated proximal overbank deposits (crevasse-splay complexes). With the aim of addressing this problem, a multi-disciplinary study is presented, combining outcrop data, high-resolution sedimentological descriptions and advanced visualization techniques based on Digital Outcrop Models. This is compared with subsurface data from behind the outcrop (core, gamma ray and borehole image logs). The Mudstone–Sandstone Unit of the Triassic Red Beds of Iberian Meseta formation in southcentral Spain was selected for the present study. The unit is characterized by the lateral and vertical stacking of four geobodies: (i) channelized sandstone bodies; (ii) asymmetrical sigmoidal-shaped sandstone bodies; (iii) lobe-shaped to sheet-like sandstone bodies; and (iv) sheet-like mudstones. These elements represent meandering channel, crevasse-channel- splay and floodplain sub-environments, comprising a distal, low-gradient meandering fluvial system. Together with well-documented outcrop and core facies, calibrated log responses are also presented for the channel bodies (bell-shape Gamma Ray profile, random azimuths and low to high dip angles), the crevasse-splay bodies (funnel-shape Gamma Ray profile, unidirectional azimuths and low dip angles) and the floodplain deposits (serrated Gamma Ray profile, unidirectional azimuths and very low dip angles). The full integration of outcrop and subsurface datasets has enabled generation of a robust conceptual model with predictive potential when establishing the three-dimensional stacking of facies, distribution of heterogeneities, and the connectivity between reservoir rock geobodies of primary (channel) and secondary (crevasse complex) interest in this type of fluvial reservoir.

4.1. Introduction

The characterization of fluvial reservoirs, and more specifically of meandering channel systems is often highly complex, due to the three-dimensional (3D) characteristics of sandstone geobodies, the rapid lateral facies variations and the associated heterogeneities at different scales (Jordan & Pryor, 1992; Legarreta *et al.*, 1993; Bridge, 2001; Pranter *et al.*, 2008). Accordingly, the accurate planning and optimization of recovery options in this type of hydrocarbon reservoir demands a detailed 3D knowledge of both geobodies and the distribution of heterogeneities (Weber, 1986; Browne & Slatt, 2002; Pranter *et al.*, 2008, 2009, 2014; Slatt *et al.*, 2011). To date, fluvial sedimentological research has tended to focus on the characterization and distribution of heterogeneities within the component sand bodies comprising the main channels (Allen, 1983; Blakey & Gubitosa, 1984; Bridge & Tye, 2000; Gouw & Berendsen, 2007; Pranter *et al*., 2009; Jenson & Pedersen, 2010; and others). However, sedimentological research focussed on the detailed study of the overbank deposits, typical of this type of depositional environment, has been limited. In fluvial systems dominated by aggradation, fine-grained floodplain deposits and sandstone geobodies related to crevasse-splay processes are a key constituent in the stratigraphic succession, and in fact provide significant insights into channel stacking, avulsion mechanisms and even distances to the main channel (Mjøs *et al.*, 1993; Kraus & Aslan, 1999; Moscariello, 2009; Varela *et al*., 2012; Burns *et al*., 2017; Gulliford *et al.,* 2017).

To achieve an appropriately realistic 3D characterization of all the variables that generate heterogeneities in fluvial reservoirs has been a long-term challenge for many workers from both an academic and industry perspective. In order to address this challenge a substantial volume of high-quality data is required for the estimation of the dimensions and distribution of the heterogeneities in this type of fluvial reservoir.

In this sense, the study of outcrop analogues is a useful tool, which complements the sparse subsurface data and aids in constructing more realistic conceptual models (Miall, 1990; Kokureck *et al*., 1991; Tyler & Finley, 1991; Wizevich, 1991; Yoshida *et al.*, 2001; Ajdukiewicz & Lander, 2010; Scott *et al.*, 2013; Pranter *et al*., 2014; Franke *et al*., 2015). If in addition to the outcrop data, subsurface data of the same examples are available, an appropriate database can be constructed in order to properly constrain the geometries and dimensions of the sandstone geobodies. From this, realistic models can be generated, that capture both facies at high resolution and the distribution of the heterogeneities within reservoirs. The integrated study of outcrop and subsurface data, known as Outcrop/Behind Outcrop characterization (hereinafter

'OBO') (Browne & Slatt, 2002; Slatt *et al.*, 2011; Viseras *et al.*, 2018; Yeste *et al.*, 2019) is the methodology chosen in this paper.

The aims of this paper are: (i) to present a detailed analysis of sedimentary facies, geometries and stacking patterns within fine-grained floodplain deposits and sandstone geobodies associated with crevasse-splay deposits in the mudstone–sandstone (M-S) Unit of TIBEM; (ii) to determine the key features necessary for the recognition and characterization in subsurface well data of these deposits; and (iii) to develop a predictive conceptual model that represents the heterogeneities in these fluvial reservoirs.

The studied example is a Triassic succession often considered as an outcrop analogue for other hydrocarbon-productive reservoirs such as the Algerian TAGI (Trias Argilo-Greseux Inferieur; Rossi *et al.*, 2002; Dabrio *et al.*, 2005; Viseras *et al.*, 2011; Henares *et al.*, 2014, 2016a, b; Viseras *et al.*, 2018; Yeste *et al.*, 2019). For this reason, the Outcrop/Behind Outcrop workflow has been employed, integrating standard 2D high resolution outcrop data and 3D outcrop data, developed from photogrammetry, with subsurface data from behind the outcrop including cores and core descriptions, Gamma Ray logs and borehole image logs (Yeste *et al.*, 2019). The integration of different but complementary data types (i.e. surface and subsurface data) leads to better constrained reservoir models which serve to improve the quantification and correlation of heterogeneities within this type of fluvial reservoir.

The results of this chapter have been published in journal *Sedimentology*:

Yeste, L.M., Varela, A.N., Viseras, C., McDougall, N.D. and García-García, F. (2020). Reservoir architecture and heterogeneity distribution in floodplain sandstones: Key features in outcrop, core and wireline logs. Sedimentology. DOI: 10.1111/sed.12747.

4.2. Data distribution

In order to study the geometry, internal structure, sequence trends and spatial relationship between the main geobodies, a total of 0.813 km^2 of outcrop has been studied. For the characterization of lateral facies variability, a total of 20 sedimentological logs have been constructed (Fig. 4.1). From the principal architectural element, or the Main Channel, in the outcrop, (CP-0, Fig. 4.1), eight sedimentological logs were completed towards the eastern margin (CPMR1 to CPMR8, Fig. 4.1) and nine towards the western margin (CPML1 to CPML9; Fig. 4.1). The lateral variability of facies was also observed in another channel complex to the north, characterized by an additional two sedimentological logs (CBML1 and CBML2) although these

have not been fully included in all aspects of the study. In addition to the 19 partial sections listed above, and to fully characterize the vertical variability of facies, a complete sedimentological log was constructed through a section of 72 m (PVN1, Fig. 4.1) in the M-S Unit.
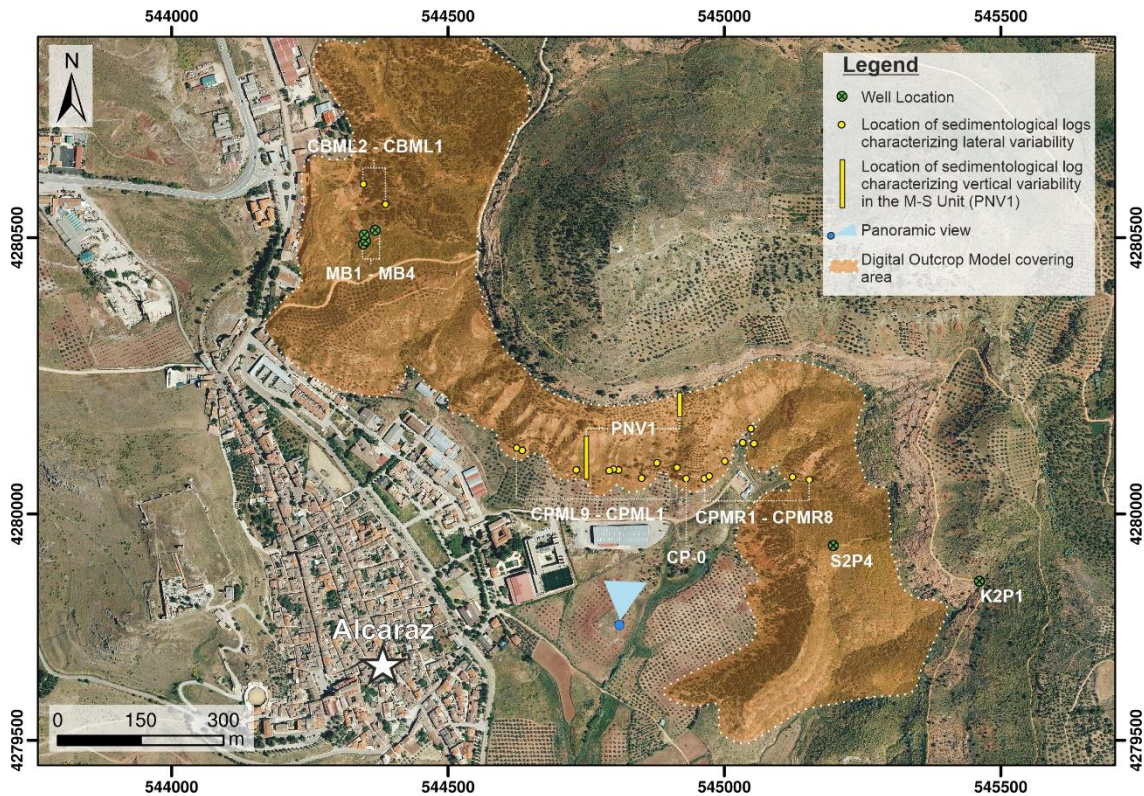
Fig. 4.1. Location of the study area (Alcaraz village, Albacete province, Spain) showing the location of the studied outcrops. The orange shading represents the outcropping study area and the area covered by Digital Outcrop Models (DOM). Yellow points and yellow rectangles represent the location of sedimentological logs constructed to enable the characterization of lateral and vertical variability, respectively. Green points are well locations. Acronyms correspond to the names of profiles and wells, as explained in the text.

Digital Outcrop Models (DOM) have also been created from photogrammetry with an RPAS (Remotely Piloted Aircraft System) to complete the outcrop-derived measurement dataset. The total covered area spans 0.813 km^2.

In the studied example, two slim-hole [85 mm diameter], behind-outcrop wells allowed subsurface characterization of the key facies. (Fig. 4.1): (i) Well S2P4, located at the top of the studied succession (M-S Unit), has a section of 70 m and; (ii) Well K2P1 located at the top of the S Unit drilled to a depth of 42 m; of which the uppermost 22 m correspond to the S Unit and the remaining 20 m to the studied unit (M-S Unit). The distance between Wells S2P4 and K2P1 is 275 m. Both wells were drilled with continuous core recovery and wireline log data was obtained. Core slabbing was subsequently carried out in order to enhance the visibility of

sedimentary features on the core surface and allow the identification of the main simple lithofacies classes (Table 4.1). Well log data include the Gamma Ray log (GR) in addition to borehole imaging from Optical and Acoustic Televiewers (OBI and ABI, respectively). Supplementary dip information is also included from four additional wells (MB1 to MB4) described in detail in Viseras *et al.* (2018).

4.3. Outcrop, core and wireline log characteristics of facies associations

Ten facies associations (MSFA) were identified from the TIBEM in the study area, each comprising an assemblage of one or more lithofacies (Fig. 4.2; Table 4.1). The following section contains a detailed description of each facies association including lateral and vertical lithofacies variation, geometric data, bounding surfaces and the dimensions of the sedimentary bodies, as described both in outcrop and subsurface (core, GR log response and image logs), in order to characterize the spatial distribution of heterogeneities. Gamma-ray log patterns (electrofacies patterns) were interpreted according to the models of Emery & Myers (1996) and Slatt (2013).

4.3.1. Facies Association 1: Main Channel

Description

Facies Association 1 (MSFA 1) comprises a fining-upward sequence ranging from conglomerates, characterized by the presence of mudstone rip-up clasts, to very fine-grained sandstones (Fig. 4.2a). MSFA 1 occurs as lenticular-shaped bodies up to 3 m thick with a lateral extension of up to 30 m perpendicular to the main flow direction. These lenticular bodies show concave-up erosive bases, whilst the tops are horizontal and sharp (Tables 4.1 and 4.2; and Fig. 4.2a). Internally they comprise conglomerates, with pebbly mudstone (Lithofacies Gm) as basal lags. Overlying the basal lags are medium to fine-grained sandstones with planar to trough cross-bedding (Lithofacies St) and very fine-grained sandstone with current ripples (Lithofacies Sr) towards the top (Table 4.1). Sometimes packages of MSFA 1 also show a final interval of laminated fine-grained deposits (Lithofacies Fl). Typically, the tops of MSFA 1 bodies are characterized by *Arenicolites* isp. and less frequently *Taenidium* isp. trace fossils (Table 4.2; Fig. 4.2a).

The GR log through MSFA 1 typically comprises several packages with an initial decrease in API values followed by repeated increases and decreases in API values on a decimetre to metre scale (Fig. 4.2a). The OBI and ABI logs show a high intensity and high amplitude contrast at the base of this facies association. Internally these image logs are characterized by common

sine wave surfaces (interpreted as cross-bed foresets) and towards the top display a speckled to massive appearance with few non-sine wave surfaces (Fig. 4.2a).

Interpretation

This fining-upward succession, together with the lenticular geometries and erosive lower surfaces suggest that MSFA 1 should be interpreted as the deposits of a main channel. Within this framework; the vertical lithofacies variation (Lithofacies Gm–St–Sr), described above, indicates decreasing flow energy (Table 4.1). The occasional presence of laminated fine-grained deposits (Lithofacies Fl) is interpreted as a mud plug due to neck cut-off of a meandering channel (Viseras *et al.*, 2018). In contrast, the common occurrence of *Arenicolites* tubes unconnected with any fine-grained deposits suggests an abrupt avulsion of the fluvial system (Hubbard *et al.*, 2011; Durkin *et al.*, 2017). The non-typical GR profile of MSFA 1, a coarsening-upward trend (funnel shape) at the base and fining-upward (bell shape) towards the top, most likely reflects the occurrence of mudstone rip-up clast conglomerates as basal lags (Selley, 2004; Henares *et al.*, 2016a, b; Viseras *et al.*, 2018). The high intensity and amplitude contrast at the base of the facies package, in both OBI and ABI logs, is interpreted to record the main channel erosive surface. Above this surface, the presence of sine wave surfaces in OBI and ABI logs corresponds to cross-stratified sandstone (correlated to the cross-stratified sandstones observed in outcrop), whereas the speckled to massive final interval without sine wave surfaces is interpreted as current rippled sandstones (Keeton *et al.*, 2015).

4.3.2. Facies Association 2: Point bar

Description

Facies Association 2 (MSFA 2) is characterized by a fining-upward facies sequence passing from mudstone rip-up clast conglomerate to very fine-grained sandstones (Fig. 4.2b). Outcrop data indicates that MSFA 2 occurs as asymmetrical, sigmoidal-shaped bodies, up to 3.6 m thick and with lateral extensions of up to 100 m. These bodies are typically bounded by horizontal and erosive bases, whilst the tops are horizontal and sharp (Tables 4.1 and 4.2; Fig. 4.2b). MSFA 2 is easily recognized, in outcrop by the occurrence of several inclined master bedding surfaces perpendicular to the palaeocurrent direction, typically showing an upward increase in dip angle. Internally, MSFA 2 comprises sets of trough cross-bedding (Lithofacies St) and current ripples (Lithofacies Sr) towards the top of the facies sequence (Table 4.1). Locally, mud drapes occur between the inclined master surfaces, both as layers within the packages and as drapes over the inclined master surfaces. In addition, the top of the MSFA 2 package shows

Table 4.1. Lithofacies identified in the Mudstone–Sandstone (M-S) Unit. See Fig. 4.2 for photographic examples of each lithofacies.

Code	Texture and Fabric	Sedimentary structures and Characteristics	Main process
Gm	Pebble-cobble. Clast or matrix supported.	Massive, weak horizontal bedding or planar cross bedding. Erosive base and mud rip-up clasts.	High energy traction current.
Sm	Fine to medium sand.	Massive. Rare presence of mud clasts.	Channel fill due to waning flow.
Sh	Fine to medium sand.	Horizontal lamination.	Sheet flow. Upper flow regime.
St	Fine to medium sand.	Trough cross bedding. Sometimes, mud chips lining the cross beds.	Migration of megaripples and dunes. Channel fill.
Sp	Very fine to medium sand.	Planar cross bedding	Megaripple migration.
Sr	Very fine to fine sand.	Current ripple lamination.	Migration of current ripples.
Sc	Very fine to fine sand.	Asymmetric climbing ripple lamination.	Combination of traction and settling from suspension.
Sw	Very fine sand.	Wave ripple lamination.	Oscillatory flow in a standing body of water.
Sd	Very fine sand.	Convolute lamination. Dish plate structure. Soft-sediment deformation structures.	Deposition from flow an unstable water-saturated substrate.
Sl	Very fine sand.	Diffuse horizontal lamination or diffuse current ripple.	Settling from suspension or migration of current ripples. Diffuse structures due to soil development.
Sb	Very fine to medium sand.	Massive. Presence of rhizoliths, *Arenicolites* isp. and *Taenidium* isp.	Structureless due to bioturbation.
Lm	Silt.	Massive. Abundant rhizoliths.	Soil develop on former overbank fines.
Lr	Silt.	Current ripple lamination. Sometimes, wave ripple lamination.	Migration of current ripples.
Ll	Silt.	Horizontal lamination. Uneven lamination.	Settling from suspension. Lower flow regime.
Fm	Clay.	Slickensides, wedge shape peds, angular and subangular blocky peds, cutans, motts and rhizoliths.	Soil develop on former overbank fines.
Fl	Clay.	Horizontal lamination (lower flow regime). Uneven lamination. Sometime, presence of plant remains and coal.	Settling from suspension.
Fb	Very fine to silt and clay.	Heterolithic bedding. Flaser, wavy and/or linsen lamination.	Settling from suspension alternating with tractive episodes.
Cm	Limestone.	Massive micritic mudstones.	Settling from suspension.

evidence of wave reworking (Lithofacies Sw) and contains both *Arenicolites* isp. and *Taenidium* isp. trace fossils (Table 4.2; Fig. 4.2b). The inclined master surfaces, first recognized in outcrop, are recognized in core as inclined erosive surfaces commonly draped by thin claystone layers (Fig. 4.2b).

The MSFA 2 GR log typically shows a decrease in API values above the base and continues with an increase in API values towards the top (Fig. 4.2b). The OBI and ABI logs also show several inclined master surfaces distinguished by high intensities and contrasts in amplitude. Between these surfaces, sine waves are typically overlain by massive to speckled intervals.

Interpretation

These asymmetrical sigmoidal geometries, observed in outcrop, together with the characteristic occurrence of several inclined surfaces perpendicular to the paleocurrent and the fining-upward succession suggest point bar deposits. The inclined surfaces with increasing dip angle are thus interpreted as lateral accretion surfaces. The presence of current ripples flowing up-slope along these accretion surfaces (i.e. perpendicular to the paleoflow), are interpreted as the result of the helicoidal flow developed in the meander band (Viseras *et al.*, 2018). The occurrence of mud drapes between the lateral accretion surfaces represents deposition during a waning flood stage (Thomas *et al.*, 1987; Viseras *et al.*, 2018). The presence of Lithofacies Sw and *Arenicolites* tubes could indicate periods of ponding and wave reworking. The basal coarsening-upward (funnel shape) interval in the GR log would correspond to the presence of mudstone rip-up clasts (Selley, 2004; Viseras *et al.*, 2018). The high contrast surfaces, seen in the image logs, represent each lateral accretion surface, whereas internal deposits of each lateral accretion package are represented by Lithofacies St (sine wave surfaces) and Lithofacies Sr (speckled to massive intervals).

4.3.3. Facies Association 3: Scroll bar

Description

Facies Association 3 (MSFA 3) is similar in some respects to MSFA 2 although the dimensions and thickness of the packages are somewhat reduced. It is characterized by a fining-upward sequence passing from mudstone rip-up clast conglomerate (Lithofacies Gm) into very fine-grained sandstones. (Fig. 4.2c). MSFA 3 typically occurs as asymmetrical sigmoidal-shaped bodies which are up to 1.5 m thick and up to 30 m in lateral extent. These bodies show horizontal and erosive bases, whilst the top surfaces are horizontal and undulated (Tables 4.1 and 4.2; Fig. 4.2c). This facies association mainly comprises sets of trough cross-bedding (Lithofacies St),

locally with mudstone rip-up clasts lining the set base and typically associated, in wells behind the outcrop, with notably higher Gamma Ray API values. Towards the top of the facies package, current ripples (Lithofacies Sr) are dominant. In core, this facies sequence of trough cross-bedding with local rip-up clast lags overlain by current ripples, is easily distinguished.

The GR log through MSFA 3 typically shows an increase in API values towards the top (Fig. 4.2c). The OBI and ABI image logs show a generally speckled appearance with sine curves at the base. Towards the top, sets of continuous sine curves, bounded by scour surfaces, can also be recognized. In the ABI log, the speckling is bright and sets of continuous sine curves are dark coloured.

Interpretation

Facies Association 3 is characterized by thin, convex-up (undulatory tops) asymmetrical–sigmoidal packages with a fining-upward facies succession, all of which can be interpreted in terms of scroll bar deposits (Nanson & Page, 1983). The undulated tops, as observed, in outcrop together with the reduced dimensions, the absence of mud drapes, the presence of rip-up clasts at the base, and the prevalence of current ripples in core characterize this facies association in contrast to MSFA 2. The presence of sets of trough cross-bedding, with rip-up clasts lining set bases overlain by current ripples, suggests lateral migration of the scroll bars. In the image logs, the speckled appearance with sine curves reflects trough cross-bedding with mudstone rip-up clasts (Lai *et al.*, 2018). Sets of continuous sine curves, bounded by scour surfaces, correspond to different lateral accretion units within the scroll bar. The continuous sine curves represent trough cross-bedding and current ripples (Lai *et al.*, 2018).

4.3.4. Facies Association 4: Chute channel

Description

Facies Association 4 (MSFA 4) is defined by a fining- upward sequence, from fine-grained sandstones into siltstones (Fig. 4.2d). In outcrop, MSFA 4 forms lenticular bodies up to 0.8 m thick with a lateral extension of up to 3 m. Internally, this facies association is characterized by an alternation between trough cross-bedding (Lithofacies St) and/or current ripples (Lithofacies Sr) and horizontal lamination (Lithofacies Sh). Towards the top of the facies sequence, heterolithic flaser bedding (Lithofacies Fb) also typically occurs. Geobodies defined as MSFA 4 in outcrop are characterized by concave-up and erosive bases cutting down into MSFA3, whilst the top surfaces are both horizontal and sharp (Tables 4.1 and 4.2; Fig. 4.2d). The base is distinguished in the cores as an inclined erosive surface overlain by horizontal lamination

(Lithofacies Sh) and current rippled (Lithofacies Sr) or, less commonly, small-scale trough cross-bedded (Lithofacies St) sandstones (Fig. 4.2d).

Facies Association 4 is characterized by an increase in API values towards the top of the GR profile (Fig. 4.2d). The OBI and ABI logs are characterized by poorly developed sine waves and a high contrast scour surface at the base. The uppermost part of the package is, in contrast, characterized by a homogeneous or structureless appearance.

Interpretation

This facies association is interpreted as a chute channel, on the basis of a fining-upward trend, geobody dimensions, a lenticular geometry and its relationship with MSFA 3. The horizontal laminated (Lithofacies Sh) and current rippled (Lithofacies Sr) sandstones represent deposition during higher flood stages (Nemec & Postma, 1993; Miall, 1996; Ghinassi, 2011). During this phase, the water overtops the point bar, scouring the chute channels (Briant, 1983; Ghinassi, 2011). The heterolithic flaser-bedded siltstones (Lithofacies Fb), in contrast, represent deposition during the receding flood stages (McGowen & Garner, 1970; Brierley, 1991; Ghinassi, 2011; Table 4.1). Within this framework, the gradual increase in GR values (bell shape) almost certainly records the fining-upward sequence seen in core and outcrop, from horizontal and current rippled sandstones to heterolithic flaser-bedded siltstones (Lithofacies Fb). It is also probable that those image log intervals characterized by poor sine waves represent horizontal laminated and current rippled sandstones, whereas the homogeneous, massive intervals correspond to the heterolithic flaser-bedded siltstones (Lai *et al*., 2018). The scour surface seen in the image logs (see Fig. 4.2d) is also clearly the erosive base of the chute channel observed in outcrop.

4.3.5. Facies Association 5: Crevasse channel

Description

Facies association 5 (MSFA 5) is characterized by a fining-upward sequence passing from mudstone rip-up clast conglomerates to very fine-grained sandstones (Fig. 4.2e). In outcrop, MSFA 5 is observed to form lenticular bodies up to 1.1 m thick with a lateral extension of up to 6 m perpendicular to the main flow direction. These lenticular bodies are characterized by concave-up, erosive bases, whilst the tops are horizontal and sharp (Tables 4.1 and 4.2; Fig. 4.2e). MSFA 5 truncates the underlying strata typically assigned to MSFA 6 and/or MSFA 7. Rarely, this facies association also truncates the mud prone MSFA 9. Internally, MSFA 5 packages show thin mudstone rip-up clast conglomerates as basal lags overlain by fine to very fine-grained sandstone with trough cross-bedding (Lithofacies St) and very fine-grained sandstone with

current ripples (Lithofacies Sr). Locally, towards the top, very fine-grained sandstone with oscillation ripples (Lithofacies Sw) also occur. In core, this association, is also characterized by the alternation of trough cross-bedded and current rippled sandstones (Fig. 4.2e).

The GR log is characterized by an increase in API values towards the top and a sharp base (Fig. 4.2e). The OBI and ABI logs show bright colours and sine waves at the base. Towards the top of the package the image logs are also characterized by thin (<10 cm), alternating bright and dark bands (bright yellow and dark brown bands in ABI log) with well-developed sine waves (Fig. 4.2e).

Interpretation

The fining-upward succession, together with the distinctive lenticular geometries and erosive lower surfaces strongly suggest deposition as a crevasse channel. The vertical lithofacies variation (Lithofacies St–Sr–Sw) and fining-upward trend (bell shape) of the GR log indicate gradual flow deceleration and overfilling of crevasse channels (Bristow *et al.*, 1999; Burns *et al.*, 2017; Table 4.1). Sine waves observed in OBI and ABI logs are interpreted as trough cross-bedded (Lithofacies St) and current rippled sandstones (Lithofacies St) (Lai *et al.*, 2018). The alternation of bright and dark bands (bright orange and dark brown bands in ABI log) with sine waves are likewise interpreted as very fine-grained sandstone with current ripples or oscillation ripples (bright yellow) whilst the dark brown colours likely represent mudstone layers (Donselaar & Schmidt, 2005; Xu *et al.*, 2009; Lai *et al.*, 2018).

4.3.6. Facies Association 6: Proximal crevasse-splay complex

Description

Facies Association 6 (MSFA 6) is composed of relatively thin, fine-grained sandstones (Fig. 4.2f). MSFA 6 occurs in outcrop as lobe-shape bodies, up to 2 m thick and up to 130 m in lateral extent, perpendicular to the main flow direction. These lobate bodies are characterized by a horizontal, sharp base, whilst the tops are convex-up and sharp (Tables 4.1 and 4.2; Fig. 4.2f). The vertical stacking of facies, whether in outcrop or core, shows a transition from horizontal laminated sandstones (Lithofacies Sh) to trough cross-bedded sandstones (Lithofacies St) and/or current rippled sandstone (Lithofacies Sr). Towards the top of MSFA 6 packages, climbing ripple cross-laminated sandstones (Lithofacies Sc) are also recognized.
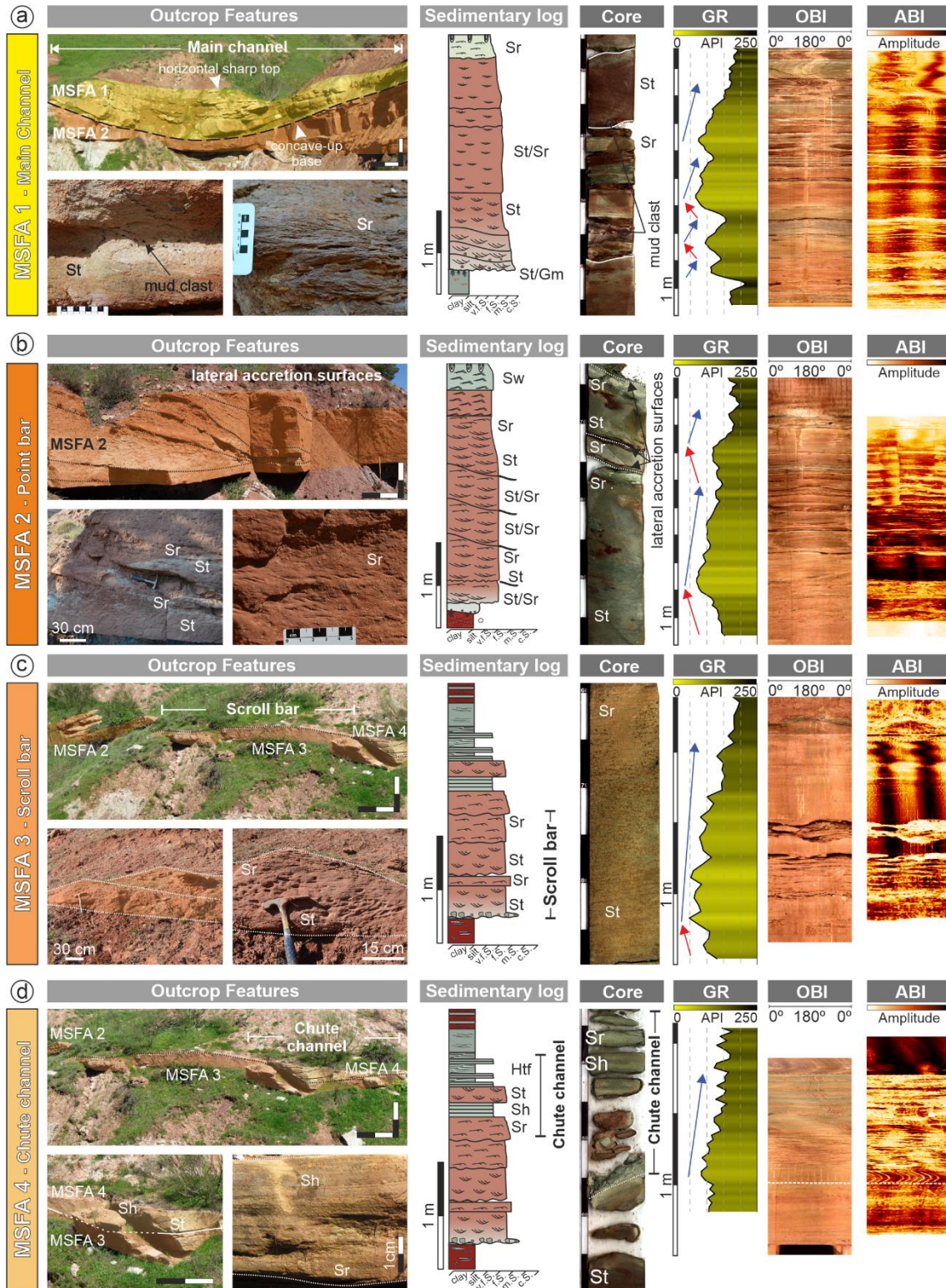
Fig. 4.2. For caption, see page 111.

Fig. 4.2. Continued.
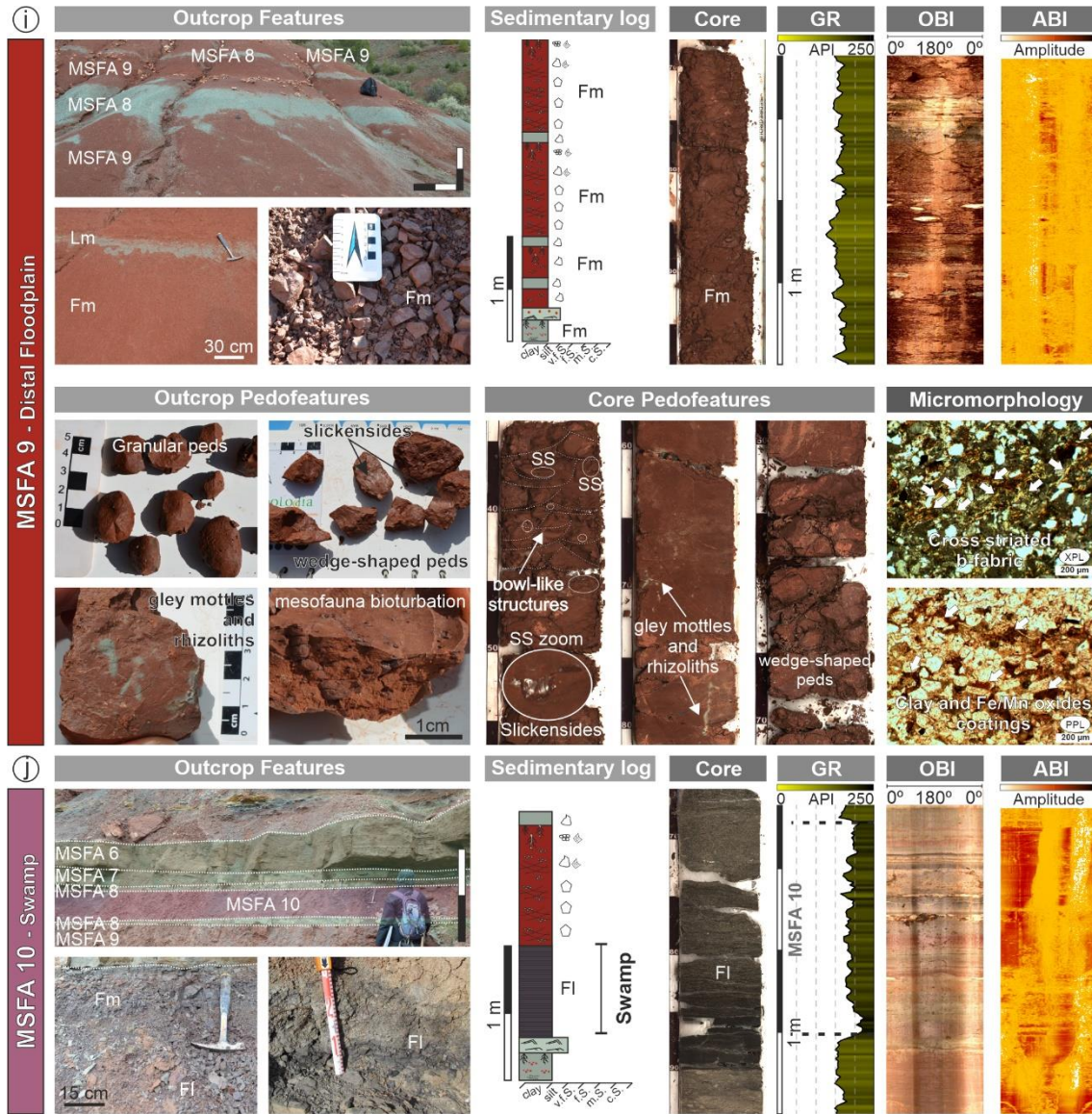
Fig. 4.2. Characteristics in outcrop, sedimentary log, core, Gamma Ray log and borehole images (GR – Gamma Ray; OBI – Optical Televiewer; ABI – Acoustic Televiewer) features for each facies association identified. **(a)** to **(j)** show outcrop and behind outcrop characteristics for Facies Associations 1 to 10, main channel, point bar, scroll bar, crevasse channel, proximal crevasse-splay, medial crevasse-splay, distal crevasse-splay, distal floodplain and swamp deposits, respectively. Hammer for scale is 28 cm long.

The GR log, in contrast to most facies sequences in the studied section, shows a decrease in API values and a sharp top (Fig. 4.2f). The OBI and ABI logs show a set of continuous sine waves, overlying a sharp to truncated basal surface (Fig. 4.2f).

Interpretation

These lobate bodies with fine-grained sandstones are interpreted as the deposits of a proximal crevasse-splay complex. The vertical stacking of facies suggests variation in flood energy during deposition (Burns *et al*., 2017). The horizontal laminated sandstones (Lithofacies Sh) indicate upper flow regime conditions during splay flood events. The overlying Lithofacies St and/ or Sr suggest a subsequent reduction in flow energy (Bristow *et al*., 1999; Table 4.1). The presence of Lithofacies Sc towards the top of the package suggests significant deposition from suspension during flow deceleration in flood splay events. The coarsening-upward trend (funnel shape) of GR logs is typical of prograding crevasse-splay lobes (Emery & Myers, 1996; Cant, 2002). Continuous sine waves interpreted in OBI and ABI logs correspond to horizontal laminated sandstones (Lithofacies Sh), trough cross-bedded sandstones (Lithofacies St) and/or current rippled sandstones (Lithofacies Sr) (Xu *et al*., 2009; Keeton *et al*., 2015; Lai *et al*., 2018).

4.3.7. Facies association 7: Medial crevasse-splay complex

Description

Facies Association 7 (MSFA 7) is defined as a package of thin bedded, very fine-grained sandstones typically occurring as lobe-shaped bodies up to 1.5 m thick and 70 m in lateral extent. These bodies show horizontal, sharp bases, whilst the tops are convex-up and sharp (Tables 4.1 and 4.2; Fig. 4.2g). This facies association comprises climbing ripples (Lithofacies Sc) and/or current rippled sandstones (Lithofacies Sr) at the base alternating with syn-sedimentary deformed sandstones (Lithofacies Sd). Locally, towards the top, this facies association also shows root and desiccation cracks.

The GR log is characterized by a decrease in API values with a sharp top (Fig. 4.2g). The OBI and ABI logs show both continuous and discontinuous sine waves. The base is represented by a sharp to truncated surface (Fig. 4.2g).

Interpretation

This facies association is interpreted as a medial crevasse-splay complex, on the basis of facies context, the very fine sand grain size, the presence of syn-sedimentary deformation (Lithofacies Sd) and current rippled sandstones (Lithofacies Sr) (Burns *et al*., 2017). The occurrence of syn-sedimentary deformation (Fig. 4.2g) reflects rapid sediment accumulation onto a water-saturated substrate (Rossetti & Santos, 2003; Owen & Santos, 2014; Burns *et al*.,

2017; Table 4.1). The coarsening-upward trend (funnel shape) of the GR log is typical of prograding crevasse-splay lobes (Emery & Myers, 1996; Cant, 2002). Continuous sine wave curves, interpreted in OBI and ABI logs, correspond to current ripple cross-lamination whereas the discontinuous sine waves correspond to syn-sedimentary deformation (Xu *et al.*, 2009; Keeton *et al.*, 2015; Lai *et al.*, 2018).

4.3.8. Facies Association 8: Distal crevasse-splay complex

Description

Facies Association 8 (MSFA 8) occurs as thin, fine-grained beds, interbedded with the mudstones of MSFA 9. Facies package geometries are lobate to tabular, characterized by horizontal and sharp bases and gently convex-up, sharp tops. They reach up to 0.8 m in thickness and up to 30 m in lateral extent. This facies association comprises laminated siltstones and subordinate, very fine-grained sandstones. Planar laminated siltstones (Lithofacies Ll) are overlain by massive and diffuse laminated siltstones and mudstones with pedogenic features (rhizoliths, mottles and cutans) and also desiccation cracks (Lithofacies Lm). Less frequently, *Arenicolites* isp. tubes occur (Tables 4.1 and 4.2; Fig. 4.2h). The key macromorphological features are reddish to yellowish rhizoliths (colours 10R 4/8 to 2.5YR 3-5/8), reddish and little brown mottles (colours 10R 4/4 and 2.5YR 3/4) and scar cutans. Slickensides sometimes also occur locally (Fig. 4.2h). MSFA 8 is also characterized by A/C-type paleosol profiles.

Even though facies packages are thin, the GR response of MSFA 8 is characterized by a smooth decrease in API values and a sharp top (Fig. 4.2h). The OBI and ABI logs show thin high contrast bedsets, characterized by horizontal and parallel surfaces, although the OBI response is not very clear in terms of internal characteristics (Fig. 4.2h).

Interpretation

This facies association is interpreted as a distal crevasse-splay complex, on the basis of the very fine-grained, silt-dominated lithology, the presence of both planar and diffuse lamination as the only sedimentary structures, together with the thin, lobate to tabular geometries (Pizzuto, 1987; Mjøs *et al.*, 1993; Bristow *et al.*, 1999; Burns *et al.*, 2017). The presence of rhizoliths, mottles and cutans, coupled with the poorly developed and often diffuse lamination suggests phases of paleosol formation. These paleosols should be classified as modern Entisols (Soil Survey Staff, 1998). The coarsening-upward trend (funnel shape), characteristic of the GR log is typical of prograding crevasse-splay lobes (Emery & Myers, 1996; Cant, 2002) but given the other distinguishing features, MSFA 8 clearly represents a distal

example of such a complex. Amalgamated coarsening-upward packages suggest multiple, periodic flooding events (i.e. crevasse-splay complex, *sensu* Mjøs *et al.*, 1993; Miall, 1996).

4.3.9. Facies Association 9: Distal floodplain

Description

Facies Association 9 (MSFA 9) is characterized by a red (colour 10R 3/4), massive mudstones (Lithofacies Fm) with abundant pedo-features such as rhizoliths, mottles, nodules, cutans, mesofauna bioturbation (earthworms, trace fossils and *Taenidium* isp.) and slickensides (Tables 4.1 and 4.2; Fig. 4.2i). MSFA 9 is also characterized by granular, subangular, blocky and wedge-shape peds as the main pedogenic structures. The geometry of MSFA 9 is tabular with horizontal and sharp bounding surfaces. Facies packages range in thickness from a few centimetres up to 10 m and may be up to 1000 m in lateral extent.

The most diagnostic macromorphological pedo-feature (both in outcrop and cores) is the presence of slickensides characterized by cross-cutting curved surfaces forming bowl-like structures as well as wedge-shape peds. Other key pedogenic features are the gley colour mottles (colour 5G 7/1), gley rhizoliths (colour 5G 5-7/1) and Fe-Mn nodules. In thin section, the cross-striated b-fabric and the presence of thin clay and both Fe-Mn oxide coatings and infillings are the most diagnostic micro-scale pedo-features (Table 4.2, Fig. 4.2i). X-ray diffraction analyses indicate that illite is the main component within the clay fraction. MSFA 9 is thus characterized by paleosol profiles with Ass(?)–Bss–C successions. The surface paleosol horizons (Ass horizons) are, however, usually absent, and where present can only be recognized by the granular ped structures reflecting poorly developed horizonation.

The GR log through MSFA 9 is characterized by higher API values, compared to the facies associations described above, and shows an aggrading, serrated trend (Fig. 4.2i). The OBI and ABI logs are characterized by a massive and homogeneous aspect, lacking any clear surfaces except the presence of very high angle sine waves in two opposing preferential directions (Fig. 4.2i).

Interpretation

This facies association is interpreted as the deposits of a distal floodplain characterized by widespread paleosol development. The abundance of vertic pedo-features (slickensides, wedge-shape peds and cross-striated b-fabric) suggests the presence of shrinking and swelling expansive clays, although this apparently contradicts the X-ray diffraction analyses that show abundant illite. However, the illitization of smectites in paleo-Vertisols due to burial diagenesis is a common process (Driese *et al.*, 2000) and may explain this apparent contradiction. The cross-

cutting curved surfaces, forming bowl-like structures, are interpreted as the microlow areas of gilgai microrelief. In this sense, the poorly developed horizonation most likely records the mixing of seasonal shrink-swell processes (Driese *et al.*, 2000; Retallack, 2001; Varela *et al*., 2012). The presence of hydromorphic features (Fe-Mn nodules, gley mottles and rhizoliths) also indicates seasonal waterlogged drainage conditions (Retallack, 2001). These pedofeatures are also consistent with Vertisol-like paleosols (Soil Survey Staff, 1998). The serrated shape (aggrading trend) of the GR log through MSFA 9 is also typical of fluvial floodplain deposits (Emery & Myers, 1996; Cant, 2002). The very high angle sine waves observed in OBI and ABI could be related to slickenside surfaces.

4.3.10. Facies Association 10: Swamp

Description

Facies Association 10 (MSFA 10) is composed of dark grey to dark purple (colours N2.5/0 to 10B 3-4/1) thin-laminated mudstones (Lithofacies Fl) and organic matter. Sporadic, thin, massive micritic limestones and massive mudstone lamina also occur. The geometry of MSFA 10 is tabular with horizontal and sharp bounding surfaces. Facies packages range in thickness from several centimetres up to 2 m with up to 100 m of lateral extension (Tables 4.1 and 4.2; Fig. 4.2j). Locally, desiccation cracks occur towards the top of the MSFA 10 succession.

The GR log through MSFA 10 is characterized by a serrate profile (aggrading trend) with the highest API values in comparison with MSFA 9. The OBI and ABI logs both show a high contrast, high amplitude base and top, between which multiple, parallel surfaces dipping <5 degrees, are observed (Fig. 4.2j).

Interpretation

Facies Association 10 is interpreted as having been deposited from suspension in a swamp environment. The dark grey and dark purple colours indicate reducing and anoxic conditions, with organic matter commonly preserved. The presence of desiccation cracks, as well as the transition to MSFA 9 most likely records swamp desiccation during dry seasons. The high API values characteristic of the GR log are probably due to an increase in the uranium associated with the organic matter (Myers & Bristow, 1989; Rider & Kennedy, 2011). Multiple, parallel, flat-lying surfaces, seen in OBI and ABI logs represent thin laminations accumulated by fall-out from suspension in extremely low energy conditions.

Table 4.2. Summary of facies associations identified in the M-S Unit. See text for details. See Table 1 for lithofacies description. See Fig. 4.2 for photographic examples of each facies association.

MSFA	Lithofacies	Description	Geometry	Boundary Surfaces (L-lower; U-upper)	Thickness	Width	Environmental interpretation
1	Gm, St, Sr, Sm, Fl	Mudstone rip-up clasts. Trough cross bed sets of 20 x 6 cm. Shows *Arenicolites isp.* and *Taenidium* isp. at the top.	Lenticular	L: Concave-up and erosive U: Horizontal and Sharp	up to 3 m	Up to 30 m perpendicular to the main flow direction	Main channel
2	Gm, St, Sp, Sr, Sc, Sw, Sb, Sd, Sm, Lr, Ll	Mudstone rip-up clasts. Lateral accretion surfaces increasing dip toward the top (5 to 20°). Internally composed of trough cross bed sets of 27 x 9 cm and counter current ripples toward the top. Sometimes shows mud drapes or mud laminae between lateral accretion surfaces. Show *Arenicolites* isp. and *Taenidium* isp. at the top.	Asymmetric sigmoidal	L: Horizontal and erosive U: Horizontal and sharp	up to 3.6 m	Up to 100 m	Lower and middle point bar
3	Sr, St, Sp, Sh, Sm	Mudstone rip-up clasts. Trough cross bed sets. Current ripples toward the top.	Asymmetric sigmoidal	L: Horizontal and erosive U: Horizontal and undulated	up to 1.5 m	Up to 30 m	Scroll bar
4	Sr, Sh, St, Fb	Alternation between Sr/St from low flow regime with Sh in high flow regime. Toward the top shows Fb as final stage filling.	Lenticular	L: Concave-up and erosive U: Horizontal and Sharp	0.7 to 0.8 m	Up to 3 m	Chute channel
5	St, Sr, Sw	Mudstone rip-up clasts at the base. Show trough cross bed sets of 25 x 2 cm and current ripples. Sometimes towards the top shows Lithofacies Sw.	Lenticular	L: Concave-up and erosive U: Horizontal and Sharp	0.4 to 1.1 m	Up to 6 m	Crevasse channel

Table 4.2. (continued)

MSFA	Lithofacies	Description	Geometry	Boundary Surfaces (L-lower; U-upper)	Thickness	Width	Environmental interpretation
6	Sh, Sr, Sc, Sd	The vertical stacking of facies shows the transition from Sh to Sr/St, finally climbing ripple and syn-sedimentary deformation toward the top.	Lobe	L: Horizontal and Sharp U: Convex-up and sharp	up to 2 m	Up to 130 m	Proximal crevasse-splay complex
7	Sr/Sc, Sm, Sl, Sw, Sd	Climbing ripple and current ripple cross-lamination at the base. Alternating with syn-sedimentary deformation. At the top rootlets. Desiccation Cracks.	Lobe	L: Horizontal and Sharp U: Convex-up and sharp	up to 1.5 m	Up to 70 m	Medial crevasse-splay complex
8	Fm, Lm, Ll, Fl, Sl	Lower flow regime lamination and paleosol development toward the top (rootlets, mottles and cutans). Desiccation Cracks. Sometimes shows *Arenicolites* isp. at the top.	Lobe to tabular	L: Horizontal and Sharp U: Convex-up and sharp	up to 0.8 m	up to 30 m	Distal crevasse-splay complex
9	Fm	Slickensides, wedge-shape peds, angular and subangular blocky peds, cutans, bowl-like structures, Gilgai microrelief, motts and rhizoliths	Tabular	L and U: Horizontal and sharp	from cm to 10 m	100 - 1000 m	Distal floodplain
10	Fl, Fm, Cm	Gley dark purple to dark grey colours mudstone. Usually laminated. Desiccation Cracks. Sporadic massive micritic limestone laminae.	Tabular	L and U: Horizontal and sharp	from cm to 2 m	100 m	Swamp

117

4.4. Stratigraphic architecture of the Mudstone-Sandstone Unit

The exceptional outcrops of the study area permit a full description of the geobodies of the M-S unit, as well as characterization of both the vertical and lateral variability of the previously described facies associations. From this, it can be seen that the main channel and point bar deposits pass laterally into floodplain and swamp deposits interbedded with the crevasse-splay complex deposits recorded in the PNV-1 section as shown in Fig. 4.3.

Amalgamated crevasse-splay deposits occur throughout but are clearly more frequent towards the eastern edge of the outcrop, although still interbedded with an abundance of floodplain and swamp deposits. Towards the western part of the outcrop, the corresponding main channel and point bar deposits occur (Fig. 4.3). Finally, towards the top of this outcrop, main channel and point bar deposits occur where the PNV-1 section is located and grade laterally into the crevasse-splay deposits to the east of the outcrop (Fig. 4.3).
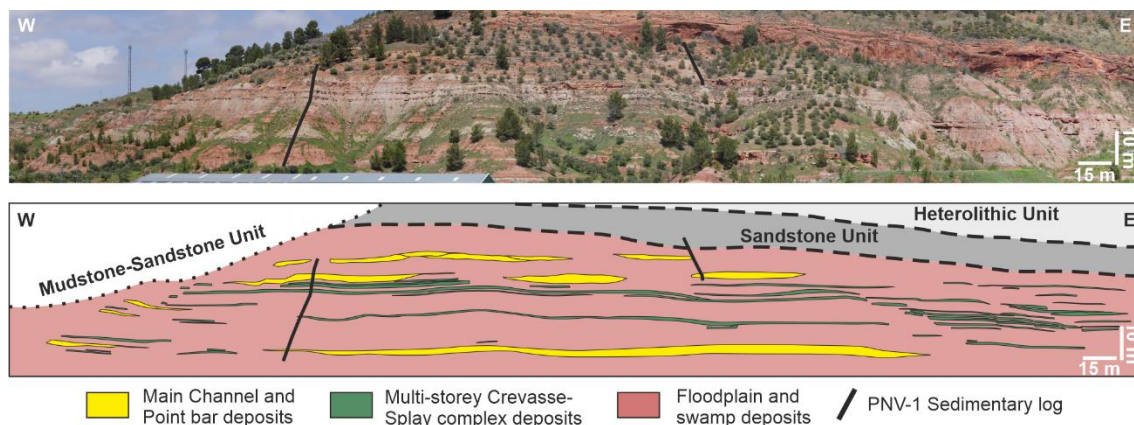
Fig. 4.3. West–East oriented panoramic view showing the key outcrop of the Mudstone–Sandstone (M-S) Unit and interpretation of the main channels, multi-storey crevasse-splay complexes, distal floodplain and swamp deposits.

4.5. Channel – Crevasse-splay complex model

4.5.1. Outcrop perspective

The 19 sedimentary logs, constructed following the same stratigraphic level (Fig. 4.4), provide a framework from which the dimensions, lateral variability, and heterogeneities of the M-S Unit can be established. Towards the south-east (CPMR1 to CPMR8), a facies transition is observed, from the main channel (CP-0), through point bar, proximal to distal crevasse-splay complex, and finally distal floodplain deposits (Fig. 4.4). In contrast, towards the north-west
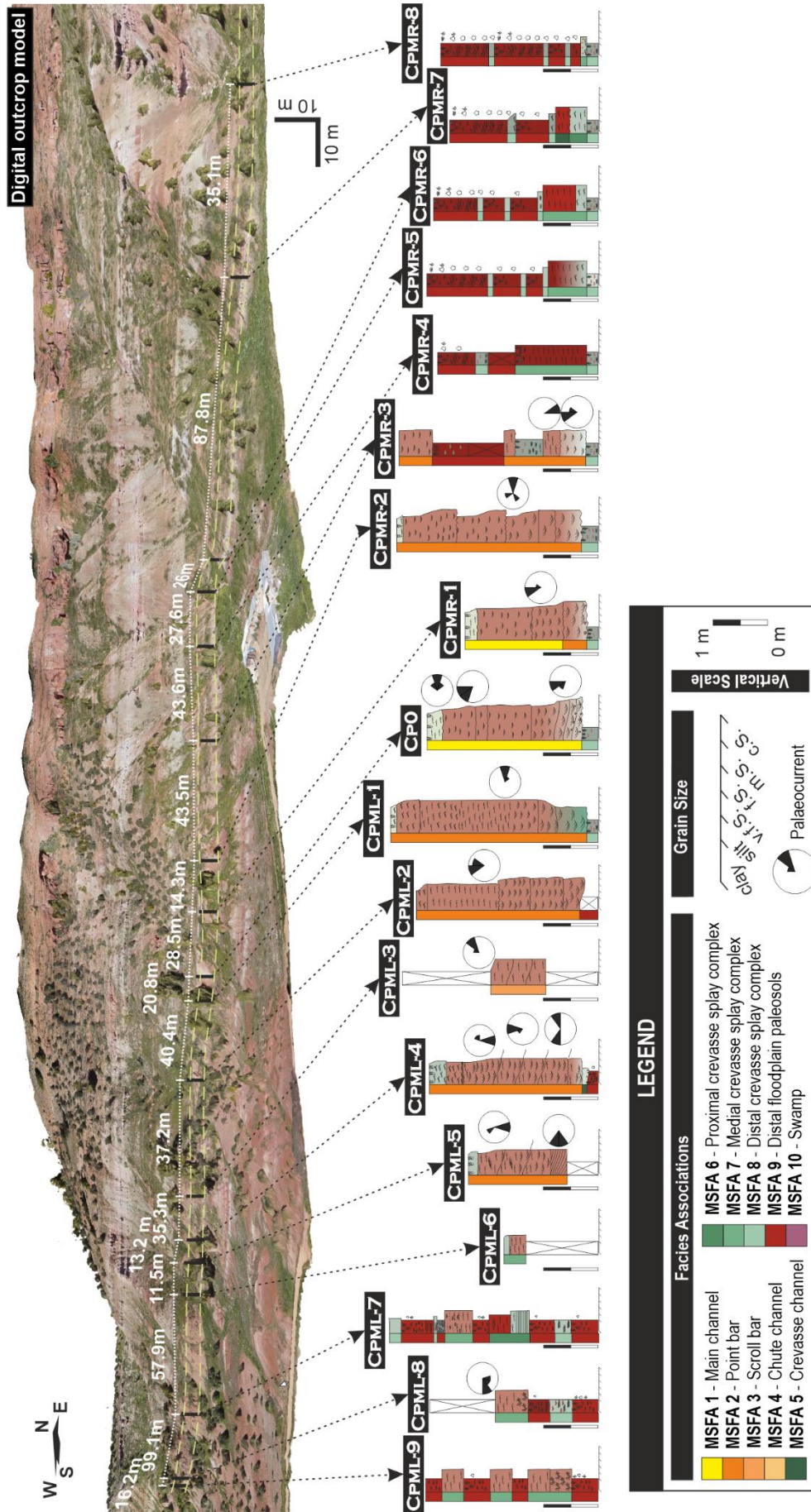
Fig. 4.4. Digital outcrop model (DOM) showing the location and measured distance between each of the sedimentary logs constructed in order to characterize lateral variability in facies sequences.

(CPML1 to CPML9), the facies transition observed is from main channel to point bar to scroll bar and, finally, proximal and medial crevasse-splay complex (Fig. 4.4).

Through the empirical determination of the lateral facies variations, the internal discontinuities and the scale (lateral and vertical measurements) of the geobodies, as well as the distance to the main channel (Fig. 4.4), a conceptual model has been developed, as illustrated in Fig. 4.5. The key elements are summarized as follows:
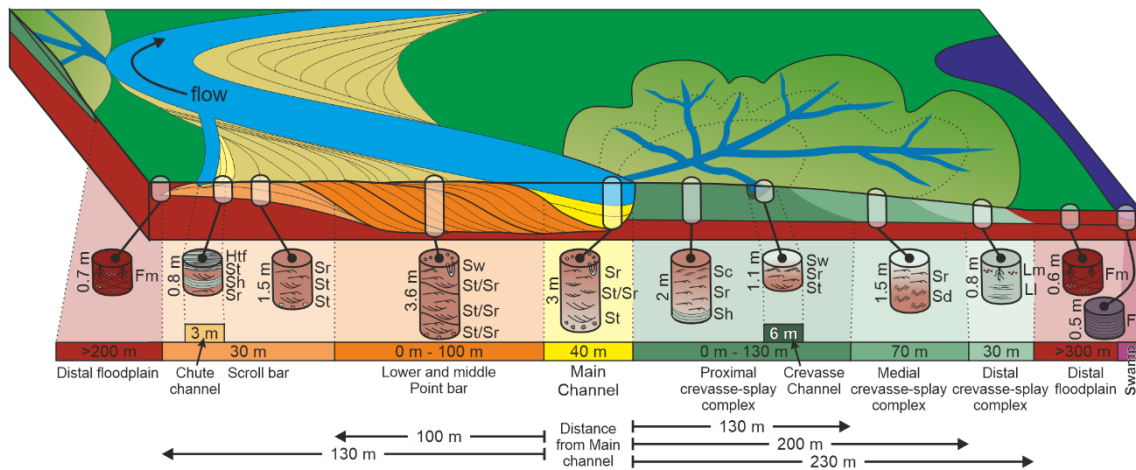
Fig. 4.5. Conceptual model of lateral variability for Facies Associations (FA 1 to FA 10) including sedimentary and pedogenic features, lateral extent or width of the associated depositional area, distance from the main channel and thickness of each facies association.

The main channel (MSFA 1) is 40 m wide and 3 m thick. On the accretional, inner margin of the thalweg, the main channel grades into lower and middle point bar deposits (MSFA 2).

The point bar is up to 3.6 m thick and 100 m wide, extending from the main channel. The deposits of the point bar pass into scroll bar deposits (MSFA 3). The scroll bar is up to 1.5 m thick, 30 m in width and located up to 130 m away from the main channel. Locally, chute channel deposits (MSFA 4) are incised into the scroll bar (Fig. 4.2d). These are up to 3.0 m in width and up to 0.8 m in thickness. The scroll bar grades laterally into distal floodplain deposits (MSFA 9).

On the erosive margin of the main channel, the crevasse-splay complex comprises a proximal crevasse-splay complex (MSFA 6) up to 130 m in width and up to 2 m thick. Crevasse channel (MSFA 5) deposits frequently cut into the proximal crevasse-splay complex (Fig. 4.2e and Fig. 4.6a-b; Bristow *et al.*, 1999). Crevasse channels are up to 6.0 m wide and up to 1.1 m thick. The proximal crevasse-splay complex passes from the main channel into the medial crevasse-splay complex (MSFA 7); and is 70 m wide and 1.5 m thick. This is located 200 m away from the main channel and is also cut by crevasse channels. The distal crevasse-splay complex

(MSFA 8) is located up to 230 m from the main channel. It is 30 m wide and 0.8 m thick. The distal crevasse-splay complex grades laterally into the distal floodplain (MSFA 9).

Distal floodplain deposits (MSFA 9) occur up to 300 m from the main channel. They vary between 100 m and 1000 m in width forming packages only 0.6 m thick. Locally, within the distal floodplain, swamp deposits (MSFA 10) occur which are up to 100 m wide and 0.5 m thick.

Sandstone geobodies interpreted as crevasse-splay deposits in the M-S Unit have a lobate form marked by a sharp base and convex-up top. The dimensions of these deposits range from tens to hundreds of metres in width, with a thickness of 0.5 to 2.0 m (Fig 4.6a-b). These lobular geo-bodies rarely occur as a single crevasse-splay lobe generated during a flood event. Rather they are formed during continuous flood events leading to overlapping lobe geobodies, giving rise to a crevasse-splay complex (Fig. 4.6c-d).

A detailed interpretation of the crevasse-splay complexes (Fig 4.6a-b) shows the amalgamation and architecture of the crevasse channel, proximal, medial and distal crevasse-splay deposits (MSFA5 to MSFA8) (Fig 4.6b). Internally, each crevasse-splay complex also displays a vertical, progradational, trend from distal crevasse (MSFA 8) to medial and proximal crevasse-splay (MSFA 7 and MSFA 6, respectively). Locally, however, distal crevasse-splay deposits are observed overlying proximal crevasse-splay deposits (Fig 4.6b).

Measurements from DOM (Fig 4.6b) show up to 2.1 m thickness for crevasse-splay lobes with proximal crevasse-splay deposits (MSFA 6) and a width of up to 52.3 m measured approximately perpendicular to the lobe propagation direction (Fig 4.6b). As described above, these crevasse-splay lobes appear to be amalgamated, forming a crevasse-splay complex. In the DOM section shown in Fig 4.6b, the crevasse-splay complexes range from 1.1 m to 4.0 m in thickness (Fig 4.6b). The dimensions for the crevasse channel, interpreted in this section, are 1.1 m thick and 28.5 m wide, measured sub-perpendicular to flow direction (Fig 4.6b).

4.5.2. Subsurface perspective

From the comparison between the largely complete outcrop sedimentary log (PNV-1; see Fig. 4.1 for locations) and the two wells (S2P4 and K2P1), located at distances of 405 m and 275 m, respectively (Fig. 4.7), it can be seen that the sequence of facies associations corresponds to the stacking of the various geobodies.

From base to top, the lowest two thirds of the PNV-1 section comprise distal floodplain and swamp deposits (MSFA 9 and MSFA 10) interbedded with crevasse-splay complex facies

(MSFA 5 to MSFA 8). In this interval, the paleocurrent measurements fall into two main groups; north-east-directed and south-east-directed for the crevasse-splay deposits. In contrast, in the uppermost third of the PNV-1 section; main channel and point bar (MSFA 1 and MSFA 2) deposits show a mean paleocurrent direction towards the north (between N280E and N095E; Fig. 4.7).

In the cored section of Well K2P1, towards the base, point bar deposits (MSFA 2) are observed. These are overlain by distal floodplain and swamp (MSFA 9 and MSFA 10) deposits, interbedded with crevasse-splay complex (MSFA 5 to MSFA 8) facies (Fig. 4.7 and Fig. 4.8a). In Well S2P4 the core comprises distal floodplain and swamp (MSFA 9 and MSFA 10) deposits interbedded with crevasse-splay complex (MSFA 5 to MSFA 8) facies (Fig. 4.7 and Fig. 4.9a). This well did not penetrate either main channel and/or point bar (MSFA 1 and/or MSFA 2) facies.
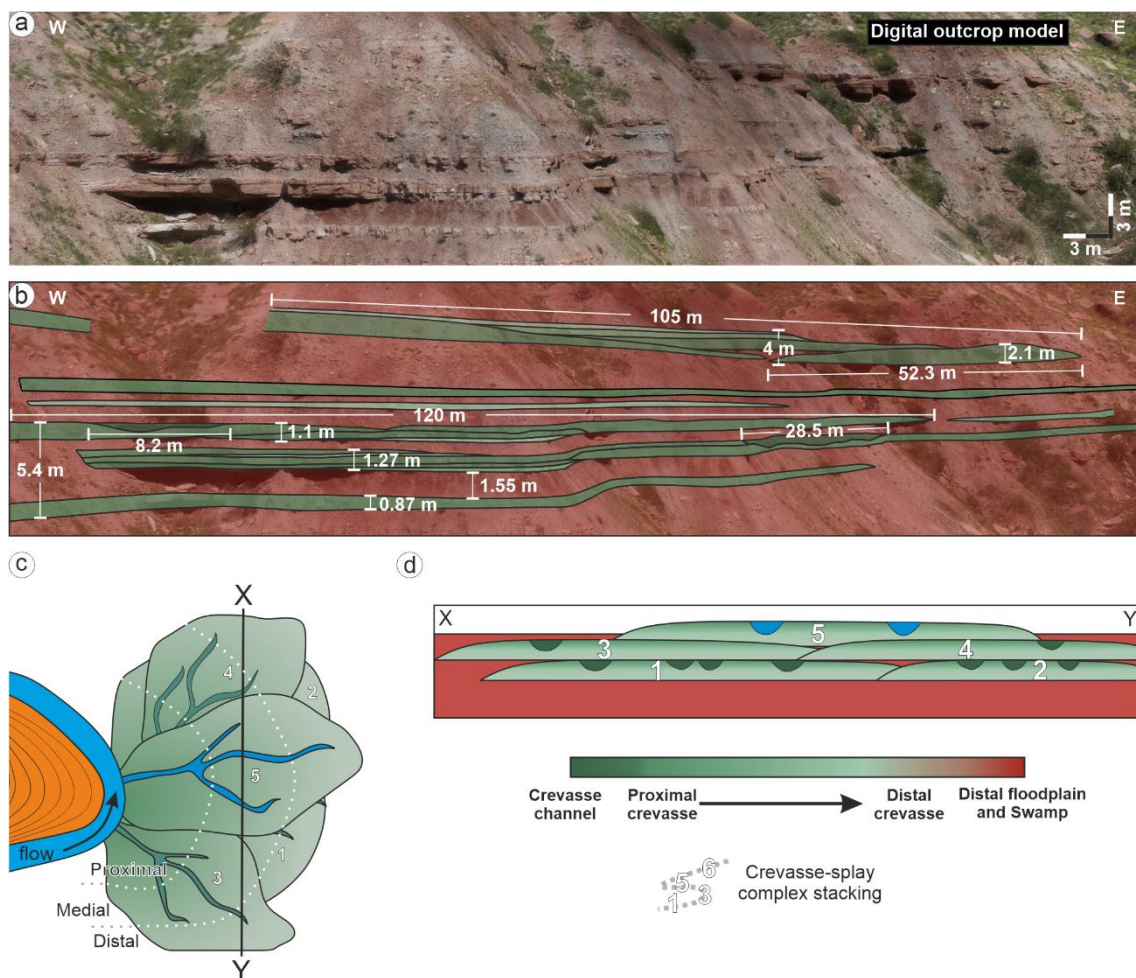
Fig. 4.6. **(a)** and **(b)** Close-up view of crevasse-splay complexes showing a detailed interpretation of internal bounding surfaces and both lateral and vertical variability of the facies associations. **(c)** Plan-view conceptual model of a crevasse-splay complex. **(d)** Cross-section conceptual model of crevasse-splay complexes. Numbers in **(c)** and **(d)** are related to the order of deposition.
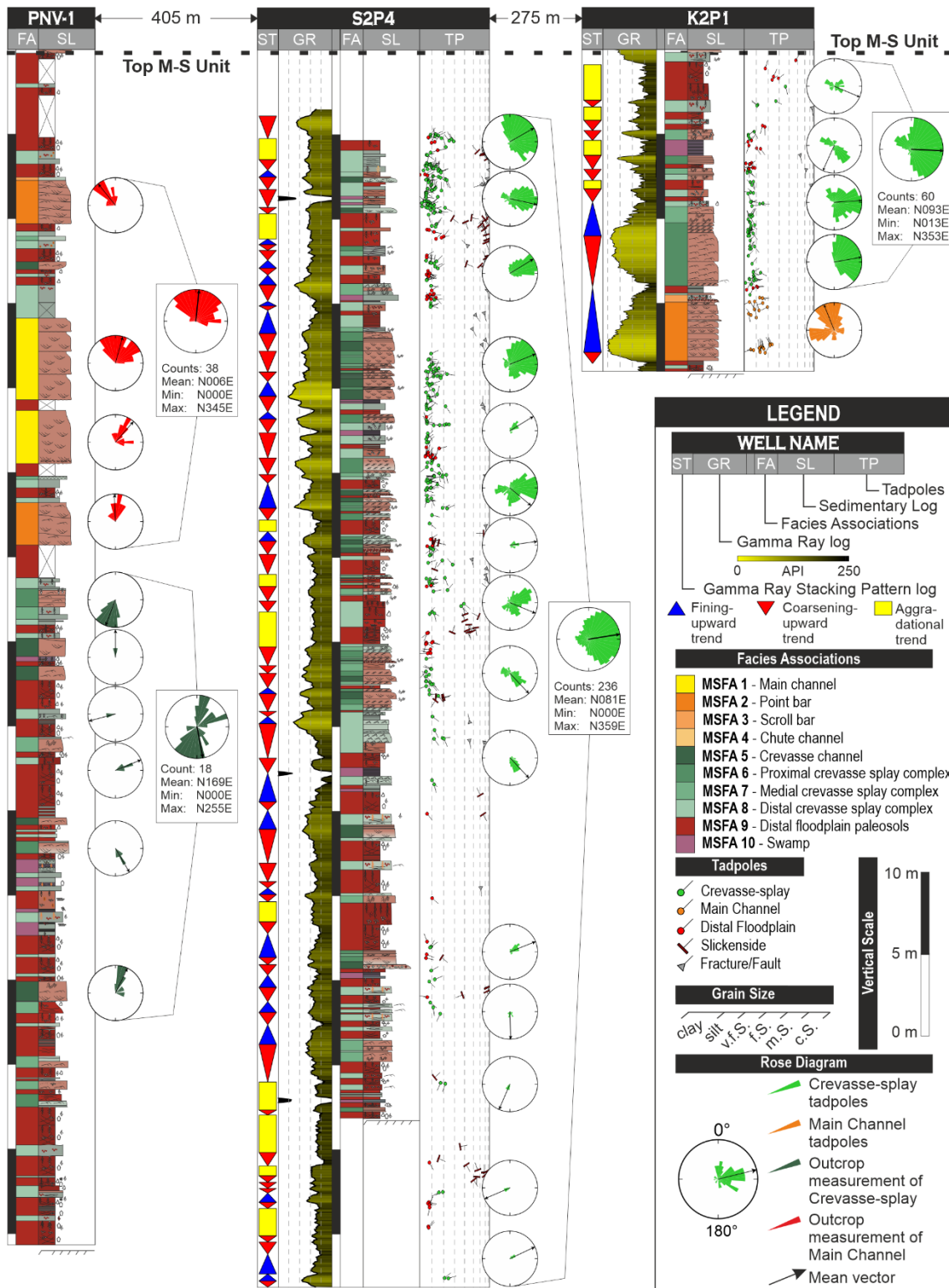
Fig. 4.7. Vertical variability of facies associations from outcrop and subsurface data. Section PNV-1 data is outcrop-derived including sedimentological log, facies associations and paleocurrent data. S2P4 and K2P1 are wells (see Fig. 4.1 for location) which include Gamma Ray (GR) log, GR stacking patterns, core description, facies associations and paleocurrent measurements from borehole images. The rose diagrams inside the rectangles show the dip azimuth measurements for the indicated interval.

The GR logs from both Wells S2P4 and K2P1, show a predominance of coarsening/ cleaning-upward trends (funnel shapes) which reflect a progradation from distal floodplain to crevasse-splay deposits (MSFA 9 to MSFA 5) and/or from distal to proximal crevasse-splay deposits (MSFA 8 to MSFA 5; Fig. 4.7). To a lesser extent, fining-upward trends (bell shapes) also occur (Fig. 4.7, Fig. 4.8b and Fig. 4.9b). These correspond to main channel deposits (MSFA 1), crevasse channel deposits (MSFA 5) with a shift from proximal (MSFA 6) to distal (MSFA 8) crevasse-splay deposits. In contrast, the aggrading trends (serrated GR profiles) represent distal floodplain and/or swamp deposits (MSFA 9 and/or MSFA 10; Fig. 4.7, Fig. 4.8b and Fig. 4.9b).

In Well K2P1, a total of 60 dip tadpoles were picked within crevasse-splay deposits with a mean azimuth of N093E, measurements ranging from N013E to N353E with the most frequent values between N014E and N137E. In point bar deposits (MSFA 2) a total of 45 dip tadpoles were picked with a mean azimuth of N346E (Fig. 4.7 and Fig. 4.8b). In this Well, a 5.2 m thick interval is shown in Fig. 4.8, as an example of such a crevasse-splay complex. High-resolution analysis of dip tadpoles, for the basal 3.6 m of this interval, shows three discrete paleocurrent packages, with azimuths, from base to top, of N092E, N044E and N134E (Fig. 4.8b), respectively. This suggests the stacking of three component crevasse-splay lobes. These lobes, in addition to prograding across the floodplain during flood events, are arranged laterally by compensation of accommodation space. Above this basal 3.6 m a bell-shaped GR profile is observed corresponding to medial and distal crevasse-splay deposits, respectively (Fig. 4.8b). In this interval, two dip tadpole packages are distinguished, with paleocurrent directions to N015E and N094E, respectively. This superposition of distal over proximal facies, and with different paleocurrent directions, strongly supports the interpretation of an amalgamated crevasse-splay complex.

In Well S2P4, a total of 236 dip tadpoles have been picked within crevasse-splay deposits with a mean azimuth of N081E, although there is a significant dispersion in paleocurrent directions (360°). Dip tadpole analysis shows that: (i) in the lowest third of the section mean paleocurrent values, for intervals, range between N065E and N247E; and (ii) the uppermost two-thirds of the section shows mean values, for intervals, ranging from N058E to N137E (Fig. 4.7 and Fig. 4.9b).

Fig. 4.8. (a) Core view showing a 10 m thick interval (from 31 m to 41 m depth) of Well K2P1. **(b)** K2P1 well composite (31 to 41 m depth interval) displaying the Gamma Ray (GR) log, the core description, facies associations interpretation and dip tadpole analysis. Red and blue arrows indicate a coarsening-upward, cleaning-upward or fining-upward GR profile, respectively.

From the foregoing descriptions of outcrop and well sections, the key features in core, GR log and paleocurrent, for each of the main facies associations, are summarized as follows and in Fig. 4.2, Fig. 10 and Fig. 11:

Main channel (MSFA 1) packages are distinguished by the stacking of several fining-upward (bell-shape) profiles in the GR log characterized by values ranging from 65 to 188 API (Fig. 4.10). The higher API values between each package represent mudstone rip-up clast conglomerates (Lithofacies Gm), occurring as basal lags. This pattern reflects the stacking of Lithofacies Gm–St–Sr (Selley, 2004; Viseras *et al*., 2018). Dip tadpole plots highlight several surfaces with dip angles of <15° and azimuths perpendicular to the dip tadpoles associated with the lateral accretion surfaces interpreted in point bar (MFSA 2). These dips correspond to the channel base erosional surfaces. Between these erosional surfaces, a set of dips with both random azimuth and dip angles between 5° and 25° are recorded (Fig. 4.11). These correspond to trough cross-bed foresets (Donselaar & Schmidt, 2005; Viseras *et al*., 2018; Yeste *et al*., 2019).

The point bar (MSFA 2) is characterized by a coarsening-upward or cleaning-upward (funnel shape) GR profile at the base, and a fining-upward (bell shape) towards the top of each facies package (Fig. 4.11), with API values ranging from 35 API to 182 API (Fig. 4.10). The lowermost bell-shaped GR packages also show higher API values reflecting the presence of mudstone rip-up clasts (Selley, 2004; Viseras *et al*., 2018). In core, point bar deposits are recognized by sets of Lithofacies St–Sr separated by inclined surfaces corresponding to the lateral accretion surfaces. Two dip tadpole groups are associated with this facies association: (a) shallow-to-steep-to-shallow dip angles towards the top (Fig. 4.11); and (b) azimuths displaying a slightly variable rotation (clockwise or anticlockwise) towards the top. These tadpoles correspond to lateral accretion surfaces (Donselaar & Schmidt, 2005; Brekke *et al*., 2017; Viseras *et al*., 2018). Tadpole sets with random azimuth and dip angles between 5° and 25°, occurring between the planar features of (a) are interpreted to represent trough cross-bed foresets (Donselaar & Schmidt, 2005; Viseras *et al*., 2018; Yeste *et al*., 2019).
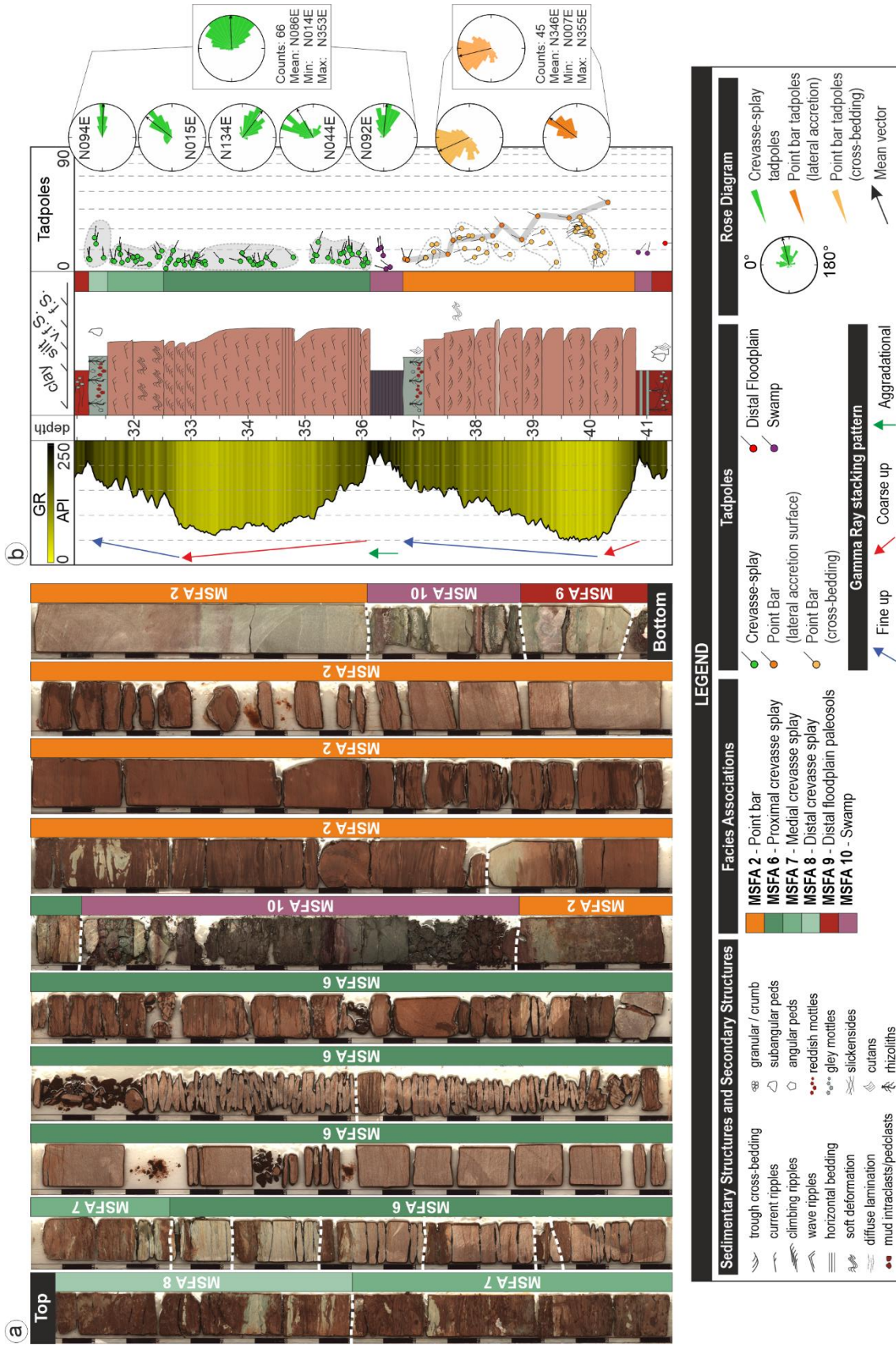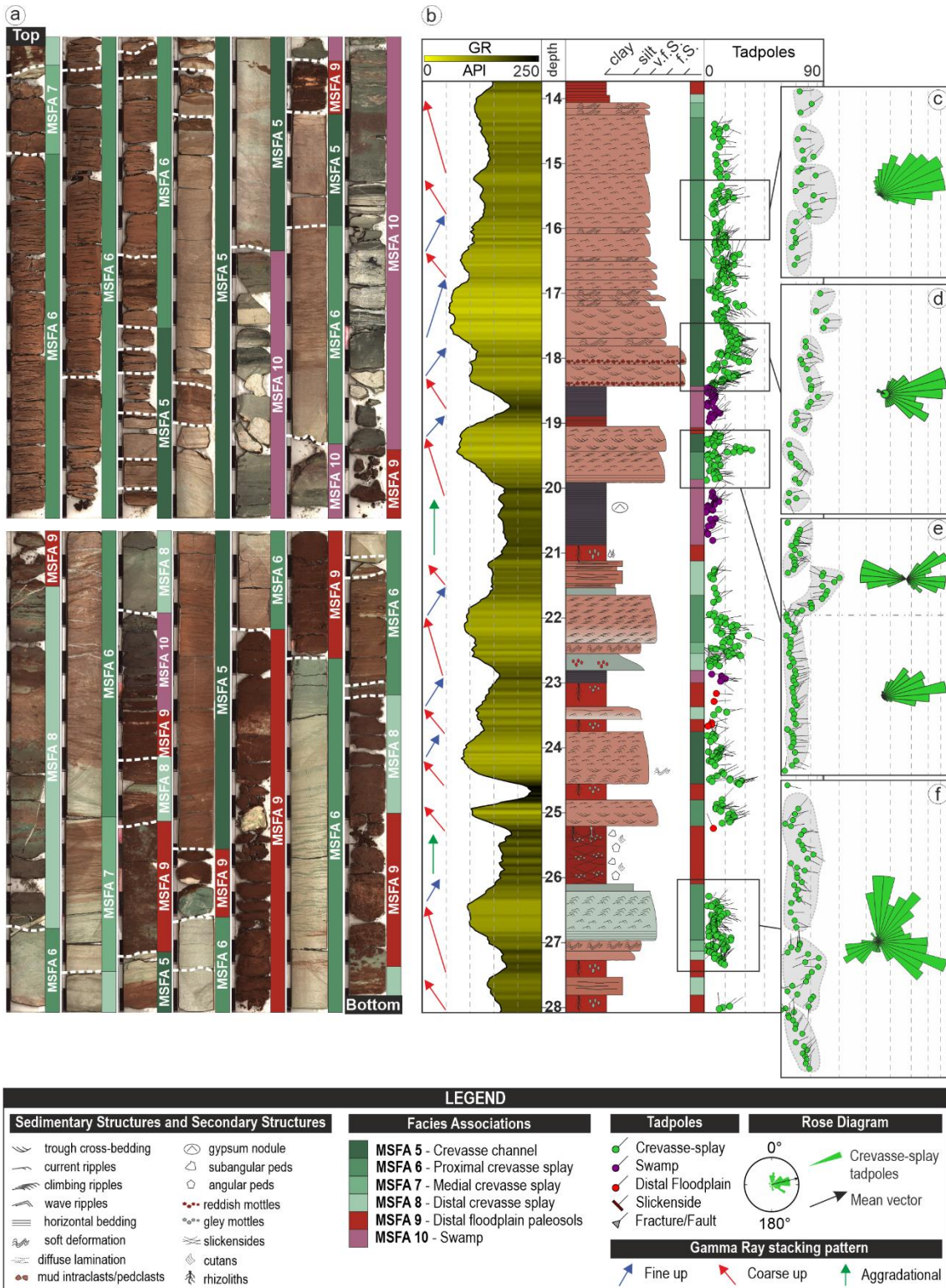
Fig. 4.9. (a) Core view showing a 14 m thick interval (from 14 m to 28 m depth) of Well S2P4. **(b)** S2P4 well composite (14 to 28 m depth interval) displaying the Gamma Ray (GR) log, the core description, facies associations interpretation and dip tadpole analysis. Red, blue and green arrows indicate a coarsening-/cleaning-upwards, fining-upwards or aggradational GR profile, respectively. **(c)** to **(f)** Selected close-up view of dip tadpole log highlighting the grouping of tadpole patterns accompanied by a rose diagram for each interval highlighted on the well composite.

Proximal crevasse-splay deposits (MSFA 6) are characterized by a coarsening-upward or cleaning-upward (funnel shape) GR response truncated by a sharp top (Fig. 4.11), API values ranging from 57 API to 197 API (Fig. 4.10). In core, this association is characterized by the lithofacies succession Sh–Sr–Sc indicating flow deceleration and significant deposition during splay events (Burns *et al*., 2017). Locally, the funnel-shaped GR profile develops into a bell-shape (fining-upward trend) towards the top of the facies package reflecting truncation by crevasse channel deposits (MSFA 5). This bell-shaped GR package corresponds, in core, with the lithofacies succession St–Sr–Sw implying a gradual flow deceleration and overbanking of the crevasse channels (Bristow *et al*., 1999; Burns *et al*., 2017). MSFA 6 is characterized by tadpoles with unidirectional azimuths and dip angles of <10° (Fig. 4.9c, e and Fig. 4.11). In contrast, MSFA 5 is characterized by sets of tadpoles with randomly distributed azimuth and dip angles between 5° and 25° (Fig. 4.9d, e and Fig. 4.11). Towards the top, this association typically shows a tadpole set with unidirectional azimuth and dip angles <10°.

Medial crevasse-splay deposits (MSFA 7), are characterized in core by the presence of syn-sedimentary deformation indicating rapid sediment accumulation onto a water-saturated substrate (Bristow *et al*., 1999; Rossetti & Santos, 2003; Owen & Santos, 2014; Burns *et al*., 2017). These deposits also comprise Lithofacies Sr and, occasionally, Sd. The associated GR profile is characterized by a coarsening-upward or cleaning-upward trend (funnel shape), API values ranging from 99 API to 200 API (Fig. 4.10). Tadpoles in MSFA 7 are characterized by randomly distributed dip angles and azimuths when syn-sedimentary deformation structures (Sd) are present (Fig. 4.9f and Fig. 4.11). In the interval where MSFA 7 is characterized by Lithofacies Sr, the tadpole pattern shows a unidirectional azimuth and dip angles of <10°.

Distal crevasse-splay deposits (MSFA 8) are also characterized by funnel-shaped (coarsening-upward or cleaning-upward trend) GR packages, albeit notably thinner than those associated with medial or proximal crevasse-splay deposits. The API values range from 99 API to 242 API (Fig. 4.10). In core, FA 8 is characterized by Lithofacies Lm and Ll suggesting poorly-developed paleosols (Retallack & Dilcher, 2012). The dip tadpoles through this association clearly highlight the bounding surfaces (bottom and top) of each package. Locally, where Lithofacies Ll is present, very low dip angle tadpoles (<10°) with unidirectional azimuths are recognized (Fig. 4.11).

Distal floodplain deposits (MSFA 9) are characterized by a typically serrated GR response (aggrading trend) with high API values (ranging from 105 API to 244 API; Fig. 4.10 and Fig. 4.11). In core, MSFA 9 is characterized by red, massive mudstones with abundant vertic pedo-features

(Lithofacies Fm), suggesting Vertisol-like paleosols (Soil Survey Staff, 1998). Two dip tadpole types are identified in MSFA 8: (i) tadpoles with very low dip angles (<7°) and a unidirectional azimuth; and (ii) tadpoles with very high dip angles (30° to 75°) and a bi-directional azimuth; the latter are associated with slickensides structures (Fig. 4.9b and Fig. 4.11).

Swamp deposits (MFA 10) show the highest GR values in the M-S Unit (ranging from 110 API to 366 API; Fig. 4.10) and a characteristically serrated GR profile (aggrading trend). In core, MSFA 10 is characterized by dark grey to dark purple-coloured, thinly-laminated mudstone (lithofacies Fl). MSFA 10 is also characterized by tadpoles with very low dip angles (<10°) and unidirectional azimuths (Fig. 4.9b and Fig. 4.11).
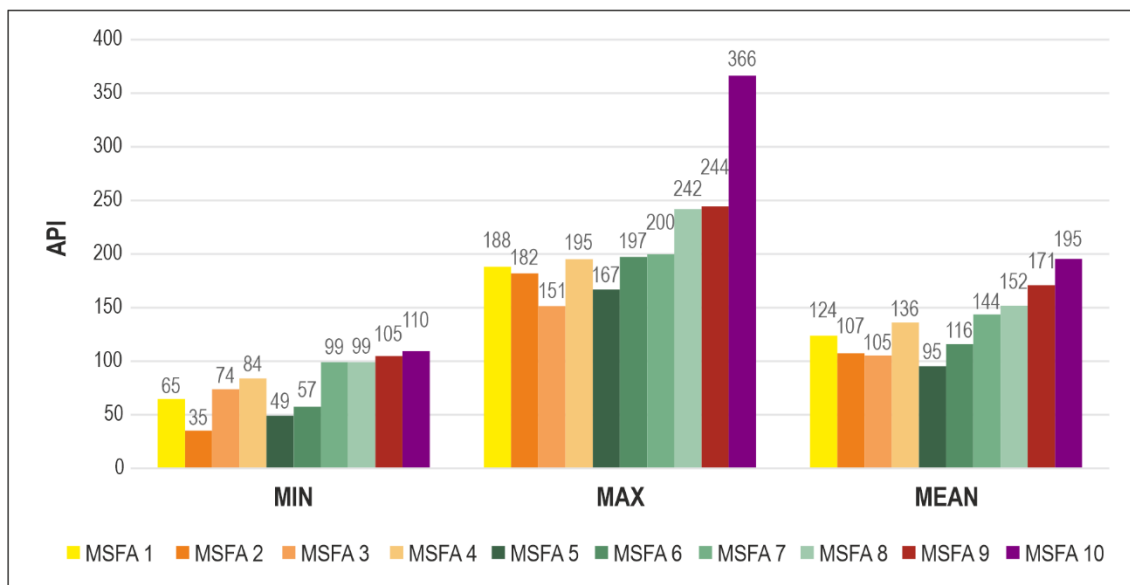
Fig. 4.10. Statistics summarizing the minimum, maximum and mean API values for each facies association.

4.6. Discussion

The detailed study of lateral facies variability using both outcrop and subsurface data (core, GR log and image log data) of the study area has enabled the definition of ten facies associations. Furthermore, with DOM data, it has also been possible to make precise measurements of both thickness and width for each of these facies associations and thereby define their geometric characteristics. In addition, the full integration of subsurface datasets and their validation with surface equivalents has enabled the development of more realistic conceptual models that include both descriptive and quantitative data related to the distribution of heterogeneities within the M-S Unit (Fig. 4.5 and Fig. 4.11).
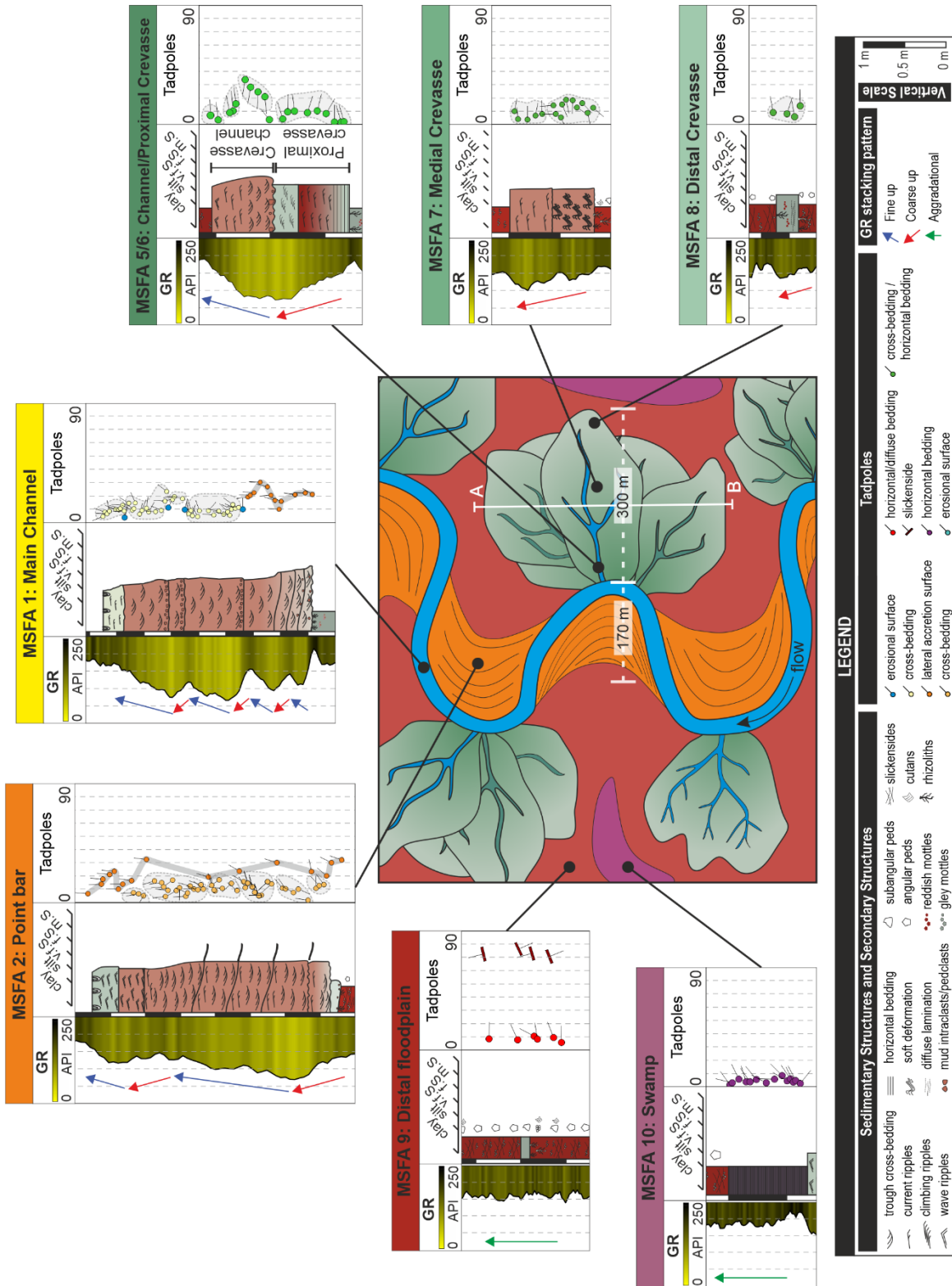
Fig. 4.11. Schematic plan-view of a conceptual model for the Mudstone–Sandstone Unit. This shows the key sedimentological, Gamma Ray log features and dip tadpole patterns for each facies association.

The predictive conceptual model presented in this study helps to reduce uncertainty surrounding the location and dimensions of the key channel element (main reservoir) on a low gradient floodplain. The proposed model only uses data essentially identical to that which would be acquired during exploration and production drilling of wells located across a floodplain. This is critical for the establishment of a more robust basis for predicting the location of primary and secondary reservoirs, in low net-to-gross fluvial settings, with greater precision and significantly reduced risk.

The method is applied to an example that has been shown to be an excellent outcrop analogue for fluvial reservoirs. More specifically, the M-S Unit is an excellent outcrop analogue for the lower TAGI (Trias Argilo-Greseux Inferieur) in the Berkine Basin, Algeria (Rossi *et al.*, 2002; Viseras *et al.*, 2011; Henares *et al.*, 2014). Recent studies (e.g. Burns *et al.*, 2017; Gulliford *et al.*, 2017; Ielpi *et al.*, 2018), also suggest how the predictive model presented here could be used as an analogue for low net-to-gross fluvial reservoirs with different ages but with similar geobody dimensions. Varela *et al.* (2019) have also established a comparative relationship between paleosol development and the fluvial architecture of sedimentary successions from both the Cretaceous of Patagonia, Argentina and Triassic Red Beds of Iberian Plateau (TIBEM). The authors have recognized an increase in maturity within the paleosol catena moving away from the main channel bodies. The most mature paleosol was, in each case, located at similar distance (200 to 300 m) from the main channels. Gil-Ortiz *et al*. (2019) have also identified a meandering fluvial-dominated system in the Lower Cretaceous pre-salt units of the distal offshore South Gabon sub-basin. These authors suggest similar dimensions and geobodies (meandering channels and crevasse-splay lobes) from image log data. The quantitative conceptual model presented for the M-S Unit could equally be applied to this Cretaceous formation and potentially many other low net-to-gross fluvial successions worldwide.

4.6.1. Distribution of heterogeneities and evolution of crevasse-splay lobes

Recent studies in outcrop of crevasse-splay deposits have shown similar facies distributions and facies belt dimensions for the same geobodies described for the M-S Unit. Burns *et al.* (2017), for example, have described facies distributions from the Cretaceous Castlegate Sandstone and Neslen Formations of Utah. Kraus & Aslan (1999) established the development of paleosol catenas related to topographic relief and to distance from the main channel. Moscariello (2009) highlights the importance of paleosol identification in low net-to-gross systems, as paleosol distribution is closely linked to channel sand distribution and reservoir

architecture. Varela *et al.* (2012) have also carried out a quantitative study in the Cretaceous Mata Amarilla Formation, of Argentina, focussed on the spatio-temporal distribution of different paleosols relative to the distance to the main channel. These authors also recognized an increase in maturity within the paleosol catena with increasing distance from the main channel bodies, so that the most mature paleosols are located in the distal floodplain at ca 200 m from the main channel. The current study has also observed a paleosol catena developed from distal crevasse-splay deposits (MSFA 8; Entisol-like) to distal floodplain deposits (MSFA 9; Vertisol- like). The measurements made in outcrop prove that the most mature paleosols of this catena are located at >300 m from the main channel deposits (Fig. 4.5).

In the most common case, the stacking of distal to medial to proximal crevasse-splay deposits is explained by the progradation of the crevasse-splay facies belts in successive flood events (sensu Mjøs *et al.*, 1993; Miall, 1996; Bristow *et al.*, 1999). However, the occurrence of distal crevasse-splay deposits overlying a proximal crevasse-splay must be explained by the stacking of successive crevasse-splay lobes through lateral compensation of accommodation space (Li *et al.*, 2014; Li & Bristow, 2015; Fig. 4.6c).

Because the stacking of successive crevasse-splay lobes is conditioned by lateral compensation, the propagation direction of lobes ranges from 15° to 130° relative to the main channel axis into the same crevasse-splay complex (Fig. 4.6c-d). This lateral and vertical amalgamation of lobes explains the significant areal extent of crevasse-splay complexes typical of the M-S unit (Mjøs *et al.*, 1993; Van Toorenenburg *et al.*, 2016; Burns *et al.*, 2017).

In addition, these crevasse-splay complexes may also stack to form amalgamated crevasse-splay complexes. In some sections, between two crevasse-splay complexes, distal floodplain and/or swamp deposits are observed (Fig. 4.6b). In other sections, a lateral overlap between two crevasse-splay complexes can also be observed (Fig. 4.6b), suggesting that these complexes may well be connected three-dimensionally when amalgamated. The excellent preservation of these crevasse-splay deposits, even in proximal facies, is due to the tendency of main channels to suffer sudden avulsions, rather than processes of gradual abandonment, thereby preventing cannibalization, linked to erosion by channel migration (Burns *et al.*, 2017). Preservation is also more likely, considering that the system was located on a very low gradient alluvial coastal plain, in a context of sea-level rise which triggers frequent avulsion processes (Fernández & Dabrio, 1985; Henares *et al.*, 2014, 2016a, b; Viseras *et al.*, 2018).

4.6.2. Implications for subsurface prediction

The high-resolution analysis of GR log trends, corroborated by both outcrop and core data, strongly suggests that the predominant funnel-shaped GR response reflects proximal, medial and distal crevasse-splay deposits (Fig. 4.9b). This funnel-shape reflects the progradation of the overbank facies in successive flood events (*sensu* Mjøs *et al*., 1993; Miall, 1996; Emery & Myers, 1996; Cant, 2002). An overlying fining-upward trend, with a distinctive bell-shaped GR response, marked by higher API values, and related to medial and/or distal crevasse-splay deposits, is interpreted to record amalgamation of crevasse-splay complexes (Fig. 4.8b and Fig. 4.9b). The crevasse channel deposits show a bell-shaped GR trend associated with a characteristic vertical lithofacies succession (St–Sr–Sw).

A high-resolution analysis of dip tadpoles, grouping those with a sedimentological significance, corroborated by both outcrop and core data, is also useful in reducing the uncertainty in sandstone depositional trends (Donselaar & Schmidt, 2005).

Brekke *et al.* (2017) also recognize the shallow-to-steep-to-shallow dip pattern in point bar deposits in the McMurray Formation of Alberta. This pattern of change in dip angles reflects epsilon cross-bedding (Allen, 1983) and is characteristic of lateral accretion surfaces in point bars. Donselaar & Schmidt (2005) interpreted the azimuth rotation (clockwise or anticlockwise) as the expression of the gradual downstream migration of the meander bend. The azimuth rotation in this case is poorly developed. This can be explained if point bar migration occurred mainly by expansion, where the bend apex migrates transversely away from the channel-belt axis (Ghinassi *et al*., 2014; Ielpi & Ghinassi, 2014). Tadpole sets with random azimuth and dip angles, between 5° and 25°, represent the foresets of trough cross-bedding (Donselaar & Schmidt, 2005; Viseras *et al*., 2018; Yeste *et al*., 2018).

Donselaar & Schmidt (2005) have also identified tadpole patterns with unidirectional azimuths and very low dip angles for crevasse-splay deposits. Keeton *et al.* (2015) highlighted the difficulty in picking tadpoles in crevasse-splay deposits, reflecting the convoluted and ripple-laminated nature of the deposits, but recognized low angle dips and a high dispersion in dip azimuths. The high-resolution analysis of tadpoles in this study reveals patterns associated with the different segments of the crevasse-splay lobes (Fig. 4.11): (i) tadpoles with randomly distributed azimuth and dip angles between 5° and 25° associated with trough cross-bedding in MSFA 5; (ii) tadpoles with unidirectional azimuths and low-dip angles associated with horizontal and ripple-laminated sandstones in MSFA 6; (iii) randomly distributed dip angles and azimuths and unidirectional azimuths associated with low dip angles corresponding respectively to syn-

sedimentary deformation structures and ripple-laminated sandstones, associated with MSFA7; and (iv) unidirectional azimuths and low dip angles between mud rock laminae in MSFA 8.

4.6.3. Implications for reservoir connectivity and modelling

The identification of amalgamated crevasse-splay complexes is of considerable importance because they can be considered potential hydrocarbon reservoirs (Van Toorenenburg *et al*., 2016). Crevasse-splay deposits connect to the main channel body, which typically constitutes the best reservoir (Fielding & Crane, 1987; Pranter *et al*., 2008). Proximal crevasse-splay and crevasse channel deposits comprise similar lithofacies, in addition to being directly connected to the main channel. Amalgamated crevasse-splay complexes can also be used to estimate the dimensions of the main channels in intervals where the channel body itself is not directly penetrated by a well. The thickness of the main channel will be similar to that of the amalgamated crevasse-splay complexes (Van Toorenenburg *et al*., 2016). Thus, a detailed study of the proposed facies associations in core, and a high-resolution study of both GR log response and dip tadpole patterns would lead to a correct identification of depositional sub-environments, sediment body geometries, dimensions, orientations and thus a better estimate of net reservoir volume.

Recent studies related to the petrophysical and diagenetic characteristics of the M-S Unit (Henares *et al*., 2014, 2016a, b) have established a strong relationship between Open Porosity (OP), permeability and early diagenetic processes. The latter are strongly related to depositional environments and thus the distribution of facies associations.

Although there is no systematic petrophysical and diagenetic study for these crevasse-splay deposits (MSFA 5 to MSFA 8), it is reasonable to assume the same relationships between OP, permeability and early diagenetic processes. Henares *et al*. (2014) recognized 4.6% of gypsum cement associated with the crevasse-splay deposits in the M-S Unit. This cement occurs as poikilotopic crystals occluding primary porosity. These authors also report values of 15.6% of OP and 2mD of permeability for one sample of crevasse-splay deposits in the M-S Unit. These values reflect the pervasive influence of the gypsum in reducing permeability by occlusion of pore throats although subsequent patchy cement dissolution does act to generate the poorly connected secondary pores mentioned previously.

Henares *et al*. (2016a, b) also conclude that there is a good match between reservoir properties and facies distribution. This relationship is a direct consequence of the primary

control exerted by depositional features, notably detrital clay abundance and distribution, on diagenetic evolution and thus on reservoir quality. As such, permeability will most probably be higher in those facies associations where grain coating clays are well-developed and significant primary porosity preserved. Conversely, those facies associations characterized by pervasive gypsum cement will show the poorest reservoir quality. This suggests that even the medial crevasse-splay facies (MSFA 7) could have favourable petro-physical characteristics, and thus be considered a potential hydrocarbon reservoir.

Through the combined integration of both outcrop and subsurface datasets, this study offers a new quantitative conceptual model for low gradient, meandering, fluvial systems, with key geometric and sediment body dimension data, which can be used in the elaboration of more robust numerical models. This is especially valuable for the crevasse-splay/floodplain elements which, otherwise, are not so well-understood and may often act as a secondary reservoir. Such data can be used directly as input in reservoir modelling of similar subsurface systems. Quantitative conceptual models are a valuable tool in geostatistical modelling, especially when it comes to planning modelling strategies as well as producing training images. The detailed study of paleosols and overbank deposits, and their integration into geostatistical modelling, also provides information on the position of the channel (main reservoir) in low net-to-gross reservoirs (Yeste *et al.*, 2019b). Based on the OBO (Outcrop/Behind Outcrop) methodology this study suggests well-calibrated criteria for recognizing the key facies elements, from purely subsurface wireline log and core data; so that if key facies can be correctly identified in the subsurface, the outcrop geometry data can subsequently be applied as input for modelling, as highlighted in Chapter 8.

4.6.4. Limitations of the predictive conceptual model

Although the potential applicability of the presented conceptual model to similar systems of different age is self-evident (Burns *et al.*, 2017; Gulliford *et al.*, 2017; Varela *et al.*, 2019), it is nonetheless prudent to indicate that it should not be considered as a general predictive model. In this respect, there are a number of key limitations associated with the conceptual model, related to three main factors: (i) scale of the fluvial system; (ii) humidity and paleoclimatic conditions; and (iii) the sequence stratigraphic framework.

The first factor is related to the scale of the fluvial system; especially the main channel from which the overbank deposits are derived. Thus, in fluvial systems dominated by a main channel with larger dimensions (depth and width) than those presented in this example,

overbank deposits may be more extensively developed. However, the dimensional ratios of the different facies zones and their relationship with the distance to the main channel should still result in patterns similar to those established in the conceptual model.

The second limiting factor is related to the humidity and paleoclimatic conditions of the floodplain. Paleosol analysis suggests a seasonal climate reflected in the development of Vertisol-like profiles in distal floodplain deposits. This was most likely promoted by seasonal rainfall and/or variations in fluvial discharge (Driese *et al.*, 2000; Retallack, 2001; Varela *et al.*, 2012). The presence of swamp deposits with preserved organic matter, and both the gley mottles and rhizoliths of the Vertisol-like paleosols evidence seasonal ponding in the studied M-S Unit. Consequently, the overbank flow is slowed by the presence of a still-water body (Bristow *et al.*, 1999). These floodplain conditions would tend to favour a reduced areal extent and lobe-shape geometry of the crevasse-splay deposits compared to those accumulating on a dry floodplain. In addition, a dry floodplain would be characterized by a more gradual transition between facies associations and also a reduced thickness for the crevasse-splay lobes, in comparison with the presented conceptual model.

Finally, it is important to consider the position of the fluvial system in the basin and the sequence stratigraphic framework in order to apply the conceptual model. The M-S Unit in the study area was most likely located on a very low gradient plain in the distal part of drainage system (Dabrio *et al.*, 2005; Viseras *et al.*, 2011, 2018; Henares *et al.*, 2014, 2016a, b). This is evidenced by the presence of wave reworking and trace fossils towards the top of channel and point bar deposits. The development of Entisol-like paleosols in the crevasse-splay deposits may also indicate high sedimentation rates and avulsion, which would inhibit the development and maturity of soils in the studied M-S Unit. As such, it seems reasonable to assume that the conceptual model presented here could successfully be applied to high sinuosity fluvial systems located in the distal part of drainage system within a framework of rising base level, which would tend to favour the development of a frequently flooded floodplain (Bristow *et al.*, 1999).

4.7. Conclusions

Ten facies associations (including core and wireline log characteristics; Fig. 4.2, Fig. 4.5 and Fig. 4.11) characterize the four geobodies recognized in the mudstone–sandstone unit of the TIBEM (Triassic Red Beds of Iberian Meseta): (i) channelized sandstone bodies consisting of three facies associations (main channel, chute channel and crevasse channel); (ii) asymmetrical

sigmoidal-shaped sandstone bodies consisting of two facies associations (point bar and scroll bar); (iii) lobe-shaped to sheet-like sandstone bodies consisting of three facies associations (proximal crevasse-splay, medial crevasse-splay and distal crevasse-splay); and (iv) sheet-like mudstone bodies consisting of two facies associations (distal floodplain and swamp).

Wireline log characteristics, constrained by Outcrop/Behind Outcrop (OBO) methodologies, allow us to distinguish, in subsurface, the four elements that constitute the crevasse bodies (this paper and others here cited) along a channel-floodplain cross-section: crevasse channel and proximal, medial and distal crevasse-splays. The Gamma Ray (GR) log is characterized by a fining-upward trend and a sharp base for crevasse channel deposits, whereas proximal, medial and distal crevasse-splay deposits are characterized by a coarsening/cleaning-upward trend and a sharp top. The GR API values (maximum, minimum and mean) increase from proximal to distal deposits. Distal floodplain and swamp deposits, in contrast, are characterized by a serrate GR profile. Crevasse channels are also characterized by randomly distributed paleocurrent azimuths and foreset dips whereas proximal crevasse-splay deposits are characterized by unidirectional azimuths and low dip angles. Medial crevasse-splay deposits are characterized by sets of either randomly oriented paleocurrent azimuths and dips, or unidirectional azimuths and low dip angle tadpole patterns. For distal crevasse-splay deposits the bounding surfaces (bottom and top) are easily distinguished whilst unidirectional azimuths and very low dip angle tadpoles occur locally.

A new outcrop analogue dataset for meandering, low gradient fluvial systems, including key geometric and sediment body dimension data, is presented in this chapter. This is especially valuable for the crevasse-splay/floodplain elements which, otherwise, are not so well-known and may often act as a secondary reservoir. A predictive model generated from outcrop and subsurface data allows to estimate, with some confidence, how far a well drilled through crevasse-splay/floodplain deposit might be from a main channel and thus potential primary reservoir, a prediction of significant value in exploration and appraisal. Such data can also be used directly as both hard and soft input in reservoir modelling of similar subsurface systems during the development of a discovery (see Chapter 8).

The use of OBO methodology also allows to establish a well-constrained link between recently refined outcrop facies models of channel-overbank systems and channel-crevasse sandstone reservoirs in the subsurface.

CHAPTER 5:

Sandstone Unit: Low-sinuosity fluvial system

Abstract   The integrated application of advanced visualization techniques – validated against outcrop, core and Gamma Ray log data – was found to be crucial in characterizing the spatial distribution of fluvial facies and internal permeability baffles to a centimetre-scale vertical resolution. An outcrop/behind outcrop workflow was used, combining the sedimentological analysis of a perennial deep braided outcrop with ground-penetrating radar profiles, behind outcrop optical and acoustic borehole imaging, and the analyses of dip tadpoles, core and Gamma Ray logs. Data from both the surface and subsurface allowed the recognition of two main geobodies – channels and compound bars – and within the latter to distinguish between the bar head and tail and the cross-bar channel. On the basis of a well-constrained sedimentological framework, a detailed characterization of the Gamma Ray log pattern in the compound bar allowed several differences between the geobodies to be identified, despite a general cylindrical trend. A high-resolution tadpole analysis showed that a random pattern prevailed in the channel, whereas in the bar head and tail, the tadpoles displayed characteristic patterns that allowed differentiation. The ground-penetrating radar profiles aided the 3D reconstruction of each geobody. Thus, the application of this outcrop/behind outcrop workflow provided a solid database for the characterization of reservoir rock properties from outcrop analogues.

5.1. Introduction

Exploration in fluvial environments may be more challenging than in other continental environments due to their potential 3D complexity in terms of architecture, the sand to mud ratio and grain size distribution (Miall, 1985; Brayshaw *et al.,* 1996; Einsele, 2000; Sharp *et al.,* 2003; Pranter & Sommer 2011; Pranter *et al.,* 2014; Allen & Pranter, 2016). Each scale of heterogeneity within fluvial deposits has a different expression, both from the proximal to distal facies and laterally, showing a specific interaction between the diagenetic processes and depositional facies.

Braided stream systems form some of the world's largest sandstone reservoirs and, at the simplest level, can be considered as largely homogenous relative to other fluvial deposits. In addition, they are also typically coarse-grained and relatively clay-free, a response to the high energy flow conditions characteristic of these systems (e.g. Cant, 1983; Atkinson *et al.*, 1990; Martin & Church, 1996; Miall, 1996, 2006; Bjorlykke & Jahren, 2010; Pranter *et al.,* 2014). Some examples of braided-type reservoirs include the Trias Argilo-Gréseux Inférieur Formation (Berkine-Ghadames Basin, Algeria; e.g. Rossi *et al.*, 2002), the Williams Fork Formation (Piceance Basin, Colorado, USA; e.g. Pranter *et al.*, 2014) and the Wolfville Formation (Fundy Basin, Canada; Leleu *et al.*, 2009). In general, they display a high continuity down the depositional dip, parallel to the channel axis (i.e. the base of the channel), and a low continuity perpendicular to the axis (i.e. to the margins) (Atkinson *et al.,* 1990; Bridge & Lunt, 2009). Nevertheless, these sheet-like sandstone bodies may present heterogeneities at several scales that the affect hydraulic conductivity. At the mesoscale (according to Weber, 1986), laterally discontinuous shale intervals may form as abandoned/slough channel fills, with thin intra-channel drapes and inter-channel muds representing potential baffles to vertical fluid flow (Miall, 1985; Atkinson *et al.*, 1990). The original, highly permeable layers (i.e. thief zones) related to laterally continuous clast-supported or sand-matrix-supported conglomerates and coarse-grained intervals must also be considered as part of the internal heterogeneity (Miall, 1985, 2006; Atkinson *et al.,* 1990).

The estimation of the dimensions and spatial distribution of the architectural elements in fluvial reservoirs from 1D core and well data is a well-known problem in reservoir modelling. In this sense, outcrop analogue studies represent a powerful tool, supplementing sparse subsurface data with outcrop-derived measurements (Miall, 1990; Kokureck *et al.*, 1991; Tyler & Finley, 1991; Wizevich, 1991; Yoshida *et al.*, 2001; Ajdukiewicz & Lander, 2010; Scott *et al.*, 2013; Pranter *et al.*, 2014; Franke *et al.*, 2015). Only by integrating both sources of information

– outcrop and subsurface – can an appropriate database be properly constructed for the reservoir geometry, dimensions and attributes, in order to generate realistic models that include both high-resolution facies interpretations and rock heterogeneities (Alpay, 1972; Kokureck *et al.,* 1991; Ambrose *et al.,* 1991; Miall, 1991; Alexander, 1992; Kostic & Aigner, 2007; Van den Brill *et al.*, 2007; Calvache *et al.,* 2010; Ozkan *et al.,* 2011; Trendell *et al*., 2012; Ghinassi *et al*., 2014; Colombera *et al*., 2014; Pranter *et al*., 2014; Klausen & Mork, 2014; Shimer *et al*., 2014).

This study aimed to determine the key criteria in the subsurface recognition and characterization of the geobodies and their associated potential permeability barriers identified in braided fluvial systems. The studied example consists of a Triassic braided system considered as an outcrop analogue for other hydrocarbon-productive reservoirs, such as the Algerian Trias Argilo-Gréseux Inférieur (Rossi *et al.,* 2002; Dabrio *et al*., 2005; Viseras *et al*., 2011b; Henares *et al*., 2011, 2016; Viseras *et al*., 2018). For this purpose, the integrated outcrop/behind outcrop characterization workflow, described in Chapter 3, was applied in this study, combining different imaging techniques – namely ground-penetrating radar (GPR), acoustic borehole imaging (ABI) and optical borehole imaging (OBI) – validated against outcrop, core and well log data. The integration of different data sources (i.e. surface and subsurface) lead to the development of more robust reservoir models which may improve the quantification and correlation of heterogeneities within this type of fluvial reservoir.

The results of this chapter have been published in the Special Publication volume *"River to Reservoir: Geoscience to Engineering"* of Geological Society of London:

Yeste, L.M., Henares, S., McDougall, N., García-García, F. and Viseras, C. (2018). Towards the multi-scale characterization of braided fluvial geobodies from outcrop, core, georradar and well logs data. In: River to Reservoir: Geoscience to Engineering (Eds Corbett, P., Owen, A., Hartley, A., Pla-Pueyo, S., Barreto, D., Hackney, C. and Kape, S.), GSL Special Publication, 488. https://doi.org/10.1144/sp488.3.

5.2. Data distribution

Two main outcrops (Outcrop North and Outcrop South), extending to a total length of 2500 m and with a total area   >0.1927 km^2 were selected for the outcrop-based facies analysis, in terms of geometry, internal structure, sequence trends and the spatial relationship between the main geobodies. Three Digital Outcrop Models (DOM) were also created by photogrammetry with an RPAS to complete the dataset of outcrop-derived measurements (see Chapter 3 for details of the DOM methodology).

In the studied example, six slim-hole (85 mm) behind outcrop wells allowed subsurface characterization based on data from both wireline logs and cored intervals. From north to south, these wells are (Fig. 5.1a): the four wells K2L1–4, located in Outcrop North, with 16, 17, 15 and 7 m of core, respectively, and an interwell spacing of 52, 7 and 8 m; K2P2, located in Outcrop S-2 with 20 m of cored section; and K2P1, located in Outcrop S-3 with 42 m of core. The interwell spacing between K2P2 and K2P1 was 296 m.
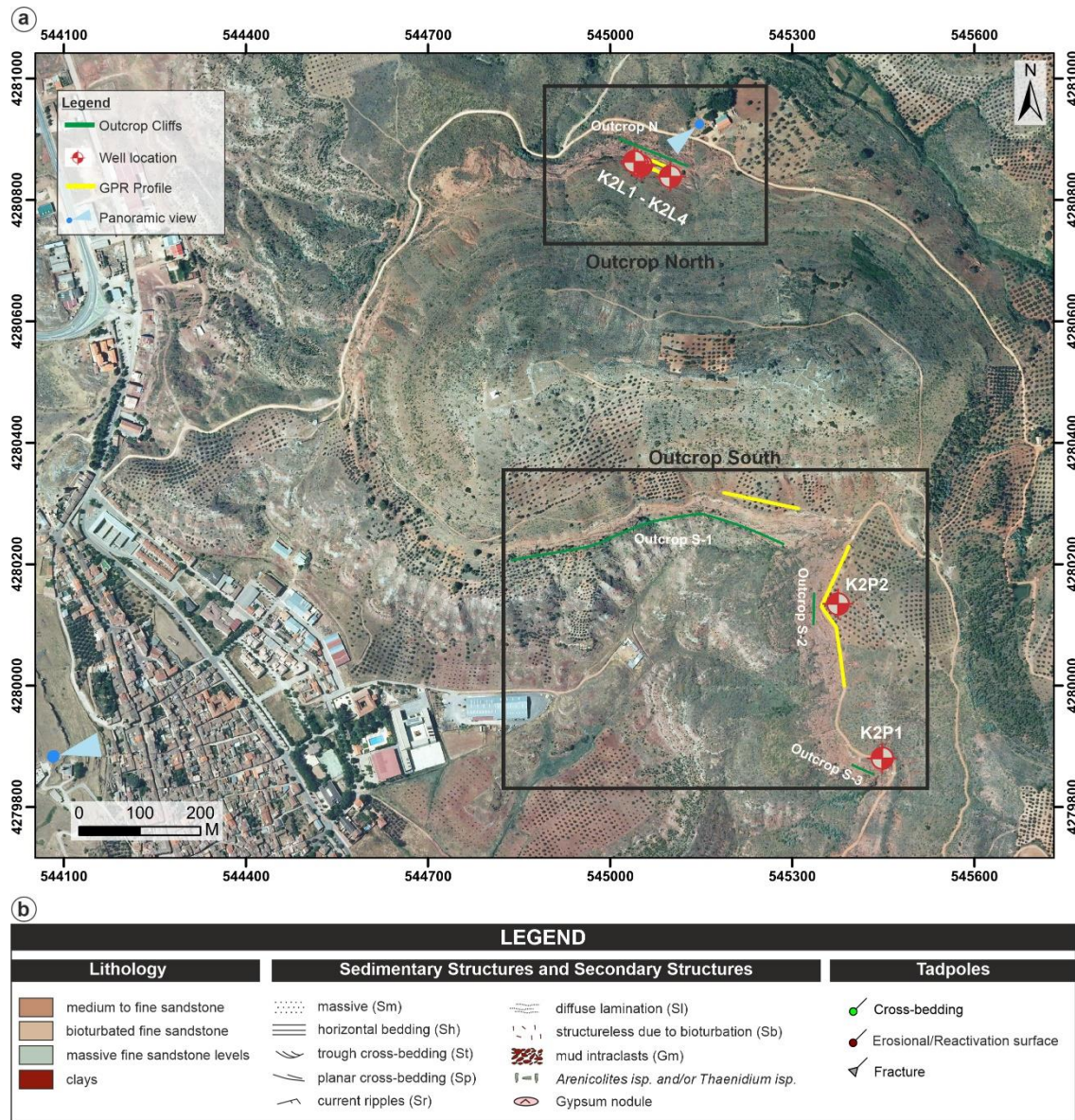
Fig 5.1. (a) Geographical location of the studied outcrops. Well and GPR profile locations are also shown. **(c)** Global legend for the lithological, sedimentary structure and tadpole logs used in this chapter.

Core slabbing was carried out to enhance the visibility of sedimentary features on the core surface and to allow the identification of the main lithofacies. The wireline log data included a Gamma Ray log and borehole imaging from optical and acoustic televiewers. Dip tadpoles,

picked from the image logs, together with Gamma Ray pattern analyses, provided data on the spatial distribution, orientation and dip of the main sedimentary surfaces and structures. In addition, three GPR profiles were acquired, covering a total of 443 m of outcrop length. In Outcrop North and Outcrop S-2, profiles 70 and 248 m long, respectively, were acquired with a shielded 200 MHz antenna that limited the penetration to 10 m below the surface, but provided high-resolution images of the internal structure of the geobody. In Outcrop S-1, a 125 m long profile was acquired with a shielded 40 MHz antenna that increased the penetration depth to 30 m below the surface.

5.3. Geometrical description and fluvial style of the Sandstone Unit

The Sandstone Unit (S Unit) is distinguished by an irregular base, eroding the underlying M-S Unit, and an undulatory or scoured top. This Unit is characterized by a high net-to-gross (sand:mud ratio of 95:5) and consists of a laterally extensive (hundreds of metres along strike and/or along depositional dip) tabular sandstone package up to 20 m thick.

The studied sandstone package was divided between two main outcrops (Fig. 5.1a): North and South. Outcrop North is represented by only one exposure with 130 m of lateral extension and an east–west orientation. Outcrop South includes three different sections (S-1, S-2 and S-3) with 350, 40 and 50 m of lateral extension and east–west, north–south and NNW–SSE orientations, respectively. These changes in orientation of the different exposures throughout the sedimentary deposit allow 3D tracing of the entire sandstone package as well as of the main elements (geobodies) identified within it.

The internal organization of this tabular sandstone package is characterized by the stacking of several small-scale thinning-upward sequences, each of which shows, from base to top: upper flow regime parallel lamination; cross-bedding and cross-lamination; and lower flow regime parallel lamination (Dabrio & Fernández, 1986; Fernandez *et al.*, 2005; Viseras & Fernández, 2010)

From the perspective of a north–south panoramic view, two main elements are distinguished within the sandstone package (Fig. 5.2a): two massive zones at both extremes of the outcrop (section S-1 and S-3), where internal erosional scours define irregular concave-up surfaces; and a central zone (section S-2) characterized by westerly-inclined mega-cross-bedding (Figs. 5.2a-b). These two well-differentiated zones correspond to the typical architectural elements or geobodies identified in deep perennial braided systems: channels (termed SFA 1;

sections S-1 and S-3) and the compound bar (termed SFA 2; section S-2; Fig. 5.2a; Ashmore, 1982; Cant & Walker, 1978).
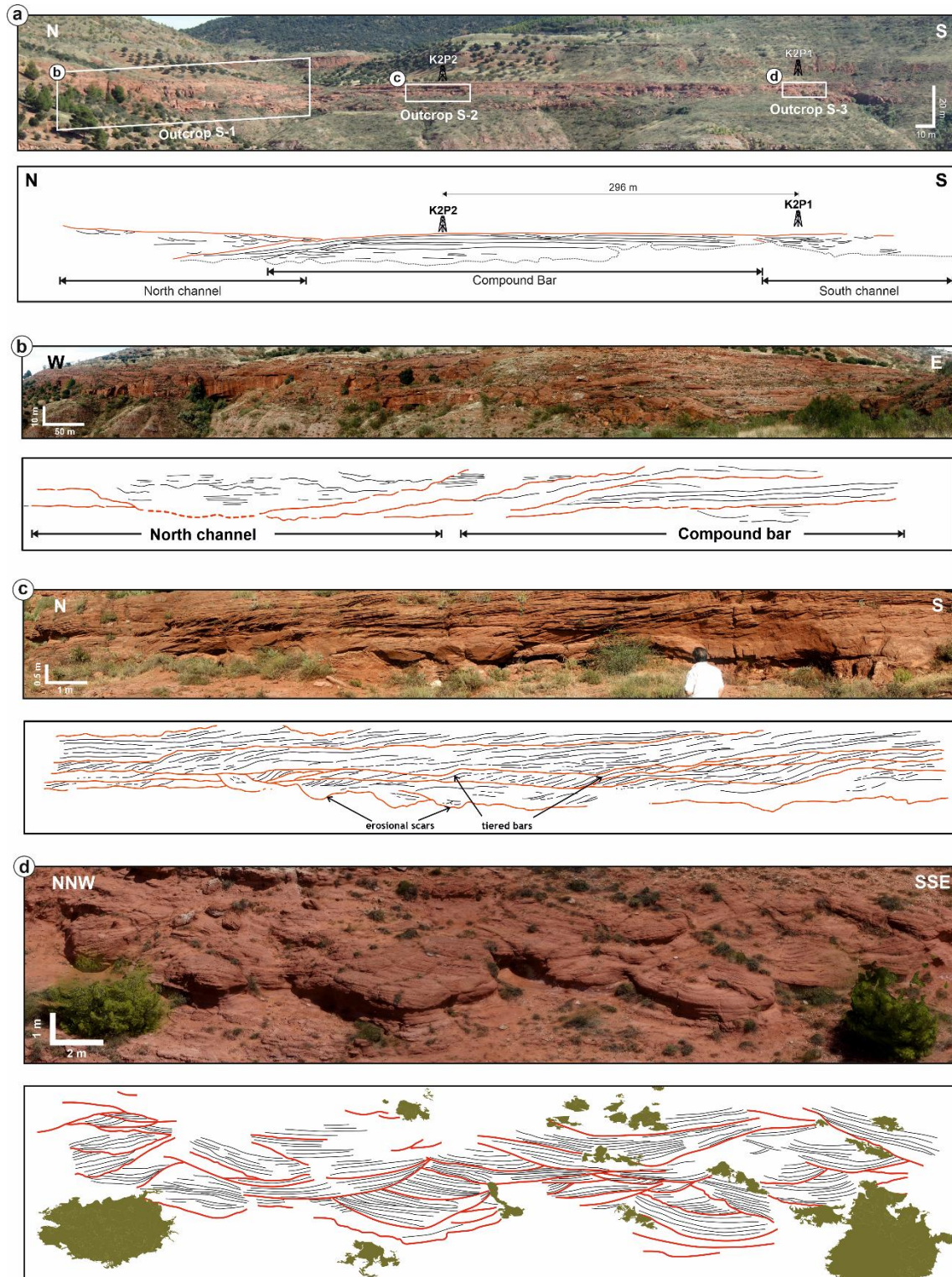
Fig. 5.2. (a) North-south panoramic view showing the three different exposures comprising Outcrop South, labelled from north to south, as outcrops S-1 to S-3, with the facies interpretation below. The location of wells K2P1 AND K2P2 is also indicated. **(b)**, **(c)**, **(d)** Close-up views of the different sections of Outcrop South with a more detailed interpretation of the depositional architecture and internal sedimentary structure.
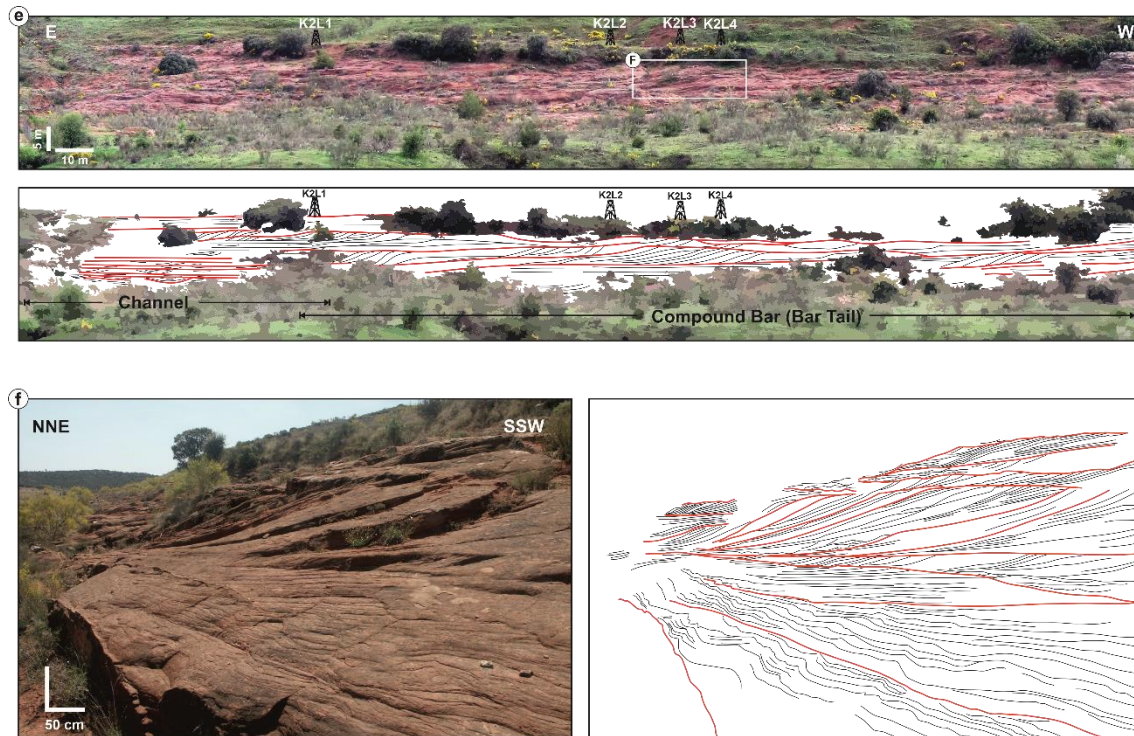
Fig 5.2. *Continued*. **(e)** East-west panoramic view showing Outcrop North with the facies interpretation below. The location of Well K2L1-4 is also indicated. **(f)** Close-up view in outcrop of the internal sedimentary structure of the compound bar in Outcrop North.

5.4. Multi-approach description of geobodies

The two geobodies identified in the studied sandstone (the channel and compound bar) are characterized on the basis of their main features in the outcrop, core, wireline log and GPR data. This includes: outcrop-derived observations and measurements in digital outcrop models; the definition of lithofacies in the cores (Table 4.1); Gamma Ray pattern analysis; dip tadpole trend analysis; and the description of key surfaces and radar facies in the GPR profiles.

5.4.1. Channel (SFA 1)

Outcrop features

Two channels have been identified in outcrop: the north channel and the south channel (Fig. 5.2a). The north channel is 20 m thick with a lateral extent of 300 m, measured perpendicular to the main flow direction, and an internal fining- and thinning-upwards trend. Above a flat base, with an upper flow regime parallel horizontal lamination, megaripples are stacked hierarchically into several smaller thinning-upwards sequences separated by clay drapes (Figs. 5.2b, d), which laterally extend over the full cross-section of the channel (Fig. 5.3a). The

south channel shows similar dimensions (18 m thick; 230 m lateral extension) and sedimentary features compared to the north channel.
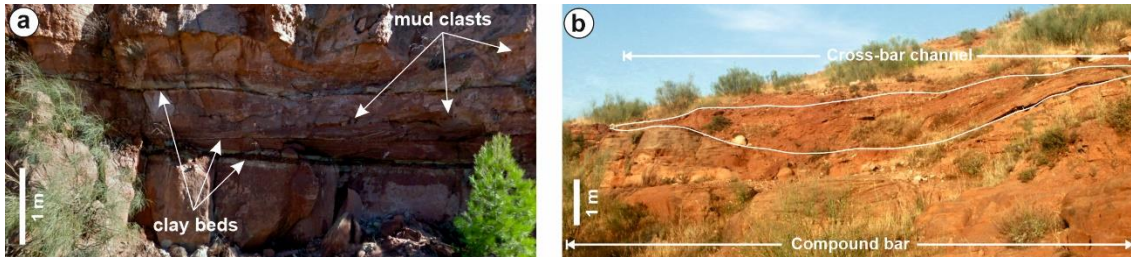
Fig. 5.3. (a) Potential permeability barriers within the channel geobody represented by laterally continuous clay drapes. **(b)** Potential permeability baffles in the compound bar geobody represented by laterally limited cross-bar channel deposits.

Core features

This geobody has only been targeted in Well K2P1 through 17.8 m of fully recovered core. At the base, the succession starts with a conglomeratic layer of centimetre- to decimetre-scale clay intraclasts (Lithofacies Gm; Fig. 5.4a). This basal layer is overlain by a thinning-upwards interval comprising beds of medium- to fine-grained sand, with faint horizontal lamination (Lithofacies Sh) or lacking any clearly visible sedimentary structures (Lithofacies Sm; Fig. 5.4d). Two clay intraclast-rich layers can also be observed towards the top of this interval (Fig. 5.4ac). The succession is capped by several thinning-upwards sandstone packages, characterized by trough cross-bedding (Lithofacies St; Fig. 5.4ef) alternating with intervals of current ripple cross-lamination (Lithofacies Sr) overlain by mudstone layers with horizontal lamination (Lithofacies Fl).

Well log data

The Gamma Ray in Well K2P1 shows a generally cylindrical pattern (Serra and Surpice, 1975; Emery and Myers, 1996; Rider, 2000; Selley, 2004) with values ranging from 22 API to 128 API and a mean of 69 API, (Fig. 5.4a). Within this broad framework, higher resolution observations show that the lower part of the section (from 23 up to 13 m depth) shows a funnel pattern at the base, which evolves to a cylindrical pattern. From 13 m to 9 m depth upwards, the Gamma Ray log shows several packages defined by funnel patterns showing an increase in API values before becoming cylindrical again. At high resolution, this final cylindrical interval can be divided into a funnel plus a bell pattern.

Fig. 5.4. Outcrop/behind outcrop characterization of the channel geobody, including data from Gamma Ray logs, optical borehole imaging, outcrop-derived facies analysis and core descriptions: **(a)** Well K2P1 composite showing the Gamma Ray, the core description, the optical borehole image, dip tadpole analysis and the location of core photographs (c, d and e); **(b)** Detailed outcrop interpretation of S-3 showing trough cross-bedding (Lithofacies St); **(c)** Core view of the clay intraclast-rich layers and the trough cross-bedding (Lithofacies St); **(d)** Core view of the massive lithofacies (Sm); **(e)** Similar trough cross-bedding (Lithofacies St) to that shown in outcrop image **(b)**; **(f)** Close-up view in core of the trough cross-bedding described in outcrop image **(b)**. See Fig. 5.1b for legend.

A total of 67 dip tadpoles were picked, based on the OBI and ABI logs, showing a significant, near random dispersion in azimuth values, ranging from N1E to N350E. However, within this framework a predominant paleoflow direction, between N20E and N80E with a mean azimuth of N46E, can still be identified (Fig. 5.4a; see also Fig. 5.8).

GPR features

In the lower part of the channel geobody (Fig. 5.7c), the reflectors are parallel or sub-parallel and locally discontinuous or chaotic. In the central part of the profile the reflectors show lower amplitudes, with a structure that varies from sub-parallel with a steep angle to a more chaotic pattern. Towards the upper part of this geobody, mounded (wave reflection) and sub-parallel reflectors are observed, interrupted by others with a concave-up shape.

5.4.2. Compound bar (SFA 2)

Outcrop features

The compound bar geobody is represented by a 20 m thick, continuous (500 m wide) and extensive (up to 1000 m parallel to the main paleocurrent) sandstone layer (Fig. 5.2a). A decimetre-thick set of planar cross-bedding is observed towards its base, overlain by several stacked, thinning-upwards sets of planar and trough cross-bedding (Fig. 5.2c). Above this geobody, an 8 m long and 1 m thick channel-shaped body is recognized, consisting of very fine-grained to silty sediments (Lithofacies Sr-Fl). This channel-shaped body is interpreted as a cross-bar channel (Fig. 5.3b). In Outcrop North (Fig. 5.1 and Fig. 5.2e), the section is characterized by the stacking of minor sigmoidal packages constructed by the hierarchical accretion of bedforms (dunes and megaripples) (Fig. 5.2f).

Core features

In the compound bar geobody, best developed in Well K2P2 (Fig. 5.5), the succession begins with a massive sandstone (Lithofacies Sm) intercalated, at a depth of 18 m, with a centimetre-scale, clay intraclast-rich layer (Fig. 5.5a, e). Horizontal lamination (Lithofacies Sh) is observed from above this clay intraclast lag upwards, locally with intercalated clayey levels (e.g.
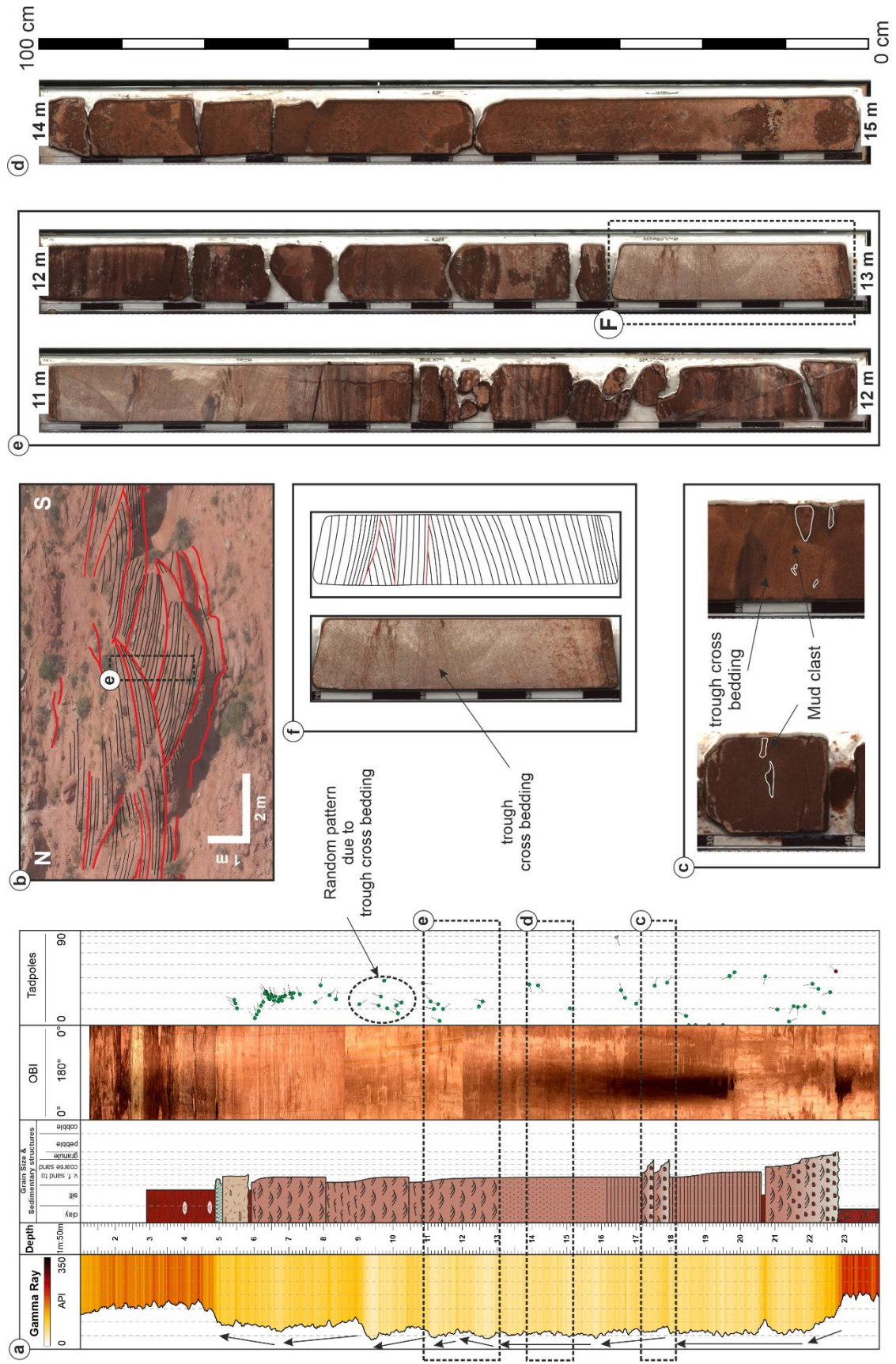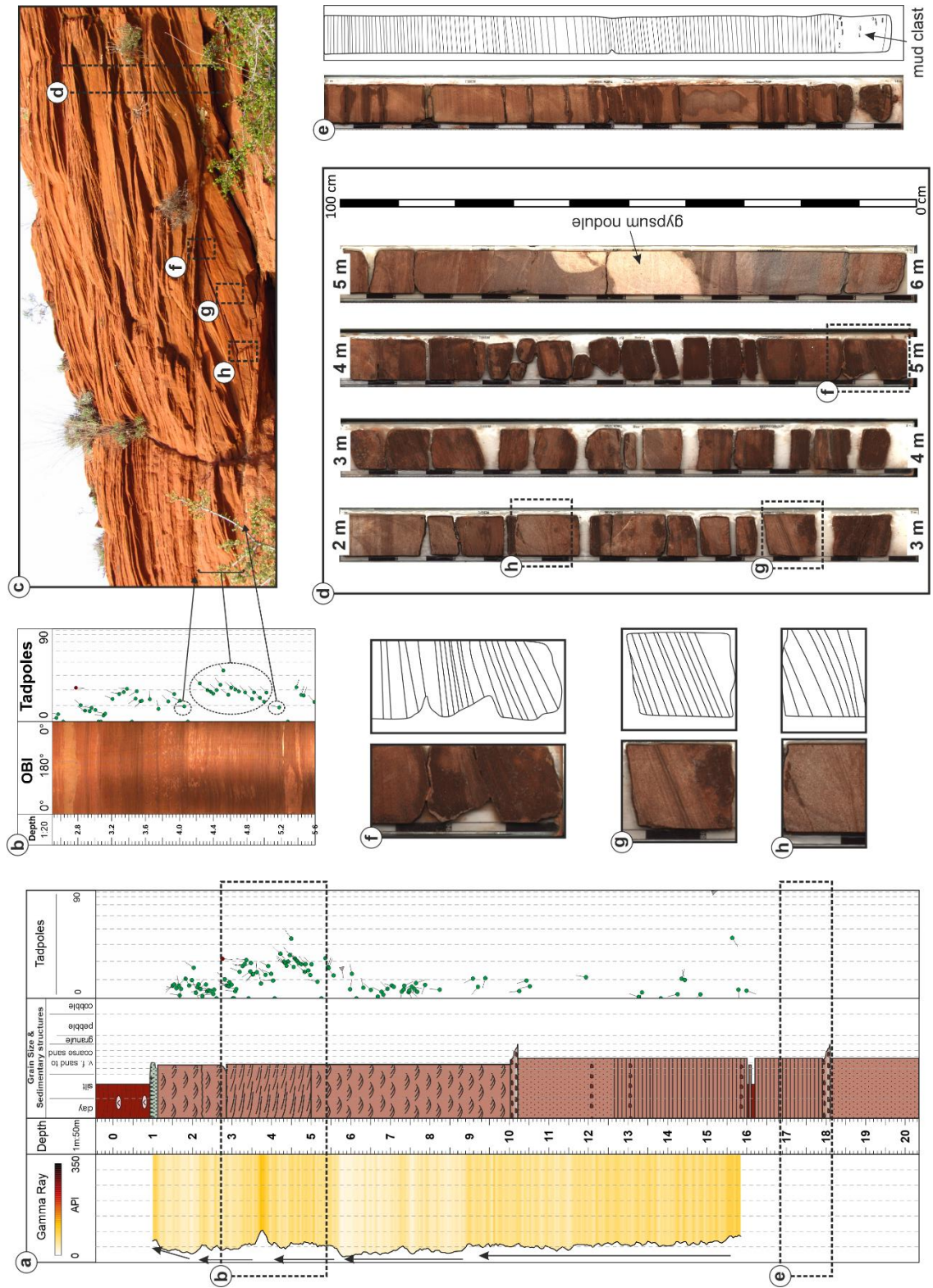
Fig. 5.5. Outcrop/behind outcrop characterization of the compound bar geobody, including data from the Gamma Ray log, optical borehole imaging, outcrop-derived facies analysis, and core descriptions: **(a)** Well K2P2 composite showing the Gamma Ray log, the core description, dip tadpole analysis and locations of OBI interval (b) and core photograph/description (e); **(b)** Close-up view of the optical borehole image and tadpole patterns between 3 and 5 m depth and their correlation with outcrop features in image **(c)**; **(c)** Detailed outcrop interpretation of S-2 showing the planar cross-bedding; **(d)** Core view of the planar cross-bedding identified in outcrop; **(e)** Core view of the horizontal bedding described in outcrop; **(f)**, **(g)** and **(h)** Close-up core views of some details of the planar cross-bedding identified in outcrop in image **(c)**. See Fig. 5.1b for legend.

at 16 m depth; Lithofacies Fl). A similar interval of massive sandstone (Lithofacies Sm) is then recognized, starting at 12.5 m depth, and capped by a centimetre-scale thin clay intraclast-rich layer. Above this, trough cross-bedding (Lithofacies St) becomes the dominant sedimentary structure up to 5 m depth, where planar cross-bedding (Lithofacies Sp) appears (Fig. 5.5ad). Lithofacies Sp is intercalated toward the top with a centimetre-scale silty layer with current ripple lamination (Lithofacies Sr-Fl) at 2.75 m depth. Overlying this silt layer, trough cross-bedding (Lithofacies St) is again recognized, grading upwards into clay. In this last cross-bedded interval, several reactivation surfaces, lined with clay intraclast lags, have been described.

This geobody has been also characterized in another outcrop (Outcrop North) and in different wells (K2L1–4; Fig. 5.1a) corresponding to a position closer to the channel (Fig. 5.6). In this position, a different facies association is observed, beginning with trough cross-bedding (Lithofacies St) and evolving upwards to horizontal bedding (Lithofacies Sh) and subsequent planar cross-bedding (Lithofacies Sp). Several repetitions of the gradation from Lithofacies Sh to Sp are observed in which the dip angle of the layers increases gradually and then decreases again (Fig. 5.6b and c). At the top, this facies association is truncated by an erosive surface overlain by very fine-grained sandstone with current ripple lamination (Lithofacies Sr) and intercalated clays (Lithofacies Fl) which are interpreted as the infill of a cross-bar channel (Fig. 5.6b).

Well log data

The Gamma Ray log in Well K2P2 shows a well-developed cylindrical pattern (Fig. 5.5a) with minor irregularities (e.g. values decrease from 9 to 6 m depth and, at 3.75 m depth, a decimetre-thick interval with higher API values is recognized). Well K2P2 shows values ranging from 16 to 110 API with a mean value of 51 API. In Well K2L1–4 (Fig. 5.6b), the Gamma Ray log also shows a general cylindrical pattern, but this can be sub-divided into several minor cycles of bell and funnel patterns. Towards the top, the general cylindrical trend is interrupted by a decimetre-thick interval characterized by higher API values. Well K2L1-4 shows GR values ranging from 24 API to 157 API with a mean of 63 API.
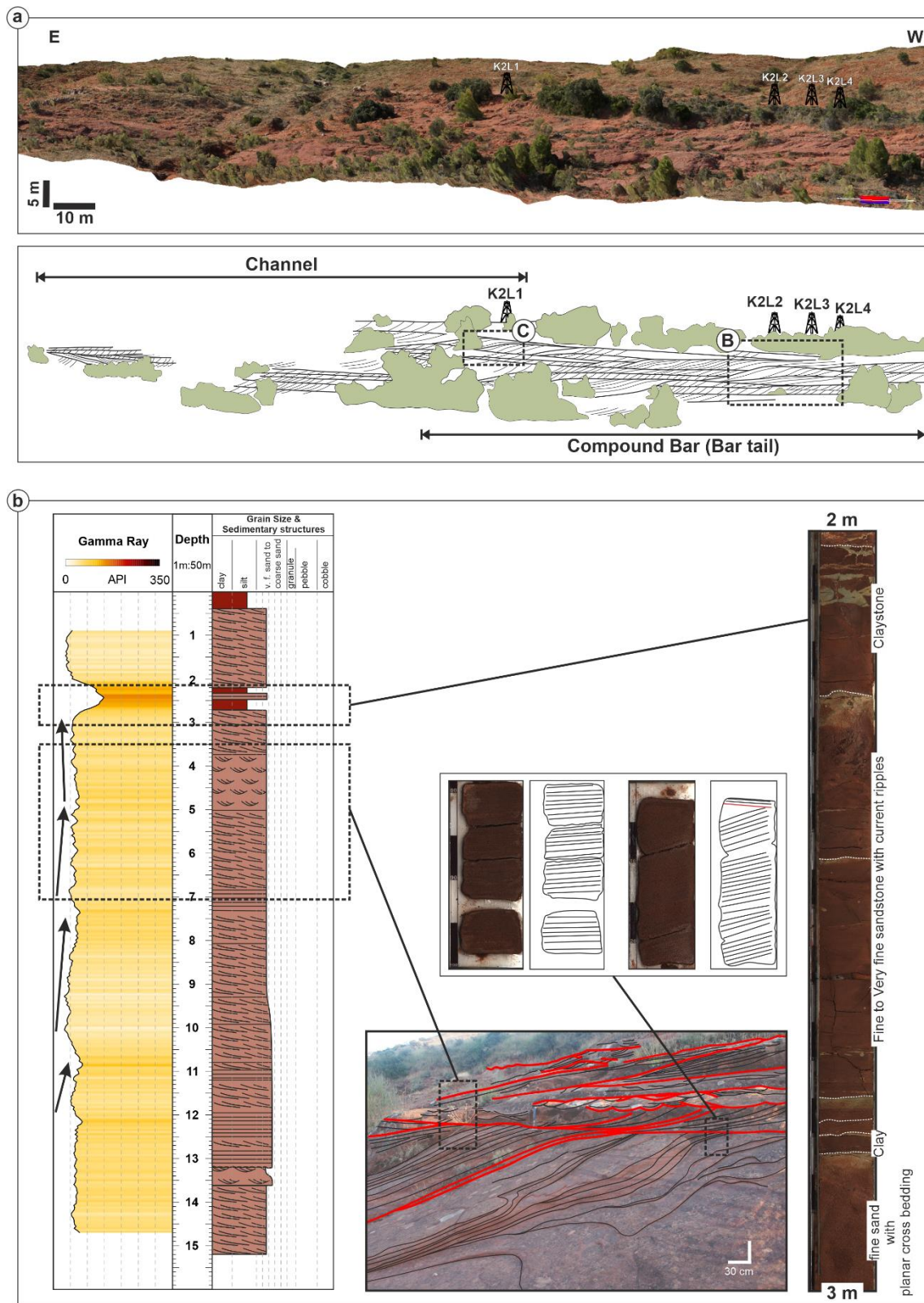
Fig. 5.6. **(a)** Digital outcrop model of Outcrop North showing the transition area between the compound bar and the channel geobodies (also so-called the bar tail). **(b)** Gamma Ray log and core description of Well K2L3 and key outcrop and core features.
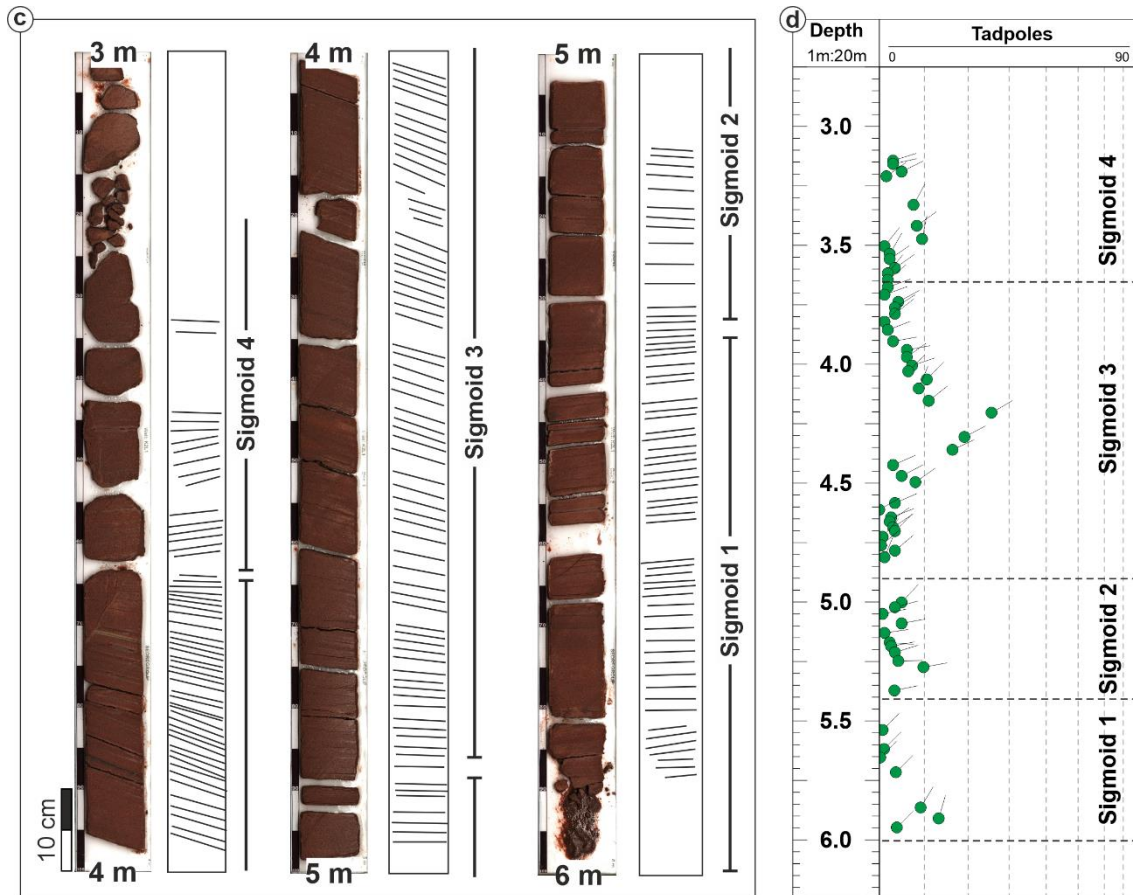
Fig. 5.6. *Continued.* **(c)** Core view of the sigmoidal cross-stratification described in outcrop and recognized in the dip tadpole analysis. **(d)** Dip tadpole analysis of Well K2L1. See Fig. 5.1b for legend.

A total of 57 dip tadpoles interpreted in Well K2P2 reveal paleocurrents which, whilst displaying a wide dispersion, ranging between N0E and N350E, are characterized by a dominant north easterly-directed flow (N0E to N45E) and a mean azimuth of N28E. Two main trends can be identified from the dip tadpoles in this well: (i) random and (ii) patterns with a predominant azimuth and a variable dip, interrupted at both the bottom and top by one tadpole with a lower dip and a slightly different azimuth (Fig. 5.5b). A total of 244 tadpoles were also interpreted in Well K2L1–4. These also show a wide dispersion, between N0E and N350E, but again with a dominant north easterly flow, ranging from N45E to N80E and a mean azimuth of N61E. The tadpole stacking trend in this well also shows two different patterns: (i) random and (ii) patterns with a predominant azimuth and a dip that cyclically varies from sub-horizontal to high angle to sub-horizontal again (Fig. 5.6d; see also Fig. 5.8).
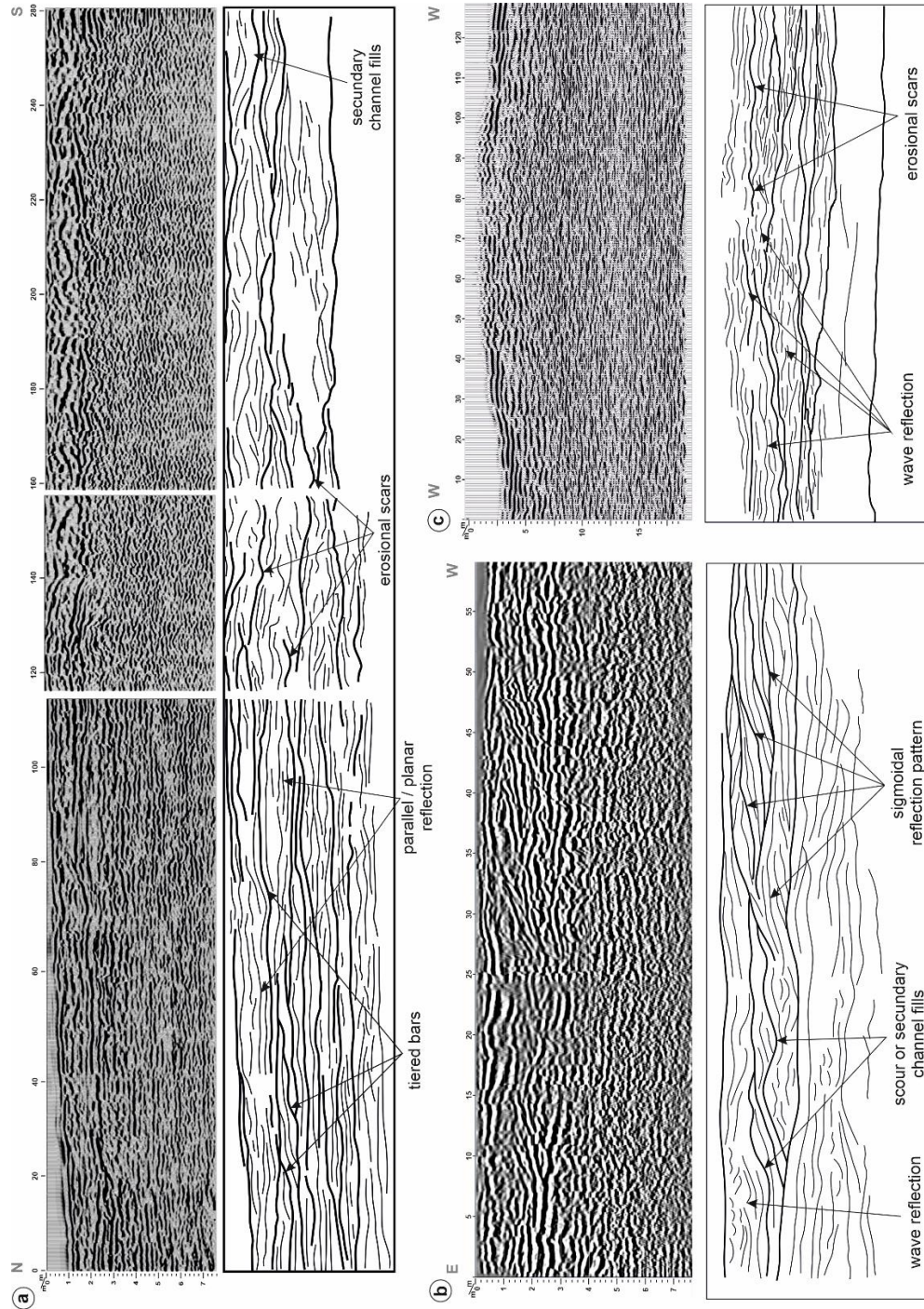
Fig 5.7. 200 MHz radar reflection profiles with 10 m penetration depth showing the spatial distribution of the main geobody-and internal structure in **(a)** Outcrop S-2 and **(b)** Outcrop North. Profiles are 248 and 70 m long, respectively. **(c)** 40 MHz radar reflection profiles with 30 m penetration depth showing the internal structure in Outcrop S-1. Profile is 125 m in length.

GPR features

The GPR profile, that targets the compound bar in Outcrop South (Fig. 5.7a), shows parallel or sub-parallel reflectors with a high amplitude and locally high dip angles. In the southernmost section, the profile slightly changes to mounded reflector patterns (wave reflection patterns), whereas in the northernmost section the parallel reflectors can be traced laterally through several metres. The GPR profile of Outcrop North (Fig. 5.7b) presents several stacked sets with a sigmoidal reflection pattern. A scour is observed towards the eastern part of the profile, above which the reflectors show a wave pattern.

5.5. Environmental reconstruction by integrating outcrop and subsurface data

By coupling the identified geobodies in outcrop, the paleocurrent dispersion identified from dip tadpoles (Fig. 5.8), the facies associations in core, the Gamma Ray profiles and reflector patterns in the GPR profiles, the S Unit sandstone package can be interpreted as a perennial deep braided fluvial system. This interpretation is consistent with previous studies in the same area (Dabrio *et al.,* 2005; Viseras *et al.,* 2011b, 2016; Henares *et al.,* 2014).

In both outcrops where the channel geobody is exposed, it shows a fining- and thinning-upwards infill trend, resulting from the hierarchical stacking of minor sequences of dunes and megaripples (Fig. 9a, b and Table 5.1). Decimetre-scale clay drapes highlight the boundaries between the different sequences, indicating the temporary abandonment of the channel associated with its migration to a new position (Dabrio & Fernández, 1986). The three-dimensional character of these clay drapes, which extend over the complete cross-section of the channels and are also recognized in the behind outcrop wells, strongly suggests that they can be considered as potential barriers to vertical fluid flow and would compartmentalize the reservoir within this facies association.

In outcrop, the compound bar geobody can be subdivided into the bar head and the bar tail (Bluck, 1976; Viseras & Fernández, 1994), on the basis of the predominant sedimentary structures. On the one hand, the thick, planar cross-bedded set corresponds to the development of a transverse bar across which the compound bar was deposited (Fernández *et al.,* 2005). This association of Lithofacies Sp–St, together with an upwards-thinning trend, records the development of a sand flat system within the framework of gradual reduction in accommodation space responding to a decrease in water column depth (Fig. 5.9a-b and Table 5.1). On the other

hand, the stacking of minor sigmoidal sequences with a thinning-upwards trend, as exposed in Outcrop North, is characteristic of the termination of the bar into the channel. This sigmoidal cross-stratification has been termed a bar tail by some researchers (Bluck, 1976), whereas others have described it as a "delta foreset" (Cant & Walker, 1978). Each of these minor sequences is characterized by the hierarchical stacking of bedforms (dunes and megaripples) (Fig. 5.9a-b and Table 5.1).
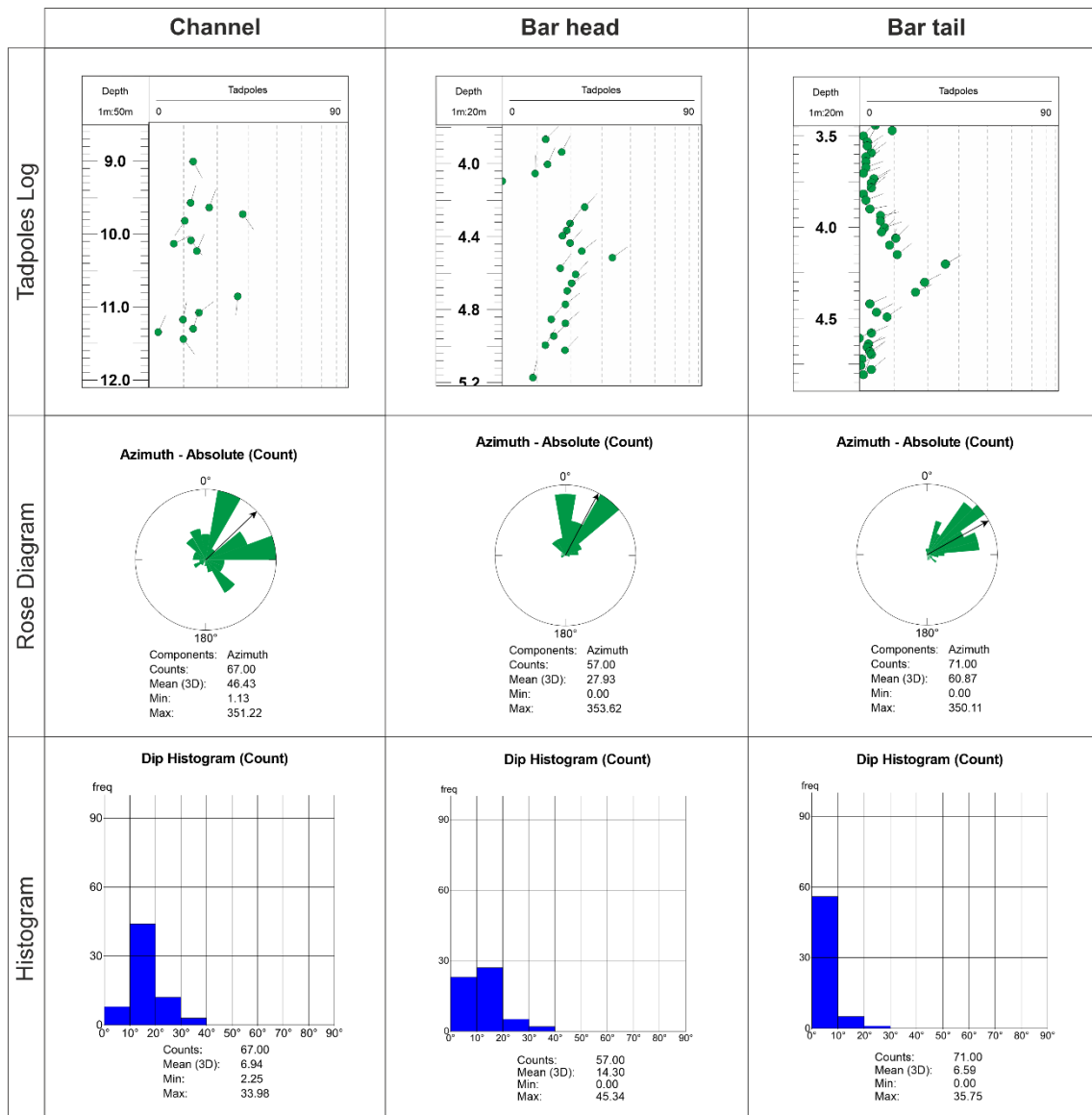
Fig. 5.8. Dip azimuth rose diagrams and dip histograms obtained from the tadpole analysis in the main geobodies of the channel, bar head and bar tail.

The lithofacies assemblage observed in the core of the southern channel (Well K2P1) is typical of a deep multi-storey channel fill (Miall, 1996). The horizontal lamination (Lithofacies Sh or Sm) indicates upper flow regime conditions, whereas the association of trough cross-bedding (Lithofacies St) and ripple cross-lamination (Lithofacies Sr) corresponds to progressive channel abandonment reflecting a gradual reduction in accommodation space (Muñoz *et al.,* 1992). The conglomeratic levels (Lithofacies Gm) may be related to short-lived increases in channel energy (Table 5.1; Bridge & Tye, 2000; Viseras *et al.,* 2009; Calvache *et al.,* 2010).

The assemblage of Lithofacies Sh–Sp observed in the core of Well K2P2, which targets the compound bar geobody (Table 5.1), is interpreted to record the aggrading stage of the bar, whereas the abandonment is represented by the gradual change from the Lithofacies Sp to St (Miall, 1996; Bridge & Tye, 2000). In the core from Well K2L1-4, the repetition of the succession comprising Lithofacies Sh–Sp–Sh interpreted as a response to the variation in dip of the cross-stratification developed in the bar tail sigmoids (Table 5.1). The association of Lithofacies Sr-Fl, with an erosive base, suggests the development of a cross-bar channel across the upper part of the bar during the maximum flooding peak.

Table 5.1. Comparison of the key features identified in both outcrop and subsurface datasets for the channel, bar head and bar tail geobodies. See Fig. 5.9 for detailed illustrations.

	Channel	Compound Bar (Bar Head)	Compound Bar (Bar Tail)
Conceptual sedimentary model	fining and thinning upward infill trend resulting from the hierarchical stacking of minor sequences of dunes and megaripples	planar cross-bedded set corresponding to aggradation of a transverse across which the compound bar developed	stacking of minor sigmoidal sequences with a thinning upwards trend
Lithofacies	Gm - Sh/Sm - St - Sr	Sh - Sp - St	Sh - Sp – Sh
High resolution GR pattern	Funnel pattern	Cylindrical pattern	Bell pattern
Dip tadpole trends	random pattern due to the stacking of trough cross-bedded sets	similar dips and azimuth sets delimited by tadpoles with lower dips and slightly different directions	predominant azimuth with a dip cyclically varying from sub-horizontal to high angle to sub-horizontal again
GPR reflector character	parallel or subparallel and wave reflectors	parallel or subparallel reflectors with high amplitude and locally high tilt angles	subparallel reflectors with high tilt angles that decrease upward
Permeability barriers/baffles	internal, laterally extensive clay drapes	laterally limited cross-bar channel at the top	laterally limited cross-bar channel at the top
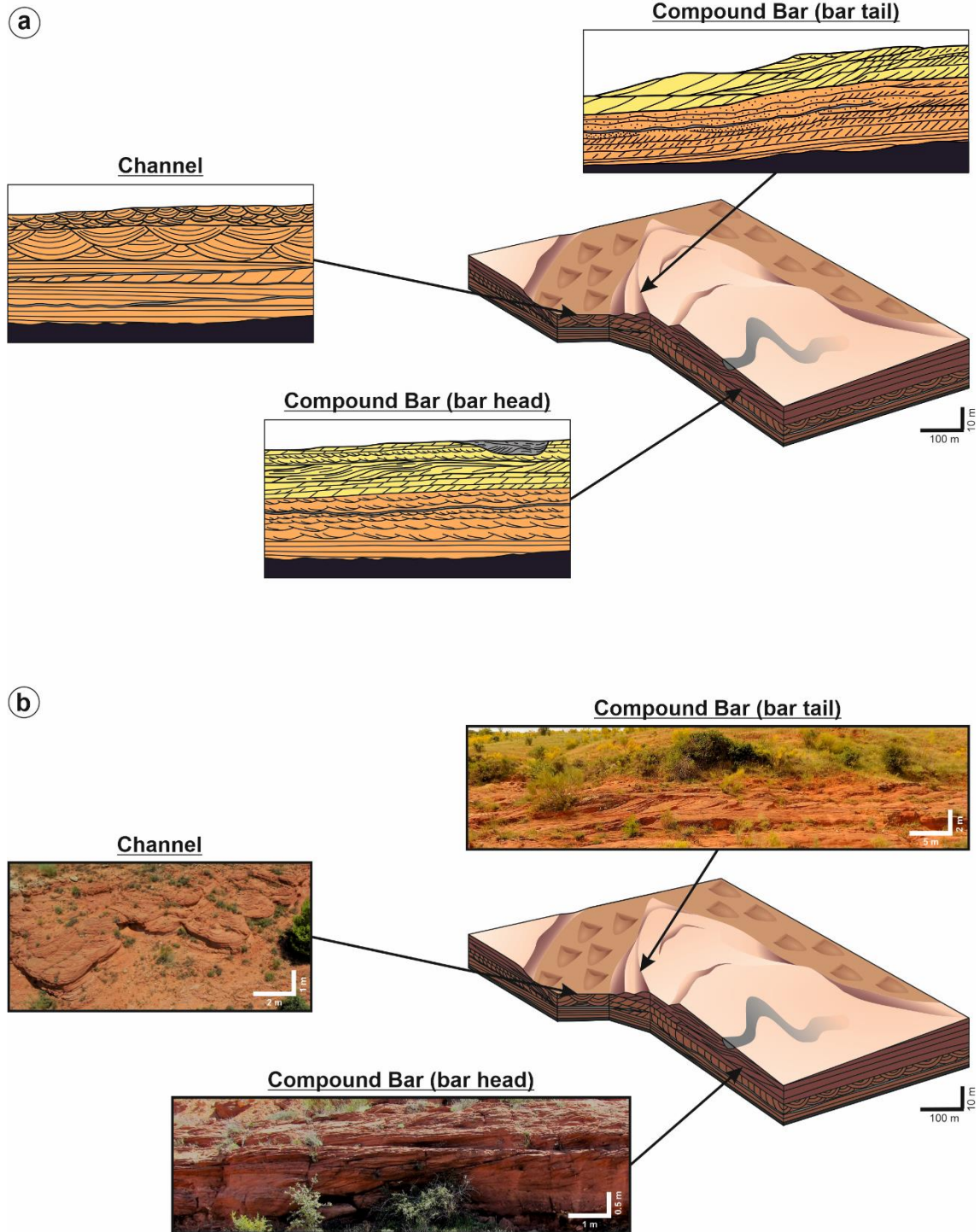
Fig. 5.9. **(a)** 3D conceptual block diagram with 2D conceptual models of the component geobodies identified in the S Unit. Colour legend: orange, sandy channel facies; yellow, sandy compound bar facies; grey, clayey facies corresponding to the permeability barriers/baffles or cross-bar channels. Note that the 2D conceptual model is not to scale. **(b)** 3D conceptual block diagram with some outcrop photographs of the component geobodies.
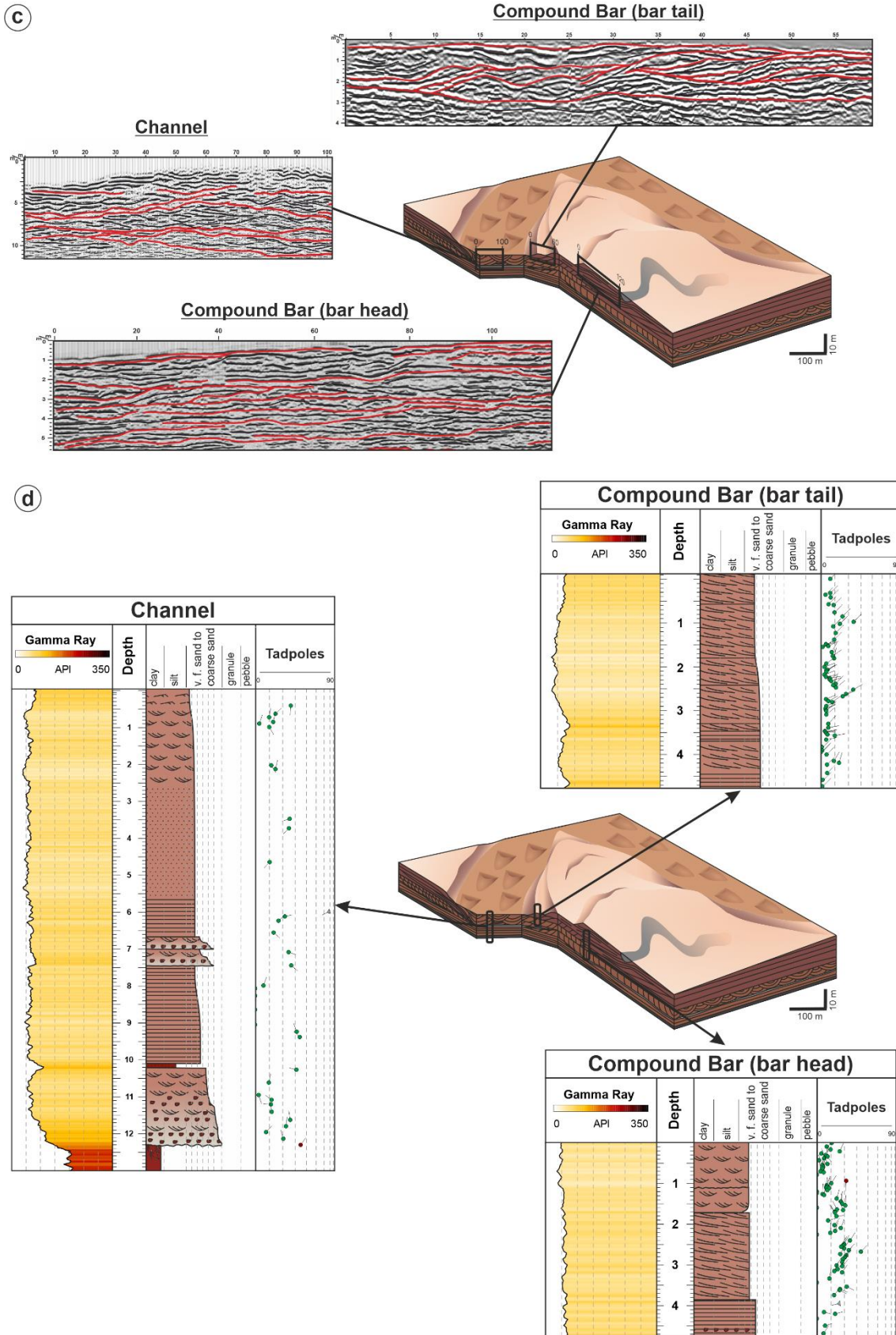
Fig. 5.9. *Continued*. **(c)** 3D conceptual block diagram highlighting the key ground-penetrating radar features of the component geobodies. **(d)** 3D conceptual model highlighting the key well log features of the component geobodies identified in the S Unit.

Despite the general cylindrical pattern in the Gamma Ray logs of both geobodies (Bridge & Tye, 2000; Bridge & Lunt, 2009; Tianjian *et al.*, 2014), higher resolution examination can identify differences between the channel and the compound bar and, within the latter, between the bar head and the bar tail (Bridge & Tye, 2000; Bridge & Lunt, 2009) (Fig. 5.9d).

Well-developed cylindrical trends are observed in the channel, related to Lithofacies Sh–Sm, whereas Lithofacies St or Gm show a more funnel-shaped Gamma Ray pattern. The higher API values (59 to 128 API, Mean 89 API) in the upper part of the facies sequence records gradual channel abandonment (Lithofacies St-Sr; Fig. 5.4) (Bridge & Tye, 2000; Bridge & Lunt, 2009). In contrast, the Gamma Ray pattern in the bar head is mostly cylindrical, with higher API values towards the top associated with Sr-Fl lithofacies typical of cross-bar channel deposits (Bridge & Tye, 2000; Bridge & Lunt, 2009). The decrease in API values between 9 and 6 m depth in Well K2P2 reflects the occurrence of diagenetic gypsum nodules in this interval (Fig. 5.5a and d).

The Gamma Ray log of the bar tail shows several superimposed bell-shaped intervals corresponding to the stacked sigmoidal units that characterize this part of the geobody. At the top of these sigmoids, the funnel pattern corresponds to Lithofacies St, reflecting short-lived increases in channel activity (Bridge & Tye, 2000; Bridge & Lunt, 2009). The uppermost interval with higher API values (87-157 API; Mean 129 API) is associated with Lithofacies Sr-Fl (Fig. 5.6), typical of the cross-bar channel (Bridge & Tye, 2000; Bridge & Lunt, 2009).

The difference in thickness between the upper intervals with higher API values in Wells K2P2 and K2L of the compound bar is the expression of the greater cross-bar channel thickness in the bar tail than in the bar head. Thus, these cross-bar channel deposits, characterized by Lithofacies Sr-Fl and with limited lateral extension, may increase reservoir heterogeneity by acting as potential permeability baffles for 3D fluid migration as they will be thicker towards the contact with the channel, parallel to the flow direction**.**

Dip tadpole analysis reveals a regional NE-directed paleocurrent flow for the braided system. However, more detailed differences can be determined between the channel and the compound bar tadpole patterns, as well as between the bar head and the bar tail (Fig. 5.8). In the channel geobody, the tadpoles show a random pattern due to the stacking of trough cross-bedded (Lithofacies St) sets (Cameron *et al.,* 1993; Williams & Soek, 1993; Dueck & Paauwe, 1994; Selley, 2004; Miall, 2006; Long, 2006; Lelpi & Ghinassi, 2015). In the compound bar head, the tadpoles show characteristic patterns with similar dips and azimuths corresponding to the planar cross-bedded (Lithofacies Sp) sets. In addition, at the bottom and the top of the geobody, these sets also typically show tadpoles with lower dips and slightly different azimuths, which

correspond to the set boundary surfaces (Selley, 2004; Lelpi & Ghinassi, 2015; Long, 2006). In the compound bar tail, the dip tadpoles have a predominant azimuth with a dip varying cyclically from sub-horizontal to a high angle to sub-horizontal again, associated with the thinning-upwards stacking of the sigmoidal units described in outcrop and cores.

The parallel or sub-parallel reflectors displayed in the lower part of the channel in the GPR profile (Fig. 5.7c) correspond to the horizontal lamination of Lithofacies Sh (Stephens, 1994; Bridge & Lunt, 2009; Lunt *et al.*, 2013; Reesink *et al.*, 2014). In the upper part of the profile, where mounded (wave reflection or chaotic) and sub-parallel reflectors are observed, interrupted by other concave-up reflectors, trough cross-bedded (Lithofacies St) sandstones (Corbeanu *et al.*, 2001; Bridge & Lunt, 2009; Lunt *et al.*, 2013; Reesink *et al.*, 2014; Franke *et al.*, 2015) with internal erosional scars have been described in outcrop (Fig. 5.9c).

The GPR profiles acquired across the compound bar geobody (Fig. 5.7a-b) show parallel or sub-parallel reflectors with high amplitude and locally with high tilt angles. The GPR profile of the bar head (Fig. 5.7a) clearly represents the features observed in outcrop, such as the occurrence of different mega-cross-bedded sets and tiered bars as well as internal erosional scours (Bridge & Lunt, 2009; Lunt *et al.*, 2013; Reesink *et al.*, 2014; Franke *et al.*, 2015). Towards the south, in this profile, there is a change to mounded radar facies reflecting the proximity to the southern channel (Bridge & Lunt, 2009; Smith *et al.*, 2006; Lunt *et al.*, 2013; Reesink *et al.*, 2014; Franke *et al.*, 2015). The GPR profile of the bar tail (outcrop north) (Fig. 5.7b) captures the sigmoidal stratification clearly identified in outcrop (Skelly *et al.*, 2003; Bridge & Lunt, 2009; Lunt *et al.*, 2013), and represented by sub-parallel radar facies with high inclination angles that decrease upwards (Fig. 5.9c).

A general paleogeographic reconstruction is presented here, based on the integration of both surface (outcrop and digital outcrop model) and subsurface (cores, wireline logs and GPR profiles) datasets (Fig. 5.10). In this model, two compound bars are represented, subdividing the braidplain into three channel branches. The dimensions of the two compound bars, estimated from the digital outcrop models and GPR profiles, are similar, characterized by a long section and cross-sections of 1000 and 600 m, respectively. The easternmost branch is 230 m wide in the channel, whereas the central branch is 300 m wide. The dimensions of the westernmost branch could not be estimated due to outcrop constraints. Dip tadpole analysis indicates that the entire braidplain is characterized by a NE-directed paleocurrent flow.

The full integration of subsurface datasets and their validation with their surface expression using outcrop analogues has been demonstrated to be one of the most effective

ways of enhancing pre-existing facies models (Donselaar & Schmidt, 2005; Miall, 2006; Colombera *et al.*, 2014). In this study, such a combination provides the key criteria for the subsurface recognition and characterization of the component geobodies and their associated permeability heterogeneities in sandy braided fluvial systems. A better understanding of the dimensions and distribution of the potential permeability barriers and baffles in this type of deposit may improve the scaling of reservoir properties and increase the reliability of quantitative facies models applied in improved/enhanced oil recovery strategies.
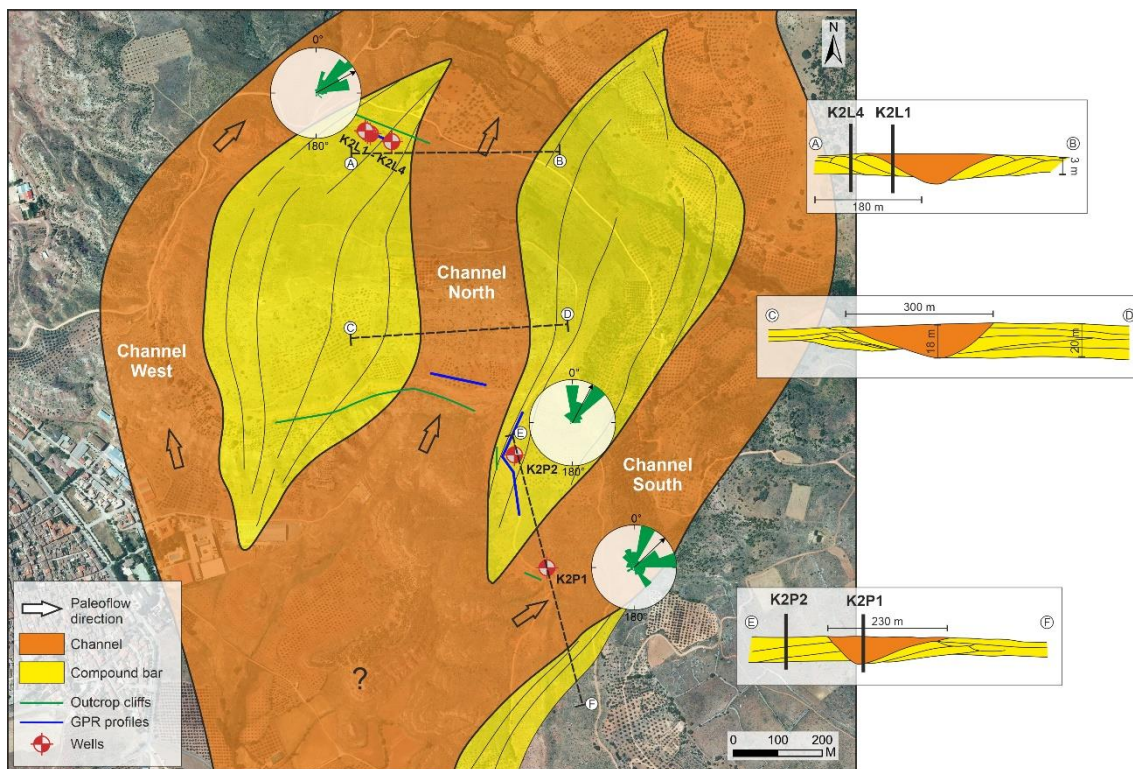
Fig. 5.10. Paleogeographic reconstruction of the braided bar channel complex resulting from the integration of the outcrop/behind outcrop workflow data. The paleocurrent directions of the main geobodies are shown in rose diagrams. (A-B, C-D & E-F; are cross-sections through different segments of the braided system).

5.6. Conclusions

The in-house designed outcrop/behind outcrop characterization workflow used in this study combined the sedimentological analysis of a deep perennial braided fluvial system, of Triassic age, with GPR profiles and behind outcrop OBI and ABI imaging techniques, in addition to the analyses of dip tadpoles, conventional core and Gamma Ray logs. By coupling the data from both surface and subsurface sources, a highly detailed analysis of the spatial distribution

of the fluvial facies and potential internal permeability baffles was carried out with a centimetre-scale vertical resolution.

The main geobodies identified are the channel and the compound bar, and within the latter; the bar head, the bar tail and a cross-bar channel. The detailed lithofacies description in both outcrop and core has also allowed us to identify the potential permeability barriers and/or baffles within each geobody. In the channel, the main permeability baffles are represented by clay drapes, which disrupt the vertical continuity of the stacked sandy lithofacies, resulting in a parallel pseudo-stratification in outcrop and GPR. Towards the upper part of the compound bar, the presence of very fine-grained, ripple-laminated sandstone and clay layers corresponding to a cross-bar channel deposit represent a potential permeability baffle within this geobody. The thickness of this element seems to be greater in the bar tail than in the bar head, so its potential impact would clearly be more important towards the contact between the channel and the compound bar.

By means of a detailed analysis of the Gamma Ray log patterns, several differences, superimposed on a general cylindrical pattern through the S Unit, have been established between the channel and the compound bar head and tail. Several minor sequences with funnel-shaped patterns can be observed in the channel. In contrast, within the compound bar, the bar head shows a more homogeneous cylindrical trend, whereas the bar tail is characterized by the stacking of several bell-shaped intervals.

Detailed analysis of the dip tadpoles was of paramount importance for the high-resolution characterization of the two main geobodies. The channel shows a predominantly random pattern in the tadpole azimuth and dip orientations. In contrast, the tadpoles in the bar head display several characteristic patterns with similar dips and azimuths, limited at the bottom and the top by tadpoles with lower dips and slightly different directions. The tadpoles in the bar tail have a predominant azimuth with a dip varying cyclically from sub-horizontal to high angle to sub-horizontal again.

By integrating both surface and subsurface data, a detailed paleogeographical reconstruction is proposed, including the dimensions and spatial distribution of the main geobodies. This study directly links sedimentological information with petrophysical and image-log responses. Thus, it highlights our view that the application of the outcrop/ behind outcrop workflow presented here provides a solid database for the characterization of the spatial distribution of reservoir rock properties from outcrop analogues.

CHAPTER 6:

Heterolithic Unit:

Mixed tidal and wave-influenced shoreline system

Abstract   Coastal depositional environments are of increasing economic importance in the hydrocarbon industry, forming a large number of significant petroleum and gas reservoirs, in many basins around the world. These reservoirs are shaped both by the interaction of a wide variety of depositional processes and are also highly sensitive to changes in sea level, subsidence and sediment supply, Consequently, they exhibit significant variability in stratigraphic architecture and sedimentological heterogeneity.

With the aim of addressing this problem, a multi-disciplinary study was undertaken on an example of well-exposed coastal sediments, combining both outcrop and subsurface data (core and wireline logs). For the purposes of this study, the Heterolithic Unit (H Unit) of the TIBEM Formation in south-central Spain was selected.

Six facies associations were identified and grouped, based on geometry and sand:mud ratio, into three types of reservoir geobody: (1) elongate geobodies and (2) asymmetrical-sigmoidal geobodies, characterized by heterolithic-dominated facies associations; and (3) tabular geobodies, characterized by sand-dominated facies associations; and one type of non-reservoir geobody, characterized by a tabular geometry and composed of mud-dominated facies associations. These reservoir geobodies were deposited within the broad framework of a tide-dominated delta system.

The full integration of outcrop and subsurface datasets has enabled the generation of a predictive conceptual model, based on facies analysis, which through integration with a sequence stratigraphic framework has allowed us to characterise the development through time of the system, in response to the changing balance between shoreline processes, all of which impacts on both geobody geometries and reservoir potential.

6.1. Introduction

The assemblage of siliciclastic depositional settings associated with deltas, coastal plain to shoreline-shelf systems and estuarine depositional environments, all of which occur at or close to sea-level, is typically termed coastal or paralic (Reynolds, 2017). The dynamic interaction of numerous factors in paralic settings results in the variable physiography of the coastline and a complex heterogeneity of nearshore deposits, observable both in modern and ancient examples (Dalrymple & Choi, 2007). However, despite many apparent differences, all paralic deposits can be characterized by a number of common depositional environments, often simply arranged in different spatial patterns and/or vertical sequences. This reflects the essential fact that many of these environments are extremely sensitive to, and respond rapidly, to changes in sea-level, climate and sediment supply.

Paralic reservoirs are globally important, but the range of environments, together with the impact of sea-level and changes in sediment supply, results in significant variability, in both stratigraphic architecture and sedimentological heterogeneity (Davis & Dalrymple, 2012; Ashworth *et al.*, 2015; Tessier & Reynaud, 2016). The idea that the genesis and shape of the geobodies associated with these environments can be usefully described and differentiated by the proportions of the wave-, fluvial- and tide generated sedimentary structures is certainly powerful (Yang *et al.,* 2005; Ainsworth *et al.*, 2011; Longhitano *et al.,* 2012), but is largely untested in the published literature (Reynolds, 2017). The extent to which these processes can be distinguished, and the capacity of the proportions determined to be predictive, are fundamental sedimentological questions for shoreline reservoirs.

In this sense, the study of outcrop analogues is a useful tool, which complements the subsurface data and helps us to construct more realistic conceptual models (Miall, 1990; Kokureck *et al.*, 1991; Tyler and Finley, 1991; Wizevich, 1991; Yoshida *et al.*, 2001; Ajdukiewicz & Lander, 2010; Scott *et al.*, 2013; Pranter *et al.*, 2014; Franke *et al.*, 2015; Yeste *et al*., 2019, 2020). New technical advances in the reconstruction of the outcrop in 3D, based on digital outcrop models built using photogrammetry, allow us to quantify the data provided by the outcrops as well as contributing to more precise interpretations. If, in addition to the outcrop data, subsurface data of the same examples are available, an appropriate database can be constructed in order to properly constrain the geometries and dimensions of the sandbodies. From this, realistic models can be generated, that capture both facies at high resolution and the distribution of the heterogeneities within reservoirs.

The aims of this chapter are: (i) to present a detailed analysis of the sedimentary facies, geometries and stacking patterns in a Triassic fluvio-marine succession; (ii) to determine the key features necessary for the recognition and characterization in subsurface well data of these shoreline deposits; and (iii) to develop a predictive conceptual model that represents the heterogeneities in these paralic reservoirs.

The studied example is a Triassic succession, often considered as an outcrop analogue for other hydrocarbon-productive reservoirs such as the Algerian TAGI (Trias Argilo-Gréseux Inférieur; Rossi *et al.* 2002; Dabrio *et al.,* 2005; Viseras *et al.*, 2011b; Henares *et al.,* 2014, 2016; Viseras *et al.,* 2018; Yeste *et al.,* 2019; Yeste *et al.,* 2020; Baouche *et al.,* 2020). For this reason, the Outcrop/Behind Outcrop workflow has been employed, integrating standard 2D high resolution outcrop data and 3D outcrop data, developed from photogrammetry, with subsurface data from behind the outcrop including cores and core descriptions, Gamma Ray logs, Spectral Gamma Ray logs and borehole image logs. The integration of different but complementary data types (i.e. surface and subsurface data) leads to better constrained reservoir models which serve to improve the quantification and correlation of heterogeneities within this type of reservoirs.

6.2. Data

The outcrop selected for the facies analysis, in terms of geometry, internal structure, sequence trends and the spatial relationships between the main architectural elements, has a total study area of 0.68 km^2 (Fig. 6.1). Digital Outcrop Models (DOM) have also been created from photogrammetry, with an RPAS (Remotely Piloted Aircraft System), to complete the outcrop-derived measurement dataset.

Shallow wells drilled, behind the outcrops, with continuous core recovery and wireline log data were also acquired (Fig. 6.1). Core slabbing was subsequently carried out in order to enhance the visibility of sedimentary features on the core surface and allow the identification of the main lithofacies classes (Table 6.1). Well log data include the Total Gamma Ray log (GR) and Spectral Gamma Ray log (SGR) in addition to borehole imaging from Optical and Acoustic Televiewers (OBI and ABI, respectively)*.* See Chapter 3 for a detailed description of technical specifications.

In the studied outcrop of the H-Unit, four slim-hole (85 mm diameter), behind-outcrop wells permitted subsurface characterization by providing data, both from wireline logs and

cored intervals (Fig. 6.1). From north to south, these wells are: HU 1, with 14.7 m of cored section and 11.7 m of well logged section; HU 2, with 15 m of core and 14.4 m of wireline logged section; HU 3, with a 34.5 m cored interval and 31.7 m of wireline logged section; and HU 4, with 3.9 m of core and 3 m of wireline logged section. The differences noted between cored and wireline logged intervals for these wells is purely due to technical issues. At the bottom of each borehole, drilling mud accumulated after coring, thereby preventing the acquisition of wireline logs over the entire drilled section.
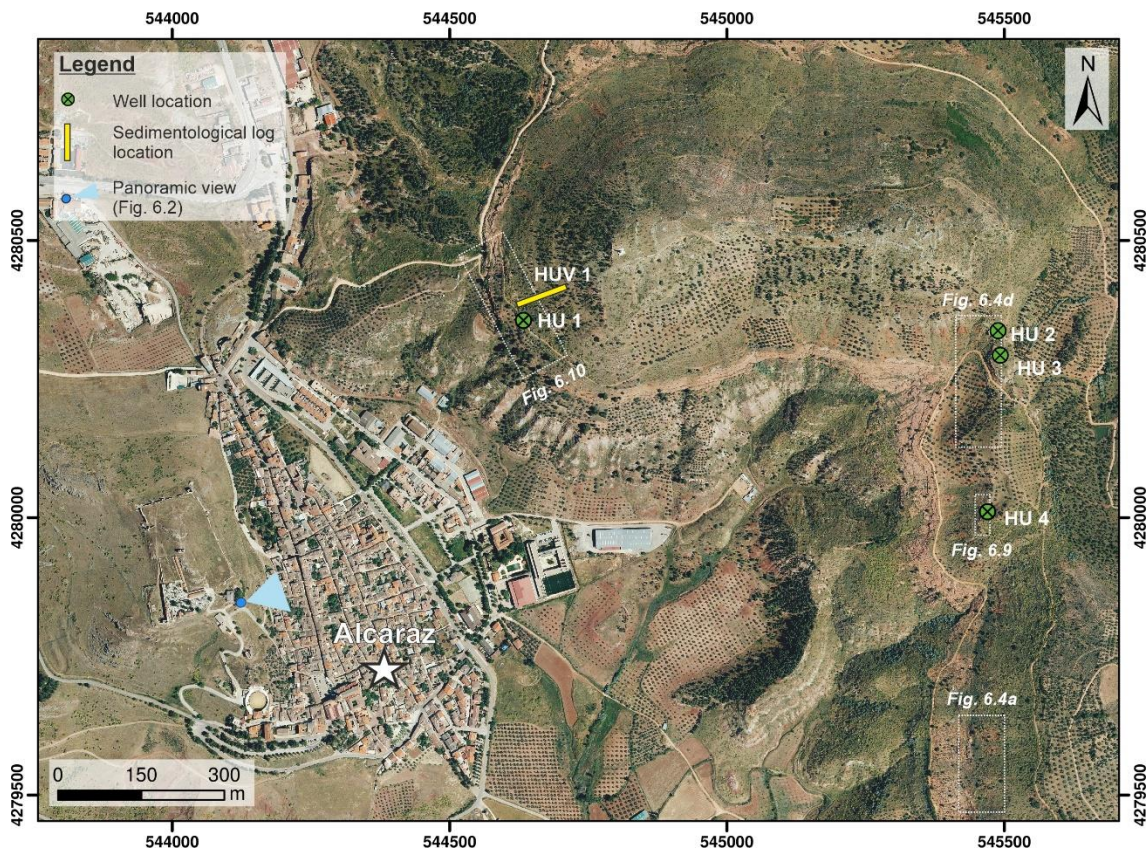
Fig. 6.1. Satellite image of the study area showing the location of the wells, sedimentological logs, outcrops and the location of Figs. 6.2, 6.4, and 6.9.

6.3. Stratigraphic framework and architecture of the Heterolithic Unit

The Heterolithic Unit (H Unit) is a 40 m-thick section, comprising five metre-scale sand-prone packages (termed Sand-Prone Packages 1-5) embedded within mudstones (Fig. 6.2 and Fig. 6.3). Along the studied north-south cross-section (Fig. 6.2), the lateral-extension of the sand-prone packages is highly variable (ranging from a few metres to a few hundred metres) as is the thickness of the packages (0.5 m to above 14 m thick).
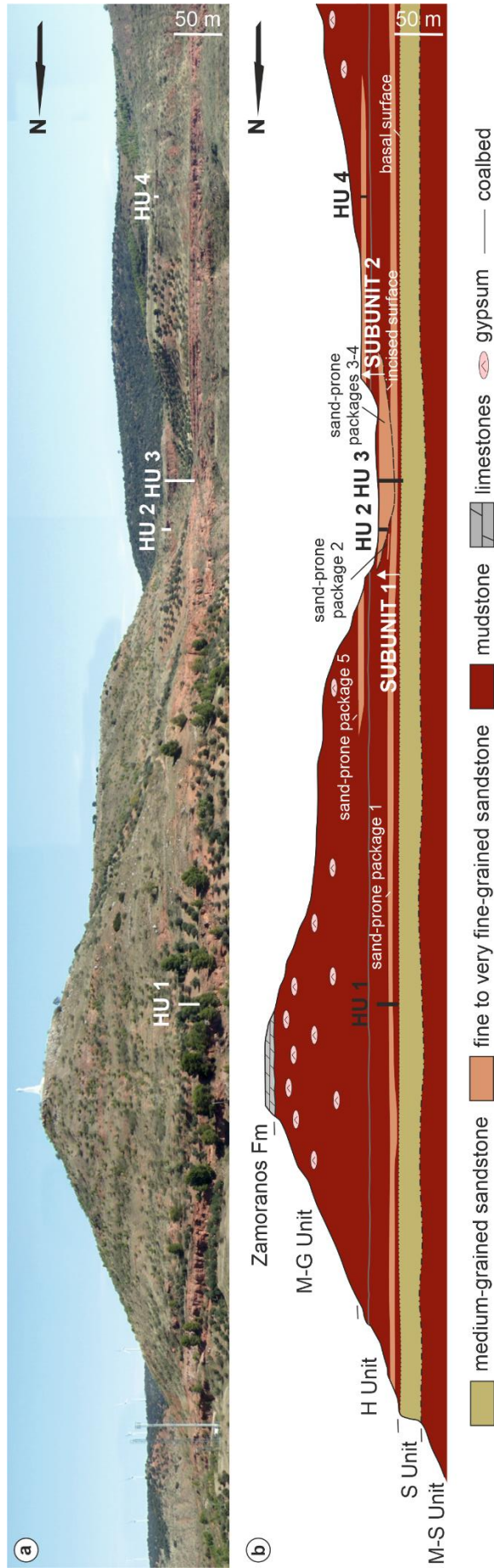
Fig. 6.2. Panoramic view (above) and line drawing (below) showing the lithostratigraphic framework of the studied cross-section. Note the two major stratigraphic surfaces in the H Unit (basal surface and incised surface in the middle of the H Unit). Note the high-, medium- and low-lateral continuity of Sand-prone Packages 1, 5 and 3-4, respectively. See Fig. 6.1 for location of panoramic view. M-S Unit: Mudstone-Sandstone Unit; S Unit: Sandstone Unit; H Unit: Heterolithic Unit; M-G Unit: Mudstone-Gypsum Unit.

170
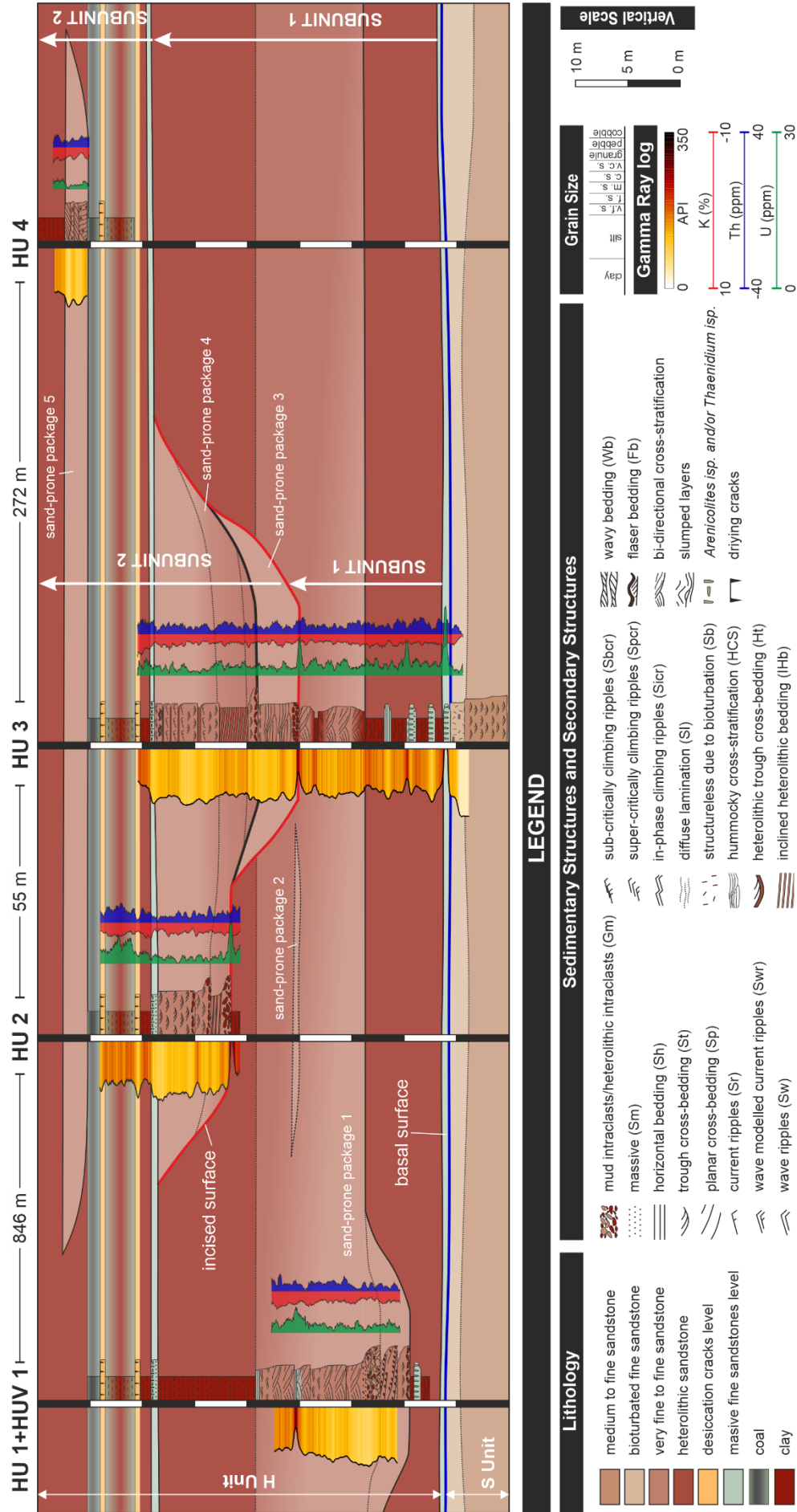
Fig. 6.3. Correlation panel containing the 4 wells (HU 1 – HU 4) and 1 outcrop-derived sedimentological log (HUV 1), which is located in the same vertical section as well HU 1 – see Fig. 6.1 for location). GR log, SGR log and core description are shown for each well. The blue line highlights the bounding surface between the S Unit and H Unit. The red line highlights the incised valley forming the boundary between Subunits 1 and 2.

171

Two major stratigraphic surfaces have been recognized within the H Unit. These are: (A) the basal surface and (B) an incised surface in the middle of the H Unit; the latter dividing the Unit into a lower and an upper subunit, termed Subunit 1 and Subunit 2, respectively.

The basal bounding surface of the H Unit is a scoured contact truncating the top of the Sandstone Unit (S Unit) (Fig. 6.4a). This distinctive surface is capped by a lag of burrowed finer-grained (than S Unit) sandstones characterized by a well-cemented bored surface (Fig. 6.4b-c).

The lowermost part of the H Unit or Subunit 1, up to 28 m thick, overlies the basal surface described above. It is formed by: (a) a laterally continuous, fining-upward (sand/mud ratio decreasing-upward) heterolithic sandstone-mudstone package (Sand-prone Package 1) up to 14 m thick and; (b) a low lateral-continuity, very-fine sandstone package (Sand-prone package 2) up to 0.5 m thick,. Both, Sand-prone packages 1 and 2, grade laterally and gradually into mudstones (Fig. 6.2).

Subunit 1 is, as indicated above, truncated by an incised surface (Fig. 6.4d-e). This constitutes the base of Subunit 2. The surface has up to 14 m of relief and up to 215 m of lateral extension. The surface is a clear example of a small- to medium-scale incised valley.

Subunit 2 is formed by two low lateral-continuity sand-prone packages (1 to 3 m in thickness, 50 to 100 m in width; Sand-prone Packages 3 and 4, respectively) confined within the limits of the incised valley described above (Fig. 6.2 and Fig. 6.4d-e). Sand-prone Package 4 grades into a succession of mudstones with interbedded coals, overlain itself by Sand-prone Package 5 which forms the top of the H Unit (Fig. 6.3).

6.4. Lithofacies and sedimentary process

Twenty-four lithofacies types are recognised, based on composition, grain size, textural characteristics and sedimentary structures (Table 6.1). The facies scheme is an extended version of the schemes of Miall (1985), Viseras *et al.* (2019) and Yeste *et al.* (2020).
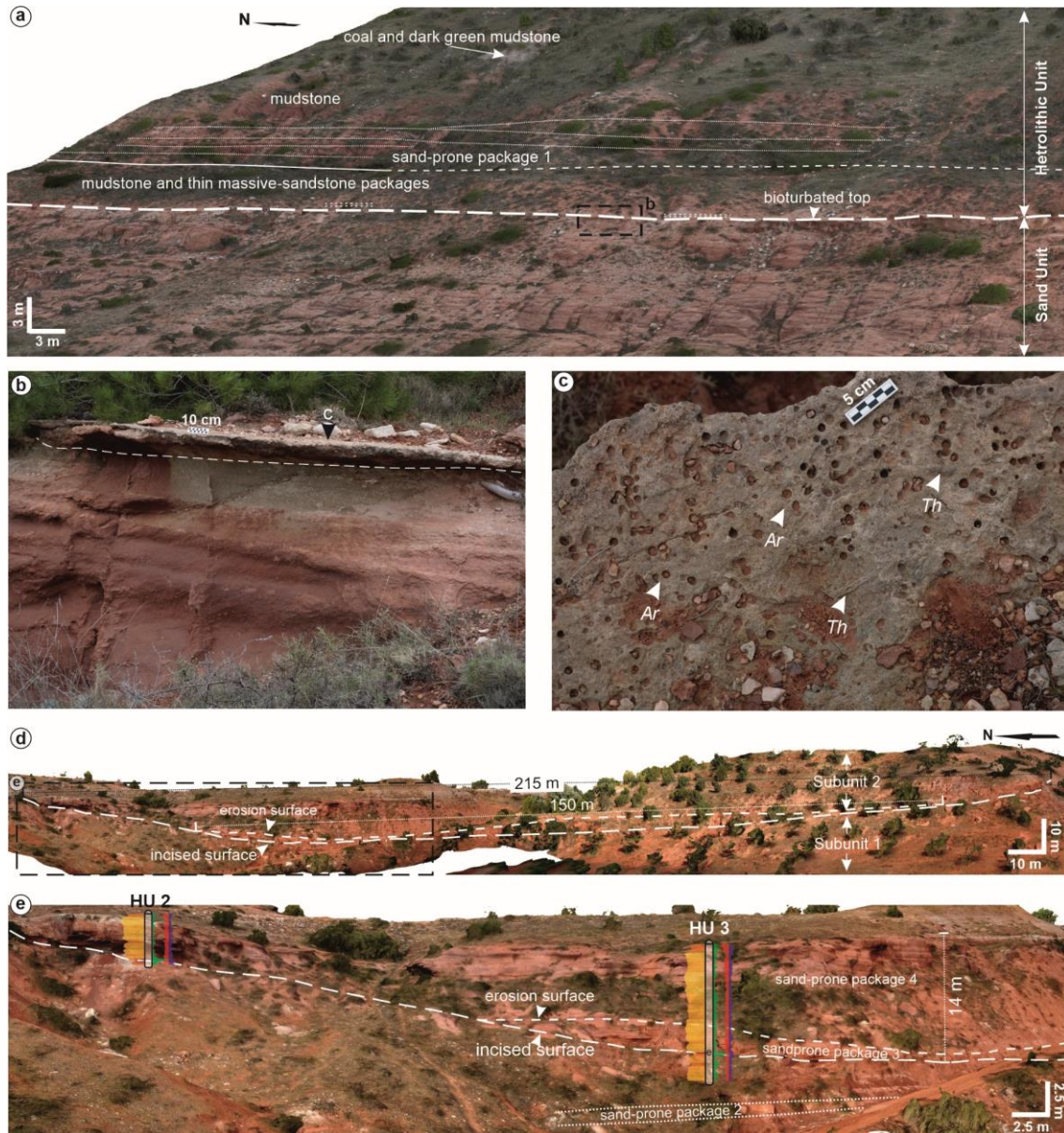
Fig. 6.4. (a) Digital outcrop model showing the S Unit – H Unit transition. Note the position of Sand-prone Package 1. **(b)** – **(c)** Close-up view of outcrop showing the bioturbated top of the S Unit. **(d)** Digital outcrop model showing the incised surface within the H Unit dividing it into the lowermost Subunit 1 and uppermost Subunit 2. **(e)** Close-up view of the digital outcrop model showing the location of Sand-prone Packages 2, 3 and 4; and also, the locations of Wells HU 2 and HU 3. For each well both the GR and SGR log are also shown.

Table 6.1. Lithofacies identified in the study area.

Lithology	Code	Texture and Fabric	Sedimentary structures and Characteristics	Main process/Interpretation
	Gm	Pebble-cobble. Clast or matrix supported	Massive, weak horizontal bedding or planar cross bedding. Erosive base and mud rip-up clasts.	Associated with high-energy traction current.
	Sm	Fine to medium sand	Massive. Rarely, presence of mud clasts.	Associated with rapid transport and deposition of sand during large-magnitude flood.
	Sh	Fine to medium sand	Horizontal lamination. Occasionally presence of mud drape and flame structures.	Associated with upper flow regime.
	St	Fine to medium sand	Trough cross bedding. Sometimes, mud chips lining the cross beds	Migration of megaripples and dunes. River and tidally influenced, moderate to strong current.
	Sp	Very fine to medium sand	Planar cross bedding. Commonly, alternation of mm-thick lamina of sand and clay-enriched and scattered mud clasts layers.	Megaripple migration. Associated with river and tidally influenced, moderate to strong current.
	Sr	Very fine to fine sand	Current ripple lamination.	Migration of current ripples. Associated with river and tidally influenced, moderate to strong currents.
	Scr	Very fine to fine sand	Critically climbing ripple lamination. Angle of climbing = stoss side angle.	Combination of traction and settling from suspension. Associated with river floods and hyperpycnal flows.
Sandstones	**Sbcr**	Very fine to fine sand	Sub-critically climbing ripple lamination. Angle of climbing < stoss side angle.	Combination of traction and settling from suspension. Associated with river floods and hyperpycnal flows.
	Spcr	Very fine to fine sand	Super-critically climbing ripple lamination. Angle of climbing > stoss side angle.	Combination of traction and settling from suspension. Associated with river floods.
	Sicr	Very fine to fine sand	In-phase climbing ripple lamination.	Balance between traction transport and sediment supply, indicating the ripples do not migrate. Associated with river floods and hyperpycnal flows.
	Sw	Very fine to fine sand	Wave ripple lamination.	Oscillatory flow during both fair weather and storm events.
	Swr	Very fine to fine sand	Combined flow ripple lamination.	Migration of current ripples modified by wave action. Associated with river floods, wind-driven residual currents and oscillatory wave action.
	Sl	Very fine sand	Diffuse horizontal lamination or diffuse current ripple lamination.	Settling from suspension or migration of current ripples. Diffuse structures due to bioturbation.
	Sb	Very fine to medium sand	Massive. Presence of rhizoliths, *Arenicolites* isp. and *Taenidium* isp.	Structureless due to bioturbation
	HCS	Very fine sand	Hummocky cross-stratification.	Storm-influenced high-energy combined flows.

Table 6.1. (continued)

Lithology	Code	Texture and Fabric	Sedimentary structures and Characteristics	Main process/Interpretation
	Ht	Very fine to silt and clay	Heterolithic trough cross bedding. Presence of sand-mud couplets forming bundles. Rarely, presence of mud clasts and convolute lamination	Tidally-influenced unidirectional currents with moderate speeds. Sand bedsets are formed by tidal currents during ebb-flood tidal cycles. Mud drapes are formed during the low energy periods of slack water
	IHb	Very fine to silt and clay	Inclined heterolithic bedding. Frequent presence of slumped layers.	Tidally-influenced unidirectional currents with moderate speeds. The sand laminae represent deposition from ebb-flood tidal flows, whereas the mud layers accumulated from suspension under low energy, slack water conditions
Heterolithic sandstones	**Wb**	Very fine to silt and clay	Wavy bedding. Roughly equal volumes of sand and mud.	Tidally-influenced unidirectional currents with low to moderate speeds. Alternation of low and high energy conditions. Sandy ripples were deposited by high energy tidal and/or fluvial flows, whilst muddy drapes were deposited during slack water conditions.
	Fb	Very fine to silt and clay	Flaser bedding. Sand alternates with minor mud drapes	Tidally-influenced unidirectional currents with low to moderate speeds. Alternation of low and high energy conditions. Sandy ripples were deposited by high energy tidal and/or fluvial flows, whilst muddy drapes were deposited during slack water conditions.
	Lm	Silt	Massive. Intense bioturbation. Presence of rhizoliths.	Structureless due to bioturbation and soil development.
Siltstone	**Lr**	Silt	Current ripple lamination. Sometimes, wave ripple lamination.	Migration of current ripples; occasional storm events dominated by oscillatory flows. Associated with fluvial and tidally- influenced currents.
	Ll	Silt	Horizontal lamination (lower flow regime). Uneven lamination.	Settling from suspension in low energy conditions.
	Fm	Clay	Massive. Intense bioturbation. Presence of rhizoliths.	Settling from suspension in very low energy conditions.
Claystone	**Fl**	Clay	Horizontal lamination (lower flow regime). Uneven lamination. Locally, presence of plant remains and coal.	Settling from suspension in very low energy conditions.

6.5. Facies associations and depositional sub-environments

The proposed facies association scheme, based on the lithofacies (Table 6.1) establishes six facies associations termed Heterolithic Unit Facies Association 1 (HFA 1) to HFA 6, assigned to broadly proximal and increasingly distal environments. The following section contains a detailed description of each facies associations, including outcrop-derived observations, lateral and vertical lithofacies, as described in Table 6.1, variation in both outcrop and cores, geometric data based on digital outcrop models, bounding surfaces, Gamma-ray log response and analysis of both paleocurrents and dip tadpole patterns based on image logs. Gamma-ray log patterns (electrofacies patterns) were also characterized and interpreted following the models of Emery & Myers (1996) and Slatt (2013).

6.5.1. HFA 1: Supratidal flat

Description

HFA 1, with up to 10 m of thickness and more than 1 km of lateral extent, is characterized by a tabular geometry with horizontal and sharp bounding surfaces. This facies association was drilled by all wells (HU 1 to HU 4) and occurs in both subunits. It is distinguished by a sand:mud ratio of 10:90, characterized by dominant mudstones alternating with single to amalgamated 10 to 50 cm thick sandstone beds (Fig. 6.5). Mudstone deposits consist principally of metre-scale bedsets of clay, clayey siltstone or siltstone. These are generally bioturbated, although, in these muddy, dark red-coloured sediments, bioturbation is commonly difficult to distinguish with confidence (Fig. 6.5a-b). Occasionally, roots traces are also recognised (Fig. 6.5b). The sandstone beds are very fine grained, well-cemented, with mud pebble lag (Lithofacies Gm) at the base, massive and/or horizontal lamination (Lithofacies Sh/Sm) and wave ripples (Lithofacies Sw) toward the top. *Arenicolites isp.* trace fossils are observed toward the top of these sandstone beds (Fig. 6.5a-b). Horizons marked by desiccation cracks and both coal and dark carbonaceous shales, characterized by horizontal lamination (Lithofacies Fl), are also present in this facies association (Fig. 6.6), especially in Subunit 2.

In the GR log, this facies association is characterized by a mean of 158 API, values ranging from 81 to 269 API. Mudstones show mean values of 162 API, whilst sandstones show surprisingly high mean values of 125 API suggestive of abundant K-Feldspars and/or heavy minerals. In terms of curve shape, mudstones show a serrated-cylindrical shape, whilst sandstones are characterized by a smooth-egg shape (Fig. 6.5d), although locally, some intervals

show a smooth funnel shape. This occurs when the top of the sandstone bed is intensely bioturbated and overlain by a cm-scale bed comprising green mudstones (Fig. 6.5b)

Dip tadpole analysis, with a total of 36 measurements, shows poly-directional azimuths and planar to high dip angles (Fig. 6.5d). The predominant azimuths are toward the southeast, with a mean azimuth of N137E, ranging from N016E to N346E.

Interpretation

This facies association is interpreted as a supratidal flat. Mudstone deposits with abundant bioturbation, paleosols and desiccation cracks levels indicate the low energies and common evidence of emergence, typical of supratidal environments. Massive sandstone beds are interpreted as episodic high energy events associated with floods of fluvial origin or storm events. A coal-bearing horizon towards the top is interpreted as the deposit of a peat bog indicative of freshwater ponds (Fig. 6.4a and Fig. 6.6).
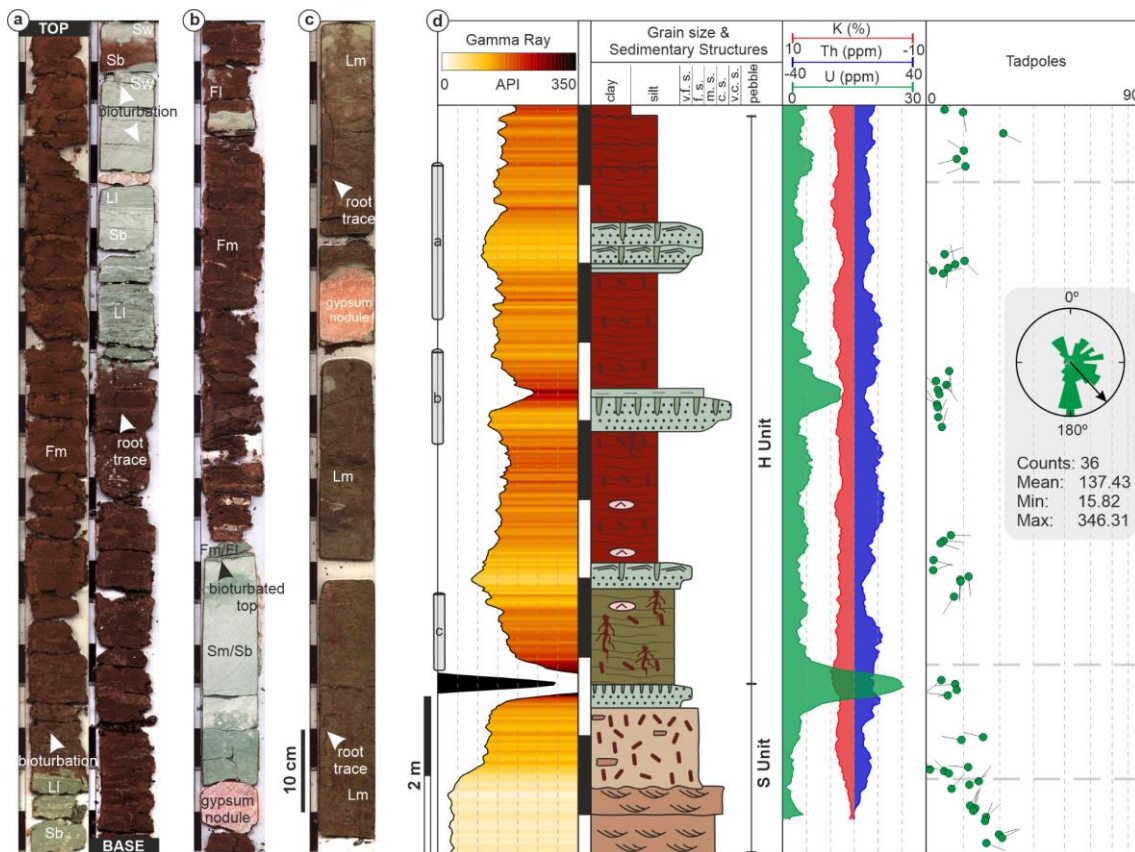
Fig. 6.5. Subsurface data characterizing the Supratidal Flat facies association (HFA 1) in Subunit 1. **(a)** - **(c)** Core view showing mudstone deposits and thin sandstone beds from Well HU 3. **(d)** HU 3 well composite displaying the GR log, core description and SGR log supratidal flat facies associations.
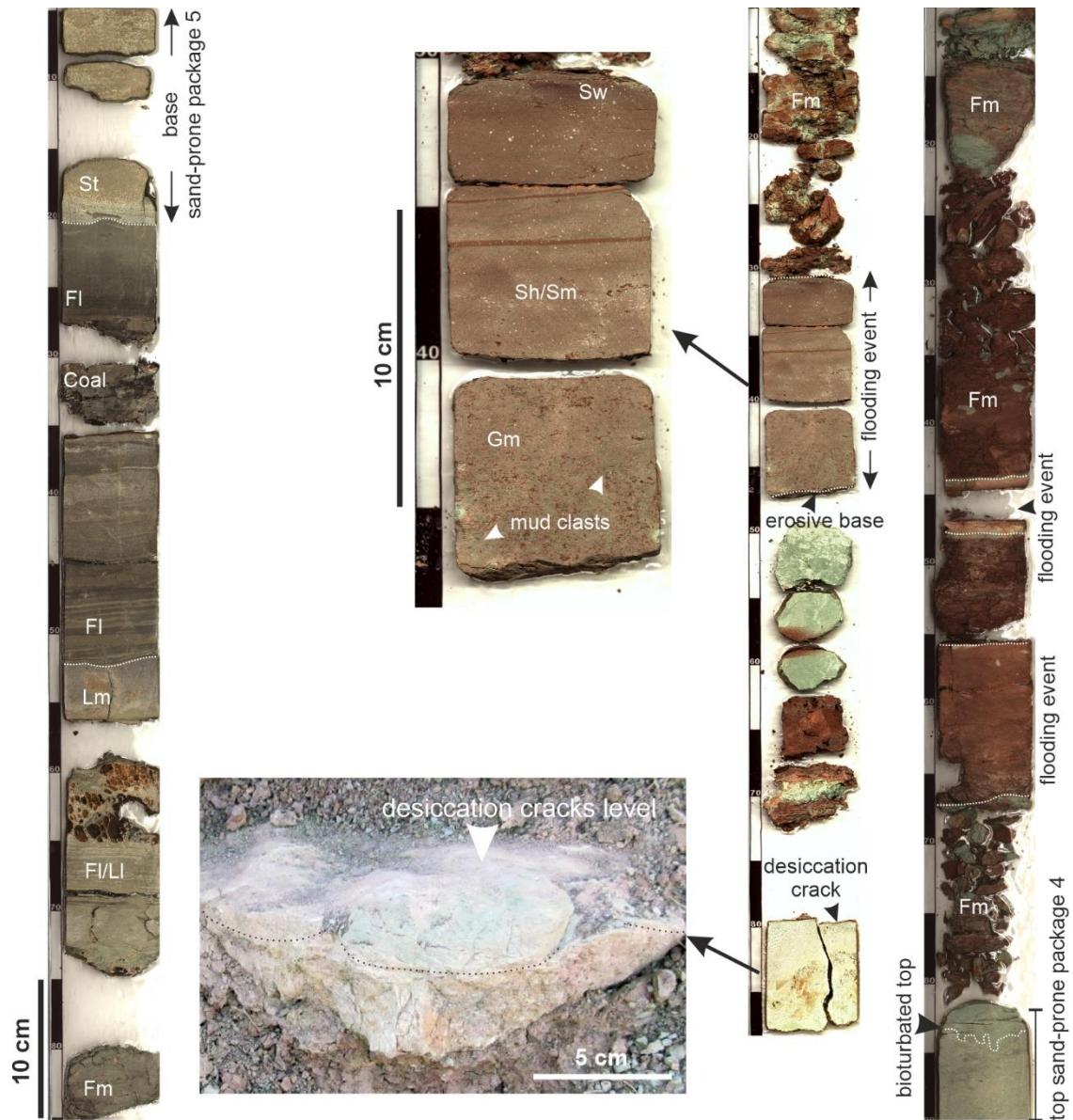
Fig. 6.6. Core views showing the Supratidal Flat facies association (HFA 1) and an outcrop photograph showing desiccation cracks in Subunit 2, from Well HU 2.

6.5.2. HFA 2: Tidal point bar

HFA 2 corresponds to Sand-prone Package 4. It is characterized by both fining-upwards and aggradational facies stacking trends, occurring as asymmetrical, sigmoidal-shaped bodies with planar and erosive bases and planar, sharp tops. This facies association was drilled by Wells HU 2 and HU 3 and appears only in Subunit 2, infilling the incised valley. On the basis of the sand:mud ratio and predominant lithofacies, two sub-divisions of this associations can be differentiated: heterolithic tidal point bar (HFA 2.1), with a sand:mud ratio of 40:60, and sand-dominated tidal point bar, with a sand:mud ratio of 60:40.

HFA 2.1: Heterolithic tidal point bar

Description

The heterolithic tidal point bar facies association (HFA 2.1), occurs as packages up to 10 m thick, characterized by a complete spectrum of heterolithic structures (flaser, wavy and lenticular bedding), although wavy bedding (Lithofacies Wb) is dominant (Fig. 6.7 a-b). Inclined heterolithic bedding (Lithofacies IHb) and dewatered, deformed layers are also observed. In addition, this association is also characterized by a basal mud clast lag (Lithofacies Gm) and several superimposed sets characterized by reactivation surfaces, rip-up mud clasts, trough cross-bedded fine sandstone (Lithofacies St) and fine to very fine sandstones with ripple cross-lamination (Lithofacies Sr); Fig. 6.7a). This facies association was only drilled by well HU3.

In the GR log, FA 2.1 is characterized by values ranging from 101 to 170 API, a mean value of 137 API and a cylindrical shape (Fig. 6.8f). Dip tadpole analysis, with a total of 34 measurements, shows principally unidirectional azimuths and low to high dip angles. Several tadpole groups showing unidirectional azimuths and shallow-to-steep-to-shallow dip angle pattern can also be identified (Fig. 6.8f). The predominant azimuths are toward the southeast, with a mean azimuth of N156E, ranging from N021E to N211E (Fig. 6.8f).

Interpretation

This facies association is interpreted as having accumulated within the point bars of meandering, strongly tidally-influenced channels under subtidal conditions. The basal lag is interpreted as deposited under high energy conditions along the thalweg of tidal or fluvio-tidal channels (Dalrymple & Choi, 2007).

HFA 2.2: Sand-dominated tidal point bar

Description

The sand-dominated tidal point bar facies association (HFA 2.2), occurs as packages up to 5 m thick, comprising cross-bedded, very-fine to medium sandstones. Inclined Heterolithic Stratification (Lithofacies IHS) and lateral accretion units are also identified. Significant lateral variability can also be observed in lithofacies in outcrop and between both Wells HU 2 and HU 3 (Fig. 6.7b).

In the HU 2 section, several fining-upward sets, characterized by basal reactivation surfaces and rip-up mud clasts (Lithofacies Gm), trough cross-bedding very-fine sandstones (Lithofacies St) and heterolithic trough cross-bedding (Lithofacies Ht), toward the top, respectively, are observed. Lithofacies Ht, characterized by convolute lamination and incorporation of mud pebbles into foresets (Fig. 6.7c and Fig 6.8b) also occurs. The reactivation surfaces are interpreted as lateral accretion surfaces. Ripples flowing up-slope along lateral accretion surfaces are also identified in outcrop (Fig. 6.7c).

In contrast, in the HU 3 section, very fine sandstones, characterized by sets of trough cross-bedding (Lithofacies St) and ripple cross-lamination (Lithofacies Sr), separated by mud drapes are observed (Fig. 6.7d and Fig 6.8e). In addition, Lithofacies Sh and also flame structures are observed (Fig. 6.8e). Wave ripples (Lithofacies Sw) and flaser bedding (Lithofacies Fb) commonly occur toward the top of this association.

The GR response is characterized by values ranging from 62 to 152 API, a mean of 108 API and a smooth-egg shape profile followed by a cylindrical shape in both Wells HU 2 and HU 3. Dip tadpole analysis, with a total of 72 measurements, shows principally unidirectional azimuths and low to high dip angles (Fig. 6.8f). The predominant azimuths are toward the southeast, with a mean azimuth of N143E, ranging from N55E to N321E. Several tadpole groups showing unidirectional azimuths and shallow-to-steep-to-shallow dip angles pattern can also be identified (Fig. 6.8f).

Interpretation

This facies association is interpreted as a sand-dominated tidal point bar. The presence of ripples flowing up-slope along lateral accretion surfaces highlights the occurrence of helicoidal flow, a hydrodynamic process typical of point bars. In addition, the mud drapes intercalated with sandstones and IHS are interpreted as the record of frequent oscillations of energy associated with tidal currents. As such, HFA 2.2 is also interpreted as a tidal-dominated meandering channel, but more proximal in comparation with HFA 2.1.
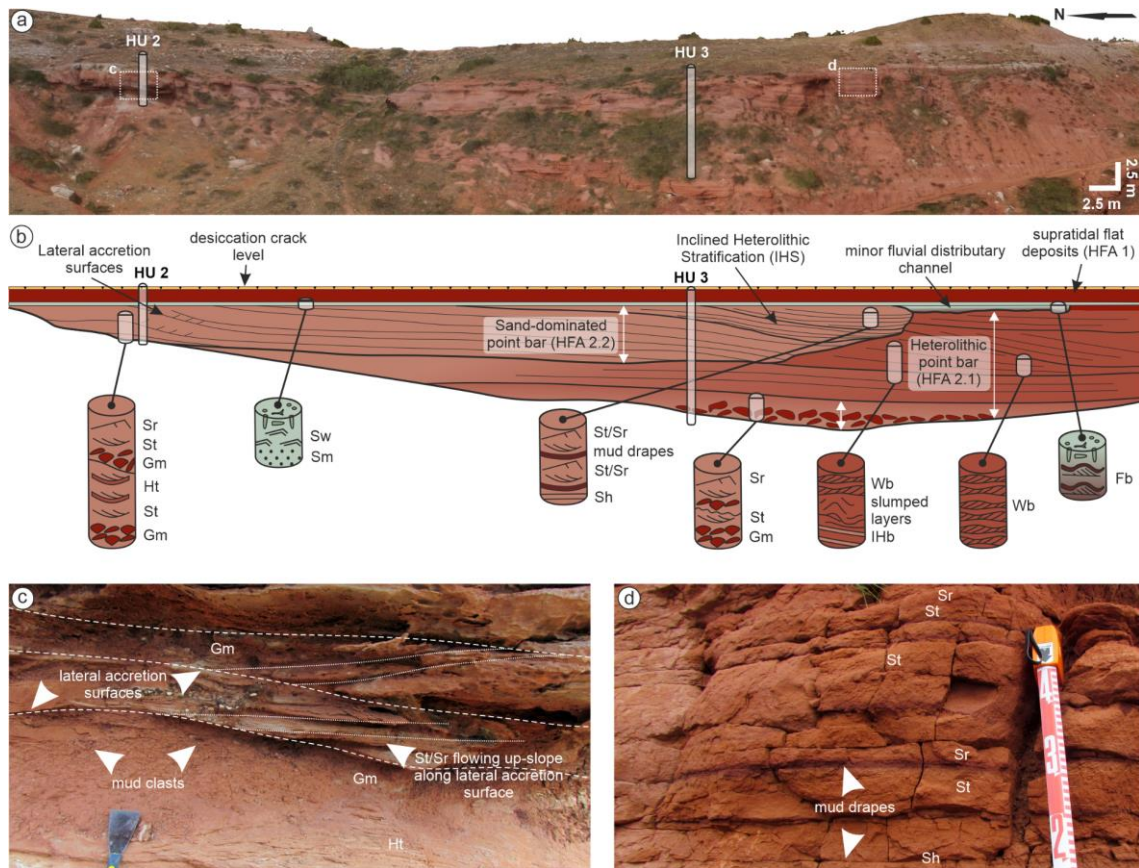
Fig. 6.7. Outcrop interpretation of the tidal point bar facies association (HFA 2). **(a)** Digital outcrop model showing the wells and location of the detailed images. **(b)** Outcrop interpretation to scale showing the spatial and vertical relationship between sub-associations, a detailed interpretation of internal surfaces and lithofacies variability highlighted by simplified core sections. **(c)** Close-up view of outcrop showing a detailed internal structure of lateral accretion units. **(d)** Close-up view of the outcrop showing very fine sandstones, characterized by thin sets of trough cross-bedding (Lithofacies St) and ripple cross-lamination (Lithofacies Sr), separated by mud drapes.
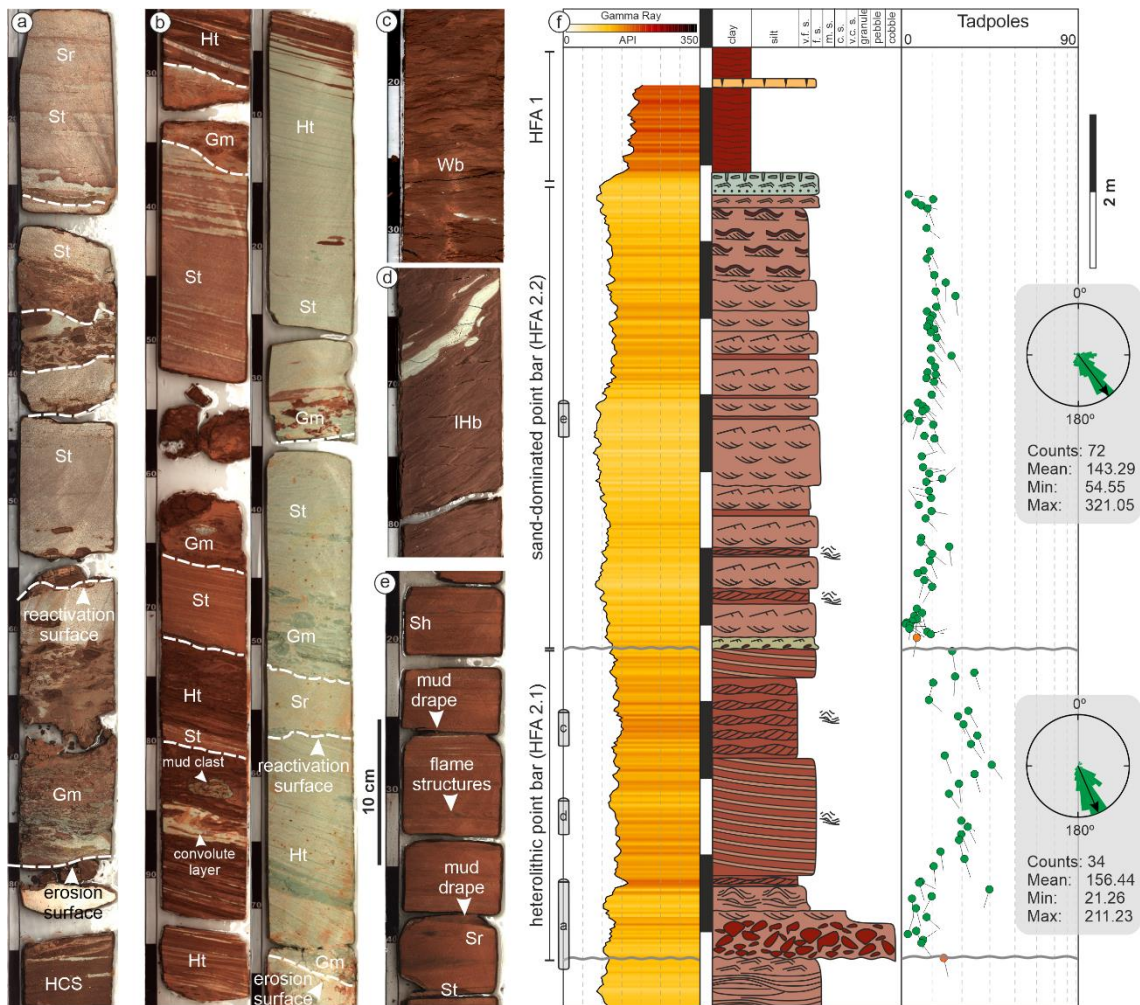
Fig. 6.8. Summary of subsurface data characterizing the tidal point bar facies association (HFA 2). **(a)** Core view from Well HU 3 showing the lithofacies at the base of the heterolithic point bar facies association (HFA 2.1). **(b)** Core view from Well HU 2 showing the lithofacies of lateral accretion units comprising the sand-dominated tidal point bar facies association (HFA 2.2.). **(c)** Core view from Well HU 3 showing the wavy bedding heterolithic sandstones characteristic of HFA 2.1. **(d)** Core view from Well HU 3 showing the Inclined Heterolithic bedding (Lithofacies IHb) typical of HFA 2.1. **(e)** Core view from Well HU 3 showing sandstone sets with mud drapes, characteristic of HFA 2.2. **(f)** Section from the Well HU 3 composite displaying the GR log, core description and dip tadpole log for the tidal point bar facies associations.

6.5.3. HFA 3: Intertidal sandbars

Description

HFA 3, occurs as thin sheet-like packages 2m thick and with up to 500 m of lateral extension. It corresponds to Sand-prone Package 5 located toward the top of Subunit 2. This facies association occurs as an elongate-shaped body with a horizontal and erosive base and a convex-up, sharp top. HFA 3 was drilled by Well HU 4 only**.** It is characterized by a sand:mud ratio of 60:40, forming a weakly fining-upward package dominated, at the base, by planar-laminated (Lithofacies Sh) and trough cross-bedded (Lithofacies St) green-coloured sandstone

(Fig. 6.9c and d) overlain by several sets of sigmoidal cross-stratified sandstones displaying a gradual upwards increase in the foreset dip angle (including parabolic contorted folds) and also separated by millimetre-scale, mud drapes, reactivation surfaces, bidirectional ripple and flaser laminations in the toesets (Fig. 6.9a-c). Scattered mud clast layers are also intercalated with foresets (Fig. 6.9e). Erosional surfaces typically truncate the top of cross-bed sets (Fig. 6.9b-c) with the sole exception of the uppermost set which has preserved the topset, showing wave ripples (Fig. 6.9f).

The GR log is characterized by values ranging from 60 to 152 API, a mean value of 99 API, and the superposition of two smooth egg shape profiles (Fig. 6.9g). Dip tadpole analysis, with a total of 37 measurements, shows bidirectional azimuths and low to high dip angles (Fig. 6.9g). The predominant azimuths are toward the south-east, with a mean azimuth of N106E, ranging from N56E to N299E. Some dip tadpole sets show a gradual upwards increase in dip angle (Fig. 6.9g).

Interpretation

HFA 3 is interpreted as the deposits of tidal- and wave-influenced bars in the estuarine/intertidal zone (intertidal sandbars). Deformed cross-bedding, reactivation surfaces and mud clasts are interpreted, on the basis of paleocurrent analysis as the deposits high-energy ebb-tidal flows (Dalrymple, 1992). The sigmoidal geometry associated with cross-stratified sandstones reflects migration of simple dunes, in response to the increase and then decrease of flow energies associated with tidal currents (Mutti *et al.,* 1985; Dalrymple, 1992; Olariu *et al.,* 2012). Fine-grained laminae in dune toesets are linked to suspension settling in ponds preserved during low-tide emersion. An upward-decrease in the flow energy is revealed by the preservation of fair-weather wave reworking structures and mudstone deposits at the top of the sandstone package. Paleocurrent measurements (dip tadpole analysis) show a bidirectional flow with a predominantly seaward migration characteristic for this facies association.
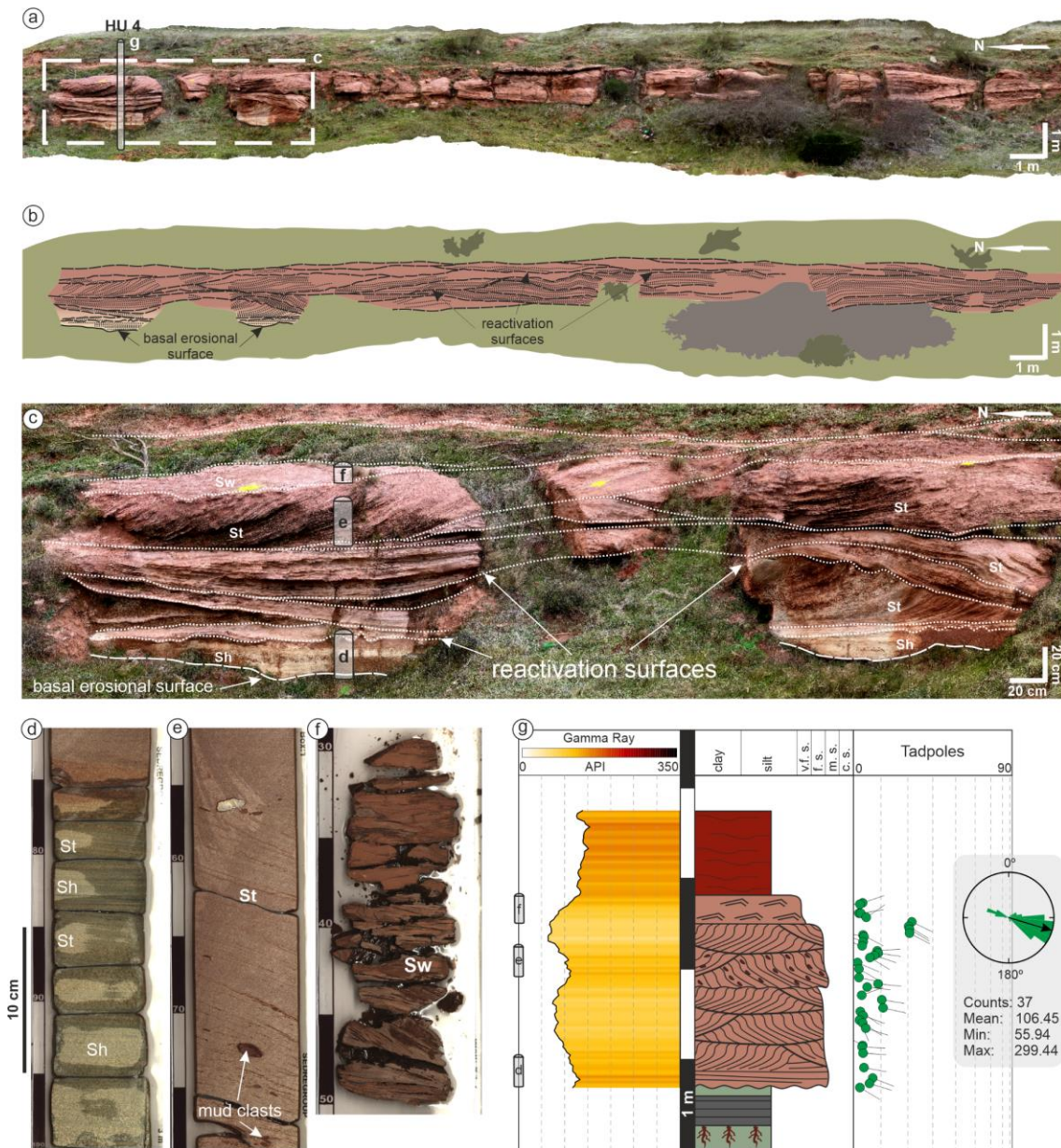
Fig. 6.9. Summary of outcrop and subsurface data for the intertidal sand bar facies association **(HFA 3)**. **(a)** Digital outcrop model of Sand-prone Package 5. **(b)** Detailed interpretation of the depositional architecture and internal sedimentary structure of Sand-prone Package 5. **(c)** Close-up view of a digital outcrop model section showing the base, top and internal reactivation surfaces of Sand-prone Package 5. **(d-f)** Core views of planar-laminated greenish sandstones (Lithofacies Sh), trough cross-bedded sandstones with mud clasts lining foresets (Lithofacies St) and wave rippled sandstones (Lithofacies Sw), respectively. **(g)** Well HU 4 composite displaying the GR log, core description and dip tadpoles for this association.

6.5.4. HFA 4: Subtidal bars

Description

Association HFA 4 corresponds to Sand-prone Package 1, occurring within Subunit 1. It is up to 14 m thick with up to 1 km of lateral extension (Fig. 6.10a), and occurs as an elongate-shaped body with a horizontal, sharp to locally erosive base and a convex-up, sharp top. HFA 4 was drilled by Wells HU1 and HU 3. Sand:mud ratios range from 60:40 to 40:60, giving the Association a broadly mixed heterolithic aspect. The most common sedimentary structure is complex cross-bedding characterized by an alternation of mm-scale sand and clay-enriched foresets (Lithofacies Ht) associated with bidirectional dipping sand-mud couplets forming bundles truncated by reactivation surfaces (Fig. 6.10e-f and Fig. 6.11f-g).

Locally, where the basal surface is erosive, Association HFA4 is characterized by massive and cross-bedded, fine to very coarse-grained sandstones (Lithofacies Sm, Sp and St; Fig. 6.10e-d and Fig. 6.11a-b). In addition, several reactivation surfaces overlain by pebbly coarse grain sandstones to pebbly gravels are observed (Lithofacies Gm, Fig. 6.11d). This lithofacies grades upwards to cross-bedded sandstones (Lithofacies St). Locally, heterolithic wave-rippled sandstones also occur (Fig. 6.10b).

Association HFA4 also shows a noteworthy lateral gradation in the heterolithic character of the geobodies. In this way, the succession penetrated by Well HU 1 shows a sand:mud ratio of 60:40, characterized principally by fine to very coarse-grained sandstones (Lithofacies Sm, Sp, St and Sw; Fig. 6.10c-d and Fig. 6.11a-d) and locally by pebbly coarse (Lithofacies Gm); whereas, in Well HU 3, the sand:mud ratio is 40:60, characterized mainly by Lithofacies Ht (Fig. 6.10e-f and Fig. 6.11f-g).

The GR response for this facies association is characterized by a mean value of 129 API. However, there is some variation between the two wells; Well HU 1 shows a lower mean value (120 API, ranging from 74 to 164 API) when compared to Well HU 3 (144 API, ranging from 86 to 204 API), reflecting the more heterolithic character in Well HU 3 compared to Well HU 1, as described above. In terms of GR curve shape, in Well HU 1, HFA 4 is characterized by the superposition of smooth cylindrical and egg shapes (Fig. 6.11h). Well HU 3 also shows a funnel shape at the base succeeded by smooth, cylindrical shapes. Similarly, smooth, cylindrical GR profiles can also be observed toward the top of the HFA4 facies sequence (Fig. 6.11i).

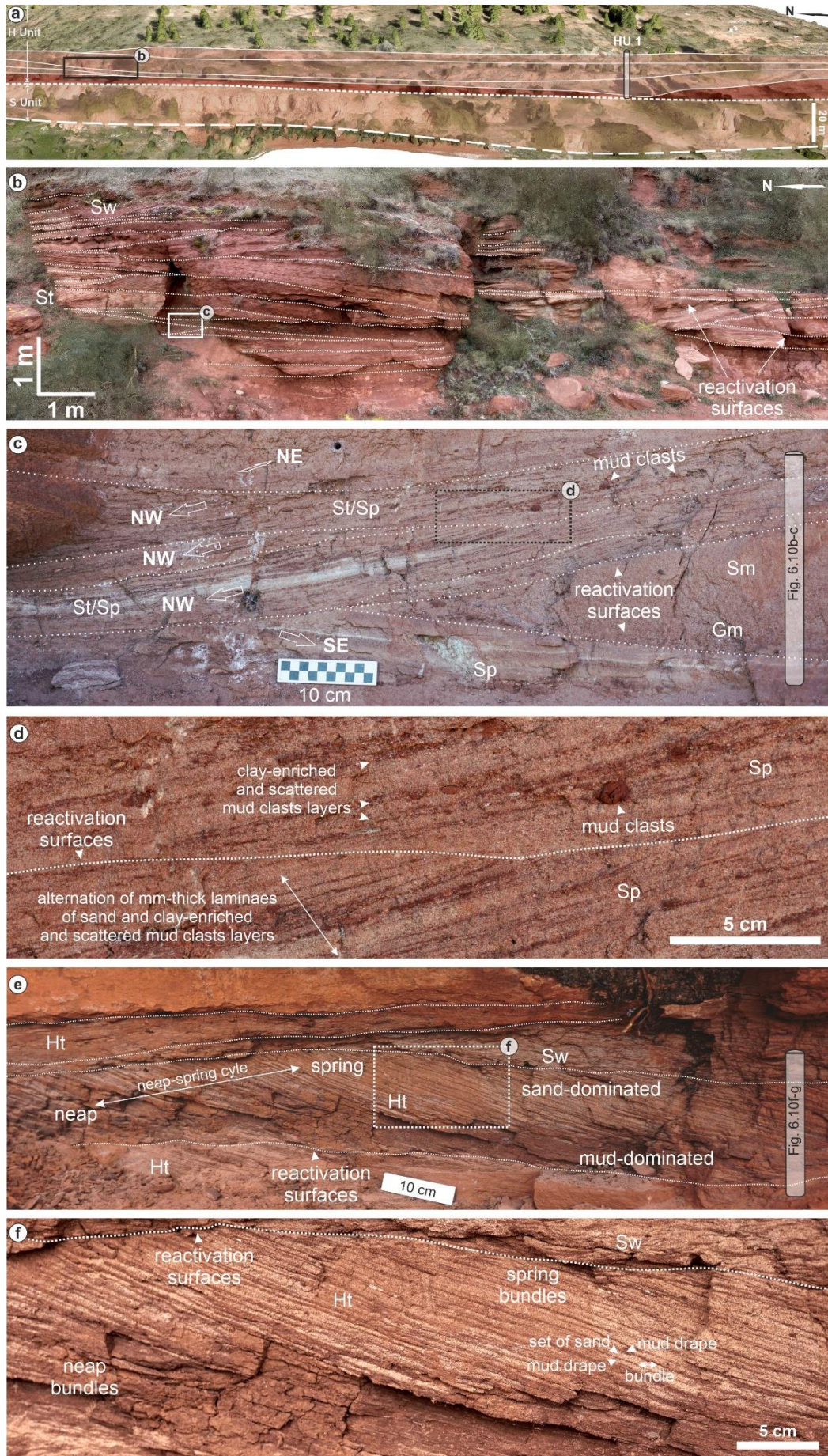**Fig. 6.10.** Outcrop interpretation of the subtidal sandbar facies association (HFA 4). **(a)** Digital outcrop model showing the location of Well HU 1 and detail image location. **(b)** Close-up view of digital outcrop model showing a detailed interpretation of the depositional architecture of Sand-prone Package 1. **(c)** Close-up view of outcrop showing cross-stratified sandstone sets, characterized by trough cross-bedded (Lithofacies St), planar cross-bedded sandstones (Lithofacies Sp), massive sandstones (Lithofacies Sm) and pebbly coarse sandstones (Lithofacies Gm). **(d)** Close-up view of (c) showing in detail the alternation of mm-thick laminae of sand and clay-enriched and scattered mud clasts layers. Also see Fig. 6.11c for a view of this facies in core. **(e)** Close-up view of outcrop showing sand-mud couplets in bundles interpreted as tidal rhythmites (Lithofacies Ht) and wave-rippled heterolithic sandstones (Lithofacies Sw). **(f)** Close-up view of (d) showing the tidal couplets in detail.

Dip tadpole analysis, with a total of 127 measurements in Well HU 1, shows principally unidirectional azimuths and low to high dip angles. Bidirectional azimuths and low to high dip angles also can be observed in this well. The predominant azimuths are toward the southeast, with a mean azimuth of N93E, ranging from N9E to N353E (Fig. 6.11h). Well HU 3, in contrast, with a total of 44 measurements, shows principally bidirectional azimuths and low to high dip angles. The predominant azimuths are toward the northeast and toward the south-southeast, with a mean azimuth of N100E, ranging from N5E to N344E (Fig. 6.11i).

Interpretation

This facies association is interpreted as the deposits of tidal sandbars migrating across a sandflat in the intertidal to subtidal transition zone of a tidal-dominated coastal plain. The basal scoured surface corresponds to the lateral migration (or major avulsion) of the tidal channel. Cross-bedded sandstones, pebbly coarse sandstones and pebbly gravels are interpreted to have been deposited under high energy conditions, as barforms developed along the thalweg of tidal channels. The alternation of mm-scale sand and clay-enriched foresets evidences the frequent oscillations of energy associated with tidal currents. Bidirectional dipping cross-stratified sand-mud couplets forming bundles are interpreted as tidal rhythmites (Coughenour *et al.*, 2009; Longhitano *et al.*, 2012). In addition, these tidal bundles show rhythmic changes in individual bed thickness reflecting the shift from spring to neap and back again as each tidal cycle takes place (Visser 1980). During spring tides, the more vigorous currents result in thick sand units and small mud drapes; whereas during neap tides, lower energy currents result in thinner sand units and thicker mud drapes (Visser, 1980; Fig. 6.10f). The characteristic cyclical stacking of sand and mud couplets indicate vertically accreted tidal facies, commonly developed in intertidal to subtidal environments as a response to alternating flood (subordinate) and ebb (dominant) tidal currents. The erosional surfaces truncating the top of these tidal bundles are interpreted as reactivation surfaces generated by the subordinate ebb currents (Klein, 1970).
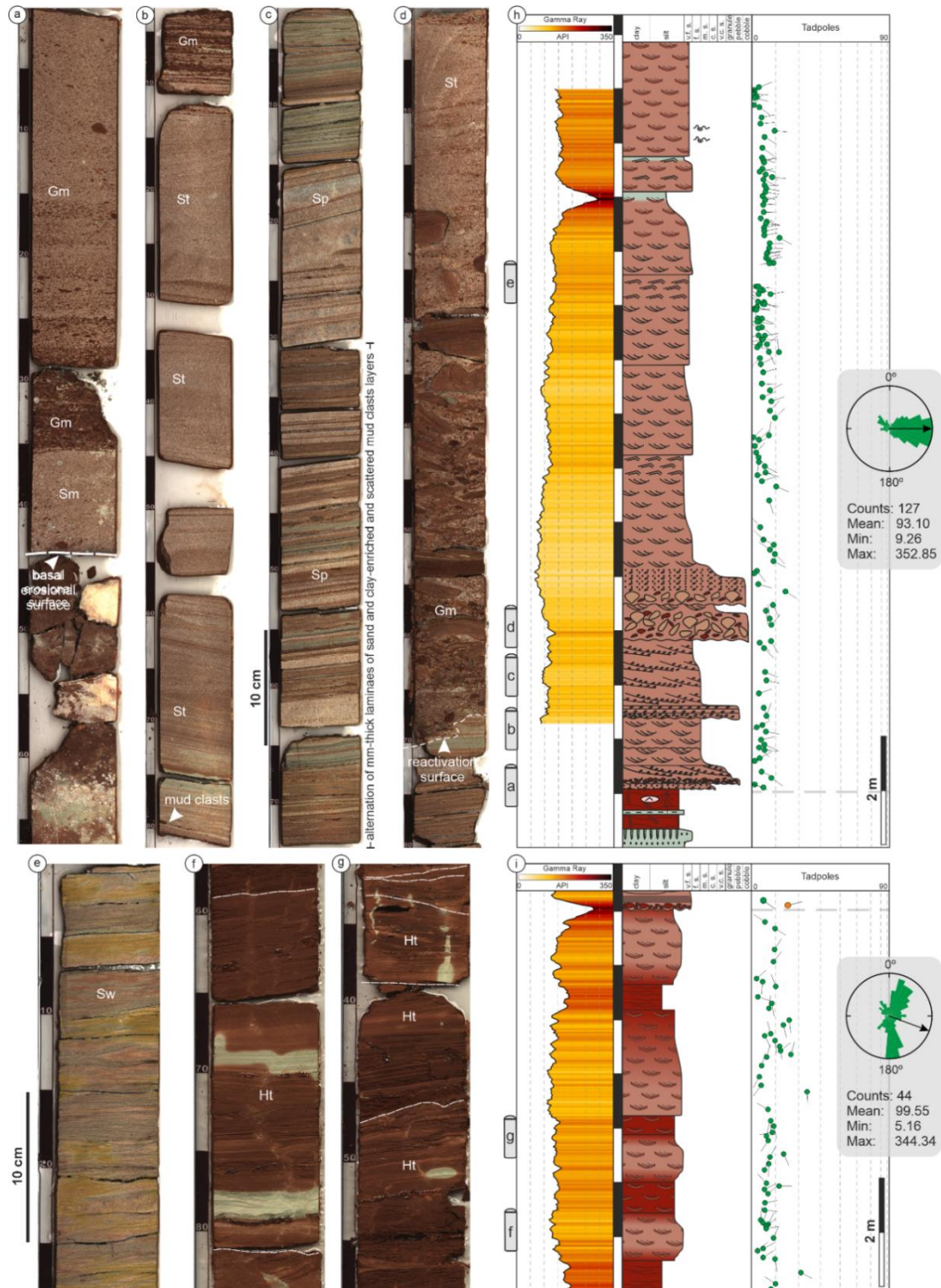
Fig. 6.11. Subsurface characteristics of the Subtidal sandbar facies association (HFA 4); **(a)** Core view from Well HU 1 showing the basal scour surface of the HFA4 facies sequence overlain by massive, coarse-grained sandstones (Lithofacies Sm) and scattered mud intraclasts. **(b)** Core view from Well HU 1 showing the cross-bedded and pebbly coarse sandstones (Lithofacies St and Gm). **(c)** Core view from Well HU 1 showing the alternation of mm-scale sand and clay-enriched foresets and scattered mud clasts lining foresets (Lithofacies Sp). **(d)** Core view from Well HU 1 showing a reactivation surface overlain by pebbly gravel (Lithofacies Gm) and trough cross-bedded sandstones (Lithofacies St). **(e)** Core view from Well HU 1 showing wave-rippled heterolithic sandstones (Lithofacies Sw). **(f)** – **(g)** Core views from Well HU 3 showing heterolithic cross bedding (Lithofacies Ht). **(h)** – **(i)** Complete HU 1 well composite and a section of the HU 3 well composite, respectively, displaying the GR log, core description and dip tadpole plot for Facies Association HFA4.

6.5.5. HFA 5: Hyperpycnite

Description

A thin sandstone package, corresponding to Sand-prone Package 2, is observed in Subunit 1 (Fig. 6.4e). This package is characterized by a tabular or sheet-like geometry, forming a body to 0.5 m thick and with up to 50 m of lateral extension (perpendicular to depositional dip), with a horizontal, sharp base and convex-up, sharp top. Internally it displays a distinctive lithofacies sequence consisting of very fine sandstones characterized by wave modelled current ripple lamination (Lithofacies Swr) at the base and sub-critically climbing ripples (Lithofacies Sbcr), super-critically climbing ripples (Lithofacies Spcr) and in-phase climbing ripples (Lithofacies Sicr) toward the top, respectively (Fig. 6.12). This facies association was not drilled by any well and is thus recognised only from outcrop

Interpretation

This facies association is interpreted as a hyperpycnite, generated by river floods in the subtidal zone. The vertical stacking of Lithofacies Swr-Sbcr-Spcr-Sicr shows a waxing to waning flow sequence typical of a density or hyperpycnal flow and strongly suggests a fluvial influence during the deposition of Subunit 1 (Mulder *et al.*, 2003; Zavala & Pan, 2018).
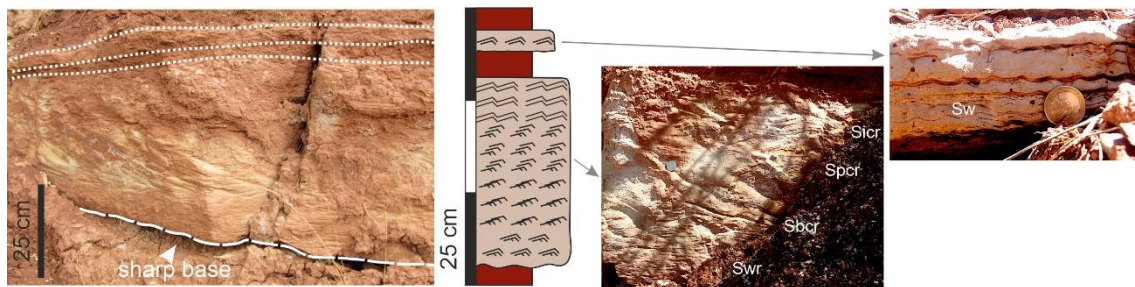
Fig. 6.12. Close-up view of outcrop, sedimentary log and detailed outcrop pictures of Sand-prone package 2. See Figure 6.4e for location of this outcrop in a general view.

6.5.6. HFA 6: Storm-dominated shoreface

Description

This facies association corresponds to Sand-prone Package 3. It is up to 4m thick, characterized by the stacking of several 15-20cm thick beds of fine-grained sandstones, a basal scoured surface lined with a mud pebbles lag, hummocky-cross bedding (HCS) or swaley cross-stratification (SCS) sandstones (Lithofacies HCS) alternating with heterolithic combined flow

wave rippled sandstones (Lithofacies Sw; Fig. 6.13). This association directly overlies the intraformational incised surface, marking the base of Subunit 2 (Fig. 6.4e). The top of this sand-prone package is also erosional, interpreted as a fluvio-tidal scour surface (Fig. 6.4e).

The GR log, is characterized by values ranging from 80 to 193 API, a mean value of 118 API, and a smooth-cylindrical shape (Fig. 6.13f). Dip tadpole analysis, with a total of 81 measurements, shows poly-directional azimuths and planar to low-angle dip angles (Fig. 6.13f). The predominant azimuths are toward the southeast, with a mean azimuth of N136E, ranging from N0E to N344E.

Interpretation

This facies association is interpreted as a storm-dominated shoreface. Hummocky-cross bedded sandstones (Lithofacies HCS) are interpreted as the deposits of high-energy oscillatory currents associated with large storm waves (Hunter & Clifton, 1982; Klein & Marsaglia, 1987; Duke *et al.*, 1991; Yang *et al.,* 2006; Ichaso & Dalrymple, 2014). The occurrence of wave ripples capping the HCS, and showing evidence of combined flow, indicates that there was a unidirectional component to the water motion, due either to wind-driven residual motion and/or the presence of superimposed tidal currents (Hill *et al.,* 2003; Yang *et al.,* 2005; Ichaso and Dalrymple, 2014). These wave ripples are characterized by draping mud lamina formed during low tide slackwater, followed by a sandy lamina formed during the flood tide. Another mud lamina is formed during the high tide slackwater, followed by deposition of a sandy lamina during the peak of the ebb tide. This rhythmic alternation of heterolithic wave ripple couplets records the periodicity typical of short-term tidal cycles (Reineck & Singh, 1980; Visser, 1980; Longhitano, 2011). Accordingly, Sand-prone Package 3 represents a storm-dominated but tidally-influenced mid to upper shoreface.

The smooth-cylindrical shape of the GR highlights the clean sand interval associated with the hummocky cross-stratification. The HCS is also distinguished in core by dip tadpoles, characterized by azimuths showing considerable dispersion (poly-directional azimuths) but still a dominantly seaward-directed paleocurrent direction (towards southeast) reflecting the importance of the combined flow component.
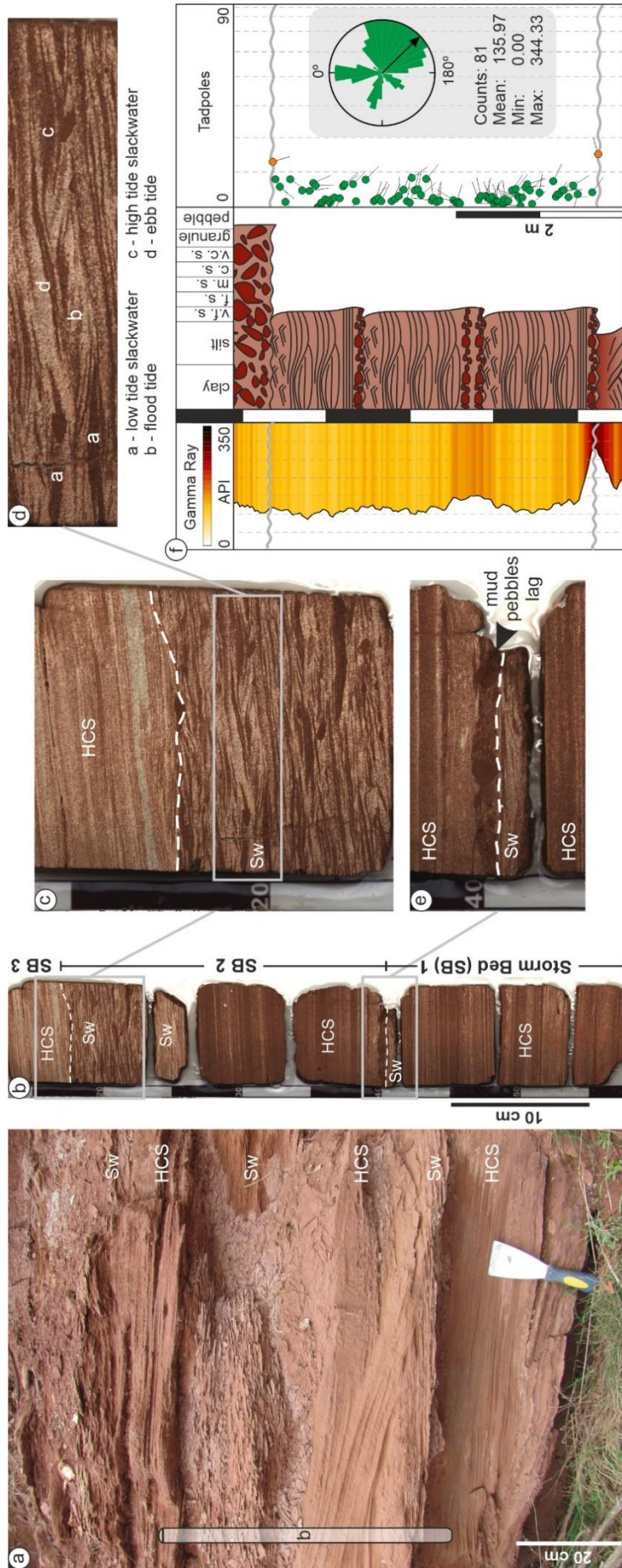
Fig. 6.13. Outcrop and subsurface data characteristic of the Storm-dominated shoreface facies association (HFA 6). **(a)** Detailed outcrop view of Sand-prone Package 3 comprising a basal scoured surface with a mud pebbles lags, hummocky-cross bedded (Lithofacies HCS) and heterolithic sandstones with wave ripples (tidal ripples, Lithofacies Sw). **(b)** Core view from Well HU 3 showing the superposition of three storm beds (SB1-SB3). **(c)** Detailed core view showing storm-wave dominated shoreface overlying fair-weather wave/tidal mixed energy-dominated shoreface. **(d)** Detailed core view of fair-weather heterolithic combined flow wave ripples (tidal ripples) showing one low to high tide cycle. **(e)** Detailed core view showing basal scoured surface typical of storm beds overlain by a mud pebble lag and hummocky-cross bedding. **(f)** Well HU 3 composite displaying the GR log, core description and dip tadpole log for the storm-dominated shoreface facies association (HFA 6).

6.6. Integrating outcrop and subsurface data in a depositional model

The assemblage of facies associations identified in this study of the H Unit can be interpreted within the framework of several published models for shoreline sedimentation (e.g. Dalrymple, 1992; Dalrymple and Choi, 2007; Ichaso and Dalrymple, 2014; Gil-Ortiz *et al.,* 2019). In general terms the complex of depositional environments identified in the H Unit may be envisaged as a mixed tidally-influenced and wave-influenced deltaic system and adjacent shoreface. Within this genetic framework, a 3D conceptual model has been constructed which includes all the observed facies associations, and their key features in terms of lithofacies and subsurface data, placed in their paleogeographic context (Fig. 6.14). Although this conceptual model is correct in terms of the spatial relationships in a 2D framework, it is important to note that processes related to relative sea-level change were also important in sequence development. These issues are addressed within a sequence stratigraphic framework of the H Unit in Chapter 7.

Based on the proposed conceptual model, facies associations can be classified into three main types of reservoir geobodies (Table 6.2): (a) elongate geobodies, typical of subtidal sandbar facies (HFA 4) and intertidal sandbar facies (HFA 3); (b) asymmetric-sigmoidal geobodies formed by tidal-dominated point-bar facies (HFA 2); and (c) tabular geobodies characterized by hyperpycnite facies (HFA 5) and open-coast shoreface facies (HFA 6). Supratidal flat facies association (HFA 1) also form mud-prone tabular geobodies but can be considered as non-reservoir. Thus, in modelling terms, these tabular non-reservoir geobodies could be considered as background.

6.6.1. Elongate geobodies

Elongate geobodies in the H Unit can be characterized as either: subtidal sandbars (HFA 4), or intertidal sandbars (HFA 3).

In this study, individual Subtidal sandbars (HFA 4) are up to 350 m in width and up to 14 m in thickness (Fig. 6.14 and Fig. 6.15a). However, by migration of these individual geobodies, sheet-like bodies with high-lateral continuity (above 1 km) can be formed. In contrast, intertidal sandbars (HFA 3) appear to be restricted to tidal channels up to 500 m in width (Fig. 6.14 and Fig. 6.15d) and up to 2 m of thick.

Internally, Subtidal sandbar deposits (HFA 4) are principally characterized by fine to very coarse-grained sandstones (Lithofacies Sm, Sp, St and Sw) and locally by pebbly coarse grain sandstones (Lithofacies Gm). This geobody is notably more heterolithic in character in a seaward direction, characterized by cross-stratified sand-mud couplets forming tidal bundles (Lithofacies Ht). As such, within this geobody, the sand:mud ratio varies from 60:40, in a landward direction (proximal subtidal sand bars) to 40:60, in a seaward direction (distal subtidal sand bars) (Fig. 6.14 and Fig. 6.15a). In addition, mud drapes are also observed to increase in thickness in a seaward direction, varying from cm-scale (in proximal subtidal sandbars) to decimetre-scale (in distal subtidal sandbars).

Paleocurrents, observed in outcrop and dip tadpole logs, often show bidirectional azimuths and low to high dip angles, although these are more common in distal subtidal sandbars (HFA 4) and intertidal sandbars (HFA 3). In marked contrast, proximal subtidal sandbars (HFA 4) predominantly show unidirectional, seaward-directed.

6.6.2. Asymmetric-sigmoidal geobodies

Asymmetric-sigmoidal geobodies, represented by Tidal-dominated point bar deposits (HFA 2), form sand-prone or heterolithic bodies, tens of metres thick, constrained by the paleorelief associated with the intraformational incised valley (Fig. 6.15c). These geobodies are up to 100 m in width and up to 10 m thick (Fig. 6.14 and Fig. 6.15c). Asymmetric-sigmoidal geobodies are characterized by higher mud contents (sand:mud ratio of 40:60) distinguished by heterolithic lithofacies (Lithofacies IHb and Wb, predominantly), indicating deposition under subtidal conditions; or characterized by a sand:mud ratio of 60:40, composed principally by HIS and Lithofacies Ht-St-Sr, indicating deposition under inter- to supratidal conditions (Fig. 6.14). Cm-scale mud drapes, intercalated with sandstones and IHS are also frequent in these geobodies.

The GR response is characterized by a smooth-egg shape and a coarsening- to fining upward trend, where these geobodies are located in proximal zones (inter- to supratidal conditions) and a smooth-cylindrical shape and aggradational trend in the distal zone (subtidal conditions). Asymmetric-sigmoidal geobodies (HFA 2) are characterized by unidirectional azimuths and shallow-to-steep-to-shallow dip patterns (Fig. 6.14).

6.6.3. Tabular geobodies

Tabular geobodies comprise (a) Hyperpycnite facies (HFA 5); or (b) a Storm-dominated linear shoreface (HFA 6). In the former case, the geobody forms a really restricted body up to 0.5 m thick and 50 m in width, perpendicular to depositional dip, characterized by a sand:mud ratio of 90:10 and very fine, rippled sandstones (Lithofacies Swr-Sbcr-Spcr-Sicr). For the latter case, the geobody corresponds to the Storm-dominated shoreface of Association HFA 6. This comprises a sand prone package, up to 4 m thick, confined by the intraformational incised valley (Fig. 6.15b). The top of this geobody is eroded by the prograding of a fluvio-tidal system (HFA2). It is also characterized by a sand:mud ratio of 80:20, and stacked storm beds comprising fine-grained sandstones dominated by Lithofacies HCS and Sw. In the subsurface, this geobody is characterized by smooth-cylindrical GR profile and an aggradational trend (Fig. 6.14). Tabular geobodies, composed of Association HFA 6, are characterized by poly-directional azimuths and planar to low-angle dip angles (Fig. 6.14).

The Supratidal flat facies association (HFA 1), with a sand:mud ratio of between 10:90 and 0:100, can also be considered as a tabular geobody, forming mud prone packages, up to 10 m thick and with more than 1 km of lateral continuity, encasing the three types of reservoir geobody, described above. This geobody is characterized, in GR, by high API values, a serrated-cylindrical shape and an aggradational trend. Some thin sandstone horizons also occur within HFA 1, recognizable in GR as thin smooth-egg shape packages with a coarsening- to fining upward trend (Fig. 6.14). From the GR log, it is also apparent that HFA 1 may show, intervals characterized by fining upward trends and high API values related to increasing organic matter content (ultimately becoming coaly horizons) and some distinctive low GR zones associated with periods of exposure characterized by desiccation cracks (Fig. 6.14).
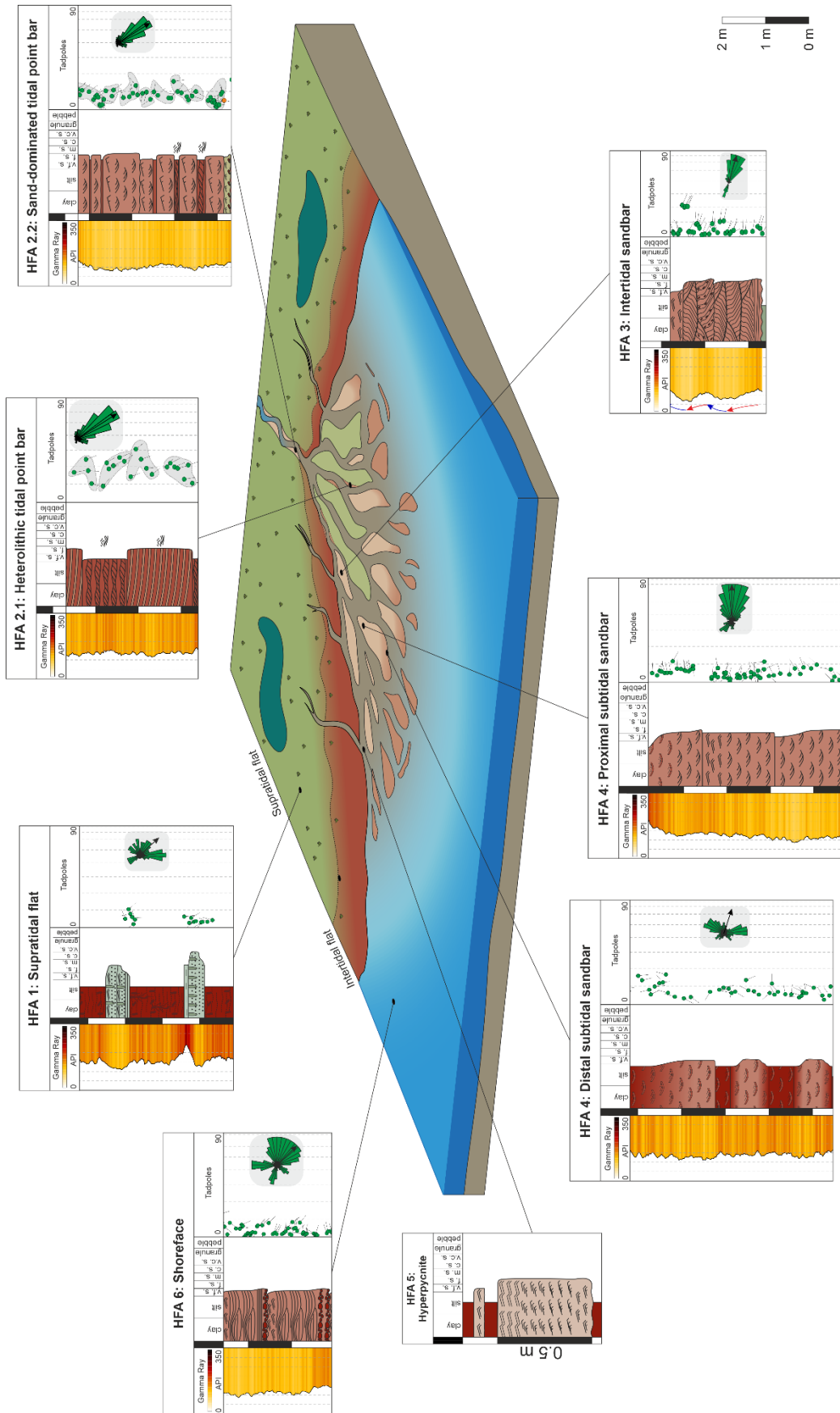
Fig. 6.14. Conceptual model of a mixed tidal and wave-influenced deltaic system and adjacent shoreface, showing the proposed paleo-locations for the interpreted facies associations comprising the Heterolithic Unit. The model also shows the key sedimentological, GR log features and dip tadpole patterns for each facies association.
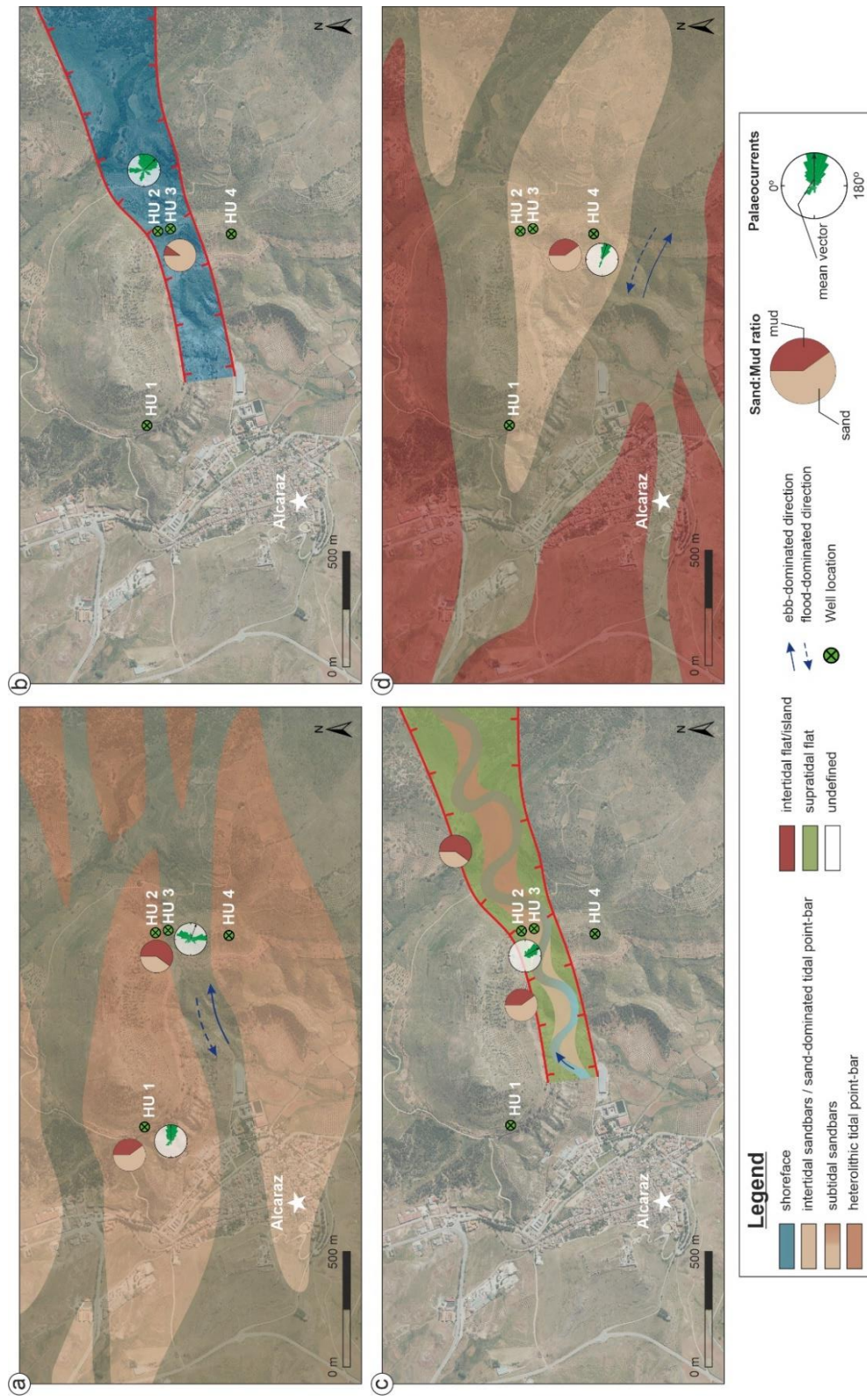
Fig. 6.15. Facies associations distribution and paleogeographic maps for the H Unit during deposition of: **(a)** the stratigraphic interval corresponding to subunit 1, composed of subtidal sandbars (HFA 4); **(b)** the lowermost part of the incised valley infill (lowermost Subunit 2), characterized by a storm-dominated shoreface (HFA 6); **(c)** the upper part of the incised valley infill (Subunit 2), characterized by tidal point bars (HFA 2); and **(d)** the stratigraphic interval corresponding to upper subunit 2, composed of intertidal sandbars (HFA 3).

Table. 2.2. Geometrical characteristics, key features in Gamma Ray and dip tadpole logs for each facies association identified in the H Unit.

Facies Association		Sand:Mud ratio	Geometry	Boundary (L-lower; U-upper)	Thickness	Width (perpendicular to depositional dip)	Gamma Ray Shape, Trend and min-max (mean) API values	Dip Tadpole patterns
HFA 1 Supratidal flat		10:90	Tabular	L and U: Horizontal and sharp	up to 7 m	more than 1 km	Serrated-cylindrical shape. Aggradational trend. 81 - 269 (158)	Poly-directional azimuths and planar to high dip angles
HFA 2 Tidal point bars	HFA 2.1 Heterolithic point bars	40:60	Asymmetric sigmoidal	L: Horizontal and erosive U: horizontal and sharp	up to 10 m	up to 100 m	Smooth-cylindrical Aggradational 101 - 170 (137)	Unidirectional azimuths and low to high dip angles
	HFA 2.2 Sand-dominated point bars	60:40	Asymmetric sigmidal	L: Horizontal and erosive U: Horizontal and sharp	up to 5 m	up to 75 m	Smooth-egg Coarsening-to fining-upward 62 - 152 (108)	Unidirectional azimuths and low to high dip angles
HFA 3 Intertidal sandbars		60:40	Elongate	L: Horizontal and erosive/sharp U: convex-up and sharp	up to 2 m	up to 500 m	Smooth-egg shape. Coarsening-to fining-upward trend. 60 - 149 (99)	Bidirectional azimuths and low to high dip angles
HFA 4 Subtidal sandbars	Proximal subtidal sandbars	60:40	Elongate	L: Horizontal and erosive U: Horizontal and sharp	up to 14 m	up to 350 m	Smooth-egg Coarsening-to fining-upward 74 - 164 (120)	Unidirectional azimuths and shallow-to-steep-to-shallow dip angles pattern
	Distal subtidal sandbars	40:60	Elongate	L: Horizontal and sharp U: Convex-up and sharp	up to 14 m	up to 350 m	Smooth-cylindrical Aggradational 86 - 204 (144)	Bidirectional azimuths and low to high dip angles
HFA 5 Hyperpycnite sandbody		90:10	Tabular to lobate	L: Horizontal and sharp U: Convex-up and sharp	up to 0.5 m	up to 50 m	-	-
HFA 6 Storm-dominated shoreface		80:20	Tabular	L: Horizontal and sharp U: Horizontal and sharp	up to 4 m	up to 150 m (restricted to incised valley)	Smooth-cylindrical shape. Aggradational trend. 80 - 193 (118)	Poly-directional azimuths and planar to low-angle dip angles

6.7. Discussion: Limitations of conceptual model

The role of shoreline systems classification in the characterization of reservoirs is a complex issue, addressed by numerous authors in recent decades (e.g. Boyd *et al.,* 1992; Dalrymple *et al.,* 1992; Shanmugam *et al.*, 2000; Harris *et al.*, 2002; Ichaso & Dalrymple, 2014; Leuven *et al.*, 2016; Nichols, 2017; Bradley *et al.,* 2018; Gil-Ortiz; 2019). This is especially so when dealing with tide-dominated systems as proximal-distal changes in both processes and facies are inherently complex. According to Dalrymple & Choi (2007) this may be explained by two fundamental factors. Firstly, tidal energy does not vary in a simple linear manner with onshore-offshore position and, secondly, these environments are characterized by complex, shifting networks of tidal channels and bars. As a direct consequence, depositional architecture is complex reflecting the migration and stacking of successive channels and the common occurrence of several different orders of erosion surface.

Boyd *et al.* (1992) and Dalrymple *et al.* (1992) propose a classification of coastal depositional environments based on a ternary diagram, summarizing the main factors (rivers, waves, and tides) controlling the geomorphology of linear shorelines, deltas, or estuaries. This is a very useful and powerful tool but, in many cases, it might be hard to apply to ancient coastal depositional systems. Even in these systems, as highlighted by Yan *et al.* (2005), changes in the relative importance of the key processes may occur on a variety of time-scales, even, for example on a seasonal basis between winter and summer. These authors have shown how sedimentation on the open-coast tidal flats of south-western Korea is controlled by seasonal variation in the intensity of onshore-directed winds and waves. As a result, an environmental oscillation takes place between tide-dominated conditions in summer and wave-dominated conditions in winter. Given observations of this type in modern systems it is clear that ancient systems will also very often present us with a need for complex, nuanced interpretations based on typically limited, incomplete data.

Focussing on modern tide-dominated systems, the distinction, morphologically, between a tide-dominated delta, with a protruding morphology, and a tide-dominated estuary, with a funnel morphology, seems evident. Dalrymple & Choi (2007) also presented a useful theoretical comparison between tide-dominated deltas and tide-dominated estuaries. These authors highlighted the subtle differences in terms of sedimentary processes, grain size distribution, bed forms, and sub-environments between both systems. Both in a tide dominated delta and, in a tide-dominated estuary, the river influence decreases in strength and relative importance in a seaward direction; the maximum tidal influence occurs on the middle to inner

part of the delta plain and in the middle estuary whereas wave action increases, on open coasts, in a seaward direction. As such it is apparent that the characteristic facies of fluvial point-bar, tidal rhythmites and HCS are not specific to any one setting and may occur in different sub-environments of both deltas and estuaries.

In addition, Brookfield (1998) and Prins *et al.* (2000) show that, in modern systems such as the Indus River delta, both tide-dominated deltas and tide-dominated estuaries can co-exist. It is only in the area of active river outflow that a true tidal-dominated system appears. The remainder of the delta plain is inactive and it is here, in response to slow transgression due to tectonic subsidence and/or compaction of the underlying mud, where tide-dominated estuary systems appear (Dalrymple & Choi, 2007).

Accordingly, and on the basis of the foregoing discussion, the conceptual model proposed for the H Unit (Fig. 6.14) represents the distribution of the facies associations within the proximal to distal zones of a mixed tide-dominated and wave influenced delta system, comprising: Supratidal flat (HFA 1), Tidal-dominated meandering channels (HFA 2), Intertidal sandbars (HFA 3), Subtidal sandbars (HFA 4), local Hyperpycnite deposits (HFA 5), and shoreface deposits (HFA 6). It is also necessary to note that, within this broad framework, processes related to relative sea-level change were important in sequence development and in the changing coastline paleogeography (Fig. 6.15; see Chapter 7).

In general, coastline paleogeography would have been similar during deposition of HFA 3 and 4 (Subunit 1 and upper part of Subunit 2, respectively; Fig. 6.15a and d), characterized by a gently-dipping coastal plain and delta front. A tide-dominated, wave-influenced delta system developed during these stratigraphic intervals. In marked contrast, a steeper coastal plain-delta front, laterally-constrained by the intraformational incised valley controlled deposition of HFA 6 and HFA 2 (lower part of subunit 2; Fig. 6.15b-c). During this time, it is most probable that a second tide-dominated, wave-influenced estuarine system developed, initially paleogeographically constrained and with a strong storm-influence (HFA 6), subsequently evolving into a tidal-dominated meandering system (HFA 2).

6.8. Conclusions

The integrated study of both outcrop (conventional outcrop data and DOM data) and well-calibrated subsurface data (core and wireline log data) has allowed us to produce a high-resolution sedimentology study of the Heterolithic Unit of the TIBEM (Triassic Red Beds of

Iberian Meseta). Six facies associations were identified, namely Supratidal flat (HFA 1), Tidal point bar (HFA 2), Intertidal sandbars (HFA 3), Subtidal sandbars (HFA 4), Hyperpycnite (HFA 5) and Storm-dominated shoreface (HFA 6).

Based on geometry and sand:mud ratios, the facies associations can be grouped into three types of reservoir geobody: (1) elongate geobodies, comprising Subtidal sandbars and Intertidal sandbars facies associations; (2) asymmetric-sigmoidal geobodies, composed of the Tidal-dominated point bar facies association; and (3) tabular geobodies, comprising Hyperpycnites and the deposits of a Storm-dominated shoreface.

Elongate and asymmetric-sigmoidal geobodies show moderate reservoir properties, characterized by heterolithic-dominated facies associations (sand:mud ratios between 40:60 and 60:40) and by the presence of mud drapes/layers that may act as significant potential flow baffles and barriers to flow. In contrast, tabular geobodies show excellent reservoir properties, characterized by sand-dominated facies associations (sand:mud ratios between 80:20 and 90:10). Supratidal flat (HFA 1) deposits, characterized by sand:mud ratios of 10:90 and 0:100, were classified as tabular, non-reservoir geobodies and for modelling purposes would be considered as background.

A mixed tidally-dominated and wave influenced delta system is proposed as a depositional model for the H Unit. However, processes related to relative sea-level change were also important in sequence evolution and in the development of coastal paleogeographies throughout deposition of the H Unit. For example, by considering changes in relative sea level, most notably a significant intraformational fall in sea level (dividing Subunits 1 and 2) we are able to explain the development of a second coastal system within the H Unit; specifically a tide-dominated estuarine system characterized initially by storm-dominated shoreface and tidal-dominated point bar facies associations, infilling an incised valley.

A new outcrop analogue dataset for paralic reservoirs, specifically for both a tide-dominated delta system and a tide-dominated estuarine system, including key geometric and sediment body dimension data, is presented here. A conceptual model generated from outcrop and subsurface data allows us to predict the paleo-locations of each facies association within the framework of proximal-distal trends of the depositional system, whether it is an estuary or a delta. Such data can also be used directly as an outcrop analogue for similar systems in the subsurface, both as hard and soft input for reservoir modelling.

CHAPTER 7:

Reservoir implications:

Key features for heterogeneity modelling

Abstract   This chapter attempts to assign appropriate geometries and dimensions to the various geobodies, summarizing their internal heterogeneities for reservoir modelling. These are then upscaled to describe the gross-scale reservoir architecture of the three TIBEM Units (M-S, S and H Units) and the key bounding surfaces (or correlation surfaces) between the units.

On the basis of geometry, a total of 6 reservoir geobodies can be differentiated in the TIBEM succession of the Alcaraz area: (i) low-sinuosity channel geobodies, comprising braided channel fills; (ii) ribbon-shaped geobodies, associated with high-sinuosity channel fills; (iii) crescent-shaped geobodies, comprising fluvial or tidal point bar deposits; (iv) elongate-shaped geobodies, characterised by fluvial compound bar or tidal bar deposits; (v) lobate-shaped geobodies, composed of crevasse-splay deposits; and (vi) tabular-shaped geobodies, composed of storm-dominated shoreface deposits.

After analysing the stacking of the facies associations in the Alcaraz succession (see Chapters 4, 5 and 6), a simplified scheme with three major depositional sequences (Sequences 1 to Sequence 3) and five reservoir zones (RZ 1 – RZ 5) was defined. A material-based sequence stratigraphic methodology (Embry, 2009), was used to recognize the key bounding surfaces delimiting genetic sedimentary packages. Sequence 1 comprises the deposits of the Mudstone-Sandstone Unit (M-S Unit), characterized by a high-sinuosity fluvial system. This sequence is broadly regressive in character (RST) and is considered as RZ 1. The boundary between Sequences 1 and 2 is marked by a sub-aerial unconformity (SU) reflecting a significant base-level fall. Sequence 2, comprising the deposits of the Sand Unit (S Unit) and much of Sub-unit 1 of the overlying Heterolithic Unit (H Unit), is broadly transgressive in character (TST). This sequence corresponds to Reservoir Zones 2 and 3, the former characterized by a low-sinuosity fluvial system, and the latter, by a tidally-dominated coastal system. The boundary between these two systems is interpreted as a diastemic shoreline ravinement surface (SR-D). The top of Reservoir zone 3 is marked by a maximum flooding surface (MFS). This is overlain by hyperpycnites, generated in response to increased sediment supply at the beginning of the regressional or progradational stage (RST), and supratidal flat deposits. A significant truncation along a major erosion surface, interpreted as a shoreline ravinement surface (SR-U) with the geometry of an incised valley, marks the boundary between Sequences 2 and 3. Sequence 3 comprises the deposits of shoreline systems, characterised by the changing influences of fluvial and coastal processes, during a series of high order Transgressive-Regressive cycles (T-R cycles) all grouped into a major regressive progradational shoreline package (RST). Sequence 3 includes both Reservoir Zones 4 and 5.

7.1. Geobody characteristics: geometry, dimensions and internal heterogeneity

This section attempts to assign appropriate geometries and dimensions to the various reservoir geobodies identified in the TIBEM succession of the Alcaraz area and review their internal heterogeneities based both on the previous chapters (Chapter 4 to 6) and available literature as a prelude to the modelling of heterogeneity in each reservoir geobody.

As introduced in Chapter 1, the term 'geobody' as used in this study refers to the geological elements in a reservoir. These elements are defined on the basis of their specific geometry (including width, thickness and orientation), bounding surfaces, internal sedimentary features (lithofacies and/or facies associations) and the location within the depositional environment. This is a term commonly used in geological modelling. Geobody is also equivalent to 'architectural element' as defined by Miall (1985), 'depositional elements' defined by Kostic & Aigner (2007) or the storeys of Ford & Pyles (2014).

7.1.1. Low-sinuosity fluvial channel deposits

Two types of reservoir geobodies linked to low-sinuosity (braided) fluvial systems are identified: (i) channel geobodies, characterised by a lenticular geometry in 2D cross section and low sinuosity in plan view; and (ii) compound bar geobodies, characterised by an elongate geometry (Fig. 7.1; Allen, 1983; Bridge & Tye, 2000; Bridge & Lunt, 2009; Ashworth *et al.,* 2011; Ielpi & Ghinassi, 2015). These geobodies were only identified in the S Unit (see Chapter 5). They are characterised by a high sand:mud ratio (sand:mud ratio of 95:5) and as such show only limited heterogeneity.

Channel geobodies, up to 20 m thick and 300 m in width (defined here as lateral extension as measured perpendicular to the main flow direction), are characterized internally by fining- and thinning-upwards sequences composed of Lithofacies Sh/Sm-St-Sr (Facies Association SFA 1). Locally, Lithofacies Gm appears toward the base of these geobodies. Thin (cm-scale) mud drapes between the different sequences could be potential baffles or even barriers to vertical fluid flow and would tend to compartmentalize these geobodies (Fig. 7.1; Yeste *et al.,* 2019).

Elongate geobodies, comprise compound bar deposits, assigned to Facies Association SFA 2, are up to 20 m thick and 500 m in width. Internally, these are principally characterized by

a stacking of Lithofacies Sh-Sp-St. Finer grained deposits and mm-scale mud drapes are also observed, associated with the gently dipping bounding surfaces between individual downstream accretionary macroforms, although these are unlikely to form significant baffles to permeability within the barform. Locally, at the top of these geobodies, an erosive surface is observed, overlain by very fine-grained sandstone (Lithofacies Sr) and mudstone deposits (Lithofacies Fl). These deposits represent cross-bar channels cutting across the top of the compound bars and, locally, could be considered as potential flow baffles (Fig. 7.1).

Fig. 7.1. Descriptive conceptual models for a low-sinuosity fluvial system showing a plan view (not to scale) and the facies stacking pattern for both the channel (SFA 1) and compound bar (SFA 2) reservoir geobodies.

7.1.2. High-sinuosity fluvial channel deposits

Two types of reservoir geobody are associated with high-sinuosity fluvial channels. (i) channel geobodies, characterized by a ribbon-shape in plan view and lenticular geometry in 2D cross section; and (ii) point bar geobodies, characterized by a crescent-shape in plan view and asymmetric-sigmoidal geometry in 2D cross section (Fig. 7.2). These reservoir geobodies were identified in the M-S Unit.

Sinuous channel fill deposits

Given the key hydrodynamic processes that operate in a meandering system, as a consequence of the existence of the helical flow model and a channel with asymmetric cross section, two main zones can be differentiated along the channel thalweg; the thalweg pool zone and the thalweg riffle zone. The channel thalweg is defined as the deepest, axial zone of the

river channel. Its gravel-paved erosional segments are referred to as pools (TP) and the shallower, inter-bar crossover segments, as riffles (TR; Bridge, 1993, 2003; Ghinassi *et al.,* 2014). Thus, as a result of hydrodynamic processes, channel fills give rise to specific lithofacies sequences during the active channel phase which differ from those deposited during the channel abandonment phase.

During the active channel phase, outer bank areas of a river bend, comprising the thalweg pool, are generally erosional. However, deposits may still be preserved due to net vertical bed aggradation, episodic channel depth changes during river stage changes and stepped migration patterns. Deeper areas along these pools, formed where flows impinged upon cut banks more strongly, may also preserve deposits in this area of a channel bend. The deposits tend to be coarse-grained lags, locally preserved directly above the most deeply incised area forming the base of a channel storey. A channel storey is defined here as the deposits formed by an individual channel segment which by increasing sinuosity, migrates across the floodplain (Allen, 1965, 1979; Willis & Sech, 2019). Where, in contrast, channels migrate by expansion over time, these deposits will also occur as coarser-grained lags at the base of point bar deposits (Willis & Sech, 2019).

In contrast, during the abandonment phase, channel fill deposits generally show a fining-upward succession, reflecting a longer-term decline in discharge when abandonment is due to channel bend cut-off. Within this framework, sandier fills are generally inferred to reflect a more gradual process of channel abandonment, whereas muddier fills suggest a more rapid abandonment. It is also expected that higher-sinuosity channel-bend segments will be cut-off faster than lower-sinuosity segments because the cut-off path of a higher-sinuosity channel segment defines a greater relative slope advantage (Allen, 1965; Bridge, 1993; Willis & Sech 2019). Willis and Tang (2010) modelled abandonment fills by gradually decreasing river discharge whilst keeping channel width constant. They predicted that bend axis pool scours would fill with sand faster than areas with flat beds near bend crossovers. The result was generally thicker, sandier, more gradually upward-fining abandonment fills along meander-bend axes and overall muddier fills in crossover areas.

In contrast to channel bend cut-off, when channel abandonment is produced by neck cut-off or river avulsion the channel is disconnected from the network of active river channels and the previous channel is transformed into an ox-bow lake that only receives suspended load during floods (Viseras & Fernandez, 2010). In both these abrupt abandonment process, neck cut-off and river avulsion, the flow velocity in the abandoned channel section decreases to zero

very quickly. In this way, the interval of sandier fill, that is above the deposits of the active phase of the channel, is usually very thin. Above the sands, however, a thick mud plug is deposited (Viseras & Fernandez, 2010; Viseras *et al*., 2018).

In the studied section, high-sinuosity channel geobodies have a ribbon-shape in plan view and lenticular geometry in 2D cross section, characterized by a fining-upward sequence comprising Lithofacies Gm-St-Sr-Fl (Fig. 7.2). Laminated fine-grained deposits (Lithofacies Fl) occur toward the top of the succession and are interpreted as mud plugs (Viseras *et al.,* 2018) with significant implications for potential flow in any analogous subsurface example. This reservoir geobody is associated with dimensions of up to 3 m in thickness and up to 40 m in width, perpendicular to the main flow direction. From paleogeographic reconstruction and the conceptual model of the M-S Unit (Fig. 4.11 and Fig. 8.6) these ribbon-shaped geobodies show an amplitude of up to 200 m and a wavelength of up to 400 m. Within the framework of the facies associations described in Chapter 4, these high-sinuosity channel reservoir geobodies correspond to Facies Association MSFA 1.

Point bar deposits

On the accretional, inner margin of the thalweg, the channel deposits grade into point bar deposits. These are distinguished by their characteristic epsilon cross-bedding (*sensu* Allen, 1963) or lateral accretion packages (LAP; *sensu* Abreu *et al.,* 2003). These deposits, at bed-scale, are characterized most typically, by a fining-upward succession composed of a basal pebble lag, attributed to deposition in the pool zone of a laterally migrating channel thalweg, overlying cross-stratified sandstones, as well as, plane-bed transport structures, with sand deposition as both ripples and small dunes in the uppermost part of the facies succession (Fig. 7.2).

In the studied section, these point bar deposits, are up to 3.6 m thick and up to 130 m in width, characterized by a crescent shape in plan view and an asymmetric-sigmoidal geometry in 2D cross section (Fig. 7.2). Within the framework of the facies associations described in Chapter 4, these point bar reservoir geobodies correspond to Facies Associations MSFA 2 to MSFA 4. Internally, at bed-scale, point bar geobodies are characterized by a fining-upward succession composed of Lithofacies Gm-St-Sr. Locally, mud drapes occur between LAPs and would be interpreted as baffles or barriers to potential flow in subsurface equivalents. Locally, these reservoir geobodies also contain minor channel geobodies toward the top of the succession, characterized by a fining-upward sequence, from fine-grained sandstones into siltstones, interpreted as chute channels. These minor channels could also be interpreted as important barriers to flow (Henares *et al*., 2016).
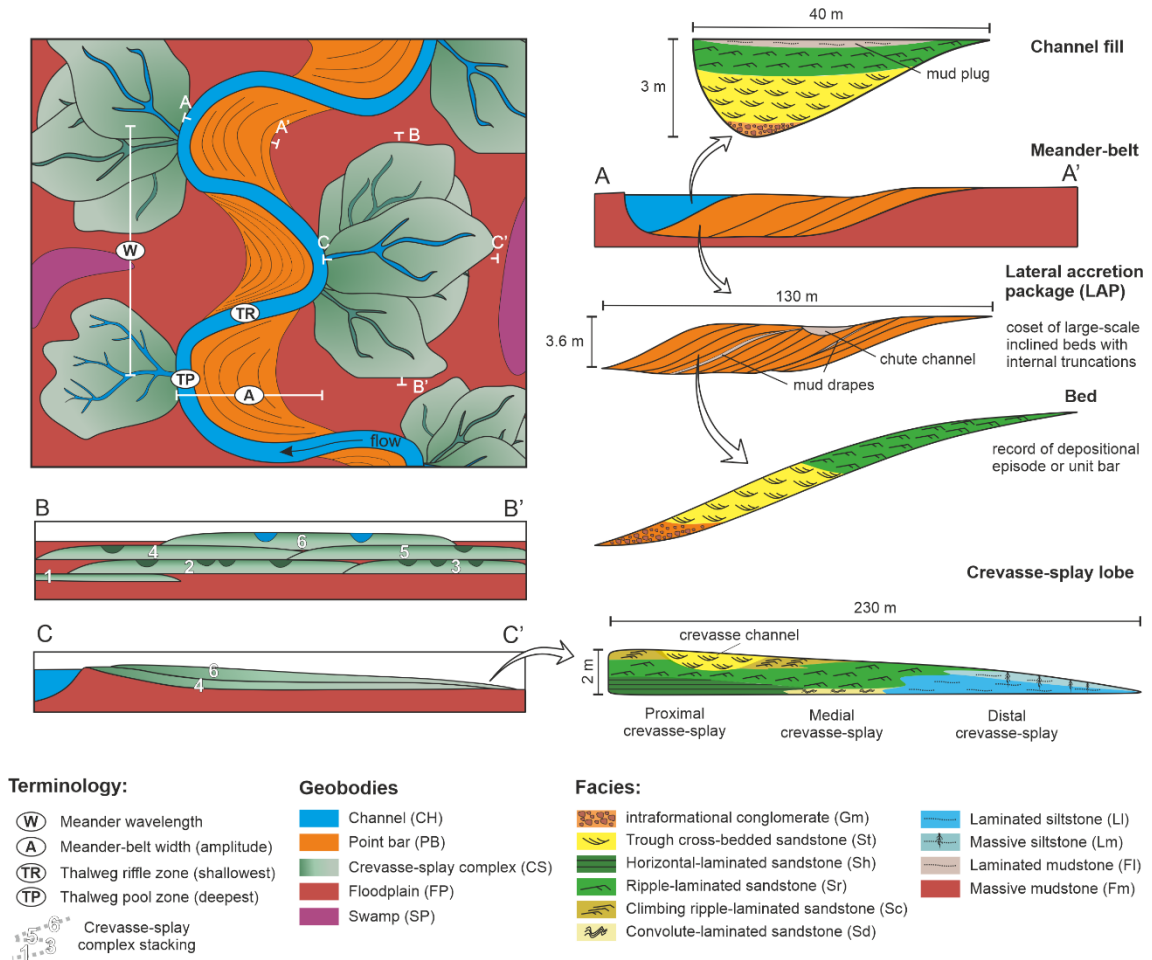
Fig. 7.2. Descriptive conceptual models for the high-sinuosity channel, point bar and crevasse-splay geobodies and the terminology used in this chapter (modified from Bridge, 2003; Ghinassi *et al.*, 2014; Ielpi & Ghinassi, 2014; Yeste *et al.*, 2020).

7.1.3. Crevasse-splay deposits

In fluvial sedimentary environments, a splay deposit is defined as a sheet-like progradational deposit, which typically is lobe-shaped in plan-view. Crevasse-splay deposits, form adjacent to an established channel, on the erosive margin of the main channel (e.g. Nichols and Fisher, 2007; Gulliford *et al.*, 2014; Burns *et al.*, 2017; Yeste *et al.*, 2020). Crevasse-splays are characterized by high-energy facies towards the axis where upper flow regime horizontal-laminated sandstones are deposited and which grade laterally into ripple-laminated sandstones towards the distal limits of the splay. Locally, a crevasse channel, in the uppermost part of the geobody, may also be preserved. These show an erosive base filled with trough cross-bedded sandstones (Burns *et al.*, 2017; Yeste *et al.*, 2020). Toward the distal limits of the splay, siltstones were deposited, corresponding to settling from suspension immediately after the tractional deposition of each phase of lobe development of the lobe, as the flow loses intensity.

207

Commonly, crevasse-splay deposits are formed during continuous flood events leading to overlapping lobe geobodies, giving rise to a crevasse-splay complex, by lateral compensation of accommodation space (Li *et al.,* 2014; Li & Bristow, 2015; Yeste *et al.,* 2020).

Crevasse-splay geobodies were identified in the M-S Unit (Chapter 4). These occur as lobe-shape bodies, up to 2 m thick (Fig. 7.2). These lobe-shape geobodies have up to 230 m in lateral extension, perpendicular to the main flow direction of the channel belt and from their insertion point (channel border); and a variable width (Fig. 7.2) ranging from 65 m in proximal zones to up to 115 m in distal zones. Internally, four facies associations have been distinguished within these geobodies: crevasse channels (MSFA 5), proximal crevasse-splay (MSFA 6), medial crevasse-splay (MSFA 7) and distal crevasse-splay (MSFA 8). The Proximal crevasse-splay facies association (MSFA 7) is characterized by the stacking of Lithofacies Sh-Sr-Sc. The Medial crevasse-splay facies association (MSFA 7) is characterized by the succession of Lithofacies Sd-Sr whilst, the Distal crevasse-splay facies association (MSFA 8) is represented by Lithofacies Ll and Lm. Locally, the Crevasse channel facies association (MSFA 5), characterized by Lithofacies St-Sr, is preserved in the uppermost part of these lobate geobodies (Fig. 7.2).

7.1.4. Tidal point bar deposits

Reservoir geobodies comprising tidal point bar deposits have similar geometrical characteristics to those associated with the previously described fluvial point bar geobodies. Accordingly, these reservoir geobodies have a crescent shape in plan view and asymmetric-sigmoidal geometry in 2D cross section. These geobodies are typically aligned perpendicular to the thalweg of the sinuous fluvio-tidal channels (Dalrymple & Choi, 2007). Other authors have labelled these geobodies as sidebars (Dalrymple & Choi, 2007; Leuven *et al.*, 2016). Tidal point bar geobodies were identified in the H Unit (Facies Association HFA 2).

Internally, reservoir geobodies composed of tidal point bar facies deposits (HFA 2) are characterized by a higher mud content under sub-tidal conditions (Heterolithic point bar facies association - HFA 2.1), in comparison with those deposited under supratidal conditions (sand-dominated tidal point bar facies association - HFA 2.2). Under sub-tidal conditions, these geobodies, with up to 10 m of thickness and up to 100 m of width, are characterized by the alternation of sand/mud layers (Predominantly Lithofacies IHb and Wb lithofacies). Recording the frequent oscillations in flow energy associated with tidal currents. In contrast, geobodies deposited under supratidal conditions are more sand-prone, although a significant proportion of cm-scale mud drapes also typically occur and would act as baffles or barriers to flow in

subsurface examples (Feldman & Demko, 2015). Supratidal point bars are up to 5 m thick and up to 75 m in width, characterized by, principally, Lithofacies Ht-St-Sr.

7.1.5. Tidal bar deposits

Reservoir geobodies composed of tidal bar deposits have an elongate shape and were identified in the H Unit (Chapter 6). On the basis of the dimensions and lithofacies stacking patterns, two elongate-shaped geobodies linked to tidal bars were differentiated: (i) elongate reservoir geobodies comprising intertidal sandbars (Facies Association HFA 3); and (ii) elongate reservoir geobodies composed of subtidal sandbars (Facies Association HFA 4). These geobodies are typically aligned parallel to depositional dip (Fig. 7.3; Shanmugam *et al.,* 2000; Wood, 2004; Dalrymple & Choi, 2007; Olariu *et al*., 2012).

Intertidal sandbar deposits

Intertidal sandbars (HFA 3) are formed by the superposition of several sigmoidal cross-stratified, fine-grained sandstone sets (Lithofacies St) separated by mm-scale mud drapes. These geobodies (HFA 3), are up to 500 m in width, 2 m thick and appear to be restricted to tidal channels (Fig. 7.3). They also show mm-scale mud drapes between the cross-bed sets. These are not considered to be significant potential barriers to flow as they are both too thin and discontinuous in character (Shanmugam *et al.,* 2000).

Subtidal sandbar deposits

Elongate reservoir geobodies comprising subtidal sandbars (Facies Association HFA 4) are principally characterized by fine to very coarse-grained sandstones (Lithofacies Sm, Sp, St and Sw) and locally by pebbly, coarse sand lags (Lithofacies Gm). This geobody becomes notably more heterolithic in a seaward direction, characterized by cross-stratified sand-mud couplets in bundles (Lithofacies Ht). This is reflected in the variation in sand:mud ratio, from proximal to distal (land- to seaward) zone from 60:40 to 40:60.

In addition, mud drapes also show a proximal to distal increase in thickness, varying from cm- to dcm-scale, respectively. These elongate geobodies are up to 350 m in width and up to 14 m thick although they are often amalgamated by lateral and vertical stacking to form sand prone packages with high-lateral continuity (Fig. 7.3). However, the shift from centimetric to decimetre-scale mud layers, in a proximal-distal direction within these geobodies may generate

significant potential baffles and barriers to flow. In addition, the flooding surfaces, characterized by laminated to massive mudstones on bar tops, may also form significant barriers to flow between stacked bars (Fig. 7.3; Sullivan *et al.*, 1997; Yoshida *et al.*, 2001; Feldman & Demko, 2015), all of which is likely to contribute to reservoir compartmentalization.
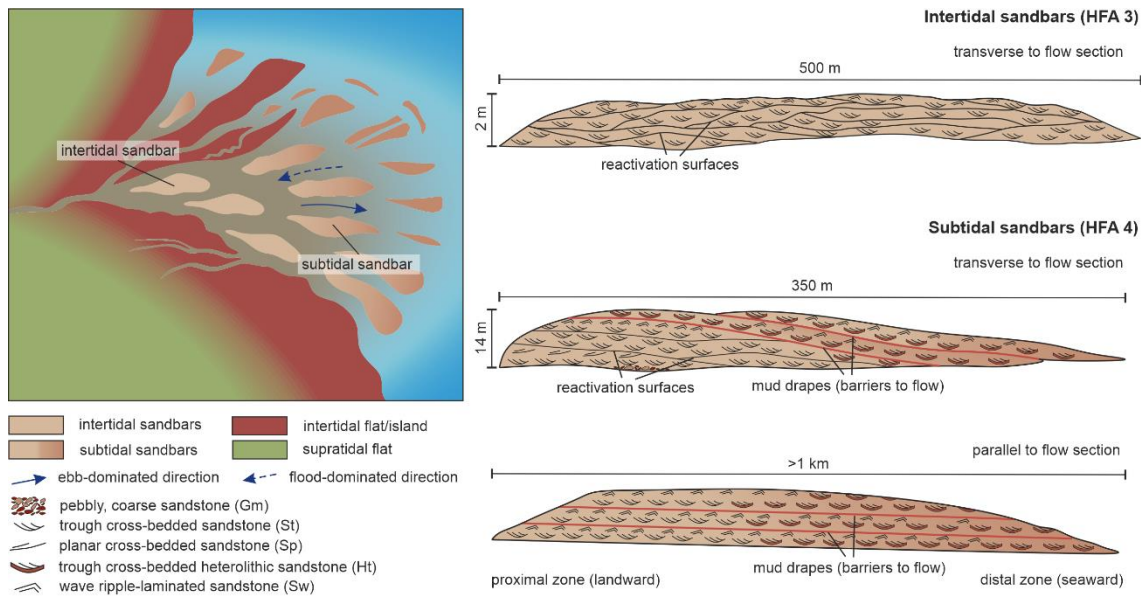
Fig. 7.3. Descriptive (geometry and internal heterogeneities) conceptual models for tidal bar reservoir geobodies.

7.1.6. Shoreface deposits

Reservoir geobodies composed of shoreface deposits (storm-dominated shoreface facies association – HFA 6) are distinguished by a tabular geometry. In the study area, they occur only in the H Unit (Chapter 6), forming a sand-prone package, up to 4 m thick, infilling the lowermost section of the intraformational incised valley (see Chapter 6). Internally, this tabular geobody is characterized by well-sorted, fine to medium sandstones dominated by Lithofacies HCS and Sw. Only the localised presence of thin mud-pebble layers, occurring at the base of stacked storm beds, could potentially act as minor baffles to flow within this otherwise homogeneous, well-connected sand body.

7.2. Reservoir architecture and sequence stratigraphy of the Alcaraz area

The purpose of this section is to distinguish and characterized those major stratigraphic surfaces representing changes in depositional trends and to interpret the resulting stratigraphic units bounded by these surfaces. In addition, a lithostratigraphic zonation, in terms of sand-mud ratios, and a hypothetical reservoir zonation, based on geobody geometries, is also presented.

Although much of the succession is terrestrial in character, which implies the recognition of the uncertainties and controversies associated with the application of sequence stratigraphic methodologies to continental systems, it was, nevertheless, decided to attempt to establish a sequence stratigraphic or genetic stratigraphic framework as this serves to better understand the development of the depositional systems through time. This framework is not intended as a rigorous, high resolution genetic stratigraphy for the TIBEM, merely as an approximation, for the Alcaraz area. For this proposed framework to be corroborated and extended, significant detailed work would be required on key sections across the TIBEM outcrop area.

Taking into consideration the limited area of the studied outcrops and the principal focus on fluvial deposits, a practical, material-based sequence stratigraphic methodology, essentially as presented by Embry (2009), was used to identify the key bounding surfaces delimiting the genetic sedimentary packages comprising the sequence stratigraphic framework in this study.

The following key surfaces were defined by Embry (2009):

- **Sub-aerial Unconformity (SU)** is an important sequence stratigraphic surface and was the surface first used to empirically define sequences (Sloss *et al.*, 1949). The defining attributes of a sub-aerial unconformity are an erosive surface or weathering zone (e.g., paleosol, karst) overlain by non-marine/brackish marine strata, associated with evidence that the surface represents a significant gap in the stratigraphic record. The occurrence of a significant stratigraphic gap across a subaerial unconformity is critical, for its recognition because this establishes the unconformable nature of the surface. The occurrence of onlapping nonmarine strata above the surface adds further support to such an interpretation. A sub-aerial unconformity is interpreted to form by sub-aerial erosional processes, especially those connected with fluvial erosion, during a time of base-level fall. In the Alcaraz succession, the only exposed example is SU-2.

- **Regressive surface of marine erosion (RMSE)** is characterized by a sharp and scoured surface separating offshore marine strata below from shallowing-upward shoreface strata above, downlapping onto the RSME. This surface occurs within an overall regressive succession but is considered to represent a change in depositional trend from deposition to non-deposition and back to deposition. However, the RSME is not a suitable surface for correlation because of its highly diachronous nature. Locally, this surface may be of use in explaining trend changes in the facies succession. This surface is not recognized at Alcaraz succession because the outcropping coastal deposition system is limited and is not ideal for identifying a RSME.

- **Shoreline Ravinement (SR)** is defined by an abrupt, scoured contact overlain by estuarine or marine strata which fine and deepen upwards. Underlying strata can vary from non-marine to fully marine. As a scoured contact, it represents a change in trend from deposition to non-deposition and it can vary along its extent from being a minor diastem to being a major unconformity. The SR begins to form at the start of transgression which occurs when rate of base-level rise exceeds the sedimentation rate at the shoreline. The SR stops being generated at the end of transgression which can occur at any time during base-level rise depending on the interaction of the rate of base-level rise with the rate of sediment supply. Because it develops over the entire time of transgression, a shoreline ravinement is often considered to be diachronous.

  However, over its extent, it can either be a diastem ("disconformity" or minor unconformity) or an unconformity. A diastemic shoreline ravinement (SR-D) has the above described general characteristics of an SR and is further characterized by the presence of non-marine strata underlying the surface and the preservation of the previously developed sub-aerial unconformity. This is a highly diachronous surface. In contrast, when a shoreline ravinement has removed any non-marine strata that were deposited behind the shoreface as it moved landward and the sub-aerial unconformity that had formed during the preceding base-level fall and regression, then this is would be a true unconformity. The SR-U has the defining characteristics of an SR and an additional characteristic is that the underlying strata are marine rather than non-marine. In terms of utility, the unconformable portion of an SR (SR-U) is very useful for correlation and for bounding sequence stratigraphic units because it is a time barrier. However, the diastemic portion of an SR (SR-D) is not useful for these purposes because of its highly diachronous nature.

- **Maximum Regressive Surface (MRS)** is a conformable horizon which marks a change in trend from coarsening and shallowing-upward to fining and deepening-upward. It is generated at or close to the start of transgression, when the rate of base-level rise exceeds the rate of sediment supply at the shoreline. The MRS is laterally equivalent to the shoreline ravinement and this relationship results from the fact that both surfaces begin to be generated at the start of transgression. The key criterion for distinguishing the SR-U and MRS is that the former is an unconformity with truncation below whereas the MRS is a conformable surface which is not associated with truncation or onlap. This surface is not so far recognized in the H Unit succession of Alcaraz but it is reasonable to assume that both SU and SR surfaces would pass laterally into an MRS, respectively in a landwards and offshore direction.

- **Maximum flooding surface (MFS)** is represented by a conformable horizon marking a change from fining and deepening- upward- to coarsening- and shallowing-upwards and is normally represented by the most mud-prone horizon in the succession, often associated with high organic matter contents and/or heavy mineral concentrations both suggesting condensation and low rates of sedimentation.

- **Slope Onlap Surface (SOS)** is a prominent, unconformable surface which is developed in slope environments and is effectively characterized by the onlap of strata onto the surface. The strata below this surface can be concordant with the SOS, without any evidence of scour or erosion; or clearly scoured and/or truncated, formed in part by erosion followed by onlap. This surface is not recognized in this coastal depositional system.

Several low-order, and numerous high-order sequences, which do not always coincide with lithostratigraphic units, can also be recognized in the stratigraphic record of the TIBEM Formation of the Alcaraz area. After analysing the stacking of the facies associations (Chapters 4, 5 and 6), a simplified scheme with three major depositional sequences (Sequence 1 to Sequence 3) and five reservoir zones (RZ 1 – RZ 5) was defined (Fig. 7.4).

Sequence 1 corresponds to the M-S Unit in its entirety, characterized by a low net-to-gross (sand:mud ratio of 10.90). The base of this sequence was not observed in either the outcrop or subsurface data of the immediate Alcaraz study area, although it is seen ~~as~~ to onlap the basement along a major erosional surface; thereby defining a sub-aerial unconformity defined as SU1. A high GR response, characterized by a serrated profile and by both bell and funnel shapes, characterize this sequence which can be considered as Reservoir Zone 1 (RZ 1) in

the Alcaraz succession. This RZ is characterized by the stacking of high-sinuosity fluvial channel and crevasse-splay reservoir geobodies (MSFA 1 to 10). Sequence 1 is broadly regressive in character (RST), comprising progradational fluvial deposits within a context in which high accumulation rates, exceeded the rate of accommodation space generation.

The boundary between Sequences 1 and 2 is marked by a distinctive erosive surface and an abrupt change in lithology, in the depositional environment and in the GR response. This surface is interpreted as a sub-aerial unconformity (SU2) and would most probably be an excellent and consistent correlatable surface across the rest of the TIBEM Formation outcrop, most likely reflecting a regional base-level fall and/or major climate change generating a major increase in sand supply. Regional evidence suggests that this is probably linked to the Carnian Pluvial Event according to Arche & López, (2014). This surface is characterized by a sharp decrease in GR response reflecting the abrupt shift from the essentially heterolithic M-S unit to the clean, sheet-like sands of the S-Unit.

Sequence 2 comprises the deposits of the Sand Unit (S Unit) and Subunit 1 of the overlying Heterolithic Unit (H Unit) and it is broadly transgressive in character (TST). The lower part of the sequence, is characterized by the lowest GR values in the entire Alcaraz succession, and a cylindrical gamma-ray profile interpreted as a low-sinuosity fluvial depositional system (Facies Associations SFA 1 to 2), which shows the highest sand:mud ratio values (95:5) in the studied area. It records both a significant drop in relative sea level and significantly increased sedimentation probably linked to a major climatic change in the hinterland ("Carnian pluvial event" of Arche & López; 2014). This part of the sequence corresponds to Reservoir Zone 2 (RZ 2).

A scoured surface truncates the fluvial deposits of the Sandstone Unit which are overlain by supratidal flat deposits. This surface is interpreted as a diastemic shoreline ravinement surface (SR-D2). This surface is represented in the subsurface by a sharp rise in the GR and by a lag of burrowed, very fine sandstones containing scattered intraclasts, topped by a well-cemented bored surface; effectively a condensed horizon marking the rapid marine flooding of the braidplain. This condensed horizon is represented by the highest GR Peak in the Alcaraz succession, associated with an excess of Uranium (see Fig. 6.2), most probably reflecting a high heavy mineral concentration, supporting the interpretation of flooding and condensation at the top of Sandstone Unit.
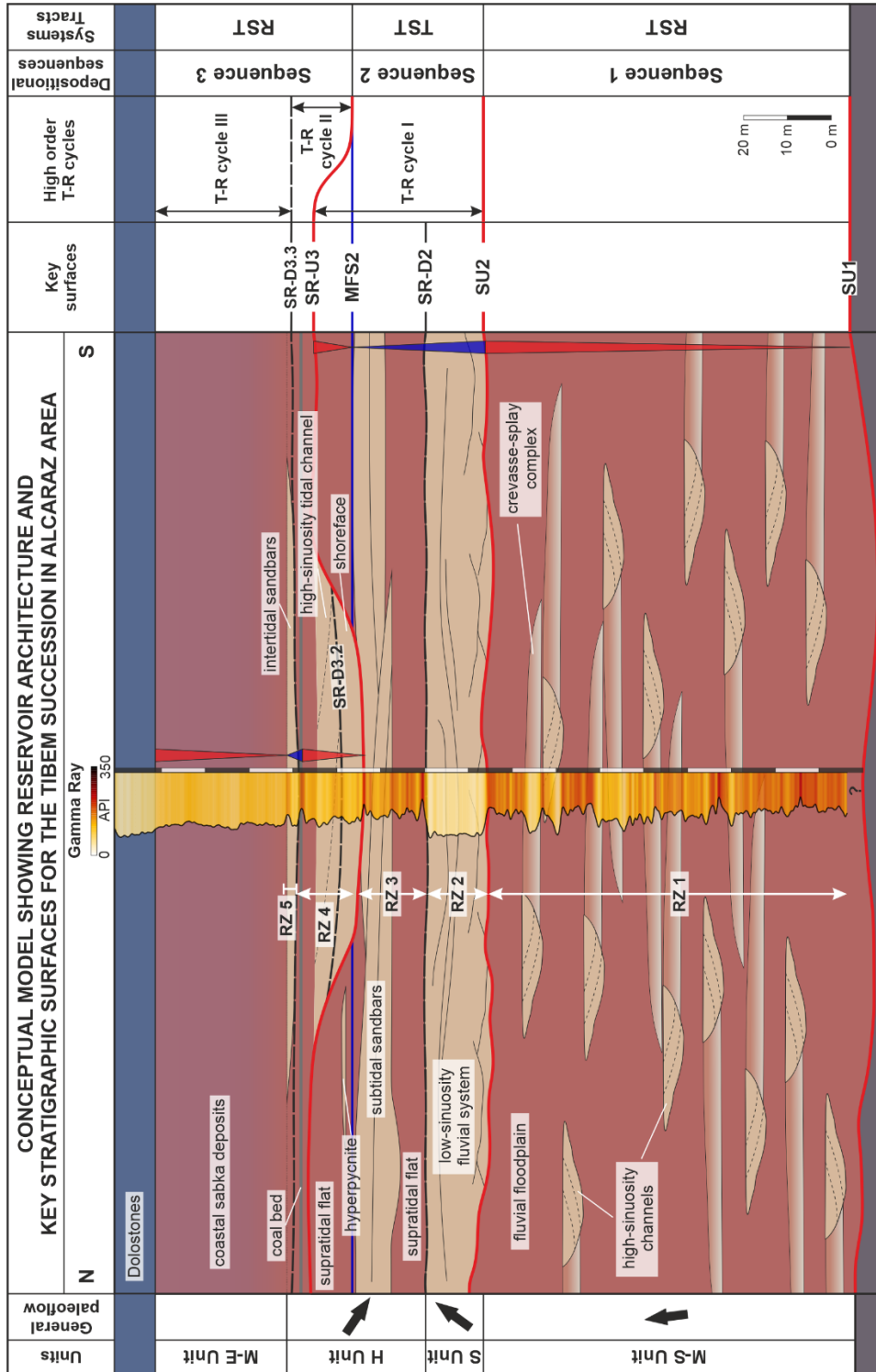
Fig. 7.4. Synthetic conceptual model of the TIBEM succession for the Alcaraz area showing the reservoir architecture, lithostratigraphy and sequence stratigraphic framework. Synthetic gamma ray log responses, a suggested reservoir zonation (RZ) based on the facies associations and the distribution of reservoir geobodies are also shown. M-S Unit: Mudstone-sandstone unit; S Unit: Sandstone unit; H Unit: Heterolithic unit; M-E Unit: Mudstone-evaporitic Unit; RZ: reservoir zone; SU: subaerial unconformity surface; SR-U: unconformable shoreline ravinement surface; SR-D: diastemic shoreline ravinement surface; MFS: maximum flooding surface; RST: regressive system tract; TST: transgressive system tract.

Above the SR-D2 surface, tidally-dominated coastal systems were developed in response to increasing accommodation space linked to the retrogradational, transgressive shoreline stage (TST), characterized by supratidal flat (Facies Association HFA 1) and subtidal sandbar (Facies Association HFA 4) deposits. Together these deposits correspond to Reservoir Zone 3 (RZ 3), largely characterized by elongate reservoir geobodies, composed of subtidal bars.

The vertical transition between the assemblage of subtidal sandbars and supratidal flat deposits in the upper part of Sequence 2 is marked by a high GR peak, associated with an excess of Uranium, characterized by a thin, laminated to massive green mudstone layer (Well HU 1, Fig. 6.2). This most probably corresponds to a maximum flooding surface (MFS2), although, in the Alcaraz area, it is more probable that there is no clear surface that determines a classical maximum flooding surface. Rather, one could speak of a transition zone ("Zone of MFS"). This is overlain by the deposits of river-influenced density pulses or hyperpycnites (Facies Association HFA 5) generated in response to increased sediment supply at the beginning of the regressional prograding stage (RST).

The RST of Sequence 2 is thin, due to significant truncation along a major erosion surface. This surface defines an incised valley, confining the lower part of Sequence 3. It is interpreted as a shoreline ravinement surface (SR-U3) characterized by a maximum GR Peak, linked to an excess of Uranium (see Fig. 6.2). This excess of Uranium is most probably associated with a high concentration of heavy minerals such as Zircon, Tourmaline or Rutile, indicating a fall in sea level, erosion, rapid forced regression (for which there is no evidence preserved at the Alcaraz area), and, finally flooding and condensation.

Sequence 3 is equivalent to the lithostratigraphic Sub-unit 2 of the Heterolithic Unit (H Unit) and also the Mudstone-Evaporitic unit (M-E Unit). This sequence, which consists of shoreline systems, characterized by both fluvial to coastal processes (river/wave and tidal), developed in response to decreasing accommodation/sediment supply (a/s) ratios during a series of high order Transgressive-Regressive cycles (T-R cycle II and III) all grouped into a major regressive progradational shoreline package (RST).

The SR-U3 surface is overlain by an asymmetrical T-R cycle (T-R cycle II). SR-U3 is initially overlain by a progradational package, characterized by storm-dominated shoreface deposits (Facies association HFA 6). The top of this initial package is eroded by high-sinuosity tidal channels (Facies association HFA 2). The progradation continues with supratidal flat deposits (Facies association HFA 1). These two packages, together with supratidal flat deposits, recording the regressive phase of T-R cycle II. The deposits linked to transgressive phase in T-R cycle II were

not preserved, or partially preserved by the very thin mud pebble lag overlying SR-U3. In addition, T-R cycle II could also be divided into two very asymmetrical, high order T-R cycles (T-R cycles II.1 and II.2), recording only the regressive phases of the two T-R cycles. The regressive phase of T-R cycle II.1 is represented by storm-dominated shoreface deposits, while T-R cycle II.2 is represented by high-sinuosity tidal channels. The surface eroding the top of shoreface deposits, and thus bounding T-R cycle II.1 and II.2, is interpreted as a diastemic shoreline ravinement (SR-D3.2). T-R cycle II (or two high-order half cycles, T-R cycles II.1 and II.2) corresponds to Reservoir Zone 4, characterized by a tabular reservoir geobody, composed of storm-dominated shoreface deposits (Facies Association HFA 6); and sigmoidal or crescent-shaped reservoir geobodies, composed of tidal point bar deposits (Facies Association HFA 2). Both reservoir geobodies are confined, infilling the incised valley defined by SR-U3 (see Fig. 6.15).

The last transgressive phase of the higher order T-R cycles is represented by a high order shoreline ravinement surface (SR-D3.3), which scoured the underlying supratidal flat deposits before being overlain by intertidal sandbar deposits (Facies associations HFA 3). This corresponds to Reservoir Zone 5, characterized by elongate reservoir geobodies. Sequence 3 culminates with the progradation of silt-rich coastal plain facies and intertidal sabkha evaporites (M-E Unit).

This simplified stratigraphic scheme is an approximation based only on outcrop and subsurface data from the Alcaraz area. Its purpose is to identify and characterize the stratigraphic units, reservoir zones and the bounding surfaces between them; as a basis for the next step of the workflow, the construction of a 3D reservoir model framework. Additional studies are necessary, in other locations of the TIBEM, in order to corroborate, perfect and adapt the proposed scheme.

7.3. Conclusions

Through the integrated outcrop/behind outcrop approach presented in this study, the TIBEM succession of the Alcaraz area can be divided into three main depositional sequences (Sequence 1 to 3), each with characteristic systems tracts bounded by key surfaces: subaerial unconformity surface, maximum flooding surface, and unconformable shoreline ravinement surface. Based upon this systems tract architecture, a genetic zonation composed of five reservoir zones has been proposed (RZ 1 to RZ 5) for the TIBEM succession of the Alcaraz area.

This proposed stratigraphic zonation should serve as valuable hard data in the construction of the 3D reservoir model framework for the TIBEM succession of the Alcaraz area.

On the basis of geometry, orientation and distributions of reservoir geobodies, as well as the potential mesoscale heterogeneities that compose these reservoir geobodies, each reservoir zone is characterized by specific types of reservoir geobodies:

- Reservoir zone 1 (RZ 1) comprises three types of reservoir geobody associated with a high-sinuosity fluvial system: (1) channel geobodies, with up to 3 m of thickness and up to 40 m width, characterized by sinuous-channel deposits; (2) crescent-shaped geobodies, with up to 3.6 m of thickness and up to 130 m in width, characterized by point bar deposits; and (3) lobe-shaped geobodies, up to 2 m thick and with up to 230 m of lateral extension, characterized by crevasse-splay deposits.

- In reservoir zone 2 (RZ 2) two types of reservoir geobody were identified, linked to a low-sinuosity fluvial system: (1) channel geobodies, up to 20 m thick and 300 m in width; and (2) elongate geobodies, up to 20 m thick and 500 m in width.

- Reservoir zone 3 (RZ 3) comprises elongate geobodies, up to 350 m in width and up to 14 m thick, characterized by subtidal sandbar deposits. These elongate geobodies are often amalgamated by lateral and vertical stacking to form sand prone packages with high-lateral continuity.

- Reservoir zone 4 (RZ 4) comprises two stacked reservoir geobody types: (1) tabular geobodies, up to 4 m thick, characterized by shoreface deposits; and (2) crescent-shaped geobodies, up to 10 m of thick and up to 100 m in width, comprising tidal point bar deposits. Both geobodies are laterally constrained by the margins of an incised valley.

- Reservoir zone 5 (RZ 5) comprises elongate geobodies, up to 500 m in width and 2 m thick, characterized by intertidal sandbar deposits.

These characteristics of the reservoir geobodies presented here, and the associated internal heterogeneities, should serve to populate the heterogeneity distribution into the 3D reservoir model framework of the TIBEM succession of the Alcaraz area.

PART II:

RESERVOIR MODELLING
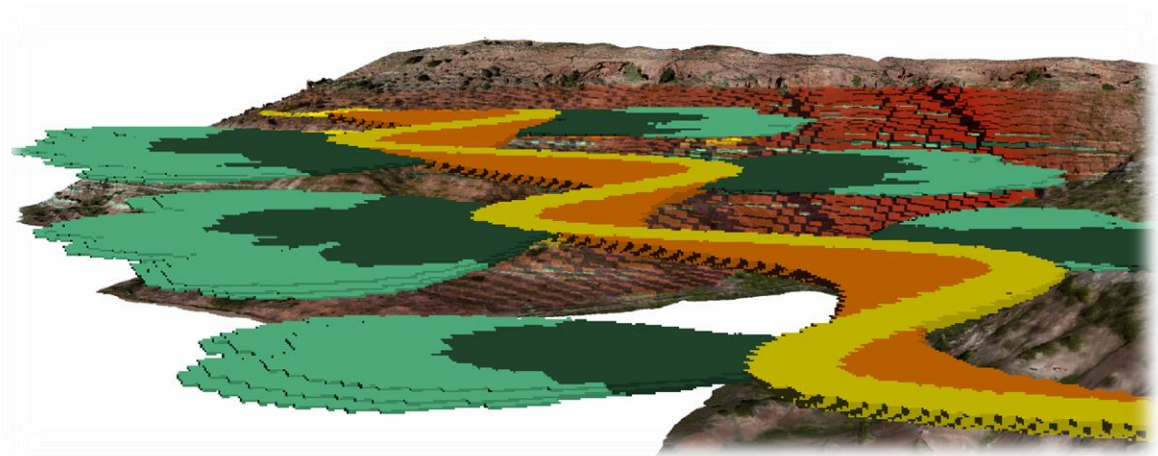
CHAPTER 8:

Reservoir Modelling of M-S Unit: Case Study of a Channel - Crevasse-splay Complex

Abstract   Fluvial sandstones deposited by meandering river systems are one of the most complex reservoirs to predict and model with confidence, a reflection of both the geometries and complex distribution of the component geobodies. This is especially so when the input data for the model are limited, which is typically the case in the subsurface. By integrating both analogue outcrop data and associated subsurface data (Outcrop/Behind Outcrop characterization), as well as new technical advances in the reconstruction of the outcrop in 3D (Digital Outcrop Models, DOM), the geostatistical parameters, which condition the modelling of these reservoirs, can be better determined. In addition, digital outcrop models also allow us to easily extract the necessary georeferenced input data (digitized outcrop interpretations, geometrical parameters, as well as, key surfaces) and so create geocellular outcrop models. These are a useful tool with which to contrast the results obtained from geostatistical simulations, as well as to quantify the uncertainty associated with the results.

In this chapter, classical field data, digital data derived from outcrop models (DOM) and subsurface data were combined in order to carry out a geostatistical modelling of the M-S Unit (Chapter 4), which includes both a meandering channel system and overbank sandstone deposits. In this unit, three sand-dominated geobodies: (1) channel geobodies, (2) point bar geobodies and (3) crevasse-splay geobodies, embedded into mud-dominated geobodies (floodplain geobodies) were recognized. Geostatistical modelling results were obtained by combining Object-based (OBM) and MultiPoint Statistics-based (MPS) modelling techniques.

A critical element in this study was the design of appropriate modelling workflows with Petrel$_{TM}$ which would best reproduce the distribution of heterogeneities, both at the scale of geobodies and at the finer scale of lithofacies by using both OBM techniques and logical statement calculations. The workflow at geobody scale was used to construct a 3D training image (TI) of a fluvial reservoir comprising both a meandering channel system and its associated overbank sandstone deposits. The resulting TI represents all geobodies described in the studied outcrop example and is exportable to similar fluvial reservoirs. This TI was then used in MPS simulations, in order to establish how it was able to assist in the prediction of the reservoir geobodies, as well as confirming to what extent this prediction matched the outcrop. MPS simulations generated good predictions for geobodies throughout the model framework with mean match values ranging from 15% to 44%, when compared with the geocellular outcrop model. The workflow at the scale of lithofacies was used to estimate the static connectivity of the reservoir in the M-S Unit. The results of this exercise reveal the importance of considering both point bar and, especially, crevasse-splay geobodies, besides channel geobody, in enhancing static reservoir connectivity at all well spacings.

8.1. Introduction

In fluvial reservoirs, heterogeneity and connectivity of hydraulic properties are related to the geometry of geobodies and facies distributions (e.g. Anderson, 1989; Koltermann & Gorelick, 1996; Davis *et al*., 1997; Klingbeil *et al*., 1999; Weissmann *et al*., 1999; Gaud *et al*., 2004, Pranter & Sommer, 2011; Cabello *et al.,* 2018; Viseras *et al.,* 2018; Yeste *et al.,* 2019, 2020). Specifically, the sedimentary dynamics of high-sinuosity fluvial systems give rise to highly complex and heterogeneous reservoirs. These systems are therefore very difficult to model given their inherent high degree of uncertainty reflecting the great variety of geometries and the wide range of possibilities in the distribution of geobodies. This problem is amplified when the input data in the model are scarce, which is typically the case in subsurface-based studies. The study of outcrop analogues is therefore essential if we are to cover these gaps (Chapter 1).

High-sinuosity fluvial depositional systems are composed principally of three sedimentary geobodies: (1) main channels, (2) point bars and (3) crevasse-splays; embedded in floodplain deposits. These geobodies generate the sedimentary heterogeneity at the macro- and mesoscale in equivalent subsurface reservoirs. The degree of juxtaposition and amalgamation of these geobodies determines the degree of connectivity in the reservoir, whereas mud plugs play a part in increasing the lateral and vertical reservoir compartmentalisation. Typically, main channel and point bar geobodies are considered as main reservoir geobodies in these fluvial depositional systems, but the consideration of crevasse-splay geobodies can be important in the evaluation of this reservoir type and play an important role in reservoir connectivity (Van Toorenenburg *et al.*, 2016; Pranter & Sommer, 2011; Pranter *et* al., 2014, Fenn & Pranter, 2014; Yeste *et al*., 2020).

There are two major conventional geostatistical techniques currently used in the modelling of fluvial reservoir: Object-Based Modelling (OBM) and Multi-point statistics-based modelling (MPS) (see Chapter 3). Object-Based modeling (OBM) involves the population of a volume by objects with different geometries and dimensions replacing a background. By incorporating the outcrop/behind outcrop characterization together with the object-based modeling it is possible to reproduce the different geobody types, including their dimensions, distribution, as well as the facies and the relationship between them. This method can be used to generate a mathematical pattern, called the training image (TI). When the TI is used as input in the Multi-point Statistics (MPS)-based modeling process it combines the strengths of both OBM and cell-based models. This produces facies models that are geologically realistic, allows for flexibility and are able to honour the geostatistics conditioned by the input data.

The connectivity of fluvial sandstones, whose dimensions are below the resolution of seismic data, is difficult to assess from one-dimensional well data. Two-dimensional connectivity, estimated from 2D maps and cross sections, is generally lower than 3D connectivity based on outcrop (Pringle *et al.*, 2004) and theoretical models (King, 1990; Hovadik & Larue, 2007). Therefore, it is appropriate to model fluvial sandstones in 3D to investigate static connectivity. Measures of static connectivity have been defined differently by different workers. Larue & Hovadik (2006) describe sandstone body and geobody connectivity as measures of the connectivity of reservoir architectural elements to each other. These measures of connectivity are reported as a percentage, defined by the volume of the largest reservoir rock divided by the total reservoir rock volume. According to Ainsworth (2005), a geobody is one or more connected reservoir rock bodies. Sandstone body and geobody connectivity are measures of the "depositional connectivity" (Ainsworth, 2005)**.** Reservoir connectivity has also been described as the part of a reservoir that is connected to wells and is also measured as a percentage (Larue & Hovadik, 2006; Pranter & Sommer, 2011). Other definitions of connectivity involve characterization of permeability heterogeneity and evaluation of subsurface fluid flow. The 3D static reservoir connectivity results provide insight into expected connected reservoir volumes for different net-to-gross ratios and well spacings. In addition, representative models of static reservoir connectivity and reservoir geometries are useful for reserve estimation, infill-drilling program design, and the selection of intervals for completion (Pranter & Sommer, 2011).

This chapter focuses on the reproduction of geobodies and facies distribution within a high-sinuosity fluvial system characterized by meandering channels and their associated overbank deposits (crevasse-splay deposits). The high-resolution sedimentological study of the M-S Unit, integrating both outcrop and subsurface data, previously described in Chapter 4, will be the basis for this study.

The aims of this chapter are to: (1) design appropriate modelling workflows with Petrel$_{TM}$ to best reproduce the distribution of heterogeneities, both at the scale of geobodies and at the scale of lithofacies, and which are exportable to other examples of high-sinuosity fluvial systems; (2) to construct a 3D training image, based on both outcrop and subsurface data, for a high-sinuosity system characterized by meandering channels and crevasse-splay deposits and, also, exportable to other reservoirs of the same type. (3) to create MPS simulations using the constructed 3D TI, in order to establish how this can help in the prediction of the reservoir geobodies, as well as evaluating how this prediction matches to the studied outcrop. In addition, several scenarios will be created in order to establish how input data influence the improvement of reservoir prediction using MPS-based modelling; and finally; (4) to evaluate the static

reservoir connectivity in the M-S Unit and to evaluate how this may vary with well spacing and geobody type.

8.2. Data and methodology

The OBO characterization workflow, including detailed sedimentological description from both surface ("classical" outcrop-derived and digital outcrop-derived observations plus measurements) and subsurface (cores and well logging) data, was applied in this study (see Chapter 3 for details). Similar data to that used in Chapter 4 was employed in this study; specifically, data from a 0.813 km^2, a total of 21 sedimentological logs (CP0, CPMR1 to CPMR8, CPML1 to CPML9 and PNV1) and 6 wells (MB1 to MB4, S2P3 and K2P1; Fig. 8.1). In addition, a Digital Outcrop Model (DOM) has been created to complete the outcrop-derived measurement dataset and digitize outcrop interpretations. Subsequently, a Geocellular Outcrop Model was created from the digitized interpretations within the digital outcrop model, using the methodology described in Chapter 3.

In the geostatistical modelling process, two facies modelling techniques were used: object-based modelling and multi-point statistics-based modelling (see Chapter 3 for full details of these modelling techniques). In addition, it is important to add that during the process of designing and computing modelling workflows, logical statement calculations were used.

8.3. Sedimentological framework: Geobody characterization and facies distribution

In Chapter 4, a high-resolution sedimentological study for the M-S Unit, integrating both outcrop and subsurface data, was presented. In this chapter, a total of eighteen Lithofacies (Table 4.1, Chapter 4) were introduced, grouped into ten facies associations (main channel, point bar, scroll bar, chute channel, crevasse channel, proximal crevasse-splay, medial crevasse-splay, distal crevasse-splay, distal floodplain and swamp; MSFA 1 to MSFA 10, respectively).
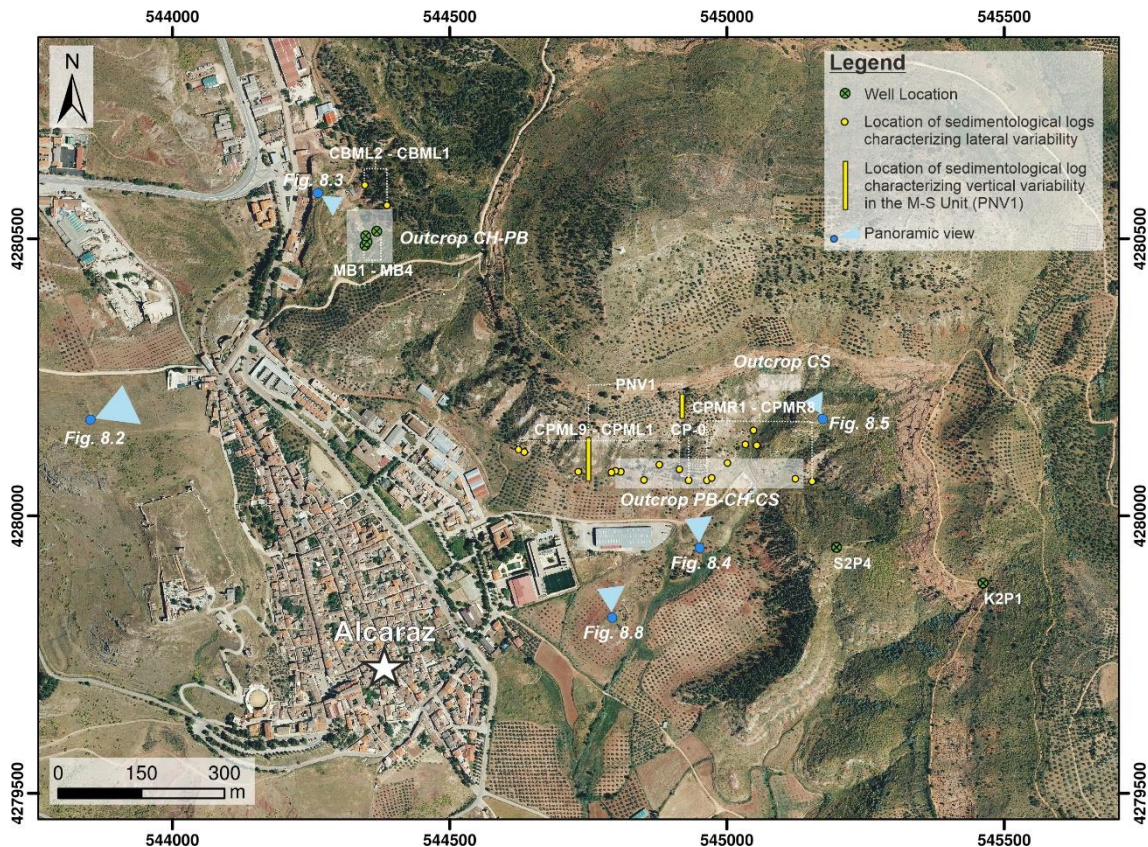
Fig. 8.1. Location of the study area (Alcaraz village, Albacete Province, Spain) showing the location of the studied outcrops for this chapter. Yellow points and yellow rectangles represent the location of sedimentological logs constructed to enable the characterization of lateral and vertical variability, respectively. Green points are well locations.

For the purposes of the present chapter, modelling the distribution of heterogeneities; and considering the limitations of the algorithms, it is not possible to support an excessive number of variables (fewer than eight; Ma, 2019). As such, these 10 facies associations are grouped in four geobody types (see Chapters 1 and 7; Table 8.1): CH (meandering channel fill), PB (point bar deposits), CS (crevasse-splay deposits) and FP (floodplain deposits).

In order to establish, and also to quantify, the lateral variability of facies and their relationship with the described geobodies, one stratigraphic interval was selected, as highlighted in Figure 8.2. This interval was selected on the basis of: (1) exceptional 3D outcrop features and significant lateral continuity, (2) the presence of the CH geobody, outcropping in two different locations at the selected stratigraphic interval, (3) well-established relationships between the four different geobodies, and (4) the selected interval has also been drilled by 5 wells (MB1-MB4 and S2P3).

Table 8.1. Summary of geobodies identified in the M-S Unit for this chapter. Geometry, thickness, width (lateral extension measured perpendicular to the main flow direction of the channel belt) and Lithofacies is showed for each geobody. The relationships of each geobody with facies associations described in Chapter 4 is also shown.

Geobody	Geometry	Thickness	Width	Facies Associations (from Yeste *et al.,* 2020)	Lithofacies
Channel (CH)	Lenticular	Up to 3 m	Up to 40 m	MSFA 1	Gm, St, Sr, Fl
Point bar (PB)	Sigmoidal	Up to 3.6 m	Up to 130 m	MSFA 2, MSFA 3, MSFA 4	Gm, St, Sr
Crevasse-splay (CS)	Lobular	Up to 2 m	Up to 230 m	MSFA 5, MSFA 6, MSFA 7, MSFA 8	Sh, Sr, Sc, Sd, Ll, Lm
Floodplain (FP)	Tabular	Up to 10 m	100-1000 m	MSFA 9, MSFA 10	Fm, Fl, Cm

8.3.1. Geobody CH: meandering channel fill

Geobody CH, composed only of MSFA 1, occurs as lenticular-shaped bodies up to 3 m thick with a lateral extension of up to 40 m perpendicular to the main paleoflow direction (Fig. 8.3 and Fig. 8.4, Table 8.1). They are characterised by a concave-up erosive base, whilst the top surface of the geobody is horizontal and sharp (Fig. 8.3c). CH geobodies are sandstone-dominated, and are also characterized by fining-upwards grain-size trend often with pebbly mudstones (Gm) as basal lags. Overlying the basal lags are medium to fine-grained sandstones with trough cross-bedding (St) and very fine-grained sandstone with current ripples (Sr) towards the top. Locally, these geobodies also show a final interval of laminated fine-grained deposits (Fl).

The fining-upward succession, together with the lenticular geometries and erosive lower surfaces suggest that CH geobodies should be interpreted as the deposits of meandering channels (Viseras *et al.*, 2018; Yeste *et al.*, 2020). The basal pebble lag (Gm Lithofacies) represents thalweg lag deposits (Bridge, 1993, 2003; Ghinassi *et al.,* 2014; Viseras *et al.*, 2018; Yeste *et al.*, 2020). The stacking of Lithofacies St and Sr reflect a gradual channel abandonment. The occasional presence of laminated fine-grained deposits (Lithofacies Fl) is interpreted as a

mud plug due to neck cut-off of a meandering channel, suggesting a high sinuosity meandering channel (Viseras *et al.*, 2018).

8.3.2. Geobody PB: point bar deposits

PB geobodies occur as asymmetrical, sigmoidal-shaped bodies, up to 3.6 m thick and with lateral extensions of up to 130 m (Table 8.1). These bodies are typically bounded by horizontal and erosive bases, whilst the tops are horizontal and sharp (Fig. 8. and Fig. 8.4). As shown in Chapter 4, both point bar (MSFA 2) and scroll bar (MSFA 3) facies associations are genetically related. In addition, the chute channel (MSFA 4) facies association is a small-scale element gradational into the scroll bar facies associations. For this reason, these three facies associations (MSFA 2 to MFSA 4) were merged into PB geobody.

PB geobodies are sand-dominated characterized by a fining-upward facies sequence passing from mudstone rip-up clast conglomerate (Lithofacies Gm) to very fine-grained sandstones (Lithofacies St and Sr). These geobodies typically display several inclined master bedding surfaces perpendicular to the paleocurrent direction (epsilon cross-bedding *sensu* Allen, 1963), which extends from base to top of the geobody, and delineates bedsets (*sensu* Ghinassi *et al.*, 2014). Internally, these bedsets are characterized by trough cross-bedding (Lithofacies St) and current ripples (Lithofacies Sr) towards the top of the facies sequence. Occasionally, conglomerate, with pebbly mudstone (Lithofacies Gm), occurs at the base. Locally, mud drapes occur between the inclined master surfaces, both as layers within the packages and as drapes over the inclined master surfaces.

The asymmetrical sigmoidal geometries together with the characteristic occurrence of several inclined surfaces perpendicular to the palaeocurrent and the fining-upward succession suggest that PB geobodies should be interpreted as point bar deposits. The low angle inclined surfaces are thus interpreted as lateral accretion surfaces. Basal pebble lags (Lithofacies Gm) are accordingly attributed to deposition in the pool zone of a laterally migrating channel thalweg. The occurrence of mud drapes between the lateral accretion surfaces represents deposition during a waning flood stage (Thomas *et al.*, 1987; Viseras *et al.*, 2018).

Fig. 8.2. Digital outcrop model showing the location of selected stratigraphic interval in the M-S Unit stratigraphic framework of study area. Selected outcrops and S2P3 well is also show.
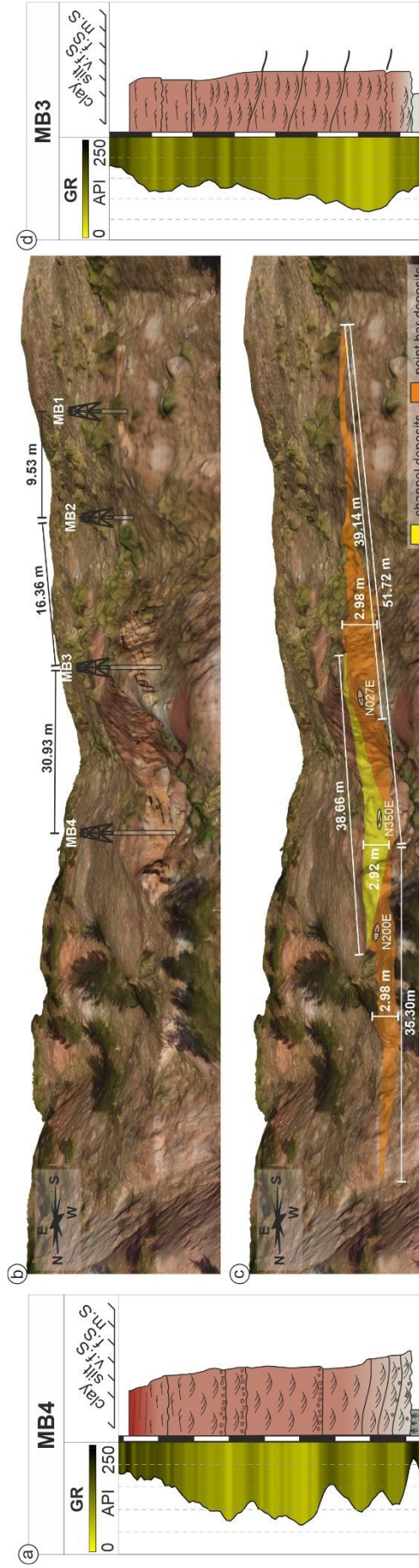
Fig. 8.3. Digital outcrop model and well data (core description and gamma ray log) of Outcrop CH-PB. **(a)** GR log and core description for Well MB 4, principally characterized by the CH geobody. **(b)** Digital outcrop model of Outcrop CH-PB showing well locations. **(c)** Interpreted digital outcrop model of Outcrop CH-PB showing width, thickness and orientation measurements for both CH and PB geobodies. **(d)** GR log and core description for Well MB 3, consisting largely of Geobody PB.

Fig. 8.4. (a) Digital outcrop model of the key interval with geobodies PB-CH-CS showing the location of sedimentological logs. **(b)** Interpreted digit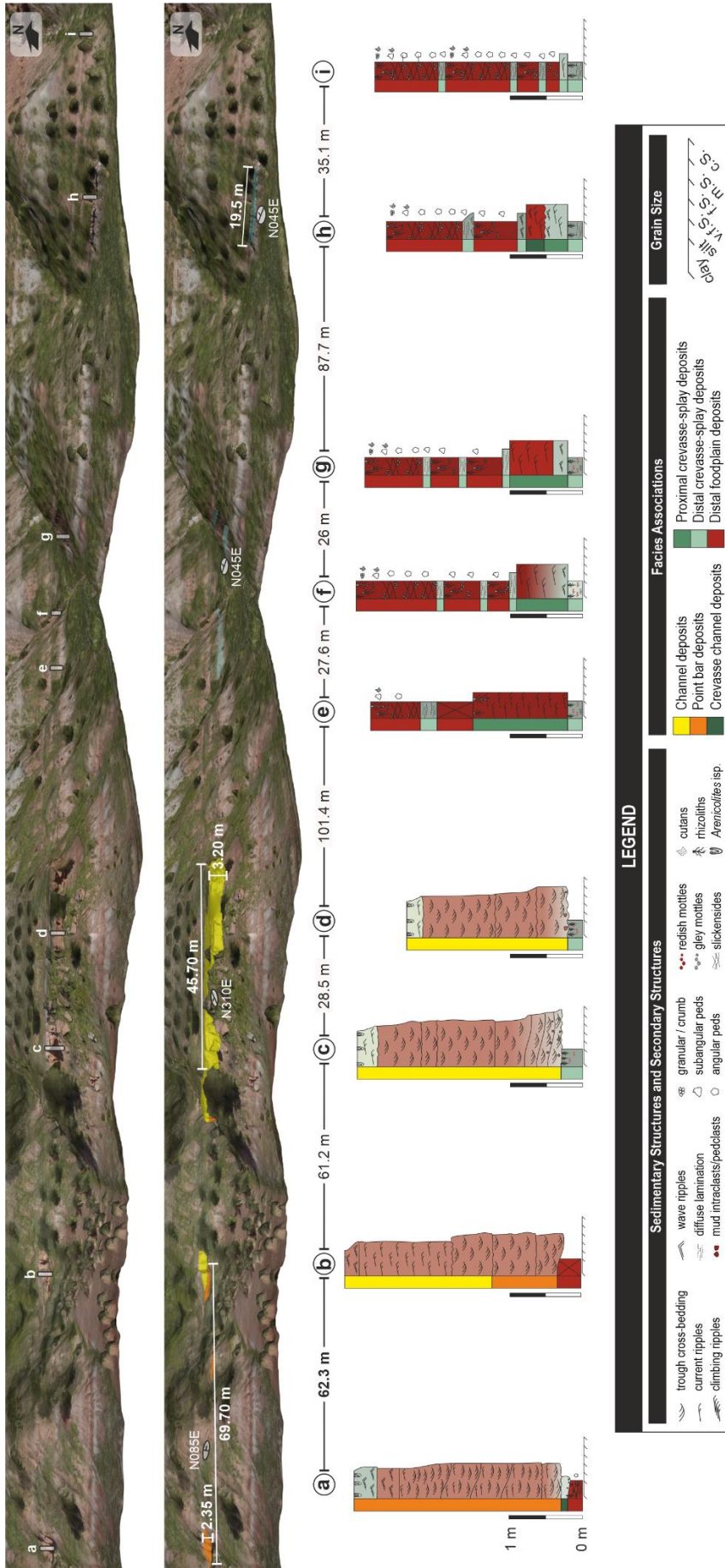al outcrop model of Outcrop PB-CH-CS showing width, thickness and orientation measurements of geobodies. See Figure 8.2 for outcrop location. **(c)** Sedimentological logs constructed for outcrop PB-CH-CS and measured distances between each sedimentological log.

8.3.3. Geobody CS: crevasse-splay deposits

CS geobodies occur as lobe-shape bodies, up to 2m thick and up to 230 m in lateral extension, perpendicular to the main paleoflow direction (Table 8.1). These lobate bodies are characterized by a horizontal, sharp base, whilst the tops are convex-up and sharp (Fig. 8.5). In Chapter 4 four component facies associations were distinguished: crevasse channels (MSFA5), proximal crevasse-splay (MSFA6), medial crevasse-splay (MSFA7) and distal crevasse-splay (MSFA8). With the aim of better modelling the distribution of heterogeneities, but also considering the practical limits of the algorithms, these four facies associations were grouped first into a single lower order geobody (CS) and then into two finer-scale geobodies: proximal crevasse-splay geobodies (CSp), characterized by high-energy facies associations (MSFA 5 and MSFA 6); and distal crevasse-splay geobodies (CSd), characterized by low-energy facies associations (MSFA 7 and MSFA 8).

CSp geobodies, with up to 2 m of thickness and 130 m of lateral extension, perpendicular to the main flow direction of the channel belt and from their insertion point (channel margin), are characterized by horizontal laminated (Lithofacies Sh) to trough cross-bedded (Lithofacies St) and/or current rippled sandstones (Lithofacies Sr). Towards the top of these geobodies, climbing ripple cross-laminated sandstones (Lithofacies Sc) are also recognized. Commonly, small lenticular bodies, up to 1.1 m thick and up to 6 m width, appear within these geobodies. These display concave-up, erosive bases and horizontal, sharp tops, and are characterized by thin mudstone rip-up clast conglomerates as basal lags overlain by fine to very fine-grained sandstone with trough cross-bedding (Lithofacies St) and very fine-grained sandstone with current ripples (Lithofacies Sr).

CSd geobodies, with up to 1.5m of thickness and 100 m of lateral extension, are characterized by climbing ripples (Lithofacies Sc) and/or current rippled sandstones (Lithofacies Sr) at the base alternating with syn-sedimentary deformed sandstones (Lithofacies Sd). In addition, planar laminated siltstones (Lithofacies Ll) overlain by massive, diffuse laminated siltstones and mudstones with pedogenic features (rhizoliths, mottles and cutans) plus desiccation cracks (Lithofacies Lm), occur at the distal limits of these geobodies.
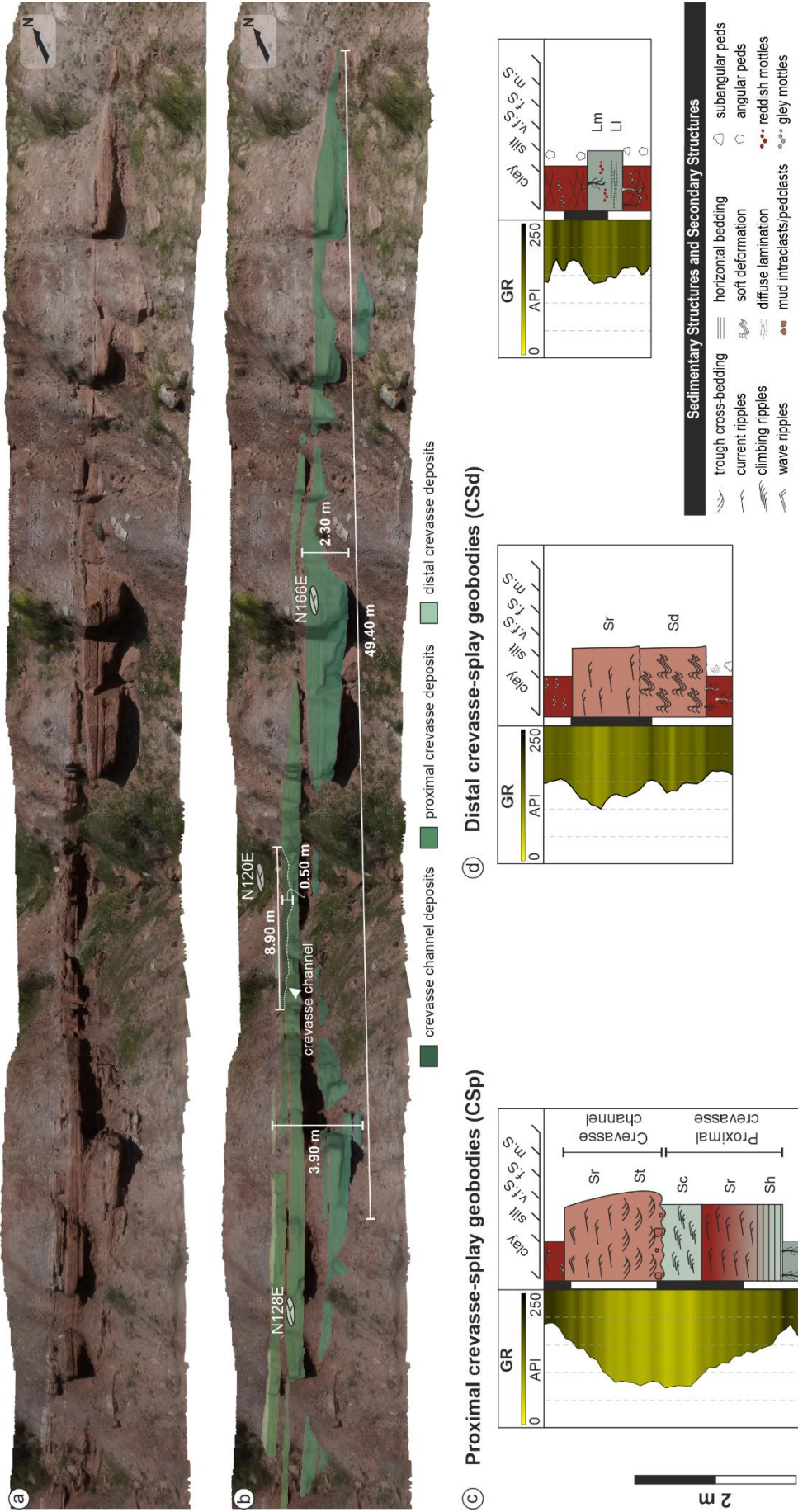
Fig. 8.5. (a) Digital outcrop model of Outcrop CS. **(b)** Interpreted digital outcrop model of Outcrop CS showing width, thickness and orientation measurements of geobodies. See Fig. 8.1 for outcrop location. **(c)** Sedimentological log from Well S2P3 penetrating a CSp geobody. **(d)** Sedimentological logs from Well S2P3 penetrating a CSd geobody.

CSp geobodies are interpreted as proximal crevasse-splay deposits. Lenticular bodies located within these geobodies, are interpreted as crevasse channel deposits. In contrast, CSd geobodies are interpreted as medial and distal crevasse-splay facies associations as described in Chapter 4. Also as highlighted in Chapter 4, CS geobodies rarely occur as a single crevasse-splay lobe. Rather they are formed during continuous flood events leading to overlapping CS geobodies, forming crevasse-splay complexes.

8.3.4. Geobody FP: floodplain deposits

FP geobodies are tabular in aspect, up to 10 m thick and may be up to 1000 m in lateral extent, with horizontal and sharp bounding surfaces (Table 8.1). These tabular bodies are characterized by massive mudstones (Lithofacies Fm) with abundant pedo-features (rhizoliths, mottles, nodules, cutans and slickensides). Locally, intervals, up to 2 m thick and with up to 100 m of lateral extension, characterized by thin-laminated mudstones (Lithofacies Fl), coal laminas and massive micritic limestones (Cm), also occur.

FP geobodies include distal floodplain (MSFA9) and swamp (MSFA10) facies associations as described in Chapter 4. Massive mudstones with abundant pedo-features correspond to deposits of a distal floodplain. Intervals with laminated mudstones, coal laminae and massive micritic limestones are interpreted as deposits associated with swamp environments on the floodplain (Yeste *et al.,* 2020).

8.3.5. Spatial relationship between geobodies and facies distribution

The full integration of both, outcrop and subsurface datasets, has enabled a significantly better understanding of the spatial relationships between described geobodies as well as, the development of conceptual models which include both descriptive and quantitative data related to the distribution of heterogeneities within the M-S Unit, as previously shown in Chapter 4 and 7. Key elements are summarised as follows (Fig. 8.6).

Geobody CH is 40 m wide and up to 3 m thick (Fig. 8.6).

Geobodies PB and CS are genetically related with Geobody CH. On the accretional, inner margin of the channel thalweg, the CH geobody grades into the PB geobody. These are up to 3.6 m thick, and extend for up to 130 m, perpendicular to the main flow direction of the channel

belt. The PB geobody extends from the main channel and grades laterally into the floodplain geobody (FP).

On the erosive margin of the channel (CH), the CS geobodies comprise proximal crevasse-splay deposits (CSp), up to 2 m thick and with up to 130 m of lateral extension, perpendicular to the main flow direction of the channel belt, stretching from their insertion point on the channel margin. Geobody CSp passes from the channel into distal crevasse-splay deposits (CSd). These are similar in dimensions to CSp; up to 1.5m thick, and with 100 m of lateral extension. The latter is located between 130m and 230 m away from the main channel geobody (Fig. 8.6) and grades laterally into the FP geobody.
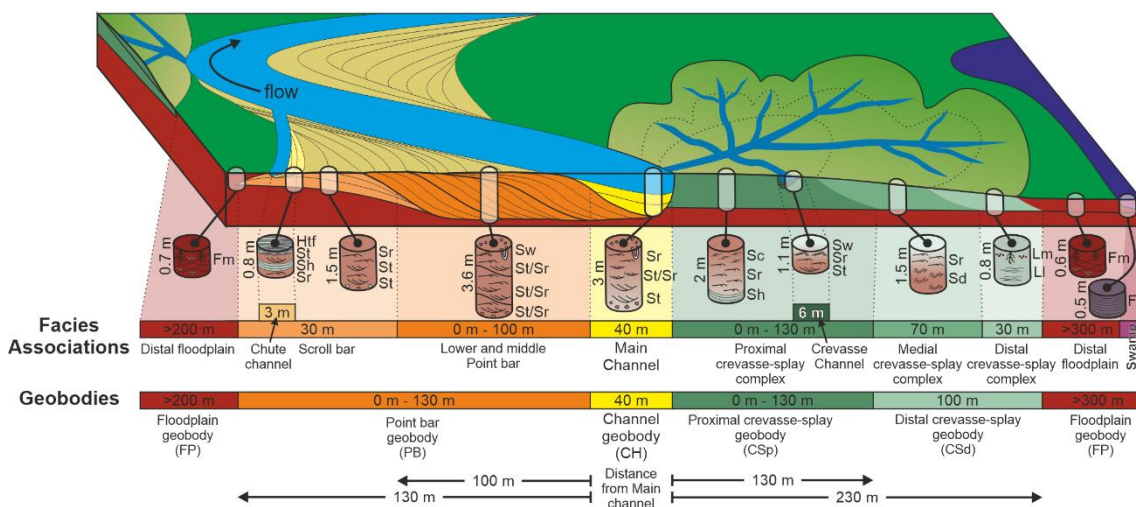

Fig. 8.6. Conceptual model of lateral variability for geobodies and facies including sedimentary features, lateral extent or width of the associated depositional area and thickness of each geobody (modified from Figure 4.5 in Chapter 4 and Yeste *et al.*, 2020).

In addition to the foregoing key observations, integrating both outcrop and subsurface data, and applying the quantitative conceptual model, a paleogeographic reconstruction was developed showing the distribution of the different geobodies for the selected interval (Fig. 8.7). This paleogeographic reconstruction will be used as a tool to test the results of geostatistical modelling in the following sections.

The complete M-S Unit stratigraphic succession is characterized both by the vertical stacking of the previously described geobodies, as well as the spatial relationships between these geobodies and lithofacies distributions, which are similar throughout the studied succession.

Considering each channel geobody as a stratigraphic level (a time equivalent interval or isochron) and its avulsion as another, younger, stratigraphic interval, a total of 16 such stratigraphic intervals (zones) were identified in the M-S Unit of the study area (Table 8.2). Zones were numbered from base to top of the M-S Unit. Zone 5 corresponds to the selected interval, previously described (section 8.3; Fig. 8.2). In each stratigraphic interval, the channel geobody was located in outcrop and/or in wells, except for the two deepest intervals, where the outcrop conditions did not permit location of the geobody.
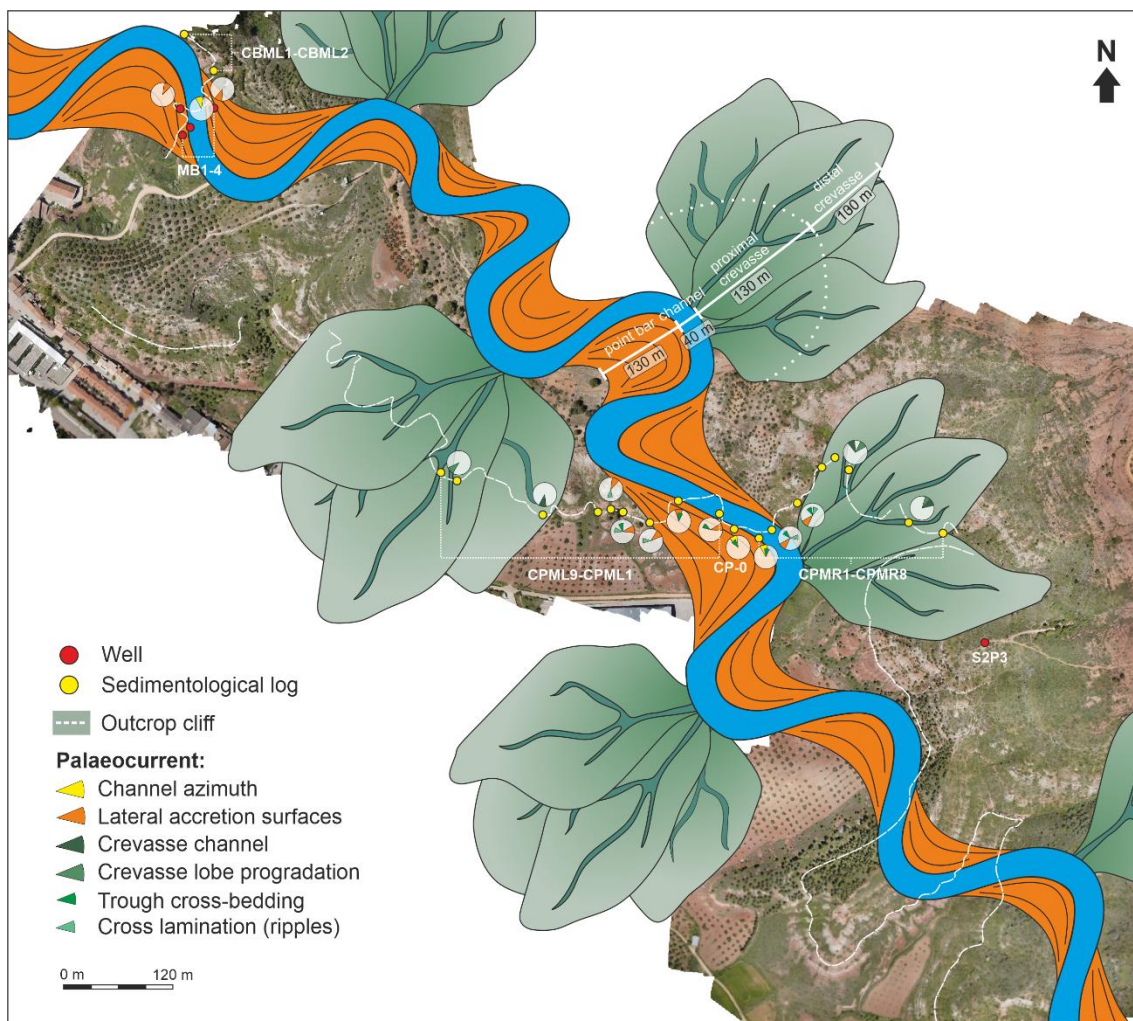
Fig. 8.7. Paleogeographic distribution of geobodies for the selected interval (Zone 5). This shows the location of both sedimentological sections and wells plus paleocurrent data**.**

In addition to the above and in order to determine the channel-belt orientation in each stratigraphic interval, channel paleocurrents were measured on outcrop and/or from well logs. In the cases where it was not possible to carry out the measurements directly on the channel

geobody, these were inferred from the point bar and/or crevasse-splay geobodies (Fig. 8.8, Table 8.2).

Fig. 8.8. West-East oriented panoramic view showing the stacking of channel geobodies in the M-S Unit. Orientation of each channel geobody is also highlighted.

Table 8.2. Stratigraphic intervals (zones) identified from the M-S Unit in the study area. Assigned number and orientation for CH geobodies in each zone are also shown. Zone 5 corresponds to the selected stratigraphic interval.

Zone	Channel Geobody	Channel-belt Orientation
16	16	N354
15	15	N319
14	14	N021
13	13	N318
12	12	N360
11	11	N333
10	10	N310
9	9	N360
8	8	N325
7	7	N332
6	6	N321
5	**5**	**N310**
4	4	N020
3	3	N309
2	2	N340
1	1	N020

8.4. 3D Reservoir modelling

This section is focused on the second key element of the methodological workflow designed for this thesis, the reservoir modelling process (Fig. 8.9), covering the research goal of planning reservoir modelling strategies from OBO characterization datasets (see Chapter 1). As previously described, a 3D reservoir model is a digital representation of the subsurface, discretized into 3D cells, for modelling rock and petrophysical properties (Ma, 2019). This digital representation requires input data to geometrically define the reservoir and condition the property modelling. Thus, data and results presented in the previous section (and also in Chapter 4) were used as input data to create the 3D model framework and reproduce the distribution of heterogeneities in the facies modelling process (Fig. 8.9).

In this section, the 3D reservoir framework and the facies modelling workflow designed for this study, as well a 3D training image (TI) which reproduces a meandering channel system and its associated overbank sandstone deposits, are presented (Fig. 8.9). In addition, modelling results focused on the prediction of the reservoir geobodies, using MPS-based modelling techniques, and on the evaluation of the static reservoir connectivity in the M-S Unit, using OBM techniques, are also presented (Fig. 8.9).

8.4.1. 3D model framework

The dimensions selected for the 3D reservoir models are 1400 m x 1200 m x 77m, and include the entire studied section of the M-S Unit in the study area (Table 8.3). Seventeen stratigraphic horizons, digitized from a Digital Outcrop Model, are used to construct the 3D model framework. Stratigraphic horizons subdivide the 3D model into 16 zones (Fig. 8.10). Zones were numbered from base to top of M-S Unit. Zone 5 corresponds to the selected interval, previously described (Fig.8.2; Table 8.2).

The 3D reservoir model contains 160 proportional layers that are each approximately 0.5 m thick. The 3D cell dimensions of 5 m x 5 m x 0.5 m result in a total for the model of 10.8 million cells (Fig. 8.10, Table 8.3). The cell dimensions are designed to be small enough to capture the geometry of the smallest geobodies and facies distribution in the model.
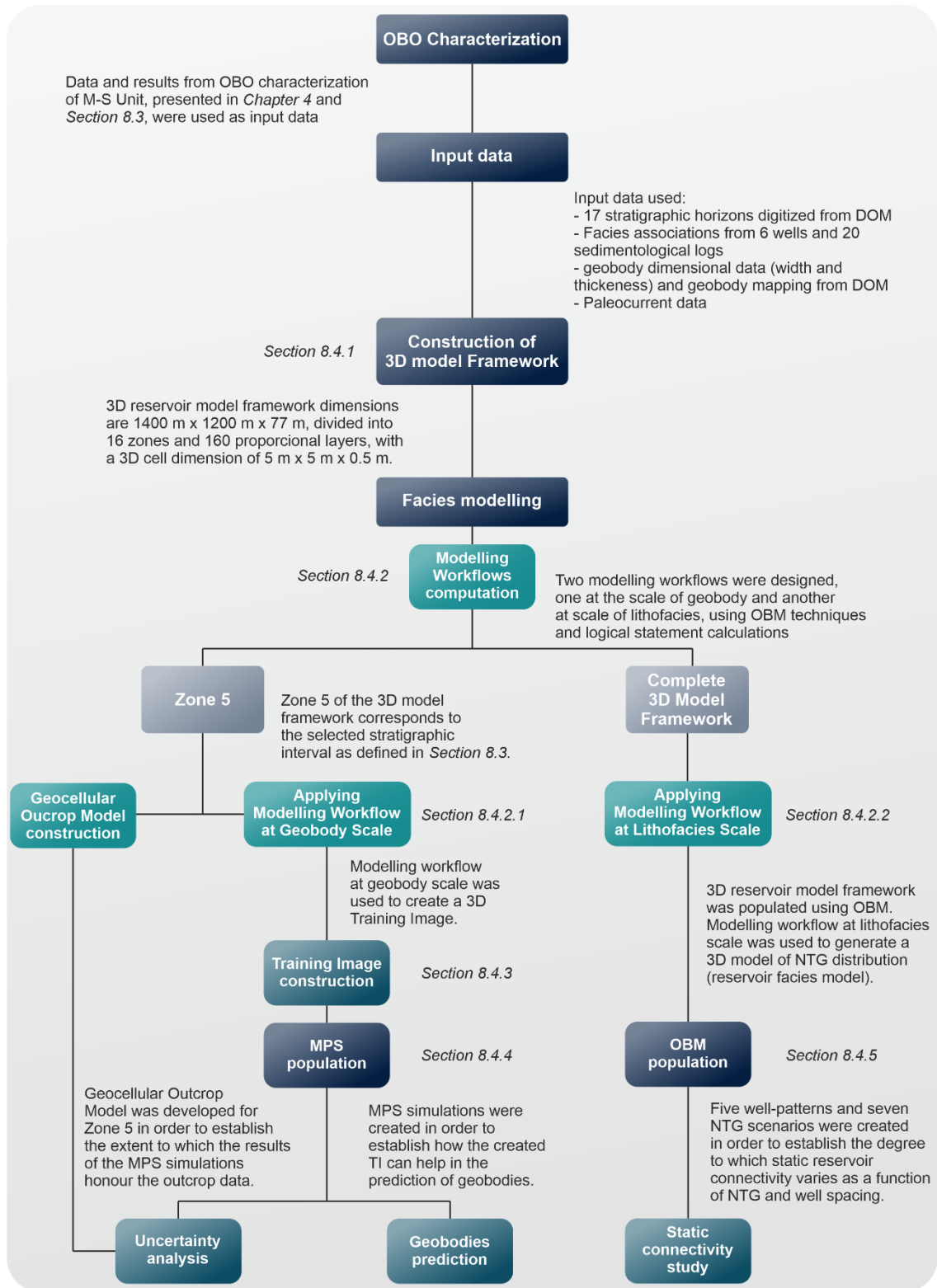
Fig. 8.9. Detailed workflow diagram applied in this study to geostatistical reservoir modelling of M-S Unit. OBO (Outcrop/Behind Outcrop); MPS (Multi-Point Statistics); OBM (Object-based modelling); DOM (Digital Outcrop Model); NTG (net-to-gross).

The following data were used as input data in both object-based and MPS-based simulations: (1) facies associations data from six wells (MB1-MB4, S2P3 and K2P1), (2) facies associations data from twenty sedimentological logs (CP0, CPMR1-CPMR8, CPML1-CPML9 and CBML1-CBML2), and (3) outcrop dimensional data (eg. width and thickness of geobodies). In addition, the digitized data from the ten facies associations in the Digital Outcrop Model were used in the construction of the geocellular outcrop model (Fig. 8.10, see Chapter 3, section 3.2.3 for an outline of the detailed methodology applied in this study for the construction of a geocellular outcrop model).

The geocellular outcrop model corresponds to Zone 5 (Table 8.10) of the 3D reservoir model. This has a total of 306 upscaled cells and comprises outcrop sections studied in the previously described selected interval, (Fig. 8.10). This geocellular outcrop model only includes data for the CH, PB and CS geobodies. The FP geobody was not included in the geocellular outcrop model as this non-reservoir element is used as the background in the modelling process. In addition, this geocellular outcrop model, with a total of 306 upscaled cells, will be used to compare the facies modelling results with the outcrop.

Table 8.3. Grid properties of reservoir model framework. Min and Max columns show the minimum and maximum coordinates values (in metres) for X and Y axis, and elevation values (Z row). Delta column shows the total extent, in metres, along the X and Y axis; whilst the Z row shows the difference in elevation between the highest point and the lowest point in the 3D model framework. The Grid cells row shows the total number of cells in the X, Y and Z axis respectively; whilst the Total number of grid cells row shows the total number of cells that comprise the 3D model framework. The Average X, Y and Z rows show the cell dimensions in X, Y and Z, respectively. The Number of zones and layers rows show the total number of zones and layers, respectively, that comprise the 3D model framework.

Axis	Min	Max	Delta
X	544100	545800	1400
Y	4279600	4280800	1200
Z	894.25	1016	121.75

Grid cells	280x240x161
Total number of grid cells	10819200
Average X	5
Average Y	5
Average Z	0.5
Number of zones	16
Number of layers	160
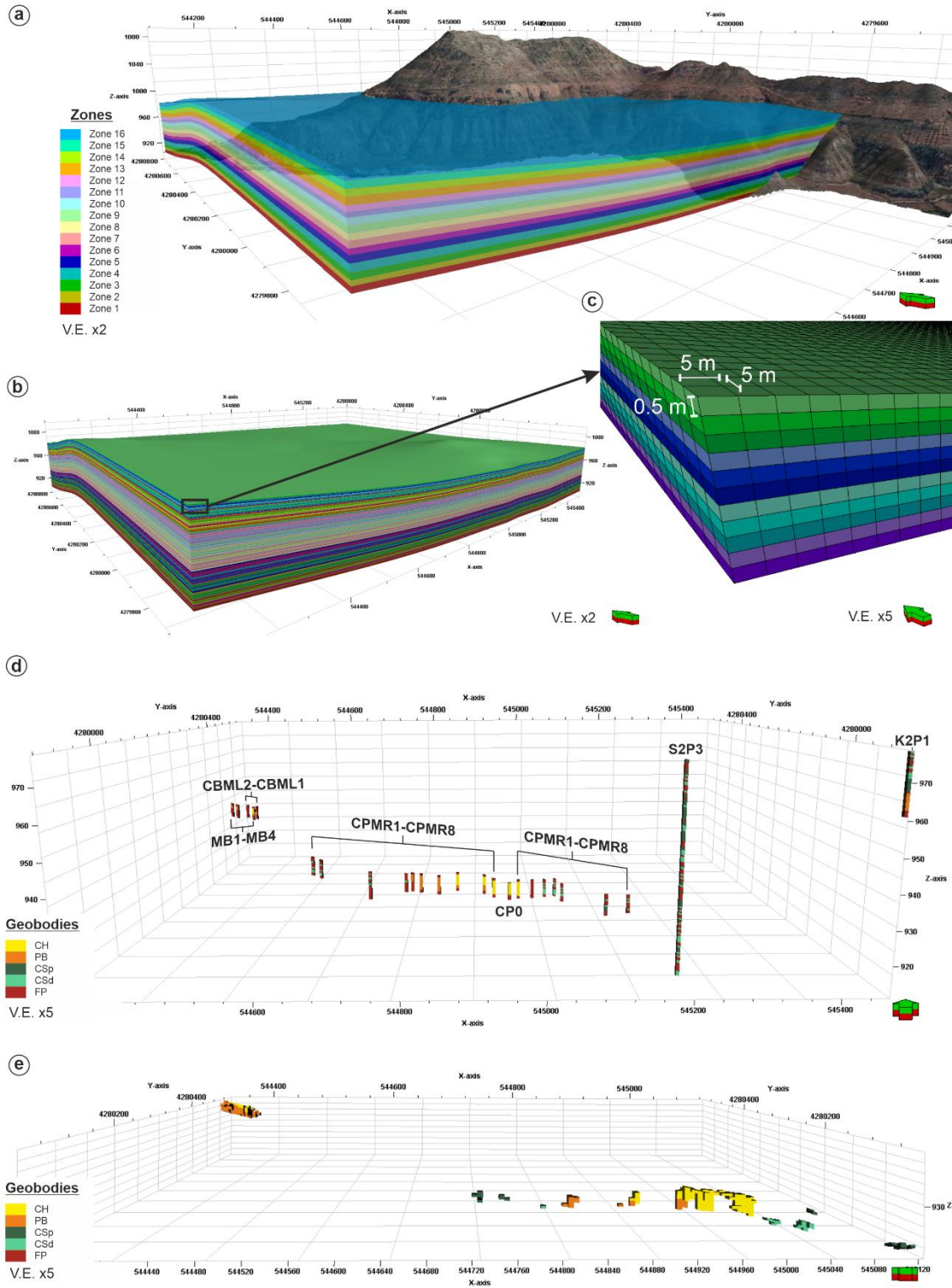
Fig. 8.10. Three-dimensional reservoir model framework, input data and geocellular outcrop model. **(a)** Zone model showing the 16 zones differentiated in the reservoir model. **(b)** Layering for the reservoir model framework. **(c)** Cell dimensions established for the reservoir model framework. **(d)** geolocated input data used in the modelling processes in this work from wells and sedimentological logs. **(e)** geocellular outcrop model of Zone 5 created from the digitizing of geobodies in the digital outcrop model.

8.4.2. Facies modelling workflows

As previously described in Chapter 3 (Section 3.2.4), the modelling workflow tool allows the design of modelling routines including a large number of steps which can be executed without interruption. Using a modelling workflow, each process and/or calculation made in the steps is documented and it is possible to rerun these steps for the generation of multiple models in order to test the uncertainty associated with specific parameters, as well as rerun the steps when data or parameters change. In addition, a designed modelling workflow can be exported and applied to other 3D reservoir model frameworks.

In this study, two modelling workflows were computed using both Object-based modelling and logical statement calculations. Logical statement calculations allow the creation of new properties, as well as perform operations between pre-existing properties. Combining Object-based modelling results and logical statements, the relationship between the geobodies, as well as the internal distribution of a specific property (eg. facies distribution) within each modelled geobody, can be reproduced.
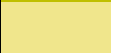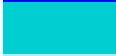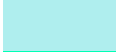
The first modelling workflow was created to populate the model framework with the previously described geobodies (CH, PB and CS, both CSp and CSd). Geometrical data obtained from outcrop and subsurface data, such as shape, width, thickness, amplitude and wavelength (Table 8.4); as well as the spatial relationship between geobodies, was used in the workflow computation. This workflow was then used to build a 3D Training Image (see Section 4.3 and 4.4). The second modelling workflow is an extension of the first. This workflow was created to reproduce the facies distribution previously interpreted in both outcrop and subsurface data. It was subsequently used to estimate the static reservoir connectivity in the M-S Unit (see Section 4.5).

In Facies modelling processes, a numerical value needs to be assigned to each geobody and lithofacies. In addition, for the correct visualization of results, it is necessary to assign a colour to each numerical value. Table 8.5 shows both the numerical values and colour codes used in this study. These codes were used in the calculations shown in the following sections as well as in the graphic representation of results.

Table 8.4. Geometrical parameters of geobodies obtained from outcrop and subsurface data. LAP: Lateral Accretion Package.

Geobody		Minor Width (m)	Maj/Min Ratio	Min Thickness (m)	Med Thickness (m)	Max Thickness (m)	Amplitude (m)	Wavelength (m)
CH		40	-	-	3	-	200	400
PB	LAP 1	40	-	-	3.6	-	60	330
	LAP 2	40	-	-	3.6	-	80	340
	LAP 3	40	-	-	3.6	-	100	350
	LAP 4	40	-	-	3.6	-	120	360
	LAP 5	40	-	-	3.6	-	140	370
	LAP 6	40	-	-	3.6	-	160	380
	LAP 7	40	-	-	3.6	-	180	390
CS	CSp	70	2	-	-	-	-	-
	CSd	115	2	0.8	1.5	2	-	-

Table 8.5. Colour and number codes used in the modelling workflows.

Geobodies			Lithofacies		
Colour Code	Number Code	Name	Colour Code	Number Code	Name
	1	CH geobody		13	Lithofacies Ll
	2	PB geobody		14	Lithofacies Lm
	3	CSp geobody		15	Lithofacies Sh
	4	CSd geobody		16	Lithofacies Sr
	5	FP geobody		17	Lithofacies Sc
	6	LAP 7		18	Lithofacies Sd
	7	LAP 6		19	Lihofacies Gm
	8	LAP 5		20	Lithofacies St
	9	LAP 4		21	Lithofacies Fl
	10	LAP 3			
	11	LAP 2			
	12	LAP 1			

8.4.2.1. Modelling workflow at geobody scale

This workflow was design to populate the 3D reservoir model at geobody scale. Four different geobodies were interpreted in the M-S Unit. As previously described, these were (1) Ch geobody, (2) PB geobody, (3) CS geobody, comprising finer scale CSp and CSd geobodies; and (4) FP geobody. The modelling workflow at geobody scale combines four different properties (bodies property, object-curvature property, directional trend property and insertion-zone property; Table 8.6) and two logical statements (logical statements 1 and 2; Table 8.7) to create the resultant geobodies model. The following sections detail the steps and calculations used for the representation of each geobody. The FP geobody was modelled as background.

Modelling of the CH geobody

The Channel geobody (CH), as previously described, is a channelized object, with up to 3 m of thickness and up to 40 m in width**.** In addition, from a paleogeographic reconstruction (Fig. 8.7) of the selected interval (Zone 5), it is apparent that channel amplitude (up to 200m) and wavelength (up to 400m) can also be inferred. (Fig. 8.11).
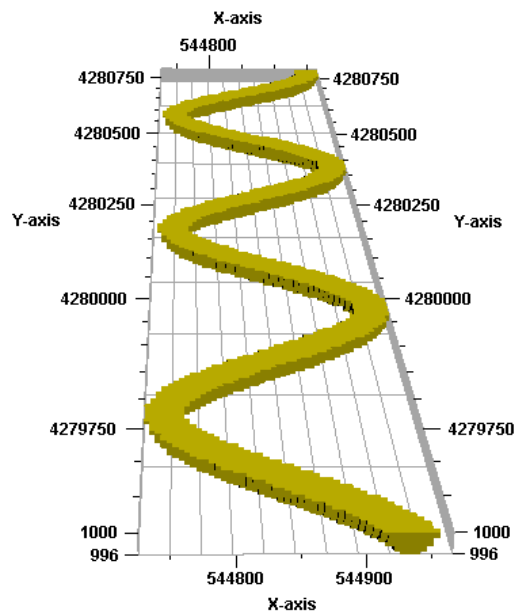
Fig. 8.11. Example of a modelled Channel geobody.

Table 8.6. Summary of the calculated properties in the modelling workflows.

Acronym	Property name	Description
GM	Geobodies model	Object-based modelling results representing geobody distribution.
FM	Lithofacies model	Object-based modelling results representing the lithofacies distribution.
B_C	Bodies property	Property with indexed numbers for each of the objects inserted from the object-based modelling result. The background facies are assigned to index number zero.
CP	Object-curvature property	Property whose values show the curvature of the edge of the nearest object. The curvature of the object's edge is calculated as the inverse of the radius of curvature of the edge, and made negative when the object is concave. The smallest radius of curvature is limited to one cell to avoid infinite curvature values when taking the inverse. The curvature away from the edge is calculated by using several nearby object-edge points, extrapolating the curvature, and then weighting by the inverse distance to the points. This causes the curvature values to asymptotically approach 0 away from objects.
DP	Depth trend property	Property which varies with the relative distance of each cell in the body from the body's base.
DTP	Object-distance property	Property whose values show the distance to the edge of the nearest object.
DAP	Directional trend property	Property with the azimuth of the inserted bodies in each cell. For standard objects, the azimuth for each cell of the body is the same. However, for channel objects, the azimuth varies with the channel direction.
IZ	Insertion-zone property	Property calculated from object-curvature property of the channel object, and whose index numbers are 1, for the zone of highest curvature of the channel object, or 0 for the rest of object-curvature property of channel object. The value 1 representing the insertion zone of the CS geobodies.
EZ_C	Energy-zones property from object-curvature property	Property, calculated from the object-curvature property, whose indexed numbers divide the object in two or more zones in function of the curvature of the object.
EZ_D	Energy-zones property from depth trend property	Property, calculated from the depth trend property of the object, whose index numbers divide the object in two or more zones as a function of object depth.
EZ_{DT}	Energy-zones property from object-distance property	Property, calculated from the object-distance property of the channel object, whose index numbers divide the object into two or more zones as a function of the distance to the channel object.

Modelling of PB geobodies

Point bar geobodies (PB), as previously described, are sigmoidal in shape, up to 3.6 m thick and with lateral extensions of up to 130 m. In addition, these geobodies always occur on the inner margin of the thalweg so that the channel geobody grades into the point bar geobody. Internally, the PB geobody is characterized by lateral accretion packages (LAPs) formed by migration, typically by expansion and rotation, of the channel thalweg (Ghinassi *et al.,* 2014; Ielpi & Ghinassi, 2014).

Considering this, PB geobodies have been modelled as successive channel objects to reproduce LAPs. Each channel object corresponds to a LAP. Each channel object also erodes the previous object and will be eroded by the next object (Fig. 8.12). To reproduce the migration by expansion and rotation, each LAP increases its amplitude (to reproduce the expansion) and wavelength (to reproduce the rotation; Fig. 8.12).

Finally, all LAPs are assigned to a PB geobody following the logical statement (Fig. 8.12j; Table 8.7):

$$GM = If\left(GM > 5 \ And \ GM \le 12, 2, GM\right) \tag{1}$$

where, GM is the Geobodies model and values 5, 12 and 2 correspond to the number code for geobodies (Table 8.5).
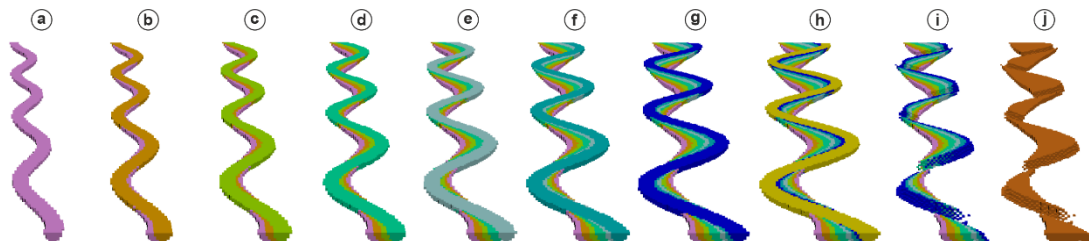
Fig. 8.12. Point bar modelling results. **(a)** – **(g)** modelling of successive channel objects representing the lateral accretion packages (LAPs). Note each channel object erodes the previous object and is itself eroded by the next object. **(h)** Final modelled channel-object which represents the CH geobody (this is the same CH object shown in Fig. 8.10). **(i)** LAP modelling results after channel object modelling. Note the final result is a series of sigmoidal-shaped geobodies corresponding to each LAP. **(j)** Final modelling result for the PB geobodies applying logical statement 1 which transforms the modelled LAPs into a single geobody. Note PB geobodies are represented by crescent-shaped objects

Modelling of CS geobodies

CS geobodies appear on the erosive margin of the channel. These geobodies have a lobe-like shape in plan view and can be sub-divided into Proximal crevasse-splay geobodies (CSp), up to 130 m in width and 2 m thick; and Distal crevasse-splay geobodies (CSd), up to 100 m in width and 1.5 m thick.

To model CS geobodies it is necessary to first obtain the curvature (CP) and directional trend properties of the channel geobody (Fig. 8.13a; Table 8.6). From the curvature property of the channel (Fig. 8.13b), and as CS geobodies occur on the erosive margin of the main channel, a property known as the "insertion-zone" (IZ) can be generated (Fig. 8.13c; Table 8.6). The highest positive values for the object-curvature property for a CH geobody correspond to the convex part of the channel object. Thus, the insertion-zone property is determined by the zone of highest curvature of the channel object. The object-curvature property for the CH geobody is associated with values higher than 0.14 for the insertion zone of CS geobodies. Within this framework, CS geobodies are generated when the insertion-zone property is characterized by values of 1, whereas for values of 0 no CS geobodies are generated. This key value is obtained with the following logical statement (Table 8.7):

$$IZ = If(CP > 0.14, 1, 0) \qquad (2)$$

where IZ is the insertion-zone property and CP is the object-curvature property of channel object. Value 0 represents the background.

The directional trend property is used to determine the orientation of CS geobodies (Fig. 8.13d).

With this established, those objects corresponding to the CSd geobodies were first modelled. Subsequently, within these (CSd objects), the objects representing the CSp geobodies were then modelled. CSd objects have a width of up to 230 m and a thickness that varies between 0.8 and 2 m. CSp objects have a width of 130 m and a thickness of up to 2 m.
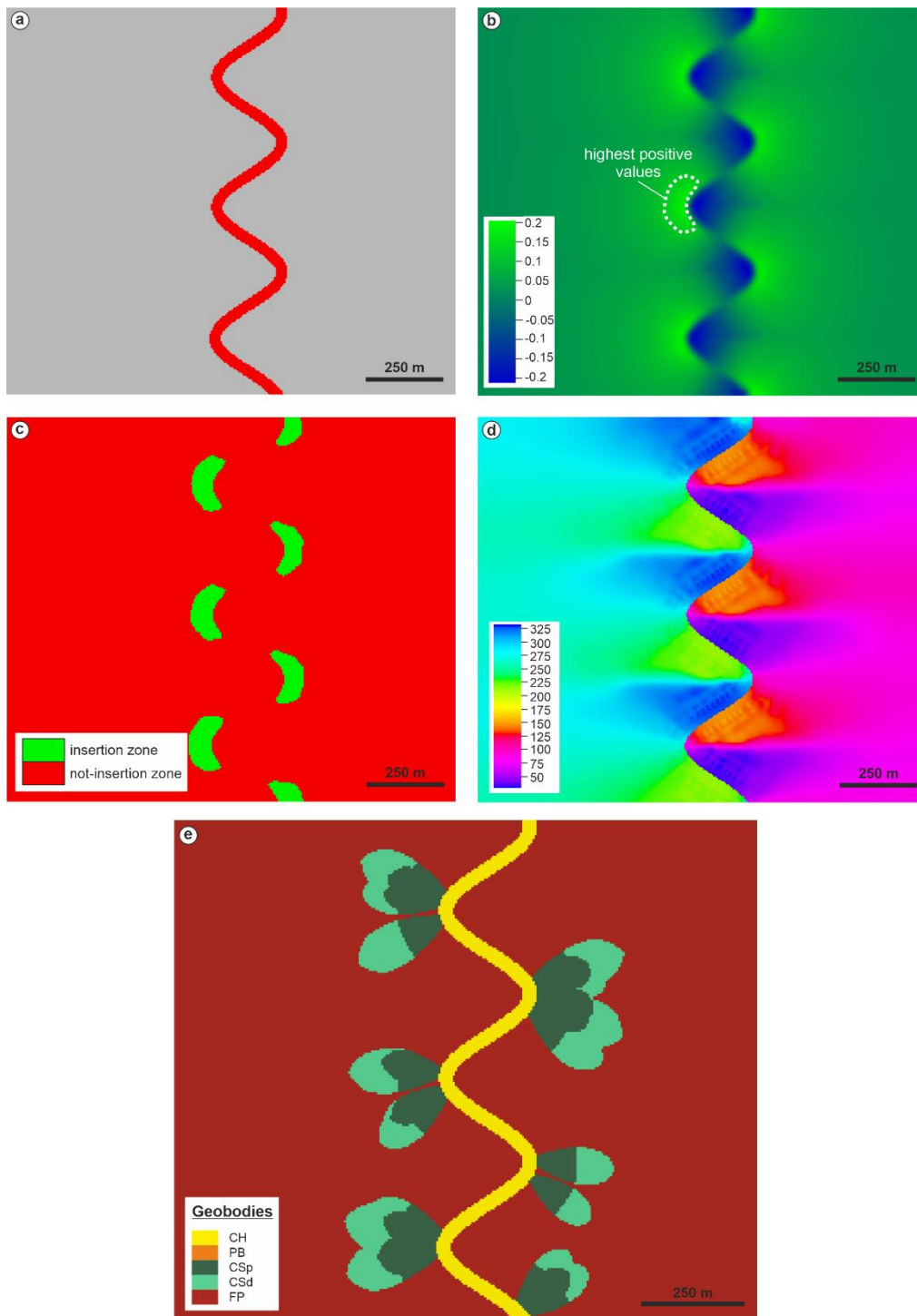
Fig. 8.13. (a) Channel object property. **(b)** Object-curvature property from channel object (a). **(c)** Insertion-zone property calculated from object-curvature property (b). **(d)** Directional trend property of channel object (a). **(e)** CS geobodies modelling result.

8.4.2.2. Modelling workflow at Lithofacies scale

This workflow was designed as an extension to the first workflow, in order to populate the 3D reservoir model at lithofacies scale. In other words, it uses the geobodies (CH, PB and CS geobodies) modelled with the previous workflow and populates them on the basis of the lithofacies variability, interpreted in both outcrop and subsurface data. The modelling workflow at lithofacies scale combines a total of seven properties (bodies property, object-curvature property, depth trend property, object-distance property, energy-zones property from object-curvature property, energy-zones property form depth trend property and energy-zones property from object-distance property; Table 8.6) and forty logical statements (Logical Statements 3 to 42; Table 8.7) to create the resultant lithofacies model. The following sections detail the steps and calculations used for the lithofacies representation of each geobody. As before, the FP geobody was modelled as background.

Lithofacies modelling into the CH geobody

To reproduce the facies variability across the CH geobody, the Curvature and Depth properties of the object were used (Table 8.6).

Curvature and the Energy Zones Model:

From the object-curvature property (CP), the thalweg pool zone (TP) and thalweg riffle zone (TR) were determined (Fig. 8.14a). Grain size is coarsest (Lithofacies Gm) in the thalweg pool zone, along the outer bank near the bend apex, and finer-grained (Lithofacies St and Sr) as flows shoal onto the bar along the inner bank. On the other hand, mean grain-size is uniform (Lithofacies St) across the thalweg riffle zone as expanding flows move coarser bed load from a TP through the bend crossover area.

Considering this, three zones can be established within the channel depending on the curvature: (1) high-energy zone, (2) middle-energy zone and (3) low-energy zone (Fig. 8.14b). The high-energy zone corresponds to the thalweg pool, where grain size is coarsest. The middle-energy zone corresponds to the transition from the outer and inner bank and with the thalweg riffle zone, where the grain size is uniform. Finally, the lower-energy zone corresponds to the inner bank, where the grain size is finest. Based on this concept, a property which defines the energy zones of a channel object and is derived from the curvature of the channel, was created (Fig. 8.14b); following the logical statements outlined below (Table 8.7):

$$EZ_C = If(CP < -0.1, 1, 0) \tag{3}$$

$$EZ_C = If(CP > -0.1 \ And \ CP < 0.05, 2, 0) \tag{4}$$

$$EZ_C = If(CP \geq 0.05, 3, 0) \tag{5}$$

where EZ_C is the energy-zone property derived from the object-curvature property, CP is the object-curvature property. Values -0.1 and 0.05 are obtained from the object-curvature property. Values 1, 2 and 3 are the code numbers assigned for the energy-zone model and represent, respectively, lower energy, middle energy and higher energy zones. Value 0 represents the background.
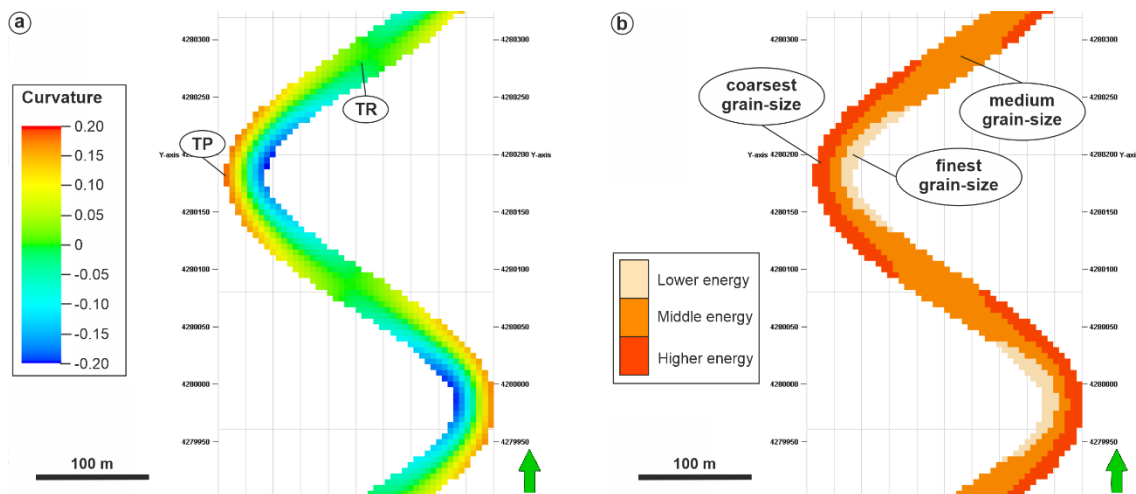
Fig. 8.14. (a) Object-curvature property derived from a channel object. Note the red colours correspond to the thalweg pool zones (TP) and green colours correspond to thalweg riffle zones (TR). **(b)** Energy-zones model calculated, using Logical Statement 3, from the object-curvature property of channel object highlighting zones of finest, medium and coarsest grain size.

Depth Trend and Energy Zones Model:

The gradual abandonment of channel fill has been reproduced by means of the depth trend property (DP). Channel abandonment, commonly observed in outcrop and subsurface data, is characterized by a fining-upward succession (stacking of Lithofacies Gm-St-Sr-Fl). Based on the relative depth of the channel object (Fig. 8.15a), 5 zones were determined: zone 1, the deepest, corresponds to the thalweg; zones 2 to 4, represent the gradual decreasing energy during channel abandonment fill; and zone 5, is the shallowest, corresponding to the last stage of channel fill in response to channel bend cut-off or avulsion. Based on this, a property that defines the energy zones of a channel object was created for the purposes of this study. This property was derived from the depth trend of the channel (Fig. 8.15b), following the logical statements outlined below (Table 8.7):

$$EZ_D = If(DP \leq 0.1, 1, 0) \tag{6}$$

$$EZ_D = If(DP > 0.1 \; And \; DP \leq 0.4, 2, 0) \tag{7}$$

$$EZ_D = If(DP > 0.4 \; And \; DP \leq 0.8, 3, 0) \tag{8}$$

$$EZ_D = If(DP > 0.8 \; And \; DP \leq 0.9, 4, 0) \tag{9}$$

$$EZ_D = If(DP > 0.9, 5, 0) \tag{10}$$

where EZ_D is the energy zone property derived from the depth trend property, DP is the depth trend property. Values 0.1, 0.4, 0.8 and 0.9 represent the relative depth obtained from DP. Values 1 to 5 are the code numbers assigned for the energy-zone model from the depth trend property and represent zone 1 to zone 5, respectively. Value 0 represents the background.

Fig. 8.15. (a) Depth trend property from a channel object. Note the red and green colours respectively represents the deepest and the shallowest parts of the channel object. **(b)** Energy-zones model calculated from the depth trend property of a channel object using Logical Statements 4 to 8.

Populating Lithofacies into CH geobody:

Combining both energy-zonation properties (energy-zones from object-curvature and energy zones from object-depth models), it is possible to reproduce the previously described lateral and vertical stacking of facies, (Fig. 8.16). This was done by means of the following logical statements which were used to populate the abandoned channel fill (Table 8.7):

$$FM = If(EZ_D = 1, 19, FM) \tag{11}$$

$$FM = If(EZ_D = 2 \; And \; EZ_C = 3, 19, FM) \tag{12}$$

$$FM = If(EZ_D = 2 \; And \; EZ_C \leq 2, 20, FM) \tag{13}$$

$$FM = If(EZ_D = 3 \; And \; EZ_C = 3, 19, FM) \tag{14}$$

$$FM = If(EZ_D = 3 \; And \; EZ_C = 2, 20, FM) \tag{15}$$

$$FM = If(EZ_D = 3 \; And \; EZ_C = 1, 16, FM) \tag{16}$$

$$FM = If(EZ_D = 4 \; And \; EZ_C = 3, 20, FM) \tag{17}$$

$$FM = If(EZ_D = 4 \; And \; EZ_C \leq 2, 16, FM) \tag{18}$$

$$FM = If(EZ_D = 5 \; And \; EZ_C \leq 2, 21, If(EZ_D = 5, 16, FM)) \tag{19}$$

where FM is the resulting lithofacies model, values 1, 2 and 3 correspond to number codes assigned to EZ_D and EZ_C; and values 16, 19, 20 and 21 correspond to Lithofacies Gm, St, Sr and Fl, as established in Table 8.5.

Fig. 8.16. Result of lithofacies modelling within a channel geobody. **(a)** 3D lithofacies model. Rectangles show the location of vertical cross-sections (b) and (c). **(b)** Cross-section through a thalweg riffle zone. **(c)** Cross-section through a thalweg pool zone.

Lithofacies modelling into PB geobodies

As previously described for the modelling workflow at geobody scale, (Section 8.4.2.1) the point bar object has been modelled as successive channel objects in order to successfully reproduce LAPs. As each channel object, corresponding to a LAP, erodes the previous object it will be eroded by the next object. As such, it is only by using the object-depth trend property that it is possible to reproduce the lateral and vertical stacking of facies (fining-upward succession; stacking of Lithofacies Gm-St-Sr) within a PB geobody.

Depth Trend and Energy Zones Model:

LAP objects have been divided into 3 zones based on relative depth (Fig. 8.17). Zone 1, the deepest, corresponds to the basal pebble lag attributed to deposition in the pool zone of a laterally migrating channel thalweg (Lithofacies Gm). Zones 2 and 3, represent, respectively, the middle and upper parts of the LAP. Thus, zone 2 has been populated with Lithofacies St and zone 3 has been populated with Lithofacies Sr.

The following logical statement was used to divide the object into the 3 zones, described above, based on the relative depth property of the object (Fig. 8.17; Table 8.7):

$$EZ_D = If(DP \leq 0.3, 1, 0) \tag{20}$$

$$EZ_D = If(DP > 0.3 \ And \ DP \leq 0.8, 2, 0) \tag{21}$$

$$EZ_D = \ If(DP > 0.8, 3, 0) \tag{22}$$

where EZ_D is the energy zone property derived from the depth trend property, DP, of the objects which represent the LAPs. Values 0.3 and 0.8 represent the relative depth obtained from the DP. Values 1 to 3 are the code numbers assigned for the energy-zone model derived from the depth trend property and represent zone 1 to zone 3, respectively. Value 0 represents the background.
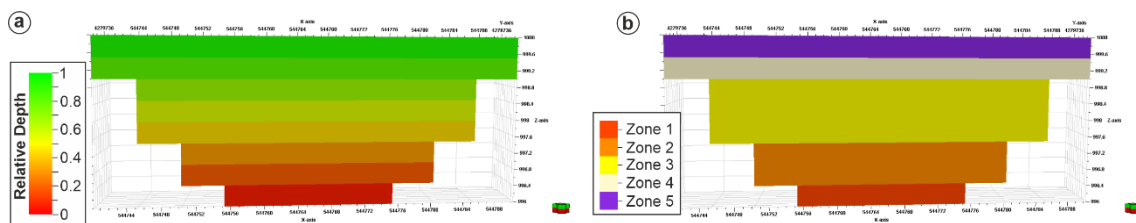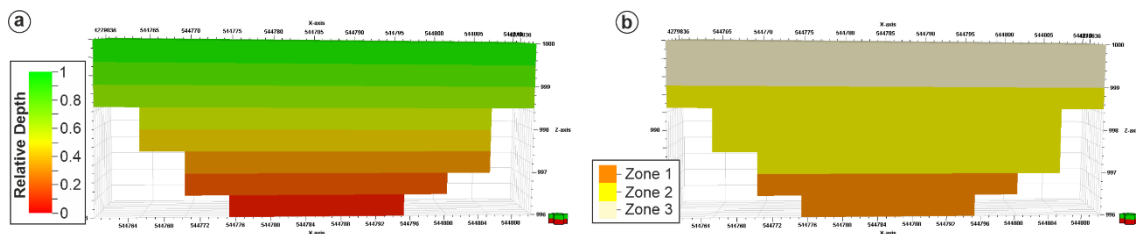

Fig. 8.17. (a) Depth trend property from a channel object. Note the red and green colours respectively represent the deepest and shallowest parts of channel object. **(b)** Energy-zones model calculated from the depth trend property of the channel object.

Populating Lithofacies into PB geobodies:

The population of Lithofacies was calculated with the following logical statements (Fig. 18; Table 8.7):

$$FM = If(EZ_D = 1, 19, FM) \tag{23}$$

$$FM = If(EZ_D = 2, 20, FM) \tag{24}$$

$$FM = If(EZ_D = 3, 16, FM) \tag{25}$$

where FM is the resulting lithofacies model; values 1, 2 and 3 correspond to the number code assigned to EZ_D; and values 16, 19 and 20 correspond to Lithofacies Gm, St and Sr, as established in Table 8.5.
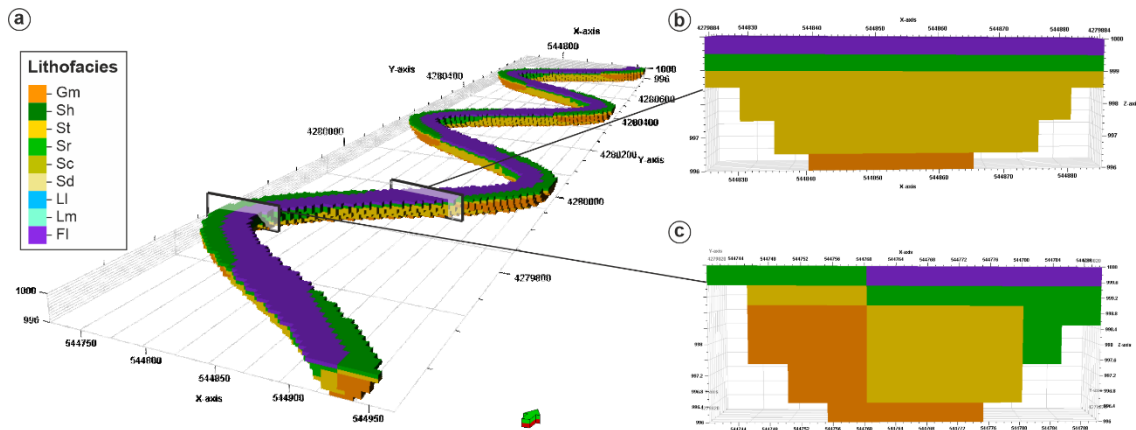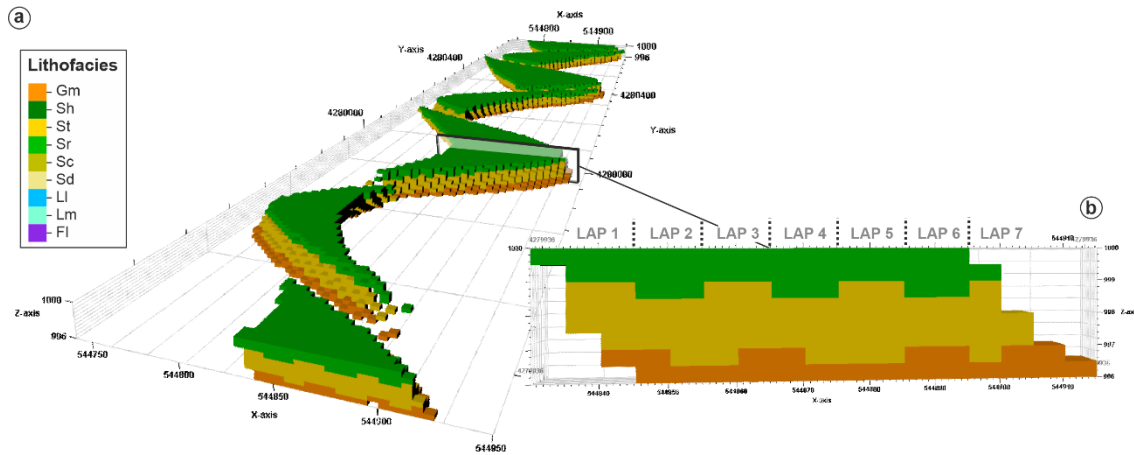
Fig. 8.18. Results of lithofacies modelling within a point bar geobody. **(a)** 3D lithofacies model. Rectangles show the location of the cross-sections of figure (b). **(b)** cross-section through a PB object showing successive stacking of each lateral accretion packages (LAP).

Lithofacies modelling into CS geobodies

To model the lithofacies distribution into the CS geobodies, 3 object properties were combined: (1) the object-curvature property of the CS object, (2) object distance property derived from distance to the channel object, and (3) the depth trend property (Fig. 8.19; Table 8.6).

Curvature and the Energy Zones Model:

Crevasse-splays are characterized by high-energy facies towards the central or axial zones where upper flow regime horizontal-laminated sandstones (Lithofacies Sh) are deposited. These evolve laterally into ripple-laminated sandstones (Lithofacies Sr) towards the margins of the geobody; On the basis of this concept and using the object-curvature property the object was divided into 3 zones: zone 1, corresponding to the central part of the object, and defined as a high energy zone; zones 2 and 3, toward the axis of the object, defined respectively as medium and low energy zones, (Fig. 8.19c-d). The following logical statements were used to determinate this zonal differentiation (Table 8.7):

$$EZ_C = If(CP \geq 2.9 \; And \; B_C > 0, 1, 0) \tag{26}$$

$$EZ_C = If(CP < 2.9 \; And \; CP \geq 0.3 \; And \; B_C > 0, 2, 0) \tag{27}$$

$$EZ_C = If(CP \leq 0.3 \; And \; B_C > 0, 3, 0) \tag{28}$$

where EZ_C is the energy-zones property derived from the object-curvature property, CP is the object-curvature property, and B_C is the crevasse-splay bodies property. Values 2.9 and 0.3 are obtained from the object-curvature property of the crevasse-splay geobodies. Values 1, 2 and 3

are the code numbers assigned for the energy-zone model and represent higher energy, medium energy and lower energy zones, respectively. Value 0 represents the background.

Distance from CH geobody and the Energy Zones Model:

In crevasse-splays, the flow energy decreases from the apex towards the margin of the lobe. Therefore, crevasse-splay lobes show a lateral gradation in lithofacies from Sh-Sr-Sc, in the proximal part of the crevasse-lobe, to Lithofacies Sd-Sr, in the medial part of the crevasse-lobe. Toward the margins, crevasse-splay lobes comprise siltstone deposits (Ll and Lm Lithofacies) corresponding to settling from suspension. Thus, from the object distance from CH property, 3 zones (proximal, medial and distal) were differentiated (Fig. 8.19e-f). The following logical statements were used to determine this zonal differentiation (Table 8.7):

$$EZ_{DT} = If(DTP \leq 130 \; And \; B_C > 0, 1, 0) \tag{29}$$

$$EZ_{DT} = If(DTP > 130 \; And \; DTP \leq 200 \; And \; B_C > 0, 2, 0) \tag{30}$$

$$EZ_{DT} = If(DTP > 200 \; And \; B_C > 0, 3, 0) \tag{31}$$

where EZ_{DT} is the energy-zones property derived from the object distance property of the channel object, DTP is the object-distance property of the channel object and B_C is the crevasse-splay bodies property. Values 130 and 200 (metres) are obtained from the conceptual model of lateral variability for geobodies and facies (Fig. 8.6). Values 1, 2 and 3 are the code numbers assigned for the energy-zone model and represent higher energy, medium energy and lower energy zones, respectively. Value 0 represents the background.

Depth Trend and Energy Zones Model:

In order to represent the vertical stacking of lithofacies in CS geobodies, a zonation conditioned by the depth trend property has also been differentiated (Fig. 8.19g-h). Thus, the object has been divided into 3 zones based on its relative depth. The following logical statements were used to determinate this zonation (Table 8.7):

$$EZ_D = If(DP \leq 0.33, 1, 0) \tag{32}$$

$$EZ_D = If(DP > 0.33 \; And \; DP \leq 0.66, 2, 0) \tag{33}$$

$$EZ_D = If(DP > 0.66, 3, 0) \tag{34}$$

where, EZ_D is the energy zone property derived from the depth trend property, DP is the depth trend property. Values 0.33 and 0.66 represent the relative depth obtained from DP. Values 1 to 3 are the code numbers assigned for the energy-zone model as derived from the depth trend property. Value 0 represents the background.
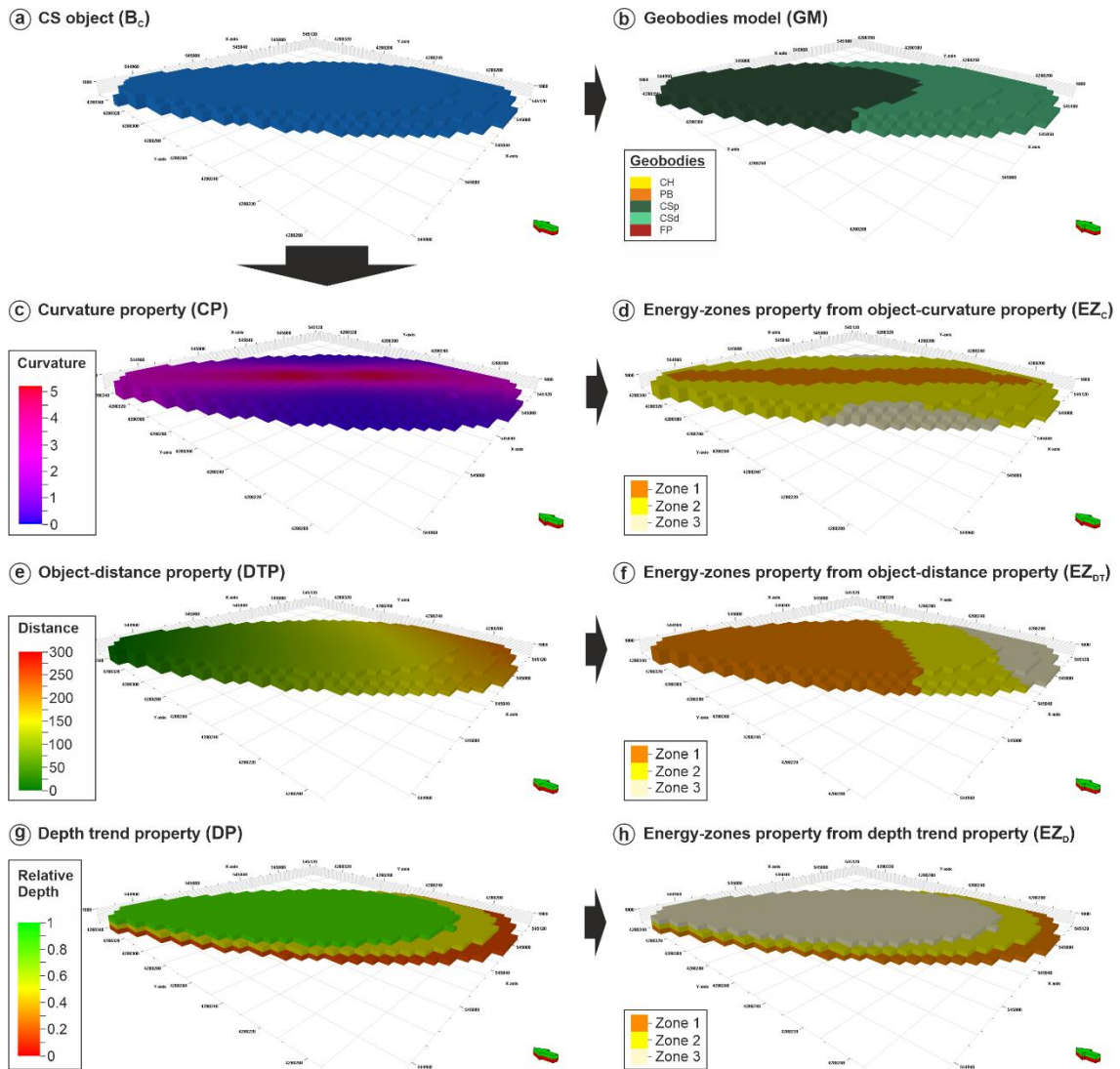
Fig. 8.19. Geometrical properties of crevasse-splay objects (CS) and energy-zones properties. **(a)** CS body model. **(b)** Geobody model of a CS geobody. Note the differentiation between proximal crevasse-splay geobody (CSp) and distal crevasse-splay geobody (CSd); **(c)** Object-curvature property of the CS object; **(d)** Energy-zones property calculated from the object-curvature property; **(e)** Distance from CH object property. **(f)** Energy-zones property from object-distance property; **(g)** Depth trend property of the CS object and **(h)** Energy-zones property calculated from the depth trend property.

Populating Lithofacies into CS geobodies:

Combining the 3 energy-zone models (EZ_C, EZ_{DT} and EZ_D), shown above, the observed lateral and vertical stacking of lithofacies has been reproduced using the following logical statements (Fig. 8.20; Table 8.7):

$$FM = If\,(GM = 3\ And\ EZ_D \geq 2\ And\ EZ_C = 1, 20, FM) \tag{35}$$

$$FM = If\,(GM = 3\ And\ EZ_D = 3\ And\ EZ_C \geq 2, 17, FM) \tag{36}$$

$$FM = If(GM = 3 \ And \ EZ_D = 2 \ And \ EZ_C \geq 2, 16, FM) \tag{37}$$

$$FM = If(GM = 3 \ And \ EZ_D = 1 \ And \ EZ_{DT} = 1, 15, FM) \tag{38}$$

$$FM = If(GM = 4 \ And \ EZ_D = 1 \ And \ EZ_{DT} \leq 2, 18, FM) \tag{39}$$

$$FM = If(GM = 4 \ And \ EZ_D \geq 2 \ And \ EZ_{DT} \leq 2, 16, FM) \tag{40}$$

$$FM = If(GM = 4 \ And \ EZ_D = 1 \ And \ EZ_{DT} \geq 2, 13, FM) \tag{41}$$

$$FM = If(GM = 4 \ And \ EZ_D \geq 2 \ And \ EZ_{DT} = 3, 14, FM) \tag{42}$$

where FM is the resulting lithofacies model; GM is the geobodies model, previously created; values 1, 2 and 3 correspond to the number codes assigned to EZ_C, EZ_{DT}, and EZ_D; and values 13 - 20 correspond to the number codes established for lithofacies and summarised in Table 8.5.
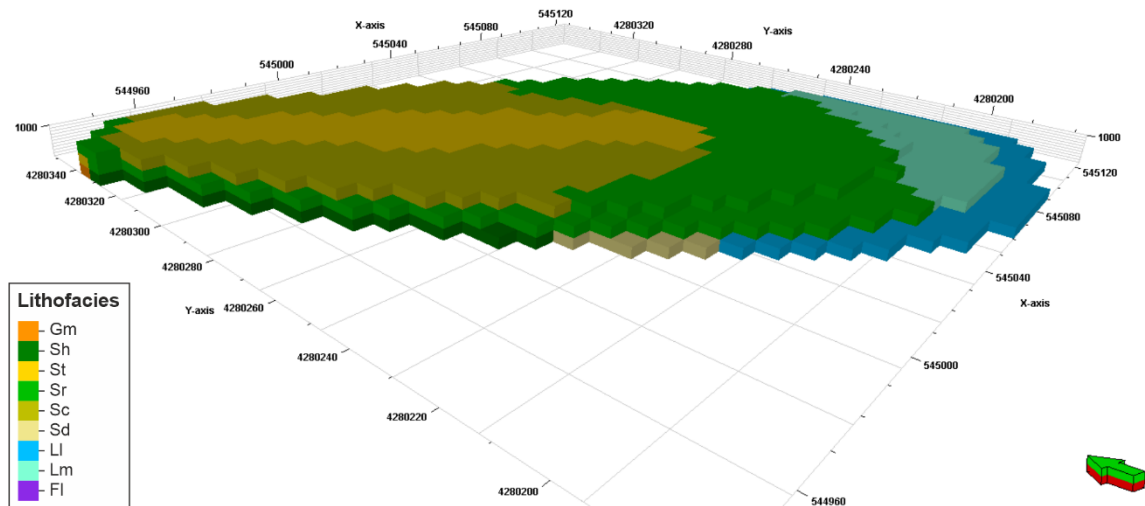
Fig. 8.20. Result of lithofacies modelling into a crevasse-splay geobody. See Figure 7.2 in Chapter 7 and Figure 8.5 for a comparison of the lithofacies model presented in this figure with the conceptual models obtained from outcrop and subsurface data.

Table 8.7. Description of the logical statements designed in this study for geobodies and lithofacies modelling workflows.

	Logical statement	Description	Resulting property or model	Applied to
(1)	$GM = If(GM > 5 \; And \; GM \leq 12, 2, GM)$	Assigns LAP objects to a single PB geobody in the geobodies model.	Geobodies model	Modelling of PB geobodies
(2)	$IZ = If(CP > 0.14, 1, 0)$	Creates the insertion-zone property assigning the value 1 when channel curvature is >0.14, which represents the zone of highest curvature of the channel object; and the value 0 when channel curvature is <0.14.	Insertion-zone property	Modelling of CS geobodies
(3)	$EZ_C = If(CP < -0.1, 1, 0)$	Assigns the inner bank, corresponds to the lower-energy zone, when the channel-object curvature is <-0.01.	Energy-zones property derived from the object-curvature property for channel object	
(4)	$EZ_C = If(CP > -0.1 \; And \; CP < 0.05, 2, 0)$	Assigns the transition from the outer and inner bank (middle-energy zone) when the channel object curvature is between -0.1 and 0.05.		
(5)	$EZ_C = If(CP \geq 0.05, 3, 0)$	Assigns the thalweg pool zone, corresponds to the high-energy zone, when the channel-object curvature is ≥0.05.		
(6)	$EZ_D = If(DP \leq 0.1, 1, 0)$	Assigns thalweg zone (energy zone 1) when relative depth of channel object is ≤0.1.		Lithofacies modelling into a CH geobody
(7)	$EZ_D = If(DP > 0.1 \; And \; DP \leq 0.4, 2, 0)$	Assigns energy zone 2 when relative depth of channel object is between 0.1 and 0.4.		
(8)	$EZ_D = If(DP > 0.4 \; And \; DP \leq 0.8, 3, 0)$	Assigns energy zone 3 when relative depth of channel object is between 0.4 and 0.8.	Energy-zones property derived from the depth trend property for a channel object	
(9)	$EZ_D = If(DP > 0.8 \; And \; DP \leq 0.9, 4, 0)$	Assigns energy zone 4 when relative depth of channel object is between 0.8 and 0.9.		
(10)	$EZ_D = If(DP > 0.9, 5, 0)$	Assigns the shallowest zone (energy zone 5), when the relative depth of the channel object is >0.9, corresponding to the last stage of channel fill.		

Table 8.7. (continued).

	Logical statement	Description	Resulting property or model	Applied to
(11)	$FM = If(EZ_D = 1, 19, FM)$	Populates Lithofacies Gm to reproduce the basal lag, deposited during the active phase through thalweg of the channel.		
(12)	$FM = If(EZ_D = 2\ And\ EZ_C = 3, 19, FM)$	Populates Lithofacies Gm through the thalweg pool zone, along the outer bank, deposited during the active phase of the channel.		
(13)	$FM = If(EZ_D = 2\ And\ EZ_C \leq 2, 20, FM)$	Populates Lithofacies St across the thalweg riffle zone, during the active phase of the channel.		
(14)	$FM = If(EZ_D = 3\ And\ EZ_C = 3, 19, FM)$	Populates Lithofacies Gm into the thalweg pool zone, deposited during the gradual abandonment of the channel.		
(15)	$FM = If(EZ_D = 3\ And\ EZ_C = 2, 20, FM)$	Populates Lithofacies St across the thalweg riffle zone, deposited during the gradual abandonment of the channel.	Lithofacies model of a channel object	Lithofacies modelling into a CH geobody
(16)	$FM = If(EZ_D = 3\ And\ EZ_C = 1, 16, FM)$	Populates Lithofacies Sr into the inner bank, deposited during the gradual abandonment of the channel.		
(17)	$FM = If(EZ_D = 4\ And\ EZ_C = 3, 20, FM)$	Populates Lithofacies St into the thalweg pool zone, deposited during the gradual abandonment of the channel.		
(18)	$FM = If(EZ_D = 4\ And\ EZ_C \leq 2, 16, FM)$	Populates Lithofacies Sr across the thalweg riffle zone and into the inner bank, during the gradual abandonment of the channel.		
(19)	$FM = If(EZ_D = 5\ And\ EZ_C \leq 2, 21, If(EZ_D = 5, 16, FM))$	Populates Lithofacies Sr into the thalweg pool zone and Lithofacies Fl across the thalweg riffle zone and into the inner bank, during the last stage of channel abandonment in response to channel bend cut-off or avulsion.		

Table 8.7. (continued).

	Logical statement	Description	Resulting property or model	Applied to
(20)	$EZ_D = If\,(DP \leq 0.3, 1, 0)$	Assigns the lower part of the lateral accretion package (LAP) when the relative depth of LAP object is ≤0.3.		
(21)	$EZ_D = If\,(DP > 0.3\ And\ DP \leq 0.8, 2, 0)$	Assigns the middle part of the lateral accretion package (LAP) when the relative depth of LAP object is between 0.3 and 0.8.	Energy-zones property derived from the depth trend property for point bar objects	
(22)	$EZ_D = If\,(DP > 0.8, 3, 0)$	Assigns the upper part of the lateral accretion package (LAP) when the relative depth of LAP object is >0.8.		
(23)	$FM = If\,(EZ_D = 1, 19, FM)$	Populates Lithofacies Gm into the lower part of the LAP, which corresponds to the basal pebble lag attributed to deposition in the pool zone of a laterally migrating channel thalweg.		Lithofacies modelling into PB geobodies
(24)	$FM = If\,(EZ_D = 2, 20, FM)$	Populates Lithofacies St into the middle part of the LAP to reproduce the fining-upward succession of a LAP.	Lithofacies model for point bar objects	
(25)	$FM = If\,(EZ_D = 3, 16, FM)$	Populates Lithofacies Sr into the upper part of the LAP to reproduce the fining-upward succession of a LAP.		

Table 8.7. (continued).

	Logical statement	Description	Resulting property or model	Applied to
(26)	$EZ_C = If(CP \geq 2.9\ And\ B_C > 0, 1, 0)$	Assigns the central part of the crevasse object, which corresponds to a high-energy zone, when the crevasse-object curvature is ≥2.9.	Energy-zones property derived from the object-curvature property for crevasse-splay objects	
(27)	$EZ_C = If(CP < 2.9\ And\ CP \geq 0.3\ And\ B_C > 0, 2, 0)$	Assigns the medium-energy zone of the crevasse geobodies, when the crevasse-object curvature ranges from 2.9 to 0.3.		
(28)	$EZ_C = If(CP \leq 0.3\ And\ B_C > 0, 3, 0)$	Assigns lower-energy zone of the crevasse geobodies, when the crevasse-object curvature is ≤0.3.		
(29)	$EZ_{DT} = If(DTP \leq 130\ And\ B_C > 0, 1, 0)$	Assigns the proximal part of the crevasse object as a function of the distance to the channel object, which is defined when the distance to the channel object is ≤130 m.		Lithofacies modelling into CS geobodies
(30)	$EZ_{DT} = If(DTP > 130\ And\ DTP \leq 200\ And\ B_C > 0, 2, 0)$	Assigns the medial part of the crevasse object in function of the distance to the channel object, which is defined when the distance to the channel object is between 130 m and 200 m.	Energy-zones property derived from the channel object-distance property for crevasse-splay objects	
(31)	$EZ_{DT} = If(DTP > 200\ And\ B_C > 0, 3, 0)$	Assigns the distal part of the crevasse object as a function of the distance to the channel object, which is defined when the distance to the channel object is >200 m.		
(32)	$EZ_D = If(DP \leq 0.33, 1, 0)$	Assigns the deepest part of the crevasse object, when the relative depth of the crevasse object ≤0.33.	Energy-zones property derived from the depth trend property for crevasse-splay objects	
(33)	$EZ_D = If(DP > 0.33\ And\ DP \leq 0.66, 2, 0)$	Assigns the medium part of the crevasse object, when relative depth of crevasse object is between 0.33 and 0.66.		
(34)	$EZ_D = If(DP > 0.66, 3, 0)$	Assigns the upper part of the crevasse object, when the relative depth of the crevasse object >0.66.		

Table 8.7. (continued).

	Logical statement	Description	Resulting property or model	Applied to
(35)	$FM = If(GM = 3\ And\ EZ_D \geq 2\ And\ EZ_C = 1, 20, FM)$	Populates Lithofacies St into the upper-deep part and into the central part of the proximal crevasse-splay geobodies, corresponding to the deposits of crevasse channels.		
(36)	$FM = If(GM = 3\ And\ EZ_D = 3\ And\ EZ_C \geq 2, 17, FM)$	Populates Lithofacies Sc into the upper-deep part and into the medium-and lower-energy zone of the proximal crevasse-splay geobodies.		
(37)	$FM = If(GM = 3\ And\ EZ_D = 2\ And\ EZ_C \geq 2, 16, FM)$	Populates Lithofacies Sr into the medium-deep part and into the medium- and lower-energy zone of the proximal crevasse-splay geobodies.		
(38)	$FM = If(GM = 3\ And\ EZ_{DT} = 1, 15, FM)$	Populates Lithofacies Sh into the deepest part of the proximal crevasse-splay geobodies.	Lithofacies model of crevasse-splay objects	Lithofacies modelling into CS geobodies
(39)	$FM = If(GM = 4\ And\ EZ_D = 1\ And\ EZ_{DT} \leq 2, 18, FM)$	Populates Lithofacies Sd into the deepest part of the medial crevasse-splay objects.		
(40)	$FM = If(GM = 4\ And\ EZ_D \geq 2\ And\ EZ_{DT} \leq 2, 16, FM)$	Populates Lithofacies Sr into the medium- and upper-part of the medial crevasse-splay objects.		
(41)	$FM = If(GM = 4\ And\ EZ_D = 1\ And\ EZ_{DT} \geq 2, 13, FM)$	Populates Lithofacies Ll into the deepest part of the medial and distal crevasse-splay objects.		
(42)	$FM = If(GM = 4\ And\ EZ_D \geq 2\ And\ EZ_{DT} = 3, 14, FM)$	Populates Lithofacies Lm into the medium- and upper-part of the distal crevasse-splay objects.		

8.4.3. Building a 3D Training Image

The 3D Training Image (TI), used in this study was produced in a simple three-dimensional grid using horizontal surfaces as base and top. The dimensions of this simple grid are 1395 m x 1195 m x 5 m. It also comprises a single zone and 10 proportional layers. The 3D cell dimensions for this simple grid are 5 m x 5 m x 0.5 m. Thus, the TI has a similar cell size to the 3D model framework.

The first modelling workflow, at geobodies scale, was used to populate the simple grid and create the 3D Training Image (Fig. 8.21a). This 3D training image will be the basis for the MPS simulations presented in the next section.

Significantly, comparison of a similar vertical section from the TI with the DOM, in order to perform a qualitative analysis of the resulting TI, reproduced the distribution, geometry, dimension and proportions of the interpreted sedimentary architecture. PB geobodies, for example, were always located on the, accretional margin adjacent to the CH geobody. In addition, the TI also captured the asymmetrical-sigmoidal shape of the PB geobodies. CS geobodies were, in contrast, always modelled on the erosive margin of the CH geobody and the lobate shape of these geobodies was successfully reproduced. Furthermore, the overlapping lobe geobodies, giving rise to crevasse-splay complexes were also reproduced by the TI as well as the differentiation between Proximal and Distal CS geobodies (Fig. 8.21).

In a plan view, the 3D TI also reproduced the distribution, geometry, dimensions and proportions of the conceptual model for the interpreted geobodies (Fig. 8.22). The CH object replicated the interpreted ribbon-like plan view geometry, as well as, the crescent-shaped planform of PB geobodies and fan-shaped planform of CS geobodies.
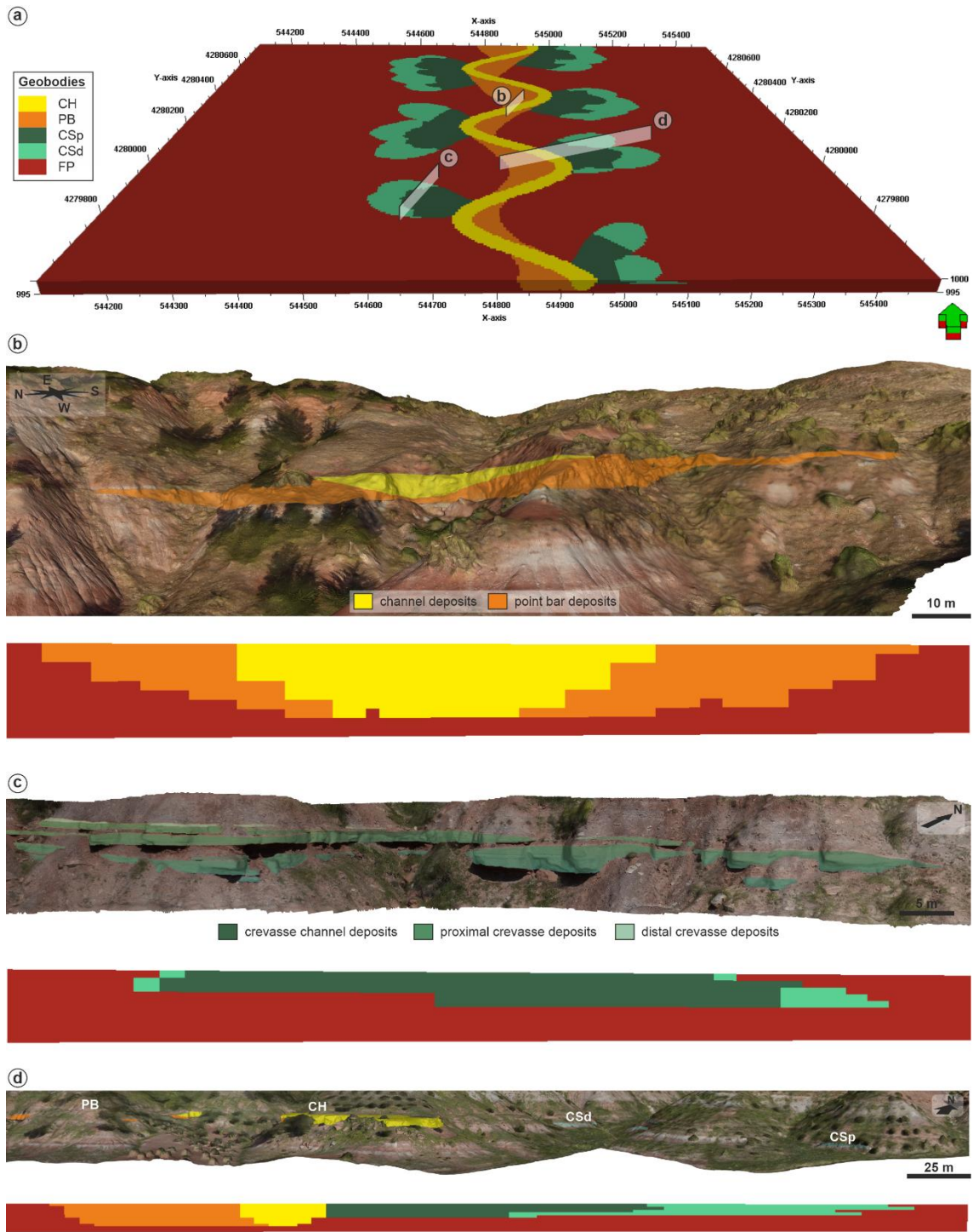
Fig. 8.21. (a) 3D training image used in this study, created from the modelling workflow at geobody scale; **(b) – (d)** Comparison of interpreted digital outcrop models with similar vertical sections in the 3D TI. See (a) for location of vertical sections in the TI.
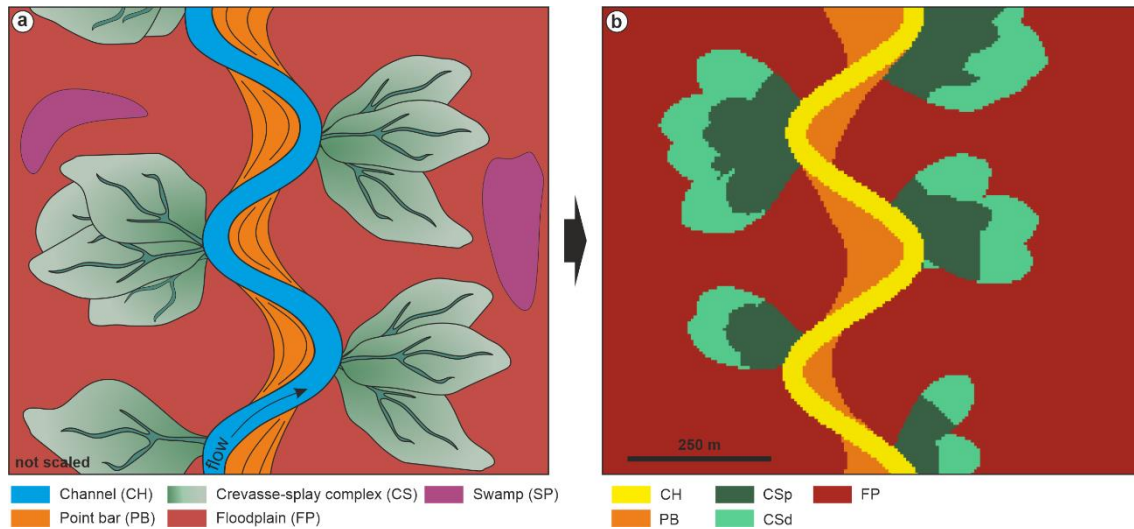
Fig. 8.22. Comparison of the 2D conceptual model interpreted for the M-S Unit **(a)** with a plan view extracted from the TI created in this study **(b)**.

8.4.4. Prediction of reservoir geobodies and uncertainty analysis from MPS-Based modelling

In order to establish how the TI can help in the prediction of the reservoir geobodies, as well as adapting this prediction to the outcrop, MPS models were created. MPS-based modelling was carried-out only for Zone 5 of the 3D reservoir model as this corresponds to the selected interval (see Section 8.3 for details of why this interval was selected). In addition, Zone 5 contains more available input data and also the geocellular outcrop model, which will be used to compare the MPS-based modelling results with the outcrop.

In addition, to establishing the influence of the input data on the predictions of the reservoir geobodies, five scenarios were generated based on the number of input data sources (wells and/or sedimentological logs). In each scenario, new input data was successively added, reducing the spacing between the hard data points.

Thus, in Scenario 1, the CP0 well, comprising a CH geobody, was used as the input data. Wells CP0 and MB4 were used in Scenario 2. Both wells also penetrated a CH geobody. In Scenario 3, the CPML7 and CPMR7 wells, comprising CSp and FP geobodies, were added in addition to Wells CP0 and MB4. In Scenario 4, the MB3 and CPML 4 wells, characterized by PB geobodies, were added as compared to Scenario 3. Finally, Scenario 5 used Wells CP0, CPMR5, CPMR7, CPMR8, CPML4, CPML7, CPML9, MB3, MB4, and CBML2. CPMR5 and CPML9 drilled CSd and FP geobodies, whereas Wells CPMR8 and CBML2 are composed only of FP geobodies. For each scenario, 250 realizations were generated.

The paleogeographic reconstruction developed for Zone 5 (Fig. 8.23) shows that the orientation of the geobodies is not stationary. In other words, the orientation of the geobodies changes throughout the selected interval. In marked contrast, the TI generated for this study was built with a N-S orientation. To solve this contradiction, an additional property was generated. This property shows the variation of azimuth trend throughout Zone 5. This azimuth trend property was used as an additional soft data input data parameter, or mask, in order to obtain results which better match the conceptual model in the Zone 5 (Fig. 8.23).
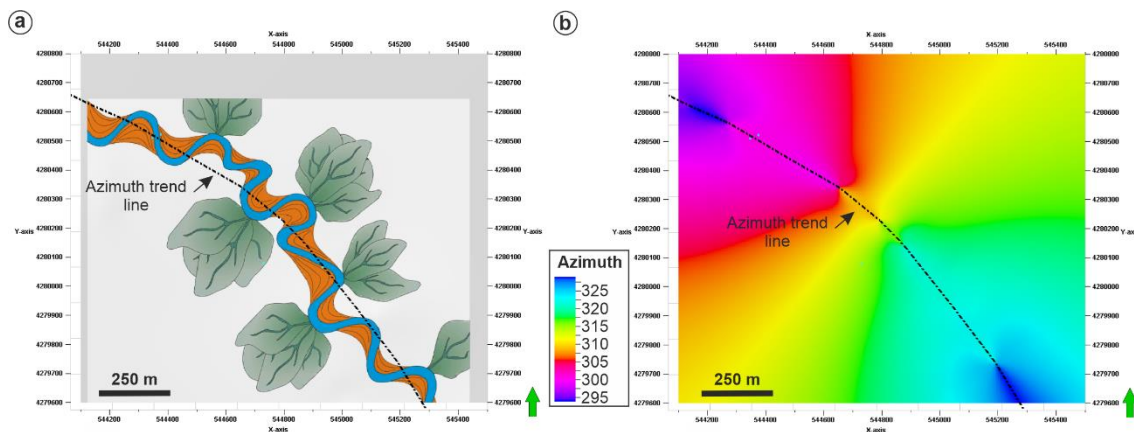
Fig. 8.23. (a) Paleogeographic reconstruction interpreted for Zone 5 showing the azimuth trend line of the channel-belt interpreted in Zone 5. **(b)** Azimuth trend property created from the azimuth trend line used as a mask in the MPS-based modelling process.

Prediction of reservoir geobodies

As interpreted, from the outcrop data, PB and CS geobodies are both linked to the CH geobody and thus provide information facilitating prediction of the location of the CH geobody. As such it would clearly be sufficient to obtain a reliable prediction for the CH geobody in order to establish the distribution of PB and CS geobodies. In addition, in order to establish the influence of input data containing PB and CS geobodies on the prediction of the CH geobody, only the calculation of CH probability, as outlined below, can help generate a better prediction. For this reason, the results shown in this section are focused on the prediction of the CH geobody.

After 250 MPS simulations for each scenario, a 3D probability volume for the CH geobody was built. This probability is defined, for a given cell, as the sum of the CH geobody population divided by the total number of realizations. In other words, a cell with a probability

value of 50 means that from 250 realizations, the CH geobody populated the same cell in 50 realizations.

A qualitative analysis of the probability results for CH geobody, for each scenario, is presented below:

Scenario 1:

Probability results in Scenario 1 showed the highest values (>10 probability values) around the channel-belt thalweg predicted in the paleogeographic reconstruction. Probability values higher than 50 were estimated near the wells and towards the southeast. However, MPS simulations overestimated probability values for the CH geobody in both the north-northeast and the south-west of the model (Fig. 8.24).

Scenario 2:

In scenario 2, results from the MPS simulations also show the highest probability values (>10 probability values) around the predicted channel-belt thalweg. Probability values higher than 50 were estimated only near the wells, in this case. MPS simulations also overestimated probability values for the CH geobody in the north-northeast and in the south-west of the model (Fig. 8.24).

Scenario 3:

In contrast to Scenarios 1 and 2, probability results in this scenario do not show the highest values (>10 probability values) around the complete predicted channel-belt thalweg. In addition, MPS simulations overestimated probability values for the CH geobody over a more extended area towards the northeast when compared with the previous scenarios. However, probability values >50 were obtained only near Wells CP0 and MB4. Wells CPML7 and CPMR7 are, in contrast, characterized by CS geobodies. Consequently, the addition of these wells helps to better constrain the highest probability values for the CH geobody location in outcrop (Wells CP0 and MB4), although, in contrast, the addition of Well CPMR7 does seem to have produced an increase of overestimated probability values for the CH geobody toward the northeast of the model grid, when compared with the previous scenarios (Fig. 8.24).

Scenario 4:

This scenario generated a similar distribution of highest probability values compared to Scenario 3. MPS simulations decreased the overestimated probability values for the CH geobody towards the east compared to Scenario 3. Probability values higher than 50 were also obtained near

Wells CP0 and MB4, although the area for these probability values increased compared to Scenario 3 (Fig. 8.24).

Scenario 5:

MPS simulations of Scenario 5 decreased the overestimated model area for CH geobody probability values towards the east, compared to Scenarios 3 and 4. Probability values higher than 50 were also obtained near Wells CP0 and MB4, and with a similar area, when compared to Scenario 4 (Fig. 8.24).

In summary, all scenarios showed an overestimation of CH geobody prediction, both in the northeast and southwest of the model. However, it is also worthy of note that the highest probability values are associated with the area suggested by the paleogeographic reconstruction. On the other hand, an increase in input data, even though these additional wells do not contain a CH geobody, clearly serves to constrain the highest probability values for the location of the CH geobody, although this appears to have been at the expense of generating an increase of overestimated probability values in other zones of the model. These overestimated probability values are produced because input data are not available in this part of the model and, thus, the algorithm has a high degree of freedom resulting in the repetition of the mathematical pattern.
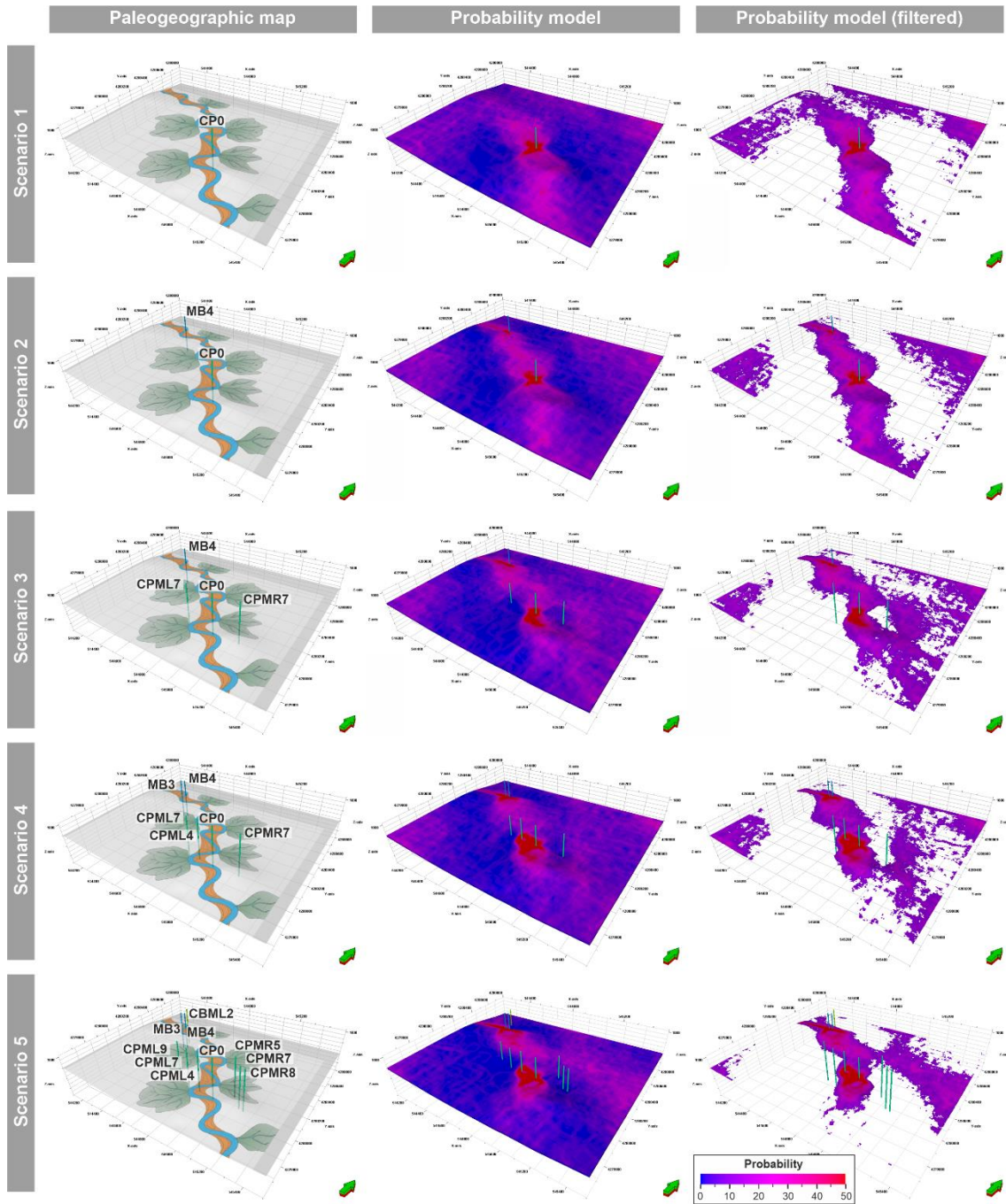
Fig. 8.24. Probability results for CH geobody prediction in each scenario. The left-hand column shows the paleogeographic reconstruction for Zone 5 (Fig. 8.7). The middle column shows the 3D probability volume for the CH geobody. Right hand column shows the 3D probability volume for the CH geobody with probability values of <10 filtered.

Uncertainty analysis

To establish the accuracy of the modelling results compared with outcrop data, each realization was compared with the geocellular outcrop model. To do this, the total number of cells in each realization which have the same value of CH, PB and CS geobodies, in comparison with the geocellular outcrop model cells, was calculated. For this study this value has been termed as "Match". The "Match" values are represented as a percentage:

$$Match\ (\%) = \frac{N_R}{N_T} \cdot 100 \tag{27}$$

where N_R is the number of cells in each realization with the same values of CH, PB and CS geobodies in the geocellular outcrop model and N_T is the total number of cells in the outcrop geocellular model (306 upscaled cells).

Match results show that, in Scenario 1, with data input only from Well CP0, match values range from 3% to 41%, with a mean value of 15% (Fig. 8.25a and Table 8.8). Adding one new source of input data, Well MB4, increased mean match values by 11%, according to results obtained in Scenario 2. This showed match values ranging from 5% to 46%, with a mean value of 26% (Fig. 8.25b and Table 8.8). Both scenarios are characterized by the presence of the CH geobody.

In Scenario 3, two new wells, CPML7 and CPMR7, were added. These wells are characterized by CSp, CSd and FP geobodies. Scenario 3 showed match values ranging from 12% to 51%, with a mean value of 29% (Fig. 8.25c and Table 8.8). However, despite adding two new data points, this scenario only increased mean match values by 3% compared to Scenario 2.

Scenario 4 showed match values ranging from 24% to 56%, with a mean value of 40% (Fig. 8.25d and Table 8.8). In this scenario Wells MB3 and CPML4 were added to the model, both of which are characterized by PB geobodies. Scenario 4, in contrast to Scenario 3 showed a notably more significant increase in the mean match values of 11%.

Finally, adding four new wells in Scenario 5, characterized by both CSd and FP geobodies, resulted in the mean match value increasing by 4% compared to Scenario 4. Match values range from 31% to 62%, with a mean value of 44% (Fig. 8.25e and Table 8.8).
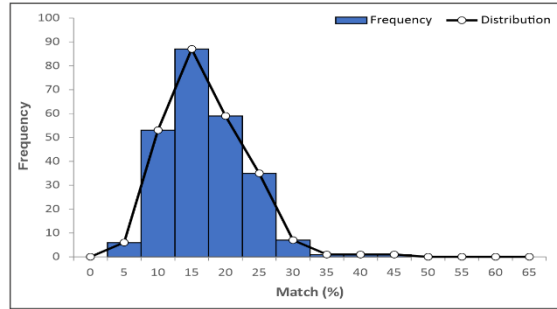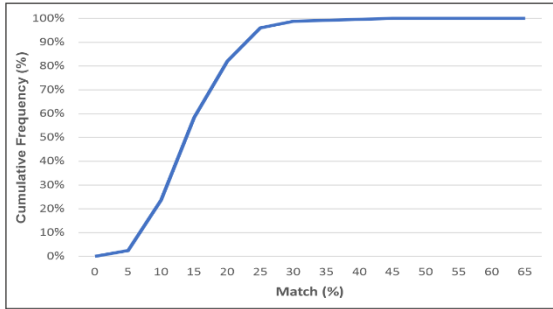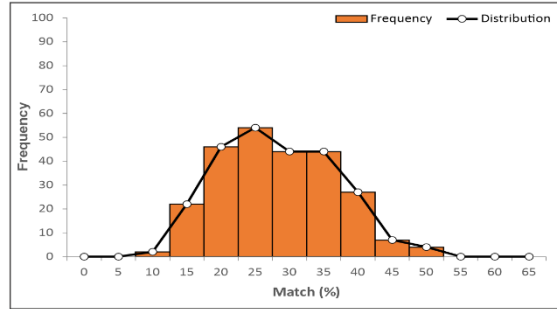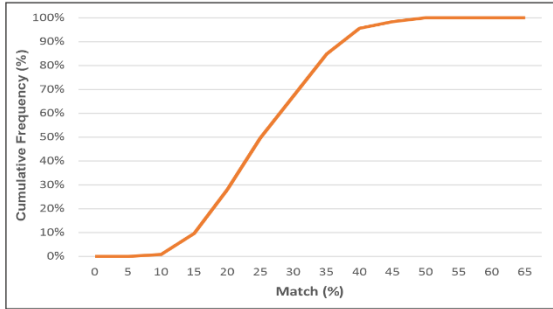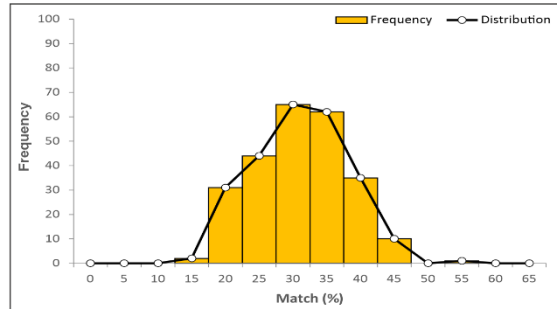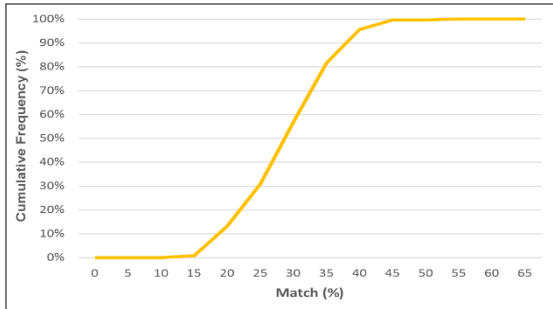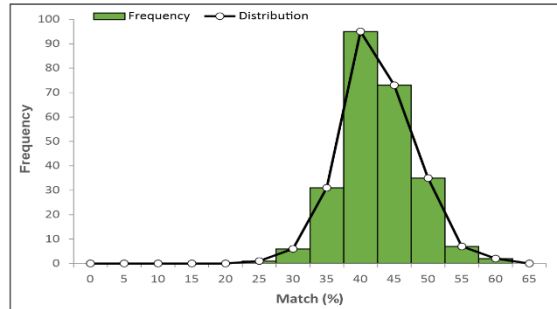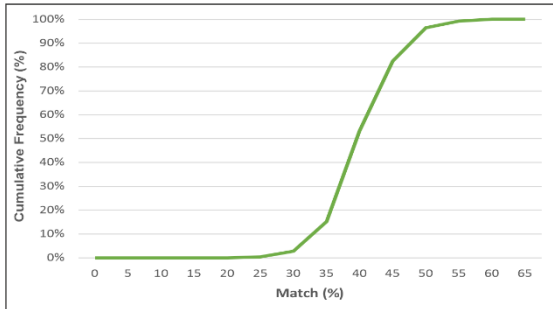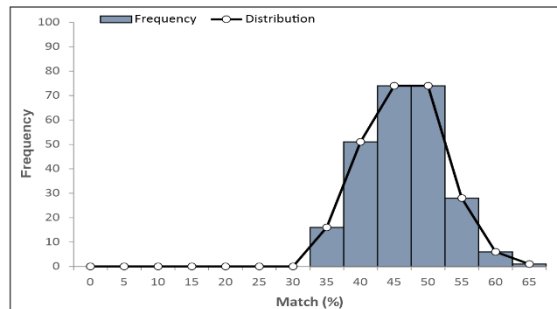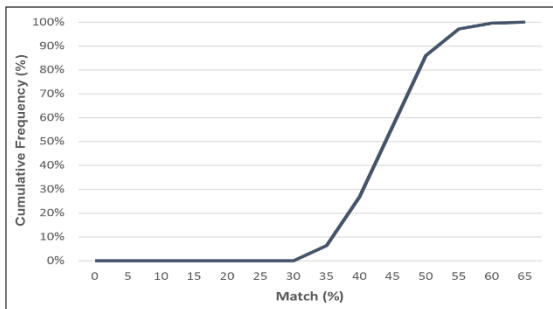
Fig. 8.25. Cumulative frequency, histogram and distribution of match values for each scenario.

Table 8.8. Number of input wells, input upscaled cells and match values for each scenario. Upscaled cells from Input wells column represents the total number of upscaled cells used as input data for each scenario. Minimum (Min), maximum (Max) and mean match values are shown. The standard deviation (Std), P10 and P90 match values also are presented, based on 250 realizations.

Scenario	Input wells	upscaled cells from wells	Match (%)					
			Min	Max	Mean	Std	P10	P90
1	1	10	3	41	15	6.0	8	23
2	2	20	5	46	26	8.4	15	38
3	4	40	12	51	29	6.9	19	37
4	6	60	24	56	40	5.5	33	47
5	10	90	31	62	44	5.7	37	52

The results of the match process for the five scenarios, described above, show a linear relationship between the number of upscaled cells (input data), used to create the simulation, and the match (Fig. 8.26). However, the highest increases in match values were observed in Scenarios 2 and 4, where the match increased by 11% in both cases, compared to Scenarios 1 and 3, respectively. Scenario 2 added as new input data, one well (MB4) characterized by a CH geobody, whilst Scenario 4 added two wells characterized by PB geobodies. Scenarios 3 and 5 also increased match values but these match increases were only of 3%, in Scenario 3, and 4%, in Scenario 5, compared to Scenarios 2 and 4, respectively. Both scenarios 3 and 5, added, as new input data, wells characterized by CS and FP geobodies.
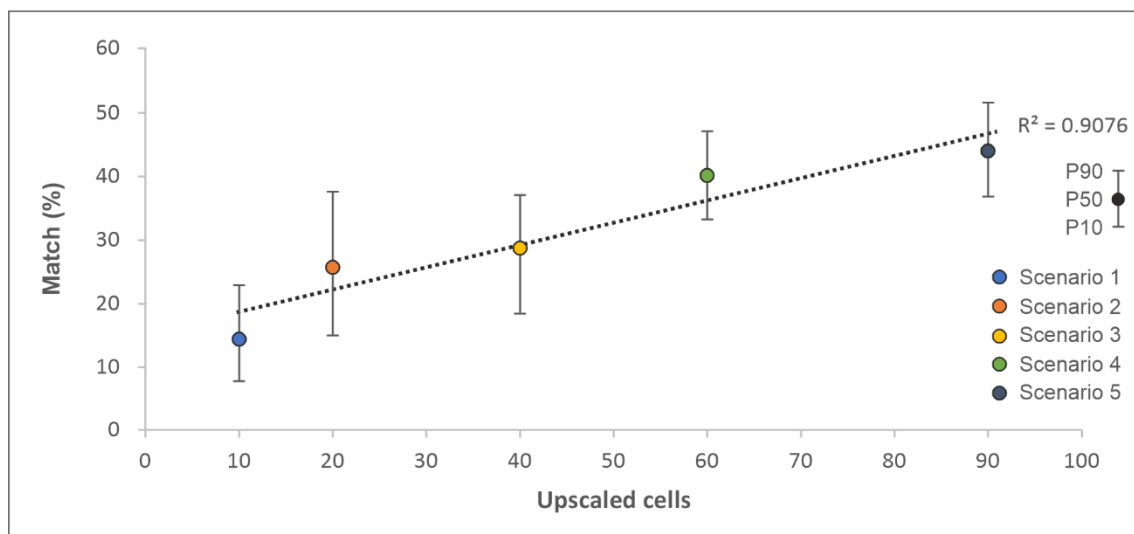
Fig. 8.26. Plot of upscaled cells from wells versus match for each scenario. P10, P50 and P90 match values, based on 250 realizations, are plotted.

In summary, match results showed an increase in match values for all scenarios, but this increase was more substantial when the input data were characterized by CH and PB geobodies in comparison to cases in which input data are characterized by CS and FP geobodies (Fig. 8.27). Furthermore, standard deviation (Std) generally decreases as upscaled cells from wells increases, indicating that an increase in input wells reduces uncertainty.
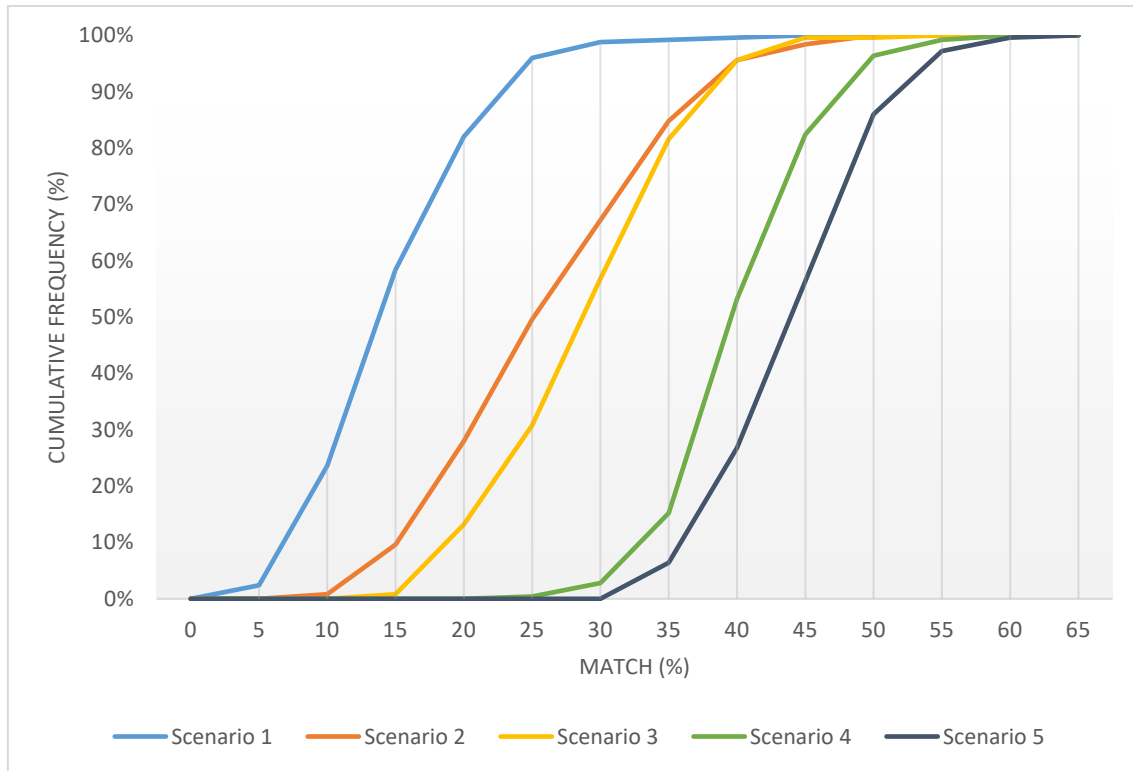
Fig. 8.27. Plot showing the cumulative match frequency for the five scenarios. Note how the cumulative frequency curve shifts to higher match values with increasing input data. The highest shift of the cumulative frequency curve towards higher match values occurs in Scenarios 2 and 4. The curve with the steepest slope occurs in Scenario 4, indicating a lower dispersion in match values in this scenario compared to the others.

8.4.5. Static Reservoir Connectivity in M-S Unit

The modelling of static reservoir connectivity provides information into expected connected reservoir volumes for different net-to-gross ratios and well spacings. These results are useful for reserve estimation, infill-drilling program design and the selection of intervals for completion (Pranter & Sommer, 2011).

Measures of static connectivity have been defined differently by different workers. Larue & Hovadik (2006) differentiated two types of connectivity: (1) geobody or sandbody connectivity where the term refers to the connectivity of individual elements in a reservoir, such

as amalgamated channel deposits; and (2) reservoir-to-well connectivity, where connectivity is defined as the proportion of the reservoir connected to wells. Reservoir connectivity has been described by Pranter & Sommer (2011) as the part of a reservoir that is connected to wells and is the volume of reservoir rock that is connected to wells divided by the total volume of reservoir rock, measured as a percentage. Other definitions of connectivity involve characterization of permeability heterogeneity and evaluation of subsurface fluid flow.

Static reservoir connectivity as used here, is a percentage calculated as the volume of sandstone bodies connected to a particular pattern of wells, directly or indirectly, divided by the total sandstone volume (Pranter & Sommer, 2011). This measure of connectivity does not account for the dynamic flow of fluids through the reservoir. For this study, the static reservoir connectivity is considered in terms of connected reservoir.

Throughout this section, in order to quantitatively evaluate the static reservoir connectivity of the M-S Unit (or Reservoir Zone 1 of the TIBEM succession in Alcaraz area), the 3D reservoir model framework, previously presented, has been populated using the Object-based modelling technique. Following the interpretation of the stratigraphic succession (Chapter 4 and Section 8.3) for the M-S Unit in the study area, 16 channel geobodies were modelled (Fig. 8.28a). Based on 200 realizations, the best realization for each zone, representing the interpretation from outcrop and subsurface data, was selected. Subsequently, workflows for geobodies and lithofacies modelling, as outlined above, were applied in order to establish the heterogeneity distribution within the M-S Unit. (Fig. 8.28b-c).

As described in Chapter 7, some lithofacies which comprise the geobodies can be considered as potential flow baffles, eg. Lithofacies Fl toward the top of the channel fill (mud plug), not all the lithofacies which comprise the reservoir geobodies described in the M-S Unit can be considered as net. In addition, recent studies focused on the petrophysical and diagenetic characteristics of the M-S Unit (Henares *et al*., 2014, 2016a, b) have established a good match between reservoir properties and lithofacies distribution. This relationship is a direct consequence of the primary control exerted by depositional features, notably detrital clay abundance and distribution, on diagenetic evolution and thus on reservoir quality. As such, permeability will most probably be higher in those facies associations where grain coating clays are well-developed and significant primary porosity preserved. Conversely, those lithofacies characterized by pervasive gypsum cement will show the poorest reservoir quality. This suggests that even the sandstone facies linked with distal crevasse-splay geobodies (medial crevasses-

splay facies association (MSFA 7) as described by Yeste *et al*., 2020) may have favourable petrophysical characteristics, and thus be considered a potential hydrocarbon reservoir.

In this sense, Lithofacies Gm, Sh, St, Sr and Sc can be considered as reservoir facies (net) whereas Lithofacies Sd, Ll, Lm and Fl can be considered as non-reservoir facies (gross). Through the resultant lithofacies model, a reservoir facies model was created (Fig. 8.28d), which is effectively a 3D model of net-to-gross distribution in the M-S Unit. This reservoir facies model will be used to estimate the static reservoir connectivity of the M-S Unit.

As described above, the static reservoir connectivity is calculated from the volume of connected sandstone bodies (or connected reservoir facies). The estimated vertical proportions from the reservoir facies model (Fig. 8.28e) and the connected volumes model (Fig. 8.28f), which represents the total of reservoir volumes from the 3D reservoir model framework (calculated from laterally and vertically connected reservoir facies), show a total of 13 volumes. In other words, of the 16 modelled channels, and their associated geobodies, only 3 are connected three-dimensionally in the reservoir facies model.

In addition, the static reservoir connectivity differs as a function of the net-to-gross ratios and well spacings. To address this issue five well-pattern-based static connectivity analyses were initially carried-out, for the reservoir facies model, each with a grid-based design (Fig. 8.29): 1 well in the centre of the model, 5 wells with 1000 m spacing, 9 wells with 500 m spacing, 25 wells with 250 m spacing and 81 wells with 125 m spacing, were used. All well distribution patterns follow a symmetrical grid (Fig. 8.29). Subsequently, and in order to estimate how static connectivity varies in relation to different net-to-gross values and, so establish the role of point bar (PB) and crevasse-splay (CS) geobodies in the static reservoir connectivity, three scenarios, combined with the five well-patterns described above (Fig 8.29) were considered. The first scenario considered only the connectivity between the reservoir facies of the CH geobodies (net-to-gross of 2.1%). The second scenario considered the reservoir facies of both CH and PB geobodies (net-to-gross of 5.8%), whilst in the third scenario all reservoir facies (CH, PB and CS geobodies; net-to-gross of 9%) were considered (Fig. 8.30).
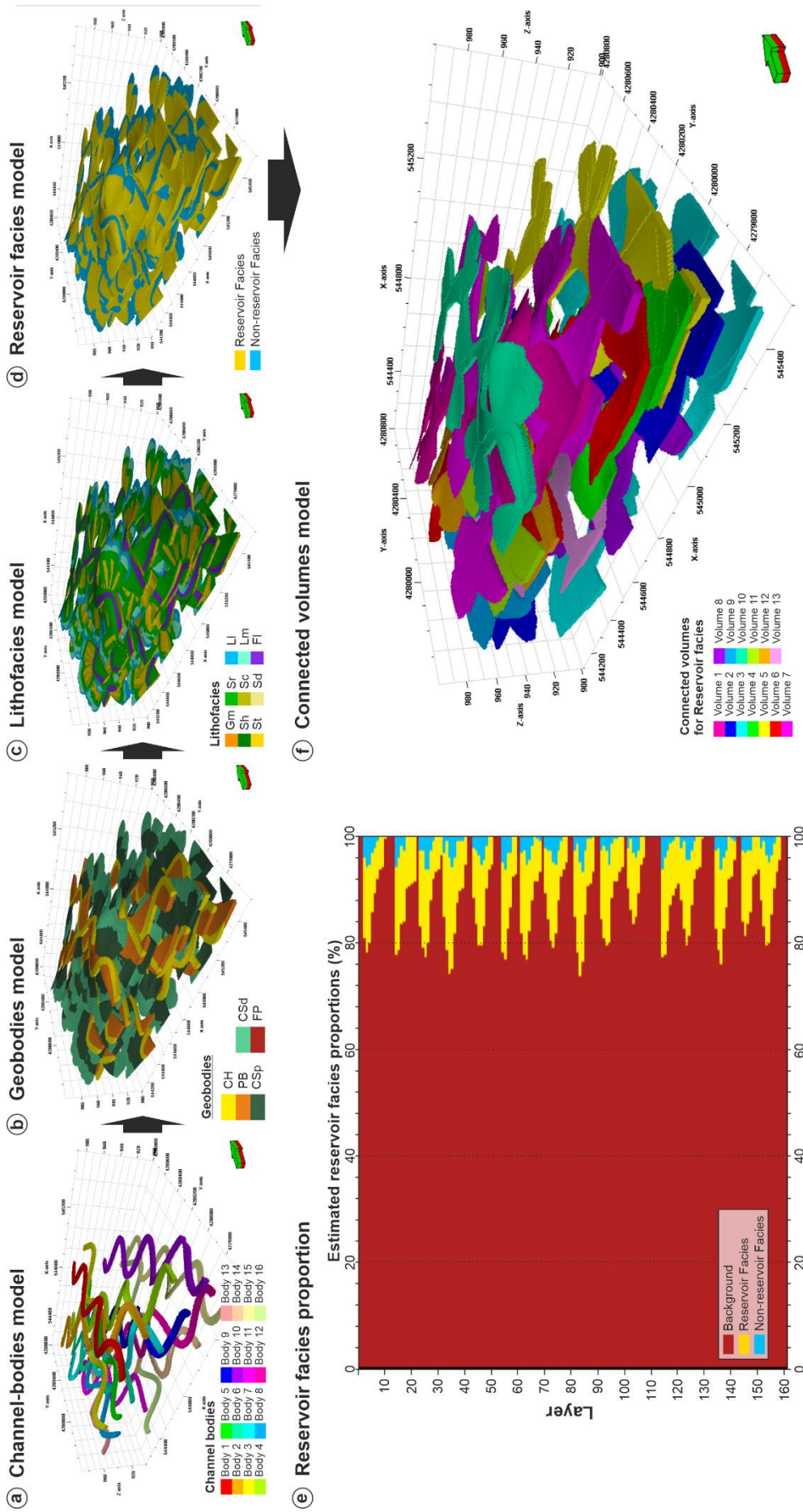
Fig. 8.28. From channel-bodies model to connected volumes model. Background facies and non-reservoir facies have been rendered transparent. **(a)** Channel-bodies modelled in the 3D reservoir model. **(b)** geobodies model created from modelling workflow at geobody scale (Section 8.4.2.1 – Modelling workflow at geobody scale). **(c)** Lithofacies model created from modelling workflow at lithofacies scale (Section 8.4.2.2 – Modelling workflow at Lithofacies scale). **(d)** Reservoir facies model considering Gm, Sh, St, Sr and Sc Lithofacies as reservoir facies and Sd, Ll, Lm and Fl Lithofacies as non-reservoir facies. Note that in only in 3 Lithofacies as reservoir facies and Sd, Ll, Lm and Fl Lithofacies as non-reservoir facies. **(e)** Estimated vertical reservoir facies proportions by layer. Note that in only in 3 stratigraphic levels (layers 30, 120 and 150), are geobodies directly connected by vertical amalgamation. **(f)** Connected volumes model derived from the reservoir facies model.
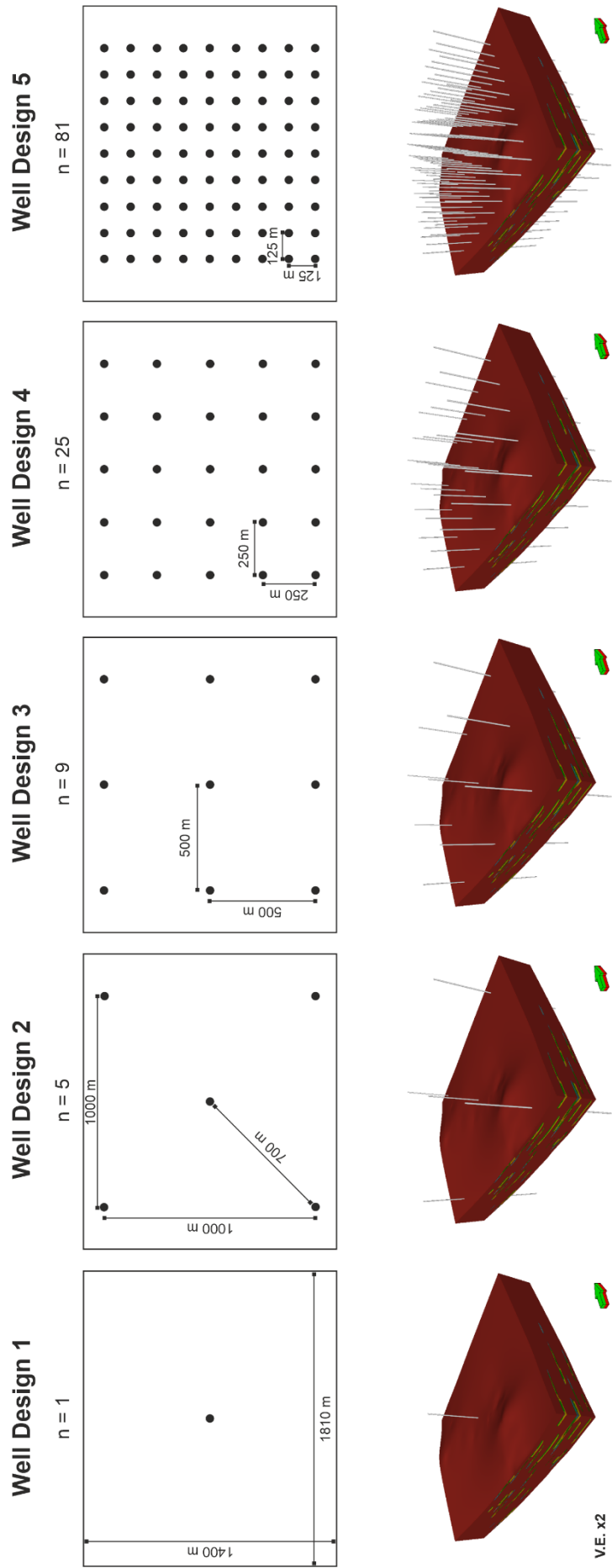
Fig. 8.29. Well-patterns and spacings analysed for each scenario. The number of wells (n) and distances between wells are shown.
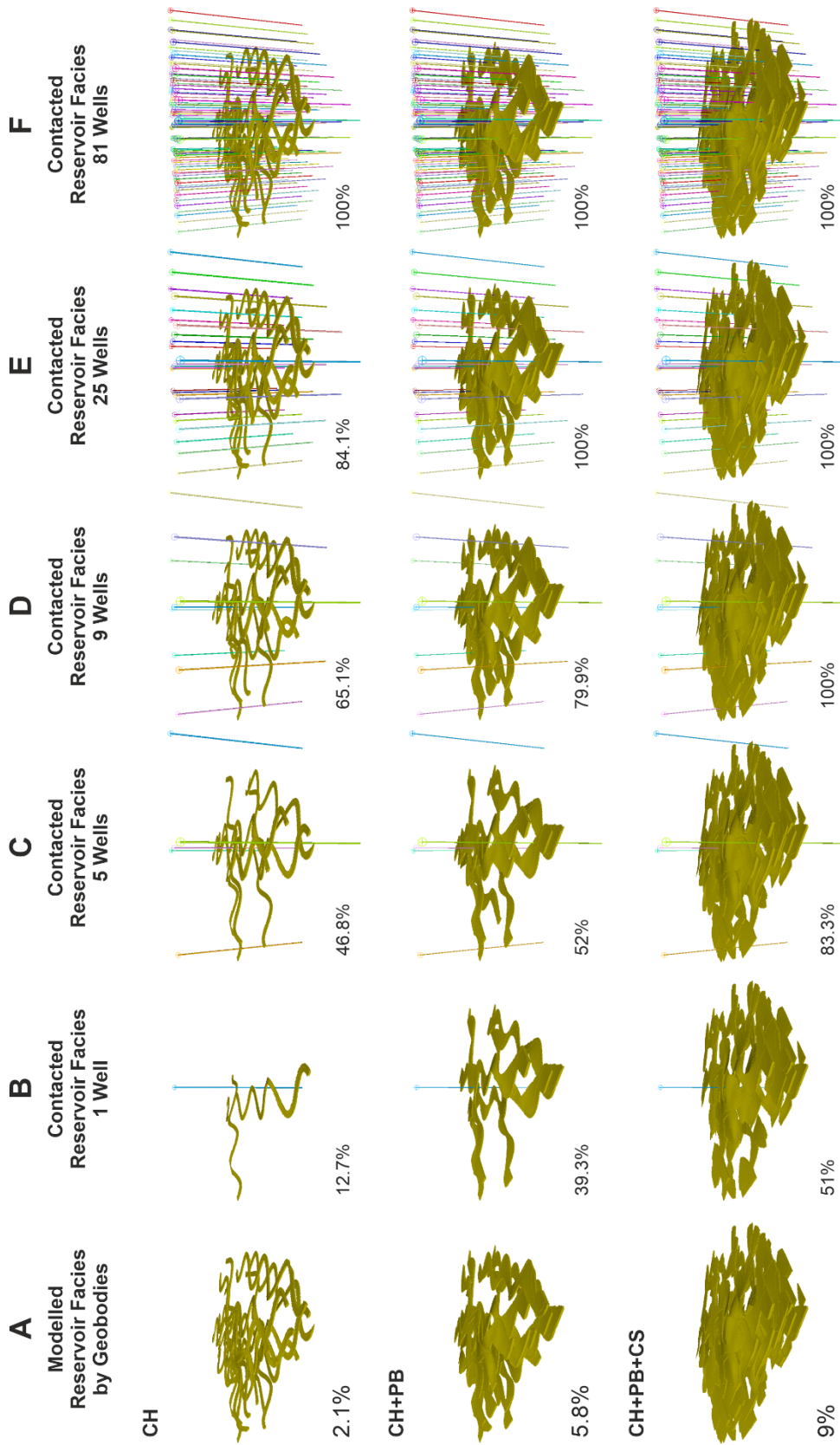
Fig. 8.30. 3D models of connected reservoir sandstones for three scenarios (considering CH geobody, CH and PB geobodies and CH, PB and CS geobodies, respectively) and five well-patterns. Non-reservoir facies have been rendered transparent. Column A shows the modelled reservoir facies for each scenario, successively considering CH reservoir facies, CH and PB reservoir facies and CH, PB and CS reservoir facies, respectively. Column B shows connected reservoir facies for the well design 1 (1 well located in the centre of the model) for each scenario. Column C shows connected reservoir facies for well design 2 (5 wells) for each scenario. Columns D-F show connected reservoir facies for well designs 3-5 (9, 25 and 81 wells respectively; with 500 m, 250 m and 125 m well spacing, respectively. The percentages posted below each model in column A are the net-to-gross ratio. The percentages posted below each model in columns B-F are the static reservoir connectivity values. Vertical exaggeration is two times.

The results of the 3D static reservoir connectivity analyses show an increase in connectivity correlated with increases in well density, and also with the net-to-gross ratio. This increase is not always linear as the 'S-curve' trend is observed for low well density. However, as well density increases, the relationship between static reservoir connectivity and the net-to-gross ratio becomes more linear (Fig. 8.31).

The cross-plot of well design scenarios versus connected reservoir (Fig. 8.31) shows, for the first scenario (considering only the reservoir facies of CH geobodies), how the static reservoir connectivity increases most steeply between the design with only a single well and the design with 5 wells, increasing the connected reservoir from 12.7% to 46.8%; whilst a strong positive correlation is observed between designs with 9, 25 and 81 wells (increasing the connected reservoir from 46.8% to 65.1%, 84.1% and 100%, respectively).

In the case of Scenario 2 (considering the reservoir facies of both CH and PB geobodies), the increase in static reservoir connectivity between the designs with 1 and 5 wells is less steep (from 39.3 to 52% of connected reservoir) when compared with Scenario 1. Similar linear relationships are also observed between designs with 5, 9 and 25 wells (from 52% to 79.9% and 100% of connected reservoir, respectively). In this scenario, with 25 wells (250 m well spacing), 100% of reservoir is connected (Fig. 8.31).

Scenario 3 (considering all reservoir facies) shows a similar linear trend between increasing well numbers and connectedness to Scenario 1. Significantly, in this scenario, with only 9 wells and a spacing of 500 m, 100% of the reservoir is connected (Fig. 8.31).

In summary, comparison of the three scenarios shows an enhancement of static reservoir connectivity when considering the reservoir facies of both PB and CS geobodies. Even with only a single well, static reservoir connectivity increases from 12.7%, considering only reservoir facies of CH geobody, to 39.3%, considering the reservoir facies of PB geobodies; and from 39.3% to 51% if reservoir facies of CS geobodies are also considered. In contrast if 5 wells are used, the enhancement to static reservoir connectivity is minimal when comparing Scenarios 1 and 2 (only 5.2% more of the reservoir is connected). In all other configurations, however, the impact on static reservoir connectivity, of considering both PB and CS geobodies is substantial.
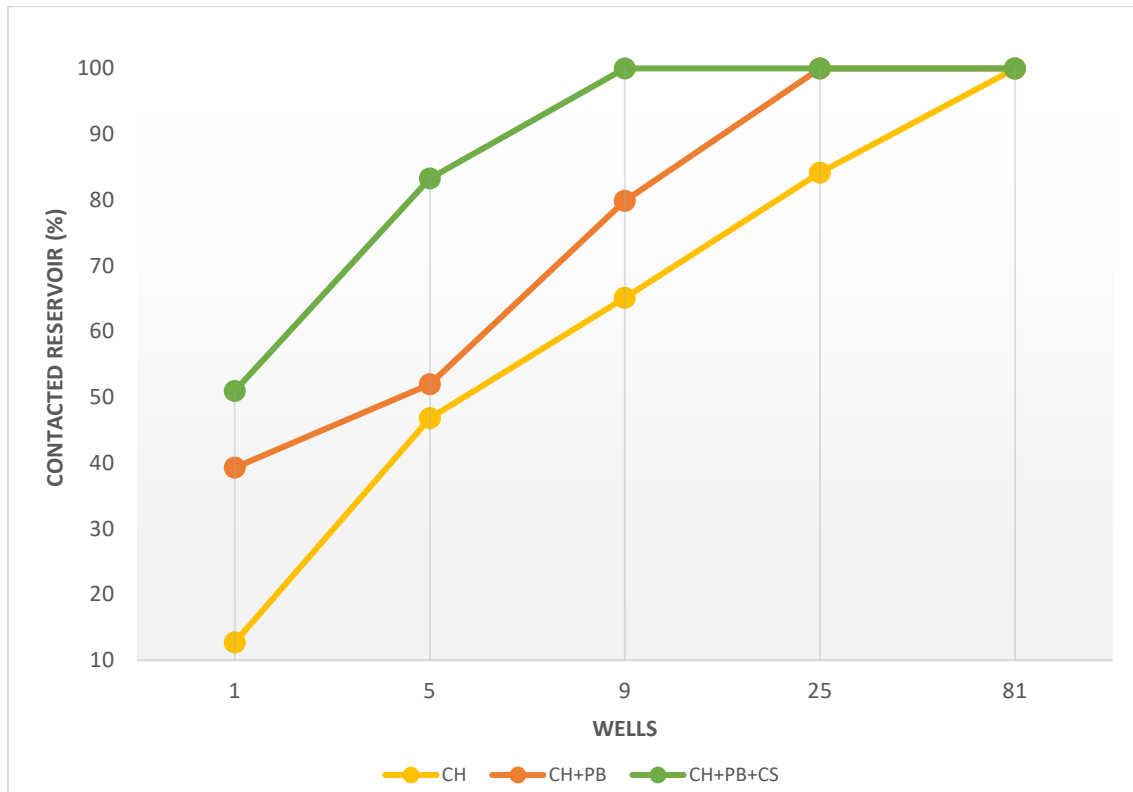
Fig. 8.31. Plot of well designs (number of wells) versus static reservoir connectivity for the three scenarios considered in this study. Static reservoir connectivity is lowest at a low well density. As might be expected, as well density increases, the static reservoir connectivity also increases with the notable exception of Scenario 3 in which case there is no increase in static reservoir connectivity after 9 wells, because 100% of reservoir facies are connected. Note static reservoir connectivity is enhanced when considering reservoir facies from PB and CS geobodies in all well designs. For example, considering only CH geobodies, for well design 1 (1 well), the static reservoir connectivity is 12.7% and can be as high as 39.3%, considering reservoir facies of PB geobodies, or 51%, considering reservoir facies of CS geobodies.

As previously demonstrated, the consideration of reservoir facies associated with CS geobodies clearly enhances the static reservoir connectivity. But how does the relative abundance of CS geobodies influence this enhancement in static reservoir connectivity?

The previous scenario (third scenario) considered a CS reservoir facies proportion (% of total net-to-gross corresponding to the CS reservoir facies) of 3.3% (5 crevasse-splays per channel storey). To establish the impact of CS geobodies on the static reservoir connectivity, four new scenarios have been considered, depending on the CS geobody proportions (Fig. 8.32):

(1) 1.1% of CS reservoir facies (1 CS geobody per channel storey), 6.8% of net-to-gross;

(2) 2.4% of CS reservoir facies (3 CS geobodies per channel storey), 8.2% of net-to-gross;

(3) Same proportions as the third scenario in the previous section (3.3% of CS reservoir facies – 5 CS geobodies per channel storey), 9% of net-to-gross;

(4) 4.5% of CS reservoir facies (10 CS geobodies per channel storey), 10.3% of net-to-gross; and

(5) 5.8% of CS reservoir facies (20 CS geobodies per channel storey), 11.5% of net-to-gross;
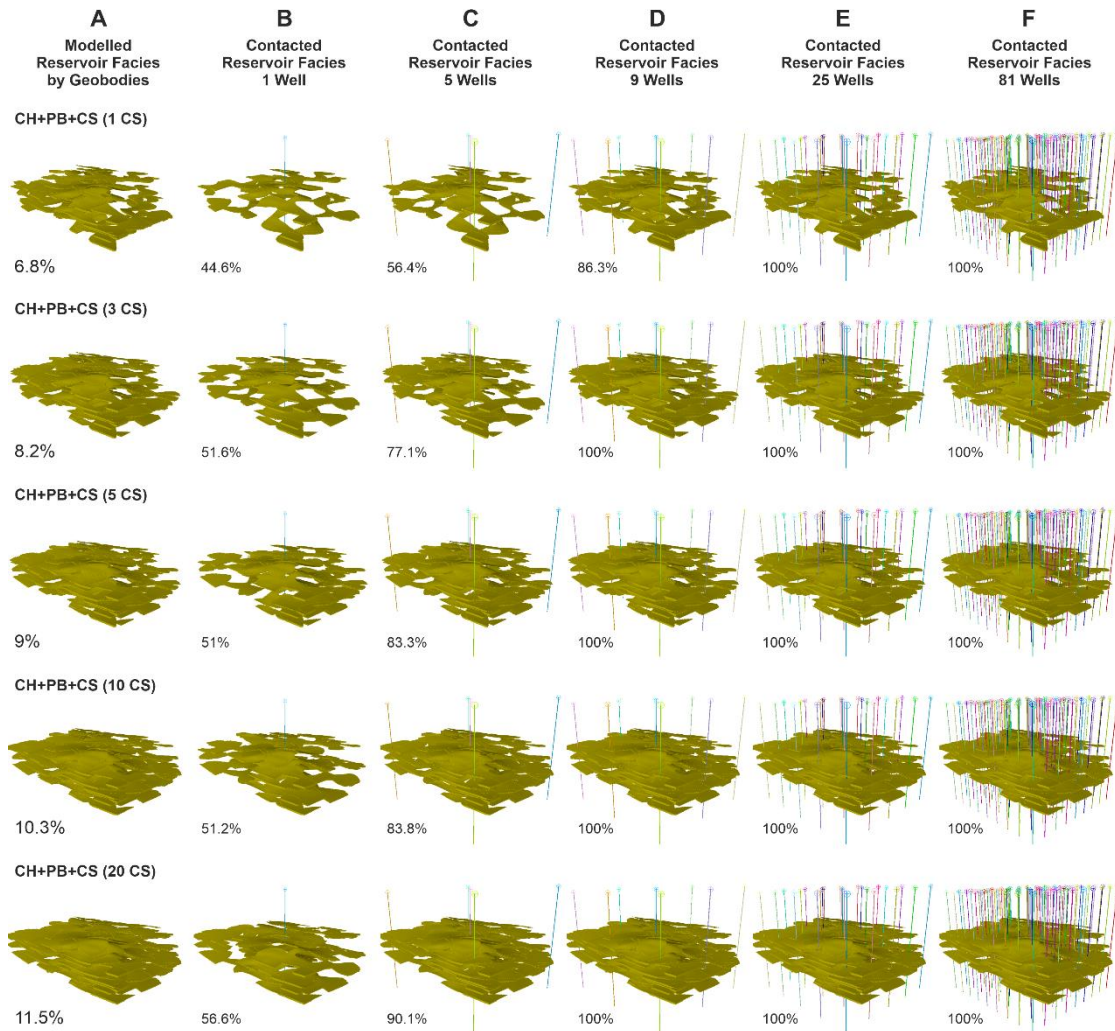
Fig. 8.32. 3D models of connected reservoir sandstones for five scenarios each reflecting differing proportions of CS geobodies (considering 1, 3, 5, 10 and 20 CS geobodies, respectively) and five well-patterns. Non-reservoir facies have been rendered transparent. Column A shows the modelled reservoir facies for each scenario, considering CH, PB and CS reservoir facies, with varying proportions of CS geobodies. Columns B to F show connected reservoir facies for well designs 1 to 5 (1, 5, 9, 25 and 81 wells respectively). The percentages posted below each model in Column A are the net-to-gross ratios. The percentages posted below each model in columns B-F are the static reservoir connectivity values (percentages of contacted net reservoirs by wells). Vertical exaggeration is two times**.**

Comparing the five scenarios, a similar trend in Scenario 1 (which considers 1 CS geobody per channel storey – 6.8% of net-to-gross) is observed compared to Scenario 2 of the previous section (which considers reservoir facies of both CH and PB geobodies – 5.8% of net-to-gross). The impact of crevasse splays, in this scenario, on reservoir connectivity appears to be minimal (only 5.3% more of the reservoir is connected compared to the impact of reservoir facies associated with PB geobodies; Fig. 8.33).

The remaining scenarios show a similar linear trend when compared to each other. In these scenarios, the impact of the CS reservoir facies is substantial, even in Scenario 2 (with 3 CS geobodies per channel). In other words, with proportions of as little as 2.4% of CS reservoir facies, the static reservoir connectivity is enhanced by 38.9%, compared to a scenario that considers only CH reservoir facies; and by 12.3%, compared to a scenario that considers reservoir facies of CH and PB geobodies, with a single well (Fig. 8.33).
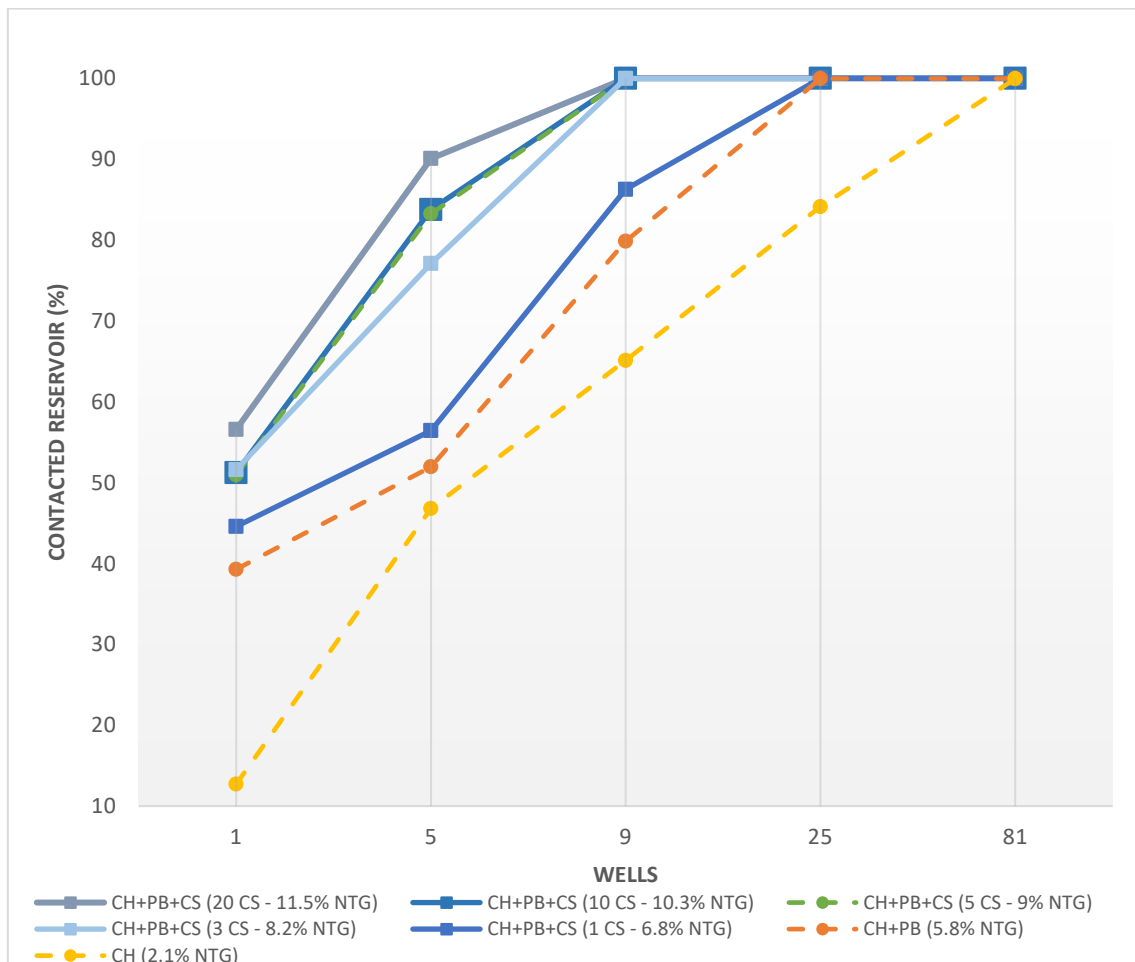
Fig. 8.33. Plot of well designs (number of wells) versus static reservoir connectivity for the five scenarios considered, depending on the proportion of CS geobodies. These are also compared with one scenario that considered only CH reservoir facies and another which considered both CH and PB reservoir facies. Note that the impact of CS reservoir facies is substantial, even in a scenario that considered only 1 CS geobody per channel step.

8.5. Discussion

The present study highlights the use of outcrop analogues in reservoir modelling (Pringle *et al.,* 2006; Enge *et al.*, 2007; Hodgetts, 2013; Howell *et al.,* 2014; Colombera *et al.,* 2016; Cabello *et al.,* 2018). This integrated study of outcrop and subsurface data has allowed the generation of quantitative conceptual models which have proven extremely useful in geostatistical modelling. This is especially so when it comes to planning modelling strategies as well as producing training images. In addition, recent technical advances in digital outcrop characterization and data capture have proven to be a valuable tool, allowing precise uncertainty analysis of the modelling results.

Recent studies clearly indicate the usefulness of digital outcrop models in reservoir modelling, as well as, in the generation of training images by integrating spatial information obtained directly from outcrop measurements (Dimitrakopoulos *et al.,* 2010; Boucher, 2011; Renard & Allard, 2013; Pickel *et al.*, 2015; Cabello *et al.*, 2018; Puig *et al*., 2019; Mitten *et al*., 2020). Current common techniques used in the construction of reservoir models are OBM (Object-Based Modelling) or SIS (Sequencial-Indicator Simulation) methods, a reflection of the inherent complexities typically associated with generating the appropriate training images required for MPS modelling techniques.

In attempts to resolve this issue, several authors have used DOM data to generate 2D TIs (eg., Comunian *et al*., 2012; Pickel *et al*., 2015). These TIs demonstrated a clear vertical facies trend but did not well represent the 3D facies pattern. An alternative approach to constructing TI is the OBM method as proposed by other authors (e.g., Pyrcz *et al*., 2008; Bezrukov & Davletova, 2010; Gottschalk *et al*., 2017; Tahmasebi, 2018). Mitten *et al.* (2020) to combine information from DOMs, to represent vertical facies patterns (Z dimension), and satellite images to represent the other two dimensions (X and Y). However, this manual development of training images is laborious, as it requires multiple iterations and manual checks of intersectional planes throughout the training image volume and target fractions to ensure that input statistics are honoured.

The current study combines the information obtained from both outcrop and subsurface data with the OBM methodology to create a 3D TI from the designed modelling workflow. The resulting 3D TI represents all heterogeneities, at geobody scale, described in the studied outcrop and, also, the spatial relationships between geobodies. Both 3D TI and modelling workflows are directly exportable to any similar reservoir.

Using the TI, subsequent MPS simulations generated reliable predictions for the CH geobody, although all scenarios showed an overestimation both in the northeast and southwest sectors of the model. This overestimation was, however, expected as a response to: (a) the spatial relationships between the geobodies generated in the TI and; (b) the dimensions of the TI. However, despite these issues, the highest probability values still occur in the area suggested by the paleogeographic reconstruction (Fig. 8.7).

Increasing the amount of input data in the model, located close to the target (CH geobody), showed a match increase (Fig. 8.27). On the other hand, although the additional wells did not penetrate the CH geobody but rather, PB or CS geobodies; they still play an important role in the MPS simulations, increasing the match and delimiting the probability zones with greater confidence (Fig. 8.25 and Fig. 8.27).

Depending on the aim, and on the basis of the results obtained in this study, a hypothetical initial field design, characterised by a low density of evenly spaced wells located across the model area, would improve the prediction of geobody location. In contrast, if the objective is a late development infill-drilling program, widely-spaced wells located along the azimuth trend of the target (CH Geobody) would also improve the prediction of reservoir geobodies.

The results for the 3D static reservoir connectivity presented in this study for the M-S Unit, reveal an increase directly correlated with increasing net-to-gross ratio for all well designs. Furthermore, the results also highlight the importance of considering the reservoir facies of both PB and CS geobodies in estimations of reservoir connectivity in this type of fluvial reservoir. Donselaar & Overeem (2008) suggested that if channel-floor sandstone ribbons connect point-bar deposits (forming a "string-of-beads" sandstone body, specifically in low-gradient, mixed load fluvial systems), this could shift the 'S-curve' trend in the plots which show the static reservoir connectivity increase as a function of the number of wells and/or net-to-gross, such that static sandstone body connectivity increases more steeply at lower net-to-gross ratios.

In this study, it has been demonstrated that if PB geobodies are included in the model, static reservoir connectivity is enhanced, showing a steep increase in connectivity compared with the scenario that considered only CH geobodies (static reservoir connectivity increased up to 26.6%, for a single well; Fig. 8.31). A similar study for static reservoir connectivity of fluvial sandstones was presented by Pranter & Sommer (2011) in the lower Williams Fork Formation (Piceance Basin, Colorado). These authors demonstrated how static connectivity is sensitive to sandstone body width and varies with net-to-gross ratio and well spacing. The authors

considered a minimum net-to-gross of 10% for their study. The results of this study thus complement the contributions of Pranter & Summer (2011) with respect to fluvial reservoirs with lower net-to-gross ratios (less than 10%; Fig. 8.30 and Fig. 8.32).

In addition, Pranter *et al.* (2014), and also Fenn & Pranter (2014), concluded that is necessary to evaluate the impact that crevasse-splays may have on static reservoir connectivity. This study has addressed this issue in some considerable detail and has shown how the consideration of crevasse-splay geobodies can substantially improve the static reservoir connectivity, although it is important to emphasize that a preliminary estimation of the proportion of CS geobodies is necessary. If these geobodies represent an increase in net-to-gross of approximately 1%, their impact on reservoir connectivity will be minimal (reservoir connectivity will be enhanced by approximately only 5%). Conversely, if CS geobodies represent a net-to-gross increase of approximately 2.5% or more, the impact will be substantial. An increase, for example, of 2.4% in net-to-gross, considering 3 CS geobodies per channel step, enhanced reservoir connectivity by 12.3% compared to a scenario that considers only the reservoir facies of CH and PB geobodies (Fig. 8.33). This confirms the importance of crevasse splay deposits in high sinuosity fluvial reservoirs, not necessarily in terms of absolute volumes, but in terms of their significant impact on improving overall connectivity within the reservoir.

8.6. Conclusions

The current study, integrating both outcrop and subsurface data, has successfully demonstrated the application of outcrop analogues as a basis for informing, designing and testing predictive tools for forecasting the reservoir architecture of high-sinuosity fluvial successions in the subsurface.

The outcrop/behind outcrop methodology has allowed the generation of quantitative conceptual models useful in geostatistical modelling. This is especially so, when it comes to planning modelling strategies as well as producing training images. High-Resolution Digital Outcrop Models (DOMs) have proven to be a useful tool in geostatistical modelling. The DOMs help to incorporate more geological data (Digitized facies, geometric data, the relationships between facies distributions, virtual sedimentological logs, etc.) into the modelling process allowing us to generate more robust geostatistical models. These then provide the necessary data to obtain a geocellular outcrop model and thereby have a greater control over the results obtained.

Modelling workflows designed for this study have successfully reproduced the distribution of heterogeneities interpreted within the M-S Unit at both geobody and lithofacies scales. These modelling workflows are potentially exportable to other examples of this type of reservoir, for the development of training images and/or directly for use in the reservoir facies modelling.

Probability models obtained from MPS simulations, and using the 3D training image created for this study, generated a good prediction of the channel geobody throughout the model framework, in agreement with the paleogeographic reconstruction, even when considering a scenario in which only one well drilled the channel. MPS simulation results also showed mean match values ranging from 15% to 44%, depending on the scenario considered. An additional key conclusion is that a low density well-spacing design oriented along the predicted azimuth trend of the channel geobody improves the prediction of the distribution of reservoir geobodies.

Well-pattern-based static reservoir connectivity analyses for the M-S Unit also demonstrated how static reservoir connectivity is sensitive to geobody type and varies with the net-to-gross ratio and well spacing. Static reservoir connectivity analyses reveal the importance of including both point bar and crevasse-splay geobodies as they produce a significant increase in static reservoir connectivity at all well spacings. Crevasse-splay geobodies enhance static connectivity at all well spacings; understanding their volumetric significance and spatial distribution is therefore of critical importance in the modelling of low gradient, high sinuosity fluvial systems in the subsurface.

CHAPTER 9:

General Conclusions

9.1. General Conclusions

The principle aim of this Thesis was to generate datasets from outcrop analogues in order to significantly improve understanding of the sedimentological variables which condition the optimal exploration and development of highly heterogeneous reservoirs. These datasets include key identifying characteristics, both in outcrop and subsurface data (core and well logs), as well as quantitative conceptual models and paleogeographic reconstructions, including geometric data and the distribution of internal heterogeneities, at lithofacies scale, of the sedimentary geobodies identified in the studied outcrops. For this purpose, a Triassic succession, exposed in Central SE Spain (Triassic Red Beds of Iberian Meseta - TIBEM), was selected for study. This succession can be considered as a reservoir-analogue outcrop for similar reservoirs composed of fluvial deposits, from both high-sinuosity and low-sinuosity systems, and the deposits of mixed tidal and wave-influenced shoreline systems. The results obtained in this study lead us to the conclusions that are detailed below.

Through the OBO characterization of the high-sinuosity fluvial system example (M-S Unit), a total of ten facies associations were identified and characterized, both from core and wireline logs; namely main channel (MSFA 1), point bar (MSFA 2), scroll bar (MSFA 3), chute channel (MSFA 4), crevasse channel (MSFA 5), proximal to distal crevasse-splay complex (MSFA 6 to MSFA 8), distal floodplain (MSFA 9) and swamp (MSFA 10) facies association. These facies associations form four different geobodies:

- (i) *Channelized geobodies* consist only of Facies Association MSFA 1. These geobodies are up to 3 m thick and up to 40 m in width, with a ribbon-shape in plan view and lenticular geometry in 2D cross section, characterized by a fining-upward sequence

comprising Lithofacies Gm-St-Sr-Fl. These ribbon-shaped geobodies show an amplitude of up to 200 m and a wavelength of up to 400 m. The presence of mud plugs toward the top of these geobodies are considered as potential flow barriers. Channelized geobodies are also distinguished in the Gamma Ray by the stacking of several bell-shape and fining-upward trend. Dip tadpole analysis highlights several low angle (dip angles of <15°) internal surfaces which correspond to the channel base erosional surfaces. Between these erosional surfaces, a set of dips with both random azimuth and dip angles between 5° and 25° are recorded, interpreted as trough cross-bed foresets.

- (ii) *Asymmetric sigmoidal-shaped geobodies* are formed by Facies Associations MSFA 2 to MSFA 4, up to 3.6 m thick and up to 130 m in width. These geobodies, distinguished by a series of stacked packages bounded by inclined master bedding surfaces (Lateral Accretion Packages – LAPs), are associated with the inner margin of channelized geobodies. Internally, at bed-scale, these geobodies are characterized by a fining-upward succession composed of Lithofacies Gm-St-Sr. Locally, mud drapes occur between LAPs and would be interpreted as baffles or barriers to potential flow in subsurface equivalents. Locally, these sedimentary geobodies also contain minor channel geobodies toward the top of the succession, characterized by a fining-upward sequence, from fine-grained sandstones into siltstones, interpreted as chute channels. These minor channels could also be interpreted as important barriers to flow. In the Gamma Ray, asymmetric sigmoidal-shaped geobodies are characterized by a funnel shape and coarsening-upward trend, at the base, and a bell shape and fining-upward trend toward the top, of GR response. Two dip tadpole groups are characteristic of these geobodies: (a) shallow-to-steep-to-shallow dip angles towards the top, correspond to lateral accretion surfaces; and (b) tadpole sets with random azimuth and dip angles between 5° and 25°, which represent trough cross-bed foresets.

- (iii) *Lobe-shaped geobodies* are up to 2 m thick with up to 230 m of lateral extension, perpendicular to the main flow direction of the channel belt and from their insertion point (erosive margin of a channelized geobody); and a variable width ranging from 65 m in proximal zones to up to 115 m in distal zones. Internally, four facies associations have been distinguished within these geobodies: crevasse channels (MSFA 5) characterized by Lithofacies St-Sr-Sw, and preserved locally in the uppermost part of these geobodies, proximal crevasse-splay complex (MSFA 6) characterized by the stacking of Lithofacies Sh-Sr-Sc, medial crevasse-splay complex (MSFA 7) characterized

by the succession of Lithofacies Sd-Sr and distal crevasse-splay complex (MSFA 8) represented by Lithofacies Ll and Lm. Commonly, lobe-shape geobodies appear to be amalgamated, forming crevasse-splay complexes ranging from 1.1 m to 4 m in thickness. The high-resolution analysis of GR log trends within these lobate geobodies showed a predominant funnel-shaped GR response for proximal, medial and distal crevasse-splay deposits, reflecting the progradation of the overbank facies in successive flood events. Crevasse channel deposits, in contrast, show a bell-shaped GR trend. The high-resolution analysis of dip tadpoles revealed patterns associated with the different segments of the crevasse-splay lobe: (i) tadpoles with randomly distributed azimuth and dip angles between 5° and 25° are associated with trough cross-bedding in MSFA 5; (ii) tadpoles with unidirectional azimuths and low-dip angles are associated with horizontal and ripple-laminated sandstones in MSFA 6; (iii) randomly distributed dip angles and azimuths and unidirectional azimuths associated with low dip angles corresponding respectively to syn-sedimentary deformation structures and ripple-laminated sandstones, are associated with MSFA7; and (iv) unidirectional azimuths and low dip angles between mud rock laminae are associated with MSFA 8.

- (iv) *Tabular geobodies* are characterized by distal floodplain (MSFA 9) and swamp deposits (MSFA 10). Distal floodplain deposits (MSFA 9), characterized by Lithofacies Fm, vary between 100 m and 1000 m in width, forming packages only 0.6 m thick. Locally, within the distal floodplain, swamp deposits (MSFA 10), characterized by Lithofacies Fl, occur and which are up to 100 m wide and 0.5 m thick. These tabular geobodies are characterized by a typically serrated shape and aggrading GR response with high API values. Dip tadpole analysis revealed very low dip angles (<10°) and unidirectional azimuths for these tabular geobodies. In addition, tadpoles with very high dip angles (30° to 75°) and a bi-directional azimuth, are associated with pedogenic slickensides structures.

This outcrop analogue dataset for high-sinuosity, low gradient fluvial systems, including key geometric and sediment geobody dimension data, is especially valuable for the crevasse-splay/floodplain elements which, otherwise, are not so well-known and may often act as a secondary reservoir. The predictive conceptual model generated from outcrop and subsurface data allows us to estimate, with some confidence, how far a well drilled through crevasse-splay/floodplain deposits might be from a main channel and potential primary reservoir, a prediction of significant value in exploration and appraisal. In addition, the identification of

amalgamated crevasse-splay complexes is of considerable importance; because they are also potential reservoirs as both proximal crevasse-splay and crevasse channel deposits comprise similar lithofacies, in addition to being directly connected to the main channel. Amalgamated crevasse-splay complexes can also be used to estimate the dimensions of the main channels in intervals where the channel body itself is not directly penetrated by a well. The thickness of the main channel will be similar to that of the amalgamated crevasse-splay complexes. Thus, a detailed study of the proposed facies associations in core, and a high-resolution study of both GR log response and dip tadpole patterns would lead to a correct identification of depositional sub-environments, geobody geometries, dimensions, orientations and thus a better estimate of net reservoir volume.

In the case of the low-sinuosity fluvial example (S Unit), two geobodies, comprising two facies associations (SFA 1 and SFA 2), were identified:

- (i) *Channel geobodies;* up to 20 m thick and 300 m in width, have a lenticular geometry in 2D cross section and low sinuosity in plan view. This reservoir geobody is characterized by Facies Association SFA 1, composed of fining- and thinning-upwards packages comprising Lithofacies Sh/Sm-St-Sr. Locally, Lithofacies Gm appears toward the base of these geobodies. Thin (cm-scale) mud drapes between the different packages could be potential baffles or even barriers to vertical fluid flow and would tend to compartmentalize these otherwise laterally extensive geobodies.

- (ii) *Elongate geobodies,* comprising compound bar deposits (Facies Association SFA 2), are up to 20 m thick and 500 m in width. Internally, these are principally characterized by a stacking of Lithofacies Sh-Sp-St. Finer grained deposits and mm-scale mud drapes are also observed, associated with the gently dipping bounding surfaces between individual downstream accretionary macroforms, although these are unlikely to form significant baffles to permeability within the barform. Locally, at the top of these geobodies, an erosive surface is observed, overlain by very fine-grained sandstone (Lithofacies Sr) and mudstone deposits (Lithofacies Fl). These deposits represent cross-bar channels cutting across the top of the compound bars and, locally, could be considered as potential flow baffles.

This example is the best potential reservoir in the studied succession, showing the highest sand:mud ratio values (95:5) and only very localized baffles or flow barriers to flow, which are more relevant in the channel geobodies than in the elongate geobodies. Given the apparent

homogeneity that this example presents, this integrated high-resolution study, allows us to identify subtle key differences which permit the differentiation of the two interpreted geobodies in subsurface. By means of a detailed analysis of the Gamma Ray log, several differences, superimposed on a general cylindrical shape and aggradational trend through the S Unit, have been established between the channel and the compound bar geobodies. Several minor sequences with funnel shape and coarsening-upward trends can be observed in the channel geobody. In contrast, within the compound bar geobody, the bar head shows a more homogeneous smooth-cylindrical trend in the GR, whereas the bar tail is characterized by the stacking of several bell shape and fining-upward trend intervals. Detailed analysis of the dip tadpoles was of paramount importance for the high-resolution characterization of the two geobodies. The channel geobody shows, predominantly, randomly distributed dip angles and azimuths. In contrast, the tadpoles in the bar head display several characteristic patterns with similar dip angles and azimuths, limited at the base and the top by tadpoles with lower dip angles and slightly different azimuth directions. The tadpoles in the bar tail have a predominant azimuth with a dip angle varying cyclically from sub-horizontal to high angle to sub-horizontal again.

Through the OBO characterization of the Heterolithic Unit (H Unit), six facies associations were identified, namely supratidal flat (HFA 1), tidal point bar (HFA 2), intertidal sandbars (HFA 3), subtidal sandbars (HFA 4), hyperpycnite (HFA 5) and storm-dominated shoreface (HFA 6). Based on geometry and sand:mud ratios, the facies associations can be grouped into three types of reservoir geobody:

- (i) *Elongate geobodies* comprise intertidal sandbars (HFA 3) and subtidal sandbars (HFA 4), divided into proximal (HFA 4a) to distal assemblages (HFA 4b). Intertidal sandbars (HFA3) are up to 500 m in width and up to 2 m thick, characterized by the superposition of several sigmoidal cross-stratified, fine-grained sandstone sets (Lithofacies St) separated by mm-scale mud drapes. These reservoir geobodies show mm-scale mud drapes between the cross-bed sets, but these are not considered to be significant potential barriers to flow. Elongate reservoir geobodies comprising subtidal sandbars (HFA 4) are up to 350 m in width and up to 14 m thick although they are often amalgamated by lateral and vertical stacking to form sand prone packages with high-lateral continuity. These reservoir geobodies are characterized by fine to very coarse-grained sandstones (Lithofacies Sm, Sp, St and Sw) and locally by pebbly, coarse sand lags (Lithofacies Gm). In addition, this geobody becomes notably more heterolithic in a seaward direction (HFA4b), characterized by cross-stratified sand-mud couplets in tidal

bundles (Lithofacies Ht). This is reflected in the variation in sand:mud ratio, from proximal to distal (land- to seaward) zone of subtidal sandbar geobodies, from 60:40 to 40:60. Mud drapes in elongate geobodies characterized by HFA 4 also show a proximal to distal increase in thickness, varying from cm to dcm-scale respectively, generating potential flow baffles and barriers which become more significant in a seaward direction. In addition, the flooding surfaces, characterized by laminated to massive mudstones on bar tops, may also form significant barriers to flow between stacked bars, all of which is likely to contribute to reservoir compartmentalization. These geobodies show a similar shape and trend in the GR response, characterized by a smooth-egg shape and coarsening- to finning upward trend, in both intertidal (HFA 3) and subtidal (HFA 4) sandbar geobodies with the difference that the distal subtidal sandbar showed a smooth-cylindrical shape and aggradational GR response. Paleocurrents observed in dip tadpole logs showed bidirectional azimuths and low to high dip angles, although these are more common in distal subtidal sandbars (HFA 4b) and intertidal sandbars (HFA 3). In marked contrast, proximal subtidal sandbars (HFA 4a) predominantly show unidirectional, seaward-directed paleocurrents.

- (ii) *Asymmetric-sigmoidal geobodies*; composed of the deposits of tidal-dominated point bars (HFA 2), have a crescent shape in plan view and asymmetric-sigmoidal geometry in 2D cross section. Internally, these reservoir geobodies are characterized by a higher mud content under subtidal conditions, in comparison with those deposited under supratidal conditions. Under subtidal conditions, these geobodies, up to 10 m thick and up to 100 m in width, are characterized by the alternation of sand/mud layers (predominantly Lithofacies IHb and Wb). In contrast, geobodies deposited under supratidal conditions, up to 5 m thick and up to 75 m in width, are more sand-prone, characterized, principally by, Lithofacies Ht-St-Sr; although a significant proportion of cm-scale mud drapes also typically occur and would act as baffles or barriers to flow in subsurface examples. These asymmetric-sigmoidal geobodies are characterized in the GR by a smooth-egg shape and a coarsening- to fining upward trend, where these geobodies were deposited under supratidal conditions, and a smooth-cylindrical shape and aggradational GR response under subtidal conditions. Asymmetric-sigmoidal geobodies (HFA 2) are characterized by unidirectional azimuths and shallow-to-steep-to-shallow dip patterns.

- (iii) *Tabular geobodies* comprise hyperpycnite (HFA 5), storm-dominated shoreface deposits (HFA 6) or supratidal flat deposits (HFA 1). The tabular geobody, composed of

hyperpycnite deposits (HFA 5), forms an areally restricted body up to 0.5 m thick and 50 m in width, perpendicular to depositional dip, characterized by a sand:mud ratio of 90:10 and very fine, rippled sandstones (Lithofacies Swr-Sbcr-Spcr-Sicr). The tabular geobody, composed of storm-dominated shoreface deposits (HFA 6), is characterized by a sand:mud ratio of 80:20, and stacked storm beds comprising fine-grained sandstones dominated by Lithofacies HCS and Sw. Only the localised presence of thin mud-pebble layers, occurring at the base of stacked storm beds, could potentially act as minor baffles to flow within this otherwise homogeneous, well-connected sand geobody. In the subsurface, this geobody is characterized by smooth-cylindrical GR profile and an aggradational trend. Tabular geobodies, composed of facies association HFA 6, are characterized by poly-directional azimuths and planar to low-angle dip angles. In addition, supratidal flat deposits (HFA 1) also form a tabular geobody. In this case, they are mud prone packages, with sand:mud ratios between 10:90 and 0:100, up to 10 m thick and with more than 1 km of lateral continuity. This geobody is characterized, in GR, by high API values, a serrated-cylindrical shape and an aggradational trend.

A mixed tidally-dominated and wave-influenced delta system is proposed as a depositional model for the H Unit. However, processes related to relative sea-level change were also important in sequence evolution and in the development of coastal paleogeographies throughout deposition of the H Unit. In this case, by considering changes in relative sea level, most notably a significant intraformational fall in sea level (dividing Subunits 1 and 2 of H Unit) we are able to explain the development of a second coastal system within the H Unit; specifically a tide-dominated estuarine system characterized initially by storm-dominated shoreface and tidal-dominated point bar facies associations, infilling an incised valley.

It has also been a key aim of this Thesis to develop hypothetical reservoir modelling strategies based on the OBO characterization datasets, thereby reproducing, as far as possible, the observed distribution of heterogeneities in the interpreted geobodies. For this purpose, results obtained from the OBO characterization of the M-S Unit, characterized by high-sinuosity fluvial system, were selected for the reservoir modelling process. The integrated study of both outcrop and subsurface data, has successfully demonstrated the application of outcrop analogues as a basis for informing, designing and testing predictive tools for forecasting the reservoir architecture of high-sinuosity fluvial successions in the subsurface. A practical and repeatable modelling workflow, designed for this study, has successfully reproduced the distribution of heterogeneities interpreted within the M-S Unit at both geobody and lithofacies scales. Proof of this are the results obtained from MPS simulations, using as a mathematical

guide the patterns generated in a 3D training image, by applying the modelling workflows. The results of these MPS simulation show a good prediction of the channel geobody throughout the model framework, in agreement with the outcrop-derived paleogeographic reconstruction, even when considering a scenario in which only one well drilled the channel. MPS simulation results also showed mean match values ranging from 15% to 44%, depending on the scenario considered. In addition, these designed modelling workflows are potentially exportable to other examples of this type of reservoir, for the development of training images and/or directly for use in the reservoir facies modelling. In addition, an evaluation of the static reservoir connectivity in the M-S Unit was also undertaken with the aim of estimating how this may vary with well spacing, net-to-gross ratio and geobody type. Static reservoir connectivity results reveal the importance of including both point bar and crevasse-splay geobodies as they produce a significant increase in static reservoir connectivity at all well spacings. Crevasse-splay geobodies enhance static connectivity at all well spacings; understanding their volumetric significance and spatial distribution is therefore of critical importance in the modelling of low gradient, high sinuosity fluvial systems in the subsurface.

In conclusion, the multidisciplinary workflow developed in this Thesis highlights the importance of studies focused on the sedimentological characterization of outcrop analogues, as an effective approach to significantly improving our knowledge of sedimentary reservoirs. The integrated study of outcrop-derived and subsurface data, has allowed the generation of quantitative conceptual models useful in geostatistical modelling. This is especially so when planning modelling strategies as well as producing exportable 3D training images that can be used as input in the facies modelling process in real reservoirs using the MPS technique. In addition, recent technical advances in digital outcrop model characterization and data capture have proven to be effective tools, that not only allow us to extract valuable information from outcrops, but also leads to accurate uncertainty analysis of reservoir modelling results.

9.2. Recommendations for Future Work.

The methodological workflow designed for this Thesis (Outcrop/Behind Outcrop methodology) has proven to be effective for the characterization of outcrop analogs and their application in reservoir modelling; laying the foundations for future research in other outcrop analogs, both in other areas of the TIBEM and in other geological formations.

Upon completion of this research, it would also be of significant interest to apply the knowledge acquired to carry out a systematic study focused on the distribution of heterogeneity at micro-scale. Conceptual models generated through this research, as well as the detailed study of facies associations, would form the basis for a systematic and high-resolution sampling focused on petrology and petrophysics for studied examples. A study of this type would contribute to the determination of the relationships between depositional facies and both the nature and distribution of both micro-scale depositional and diagenetically-induced heterogeneities. Quantitative porosity and permeability data would be obtained, and the reservoir quality of each geobody would be established. A study of this type, published by Henares *et al.* (2016), focused on the channel and point bar geobodies from the M-S Unit, presented in this study. Extending this type of study to the crevasse-splay deposits would generate valuable data and insight into the importance of considering these geobodies as reservoirs and, consequently, the implications for Net to Gross estimations and reservoir connectivity. In addition, this study would provide the quantitative porosity and permeability data necessary to continue with the next phase of reservoir modelling process, the petrophysical and dynamic modelling of the M-S Unit.

Furthermore, such a detailed petrographic study, supported by chemostratigraphic data, would also provide mineralogical and geochemical data which should resolve the currently open question of the anomalously high GR responses been observed in wireline logs. Objectives for such an analysis would include the transition between the S Unit and H Unit, as well the intraformational incision surface (incised valley surface) located within the H Unit.

In addition to the extensive fieldwork and subsurface data characterizing the Heterolithic Unit (H Unit); a high-resolution study of the ichnology is also necessary in order to complete our understanding of the H Unit. This is especially so for the transition zone between S and H Units and in Facies Associations HFA 1 and HFA 2, locally characterised by a high bioturbation index. Such a study would provide highly relevant, additional data on paleoenvironmental conditions improving our understanding of the sub-environments

comprising the depositional system and/or provide a major input into the decision as to whether a delta, estuarine or combined system model is applicable, as a whole, or only partly to the H Unit in the studied area

Furthermore it is also of key importance that the issue of sequence stratigraphy be addressed for the H Unit, especially focussing on the transition between the S and H Units, as well as the intraformational incision surface (is this incision surface observed in other sections of the TIBEM? or, is it confined to the Alcaraz section?). Extending the knowledge gained during the high-resolution study presented in this Thesis, integrating outcrop and subsurface data, to selected areas of the TIBEM would answer these questions and allow us to establish a regional-scale high-order sequence stratigraphic framework for the H Unit.

It is also important to note that for this Thesis, reservoir modelling process was only carried-out for the M-S Unit. Extending the presented workflow, as well as designing specific modelling workflows that represent the distribution of geobodies and heterogeneities in both the S Unit and H Unit, would complete the reservoir model and establish modelling strategies for each lithostratigraphic unit of the studied succession. In addition, a library of modelling workflows and training images, for the interpreted depositional systems would be generated. This would be potentially exportable to the facies modelling process in real reservoirs, not just of high sinuosity, low Net to Gross fluvial systems, as demonstrated in this Thesis, but also high Net to Gross, low sinuosity, braided fluvial systems and complex, highly heterogenous coastal depositional systems dominated by both tides and wave action.

REFERENCES

Abatan, O., Kerr, D. and **Ramachandran, K.** (2013) Meandering Channel Facies Architecture Using Ground Penetrating Radar, Ferron Sandstone (Upper Cretaceous) Emery Co., Utah. *AAPG Search and Discovery Article, #41134.*

Abreu, V., Sullivan, M., Pirmez, C. and **Mohrig, D.** (2003) Lateral accretion packages (LAPs): an important reservoir element in deep water sinuous channels. *Mar. Petrol. Geol.*, **20**, 631-648.

Ainsworth, R. B. (2005) Sequence-stratigraphic–based analysis of reservoir connectivity: Influence of depositional architecture—A case study from a marginal marine depositional setting. *Petroleum Geoscience*, **11**, 257–276. DOI: 10.1144/1354-079304-638.

Ainsworth, R.B., Vakarelov, B.K., and **Nanson, R.A.** (2011) Dynamic spatial and temporal prediction of changes in depositional processes on clastic shorelines: toward improved subsurface uncertainty reduction and management. *AAPG Bull.*, **95**, 267–297.

Ajdukievwick, J.M. and **Lander, R.H.** (2010) Sandstone reservoir quality prediction: the state of the art. *AAPG Bull.*, **94**, 1083–1091.

Akaku, **K.** (2008) Numerical simulation of CO2 storage in aquifers without trapping structures. International Petroleum Technology Conference, 3–5 Dec. 2008, Kuala Lumpur, Malaysia, IPTC −12304-MS.

Alexander, J. (1993) A Discussion on the use of analogues for reservoir geology. In: Ashton, M. (ed.) *Advances in Reservoir Geology*. Geological Society, London, Special Publications, **69**, 175–194. DOI: 10.1144/GSL.SP.1993.069.01.08.

Allen, D.B. and **Pranter, M.J.** (2016) Geologically constrained electrofacies classification of fluvial deposits: an example from the Cretaceous Mesaverde Group, Uinta and Piceance basins. *AAPG Bull.*, **100**, 1775–1801.

Allen, **J.R.L.** (1963) The classification of cross-stratified units, with notes on their origin. *Sedimentology,* **2**, 93–114.

Allen, **J.R.L.** (1965) A review of the origin and characteristics of recent alluvial sediments. *Sedimentology*, **5**, 88–191.

Allen, **J.R.L.** (1979) Studies in fluviatile sedimentation: an elementary geometrical model for the connectedness of avulsion-related channel sand bodies. *Sed. Geol.*, **24**, 253–267.

Allen, **J.R.L.** (1983) Studies in fluviatile sedimentation: bars, bar-complexes and sandstone sheets (low-sinuosity braided streams) in the brownstones (L. Devonian), Welsh Borders. *Sed. Geol*., **33**, 237–293.

Alpay, O.A. (1972) A practical approach to defining reservoir heterogeneity. *Journal of Petroleum Technology*, **24**, 841–848.

Ambrose, W.A., **Lakshminarasimhan, S., Holtz, M.H., Núñez-López, V., Hovorka, S.D.** and **Duncan, I.** (2008) Geologic factors controlling CO2 storage capacity and permanence: case studies based on experience with heterogeneity in oil and gas reservoirs applied to CO2 storage. *Environ. Geol.*, **54**, 1619 − 1633.

Ambrose, W.A., Tyler, N. and **Parsley, M.J.** (1991) Facies heterogeneity, pay continuity and infill potential in barrier-island, fluvial and submarine-fan reservoirs: examples from the Texas Gulf Coast and

References

Midland Basin. In: *The Three- Dimensional Facies Architecture of Terrigenous Clastic Sediments and its Implications for Hydrocarbon Discovery and Recovery (*Eds Miall, A.D. and Tyler, N.*),* SEPM, Concepts in Sedimentology and Paleontology, **3**, 7–13.

Anderson, M.P. (1989) Hydrogeologic facies models to delineate large-scale spatial trends in glacial and glaciofluvial sediments. *Geol. Soc. Am. Bull.*, **4** (101), 501– 511. DOI: 10.1130/0016-7606(1989)101%3C0501:HFMTDL%3E2.3.CO;2.

Angiolini, L., Crippa, G., Muttoni, G. and Pignatti, J. (2013) Guadalupian (Middle Permian) paleobiogeography of the Neotethys Ocean. *Gondwana Research,* **24**, 173–184.

Arche, A. and López-Gómez, J. (1996) Origin of the Permian-Triassic Iberian Basin, central-eastern Spain. *Tectonophysics*, **266**, 443–464.

Arche, A. and López-Gómez, J. (2014) The Carnian Pluvial Event in Western Europe: new data from Iberia and correlation with the Western Neotethys and Eastern North America–NW Africa regions. *Earth Sci. Rev.*, **128**, 196–231.

Arche, A., López-Gómez, J. and García-Hidalgo, J.F. (2002) Control climático, tectónico y eustático en depósitos del Carniense (Triásico Superior) del SE de la Península Ibérica. *Journal of Iberian Geology*, **28**, 13-30.

Ashmore, P.E. (1982) Laboratory modelling of gravel braided stream morphology. *Earth Surface Processes and Landforms*, **7**, 201–225.

Ashworth, P.J., Sambrook Smith, G.H., Best, J.L., Bridge, J.S., lane, S.N., Lunt, I.A., Reesink, A.J.H., Simpson, C.J. and Thomas, R.T. (2011) Evolution and sedimentology of a channel fill in the sandy braided South Saskatchewan River and its comparison to the deposits of an adjacent compound bar. *Sedimentology*, **58**, 1860-1889. DOI: 10.1111/j.1365-3091.2011.01242.x.

Atkinson, C.D., McGowen, J.H., Bloch, S., Lundell, L.L. and Trumbly, P.N. (1990) Braidplain and deltaic reservoir, Prudhoe Bay Field, Alaska. In: *Sandstone Petroleum Reservoirs* (Eds Barwis, J.H., McPherson, J. G. and Studlick, J.R.J), pp. 205-224. Springer, Berlin.

Baouche, R., Sen, S., Debiane, K. and Ganguli, S.S. (2020) Integrated reservoir characterization of the Paleozoic and Mesozoic sandstones of the El Ouar field, Algeria. *Journal of Petroleum Science and Engineering*, **194**, 107551. DOI: 10.1016/j.petrol.2020.107551.

Barboza, S.A., Alway, R., Akpulat, T., Esch, W.L., Hicks, P.J. and Gerdes, M.L. (2009) Stochastic evaluation of fluvial to marginal marine sealing facies. *Marine and Petroleum Geology*, **26**, 445-456. DOI: 10.1016/j.marpetgeo.2009.01.013.

Bastante, F.G., Ordóñez, C., Taboada, J. and Matías, J.M. (2008) Comparison of indicator kriging, conditional indicator simulation and multiple-point statistics used to model slate deposits. *Engineering Geology*, **98**, 50-59.

Bataller, F.J., McDougall, N.D. and Moscariello, A. (2020) Reviewing the correlation potential of spectral gamma ray: A case study in Ordovician glacial environments in the Murzuq. *AAPG Bull. In Press.*

Bellian, J. A., Kerans, C. and Jennette, D. C. (2005) Digital Outcrop Models: Applications of terrestrial scanning LiDAR Technology in stratigraphic modeling. *Journal of Sedimentary Research*, **75**, 166-176.

Besems, R.E. (1981) Aspects of Middle and Late Triassic palynology. 1. Palynostratigraphical data from the Chiclana de Segura Formation of the Linares-Alcaraz region (SE Spain) and correlation with palynological assemblages from the Iberian Peninsula. *Rev. Paleobot. Palynol.*, **32**, 257–273.

Bezrukov, A. and Davletova, A. R. (2010) Implementation prospects of multi-point statistics methods into the practice of geological modeling: Society of Petroleum Engineers Russian Oil and Gas

Conference and Exhibition, 26–28 Oct., 2010, Moscow, Russia, SPE-135911-MS, 5. DOI: 10.2118/135911-MS.

Bjorlykke, K. and **Jahren, J. (**2010) Sandstones and sandstones reservoir. In: *Petroleum Geoscience – From Sedimentary Environments to Rock Physics* (Ed. Bjorlykke, H.), pp. 119-150. Springer, Berlin.

Blakey, R.C. and **Gubitosa, R.** (1984) Controls of sandstone body geometry and architecture in the Chinle formation (Upper Triassic), Colorado Plateau. *Sed. Geol.*, **38**, 51–86.

Bluck, B.J. (1976) Sedimentation in some Scottish rivers of low sinuosity. *Transactions of the Royal Society of Edinburgh – Earth Sciences*, **69**, 425–456.

Boucher, A. (2011) Strategies for Modeling with Multiple-point Simulation Algorithms, Closing the Gap: Advances in Applied Geomodeling for Hydrocarbon Reservoirs. *Canadian Society of Petroleum Geologists*, Calgary, 67–73.

Bowman, M.B.J. and **Smyth, H.R.** (2016) Reducing uncertainty and risk through field-based studies. In: *The Value of Outcrop Studies in Reducing Subsurface Uncertainty and Risk in Hydrocarbon Exploration and Production* (Eds Bowman, M., Smyth, H. R., Good, T. R., Passey, S. R., Hirst, J. P. P. & Jordan, C. J.), *Geological Society*, London, *Special Publications*, **436**, 1–8. DOI: 10.1144/SP436.13.

Boyd, R., Dalrymple, R.W. and **Zaitlin, B.A.** (1992) Classification of coastal sedimentary environments. *Sedimentary Geology*, **80**, 139–150.

Bradley, G., J. Redfern, D. Hodgetts, A. D. George, and **G. D. Wach**. (2018) The applicability of modern tidal analogues to pre-vegetation paralic depositional models. *Sedimentology*, **65**, N.6, 2171–2201. DOI: 10.1111/sed.12461.

Brayshaw, A.C., Davies, G.W. and **Corbett, P.W.M.** (1996) Depositional controls on primary permeability and porosity at the bedform scale in fluvial reservoir sandstone. In: *Advances in Fluvial Dynamics and Stratigraphy* (Eds Carling, P.A. & Dawson, M.R.), pp.374-394. Wiley, Chischester.

Brekke, H., **MacEachern, J.A.**, **Roenitz, T.** and **Dastgard, S.E.** (2017) The use of microresistivity image logs for facies interpretations: an example in point bar deposits of the McMurray Formation, Alberta, Canada. *AAPG Bull.*, **101**, 655–682.

Briant, I.D. (1983) Facies sequences associated with some braided river deposits of the Late Pleistocene age from southern Britain. *Int. Assoc. Sedimentol. Spec. Publ.*, **6**, 267–275.

Bridge, J.S. (1993) Description and interpretation of fluvial deposits: a critical perspective. *Sedimentology*, **40**, 801–810.

Bridge, J.S. (2001) Characterization of fluvial hydrocarbon reservoirs and aquifers: problems and solutions. *AAS Revista*, **8**, 87–114.

Bridge, J.S. (2003) *Rivers and Floodplains: Forms, Processes, and Sedimentary Record*, p.491. Blackwell Publishing, Malden.

Bridge, J.S. and **Lunt, I.A.** (2009) Depositional models of braided rivers. In: *Braided Rivers: Processes, Deposits, Ecology and Management* (Eds Sambrook Smith, G.H., Best, J.L., Bristow, C.S. and Petts, G.E.), *International Association of Sedimentologist, Special Publications*, **36**, 11–50.

Bridge, J.S. and **Tye, R.S.** (2000) Interpreting the dimensions of ancient fluvial channel bars, channels, and channel belts from wireline-logs and cores. *American Association of Petroleum Geologists Bulletin*, **84**, 1205–1228.

Bridge, J.S. and **Tye, R.S.** (2000) Interpreting the dimensions of ancient fluvial channel bars, channels, and channel belts from wireline-logs and cores. *AAPG Bull.*, **84**, 1205–1228.

References

Brierley, G.J. (1991) Bar sedimentology of the Squamish River, British Columbia: definition and application of morphostratigraphic units. *J. Sed. Petrol.*, **61**, 211–225.

Bristow, C.S., **Skelly, R.L.** and **Ethridge, F.G.** (1999) Crevasse splays from the rapidly aggrading, sand bed, braided Niobrara River, Nebraska: effect of base level rise. *Sedimentology*, **46**, 1029–1047.

Brookfield, M.E. (1998) The evolution of the great river systems of southern Asia during the Cenozoic India–Asia collision: rivers draining southwards. *Geomorphology*, **22**, 285–312.

Browne, G.H. and **Slatt, R.M.** (2002) Outcrop and behind-outcrop characterisation of a late Miocene slope fan system, Mt. Messenger Formation, New Zealand. *AAPG Bull.*, **86**, 841–862.

Bruguier, O., Becq-Giraudon, J.F., Champenois, M., Deloule, E., Ludden, J. and **Mangin, D.** (2003) Application of in situ geochronology and accessory phase chemistry to constraining basin development during post-collisional extension: a case study from the French Massif Central. *Chemical Geology*, **201**, 319–336.

Bryant, I. D. and **Flint, S. S.** (1993) Quantitative clastic reservoir geological modeling: problems and perspectives. In: *The Geological Modeling of Hydrocarbon Reservoirs and Outcrop Analogues* (Eds **Flint, S. S.** and **Bryant, I. D.**). *International Association of Sedimentologists, Special Publications*, **15**, 3–20.

Bryant, I. D., Carr, D., Cirilli, P., Drinkwater, N., McCormick, D., Tilke, P. and **Thurmond, J.** (2000) Use of 3D digital analogues as templates in reservoir modelling. *Petroleum Geoscience*, **6**, 195–201.

Buckley, S. J., Enge, H. D., Carlsson, C. and **Howell, J. A.** (2010) Terrestrial laser scanning for use in virtual outcrop geology. *The Photogrammetry Record*, **25**, 225-239.

Buckley, S., Howell, J., Enge, H. and **Kurz, T.** (2008). Terrestrial laser scanning in geology: data acquisition, processing and accuracy considerations. *Journal of the Geological Society*, **165** (3), 625–638.

Burns, C.E., **Mountney, N.P.**, **Hodgson, D.M.** and **Colombera, L.** (2017) Anatomy and dimensions of fluvial crevasse-splay deposits: examples from the Cretaceous Castlegate sandstone and Neslen formation, Utah, USA. *Sed. Geol.*, **351**, 21–35.

Burns, C.E., Mountney, N.P., Hodgson, D.M. and **Colombera, L.** (2017) Anatomy and dimensions of fluvial crevasse-splay deposits: examples from the Cretaceous Castlegate sandstone and Neslen formation, Utah, USA. *Sed. Geol.*, **351**, 21–35.

Cabello, P., Domínguez, D., Murillo-López, M. H., López-Blanco, M., García-Sellés, D., Cuevas, J. L., Marzo, M. and **Arbués, P.** (2018) From conventional outcrop datasets and digital outcrop models to flow simulation in the Pont de Montanyana point-bar deposits (Ypresian, Southern Pyrenees), *Marine and Petroleum Geology*, **94**, 19-42. DOI: 10.1016/j.marpetgeo.2018.03.040.

Cabello, P., Falivene, O., López-Blanco, M., Howell, J., Arbués, P. and **Ramos, E.** (2010) Modelling facies belt distribution in fan deltas coupling sequence stratigraphy and geostatistics: The Eocene Sant Llorenç del Munt example (Ebro foreland basin, NE Spain). *Marine and Petroleum Geology*, **27**, 254–272. DOI: 10.1016/j.marpetgeo.2009.08.009.

Calvache, M.L., Fernández, J., García-García, F., Soria, J.M. and **Viseras, C.** (2010) From the geomorphic process to basin architecture: anatomy of the infill of an alluvial–lacustrine system in southern Spain. *The Open Geology Journal*, **04**, 82–99.

Cameron, G., Collinson, J.D., Rider, M.H. and **Li, X.** (1993) Analogue dipmeter logs through a prograding deltaic sandbody. In: ASHTON, M. (ed.) *Advances in Reservoir Geology*. *Geological Society*, London, *Special Publications*, **169**, 195–217. DOI: 10.1144/GSL.SP.1993.069.01.09.

Cant, D.J. (1983) Subsurface sedimentology, *Geoscience Canada*, **10**, 115–121.

Cant, D.J. (2002) Subsurface facies analysis. *Geol. Surv. Can. Alberta*, **1**, 27–44.

Cant, D.J. and **Walker, R.G.** (1978) Fluvial processes and facies sequences in the sandy braided South Saskatchewan River, Canada. *Sedimentology*, **25**, 625–648.

Casas, A., Pinto, V. and **Rivero, L.** (2000) Fundamentals of ground penetrating radar in environmental and engineering applications, *Annali di Geofisica*, **43**, 1091-1103.

Cassinis, G., Durand, M. and **Ronchi, A.** (2003) Permian-Triassic continental sequences of Northwest Sardinia and South Provence: Stratigraphic correlations and palaeogeographical implications. *Bollettino della Società Geologica Italiana*, *Volume Speciale*, **2**, 119–129.

Clement, R., Hurst, A. R., Knarud, R. and **More, H.** (1990) A computer program for evaluation of fluvial reservoirs. In: *North Sea oil and gas reservoirs-II* (Eds A. T. Buller, E. Berg, O. Hjelmeland, J. Kleppe, O. Torsæter, and J. O. Aasen), pp.373-385. Springer Publishing.

Colombera, L., Mountney, N.P., Felletti, F. and **McCaffrey, W.D**. (2014) Models for guiding and ranking well-to-well correlations of channel bodies in fluvial reservoirs. *American Association of Petroleum Geologists Bulletin*, **98**, 1943–1965.

Colombera, L., Mountney, N.P., Howell, J.A., Rittersbacher, A., Felletti, F. and **McCaffrey, W.D.** (2016) A test of analog-based tools for quantitative prediction of large-scale fluvial architecture*. AAPG Bulletin*, **100** (2), 237–267. DOI: 10.1306/11181514227.

Colombera, L., Mountney, N.P., Medici, G. and **West, L.J.** (2019) The geometry of fluvial channel bodies: Empirical characterization and implications for object-based models of the subsurface. *AAPG Bulletin*, **103** (4), 905-929. DOI: 10.1306/10031817417.

Comunian, A., Renard, P.N. and **Straubhaar, J.** (2012. 3D multiple-point statistics simulation using 2D training images. *Computer Geoscience*, **40**, 49–65. DOI: 10.1016/j.cageo.2011.07.009.

Corbeanu, R.M., Soegaard, K., Szerbiak, R.B., Thurmond J., McMechan G., Wang D., Snelgrove S., Forster, C. and **Menitove, A.** (2001) Detailed internal architecture of a fluvial channel sandstone determined from outcrop, cores, and 3-D groundpenetrating radar: example from the middle Cretaceous Ferron Sandstone, east-central Utah. *AAPG Bulletin*, **85** (9), 1583–1608.

Corbett, P.W.M. and **Potter, D.K**. (2004) Petrotyping: a base map and atlas for navigating through permeability and porosity data for reservoir comparison and permeability prediction. In: *International Symposium of the Society of Core Analysts*, Abu Dhabi, UAE. **30**, pp. 385–396. SCA Papers.

Cortesogno, L., Cassinis, G., Dallagiovanna, G., Gaggero, L., Oggiano, G., Ronchi, A., Seno, S. and **Vanossi, M.** (1998) The Variscan post-collisional volcanismin Late Carboniferous – Permian sequences of Ligurian Alps, Southern Alps and Sardinia Italy: a synthesis. *Lithos*, **45**, 305–328.

Coughenour, Ch. L., Archer, A.W. and **Lacovara, K.** (2009) Tides, tidalites and secular changes in the Earth-Moon system. *Earth-Science Reviews*, **97**, 59-79

Dabrio, C., Fernández, J. and **Viseras, C.** (2005) Triassic fluvial sandstones (central south Spain) – an excellent analogue for the TAGI reservoir of Algeria. *In: 67th European Association of Geoscientists and Engineers Conference and Exhibition.* Field Trip Guide incorporating SPEEUROPEC 2005, 13–16 June 2005, IFEMA, Madrid, Spain.

Dabrio, C., **Fernández, J.** and **Viseras, C.** (2005) Triassic fluvial sandstones (Central South Spain) – an excellent analogue for the TAGI Reservoir of Algeria, European Association of Geoscientists and Engineers. *67th EAGE Conference and Exhibition, Field Trip Guides* 1, Van Houten (Holanda), 35 p.

References

Dabrio, C.J. and Fernández, J. (1986) Evolución del estilo aluvial en el Triásico de Alcaraz (Albacete). *Cuadernos de Geología Ibérica*, **10**, 173–206.

Dallagiovanna, G., Gaggero, L., Maino, M., Seno, S. and Tiepolo, M. (2009) U-Pb zircon ages for post-Variscan volcanism in the Ligurian Alps (Northern Italy). *Journal of Geological Society of London*, 166, 101–114.

Dalrymple, R. W. and Choi, K. (2007) Morphologic and facies trends through the fluvial–marine transition in tide-dominated depositional systems: A schematic framework for environmental and sequence-stratigraphic interpretation. *Earth-Science Reviews*, **81**, 135-174. DOI: 10.1016/j.earscirev.2006.10.002.

Dalrymple, R.W., Zaitlin, B.A. and Boyd, R. (1992) Estuarine facies models: conceptual basis and stratigraphic implications. *Journal of Sedimentary Petrology*, **62**, 1130–1146.

Daly, C. and Caers, J. (2010) Multi-point geostatistics – An introductory overview. *First Break*, **28**, 39–47. DOI: 10.3997/1365-2397.2010020

Davis, J.M., Wilson, J.L., Phillips, F.M., and Gotkowitz, M.B. (1997) Relationship between fluvial bounding surfaces and the permeability correlation structure. *Water Resour. Res.*, **33** (8), 1843–1854. DOI: 10.1029/97WR01003.

Davis, R.A. and Dalrymple, R.W., Eds (2012). *Principles of tidal sedimentology,* pp. 621. Springer.

Decarlis, A., Dallagiovanna, G., Lualdi, A., Maino, M.and Seno, S. (2013) Stratigraphic evolution in the Ligurian Alps between Variscan heritages and the Alpine Tethys opening: A review. *Earth-Science Reviews*, **125**, 43–68.

Dell'Arciprete, D., Bersezio, R., Felletti, F., Giudici, M., Comunian, A. and Renard, P. (2011) Comparison of three geostatistical methods for hydrofacies simulation: a test on alluvial sediments. *Hydrogeology Journal*. DOI: 10.1007/s10040-011-0808-0.

Deng, H., Stauffer, P.H., Dai, Z., Jiao, Z. and Surdam, R.C. (2012) Simulation of industrial-scale CO2 storage: multi-scale heterogeneity and its impacts on storage capacity, injectivity and leakage. *Int. J. Greenh. Gas Control*, **10**, 397–418.

Deutsch, C. V. (2002) *Geostatistical Reservoir Modelling: Applied Geostatistics Series*. Oxford University Press, New York.

Deveugle, P.E.K., Jackson, M.D., Hampson, G.J., Stewart, J., Clough, M.D., Ehighebolo, T., Farrell, M.E., Calvert, C.S. and Miller, J.K. (2014) A comparative study of reservoir modeling techniques and their impact on predicted performance of fluvial-dominated deltaic reservoirs. *AAPG Bulletin*, v. **98**, 729-763. DOI: 10.1306/08281313035.

Dimitrakopoulos, R., Mustapha, H. and Gloaguen, E. (2010) High-order statistics of spatial random fields: exploring spatial cumulants for modeling complex non-Gaussian and non-linear phenomena. *Math. Geosci.*, **42** (1), 65–99. DOI: 10.1007/s11004-009-9258-9.

Donovan, J. and Lebaron, A. (2009) A comparison of photogrammetry and laser scanning for the purpose of automated rock mass characterization. Presented at *the 43rd U.S. Rock Mechanics Symposium & 4th U.S.–Canada Rock Mechanics Symposium*. American Rock Mechanics Association.

Donselaar, M. E., and Overeem, I. (2008) Connectivity of fluvial point-bar deposits: An example from the Miocene Huesca fluvial fan, Ebro Basin, Spain: *AAPG Bulletin*, **92**, 1109–1129. DOI: 10.1306/04180807079.

Donselaar, M.E. and Schmidt, J.M. (2005) Integration of outcrop and borehole image logs for high-resolution facies interpretation: example from a fluvial fan in the Ebro Basin, Spain. *Sedimentology*, **52**, 1021–1042.

Driese, S.G., **Mora, C.I**., **Stiles, C.A.**, **Joeckel, R.M.** and **Nordt, L.C.** (2000) Mass-balance reconstruction of a modern Vertisol: implications for interpreting the geochemistry and burial alteration of paleo-Vertisols. *Geoderma*, **95**, 179–204.

Druguet, E., Castro, A., Chichorro, M., Pereira, M.F. and **Fernández, C.** (2014) Zircon geochronology of intrusive rocks from Cap de Creus, Eastern Pyrenes. *Geological Magazine*, **151** (6), 1095–1114. DOI: 10.1017/s0016756814000041.

Dueck, R.N. and **Paauwe, E.F.**W. (1994) The use of borehole imaging techniques in the exploration for stratigraphic traps: an example from the Middle Devonian Gilwood channels in north-central Alberta. *Bulletin of Canadian. Petroleum Geologists*, **42**, 137–154.

Duke, W.L., Arnott, R.W.C. and **Cheel, R.J.** (1991) Shelf sandstones and hummocky cross-stratification: New insights on a storm debate. *Geology*, **19**, 625–628.

Duncan, I. (2008) Geologic factors controlling CO2 storage capacity and permanence: case studies based on experience with heterogeneity in oil and gas reservoirs applied to CO2 storage. *Environ. Geol.*, **54**, 1619–1633.

Durkin, P.R., **Boyd, R.L.**, **Hubbard, S.M.**, **Schultz, A.W.** and **Blum, M.D.** (2017) Three-dimensional reconstruction of meander-belt evolution, Cretaceous McMurray Formation, Alberta Foreland Basin, Canada. *J. Sed. Res.*, **87**, 1075–1099.

Einsele, G. (2000) *Sedimentary Basins. Evolution, Facies, and Sediment Budget*. 2nd edn. Springer, Berlin.

Embry, A. (2009) *Practical sequence stratigraphy*, pp. 79. Canadian Society of Petroleum Geologists, Canada.

Emery, D. and **Myers, K.J.** (1996) *Sequence Stratigraphy,* pp. 297. Blackwell, Oxford, UK.

Enge, H.E., Buckley, S.J., Rotevatn, A. and **Howell, J.A.** (2007). From outcrop to reservoir simulation model: Workflow and procedures. *Geosphere*, **3**, 469-490. DOI: 10.1130/GES00099.1.

Fabuel-Pérez, I., Redfern, J. and **Hodgetts, D.** (2009) Sedimentology of an intra-montane rift-controlled fluvial dominated succession: The Upper Triassic Oukaimeden Sandstone Formation, Central High Atlas, Morocco. *Sedimentary Geology*, **218**, 103-140

Falivene, O., Cabrera, L., Muñoz, J.A., Arbués, P., Fernández, O. and **Sáez, A.** (2007) Statistical grid-based facies reconstruction and modelling for sedimentary bodies. Alluvial-palustrine and turbiditic examples. *Geologica Acta*, **5** (3), 199-230.

Faure, M. and **Pons, J.** (1991) Crustal thinning recorded by the shape of the Namurian-Wesphalian leucogranite in the Variscan Belt of the northwest Massif Central, France. *Geology*, **19**, 730–733.

Faure, M., Monié, P., Pin, C., Maluski, H. and **Leloix, C.** (2002) Late Visean thermal event in the northern part of the French Massif Central: new ^{40}Ar/^{39}Ar and Rb–Sr isotopic constraints on the Hercynian syn-orogenic extension. International Journal of Earth Sciences, **91**, 53–75.

Feldman, H. and **Demko, T**. (2015) Recognition and prediction of petroleum reservoirs in the fluvial/tidal transition. In: *Fluvial-Tidal Sedimentology: Developments in Sedimentology* (Eds Philip J. Ashworth, James L. Best and Daniel R. Parsons), **68**, 483-528. DOI: 10.1016/B978-0-444-63529-7.00014-6.

Fenn, C. and **Pranter, M.** (2014) Outcrop to subsurface reservoir characterization of the Lower Mesaverde Group, Red Wash Field, Uinta Basin and Douglas Ceek Arch, Utah and Colorado. *AAPG Annual Convention and Exhibition*, Houston, Texas, April 6-9. *Search and Discovery Article*, *#50995*.

References

Fernández J., **Dabrio, C.** and **Pérez-López, A.** (1994) El Triásico de la región de Siles Alcaraz (Cordillera Bética). In: *III Coloquio Estratigrafía Paleogeografía del Pérmico y Triásico de España. Field Guide.* (Ed. A. Arche). Cuenca, Spain.

Fernández, J. (1977) Sedimentación triásica en el borde Sureste de la Meseta. PhD dissertation, Universidad de Granada, 173 pp.

Fernández, J. and **Dabrio, C.** (1985) Fluvial architecture of the Buntsandstein-facies redbeds in the Middle to Upper Triassic (Ldinian–Norian) of the southeastern edge of the Iberian Meseta (southern Spain). In: *Aspects of Fluvial Sedimentation in the Lower Triassic Buntsandstein of Europe* (Ed. D. Mader). Lecture Notes in Earth Sciences, **4**, 411–435.

Fernández, J. and **Gil, A.** (1989) Interpretación sedimentaria de los materiales triásicos de facies Buntsandstein en las Zonas Externas de las Cordilleras Béticas y en la Cobertura Tabular de la Meseta. España. *Revista de la Sociedad Geológica de España*, **2**, 114-124.

Fernández, J. and **Pérez-López, A.** (2004) Triásico de la Cordillera Bética y Baleares. In: *Geología de España* (Ed. J.A. Vera), pp. 365-366, SGE-IGME, Madrid.

Fernández, J., Dabrio, C.J. and **Viseras, C.** (2005) Triassic fluvial sandstones (Central South Spain) – an excellent Analogue for the TAGI reservoir of Algeria. *In*: *67th European Association of Geoscientists and Engineers Conference and Exhibition*, Field Trip Guide.

Fernández, J., Viseras, C. and **Dabrio, C.** (2005) Triassic fluvial sandstones (Central South Spain): an excellent analogue for the TAGI reservoir of Algeria. In: *67th European Association of Geoscientists and Engineers* (Eds J. Fernández, C. Viseras and C. Dabrio), pp. 18. Field Guide F1.

Fernández-Suárez, J., Dunning, G.R., Jenner, G.A. and **Gutiérrez-Alonso, G.** (2000) Variscan collisional magmatism and deformation in NW Iberia: constraints from U–Pb geochronology of granitoids. Journal of the Geological Society of London, **157**, 565–576.

Fielding, C.R. and **Crane, R.C.** (1987) An application of statistical modelling to the prediction of hydrocarbon recovery factors in fluvial reservoir sequences. In: *Recent Developments in Fluvial Sedimentology* (Eds F.G. Ethridge, R.M. Flore and M.D. Harvey), *SEPM Special Publication*, **39**, 321–327.

Ford, G.L. and **Pyles, D.R.** (2014) A hierarchical approach for evaluating fluvial systems: architectural analysis and sequential evolution of the high net-sand content, middle Wasatch Formation, Uinta Basin, Utah. *AAPG Bulletin*, **98**, 1273–1304.

Franke, D., Hornung, J. and **HInderer, M.** (2015) A combined study of radar facies, lithofacies and threedimensional architecture of an alpine alluvial fan (Illgraben fan, Switzerland). *Sedimentology*, **62**, 57–86.

García-García, F., Yeste, L.M., Henares, S. and **Viseras, C.** (2017) Tides and waves influence variability on the shoreline systems of the heterolithic unit from the Triassic Tabular Cover of the Iberian Meseta. 33rd IAS Meeting of Sedimentology, 10-12 Oct 2017, Toulouse - France.

Gaud, M.N., Smith, G.A., and **McKenna, S.A.,** (2004) Relating small-scale permeability heterogeneity to Lithofacies distribution. In: *Aquifer Characterization* (Eds J. Bridge and D.W. Hyndman). *SEPM, Special Publication*, **80**, 55–66.

Gay, S.P. (1989) Gravitational compaction, a neglected mechanism in structural and stratigraphic studies: new evidence from Mid-Continent, USA. *American Association of Petroleum Geologists Bulletin*, **73**, 641–657.

GEODE (2020)**.** Mapa Geológico Digital continuo de España. Retrieved from http://mapas.igme.es/gis/rest/services/Cartografia_Geologica/IGME_Geode_50/MapServer.

Ghinassi, M. (2011) Chute channels in the Holocene high-sinuosity river deposits of the Firenze plain, Tuscany, Italy. *Sedimentology*, **58**, 618–642.

Ghinassi, M., Nemec, W., Aldinucci, M., Nehyba, S., Özaksoy, V. and **Fidolini, F.** (2014) Planform evolution of ancient meandering rivers reconstructed from longitudinal outcrop sections. *Sedimentology*, **61**, 952–977.

Gil-Ortiz, M., McDougall, N.D., Cabello, P., Marzo, M. and **Ramos, E.** (2019) Sedimentology of a "nonactualistic" Middle Ordovician tidal-influenced reservoir in the Murzuq Basin (Libya). *AAPG Bulletin*, **103**, N.9, 2219–2246. DOI: 10.1306/02151918138.

Gil-Ortiz, M., **Tur, N**., **García, D**., **Leandro, F**., **Jiménez, A**., **Ochoa, M**., **Net, L.I.**, **Fernández, O**., **Manrique, C**., **García, V** and **Macarena, N.** (2019) Sedimentology of pre-salt clastic reservoirs in the South Gabon sub-basin with image log tools. 34th IAS Meeting of Sedimentology, 10–13 Sep 2019, Rome, Italy.

Gottschalk, I. P., Hermans, T., Knight, R., Caers, J., Cameron, D. A., Regnery, J. and **McCray, J. E.** (2017) Integrating non colocated well and geophysical data to capture subsurface heterogeneity at an aquifer recharge and recovery site. *Journal of Hydrology*, **555**, 407–419, DOI: 10.1016/j.jhydrol.2017.10.028.

Gouw, M.J.P. and **Berendsen, H.J.A.** (2007) Variability of channel belt dimensions and the consequences for alluvial architecture: observations from the Holocene Rhine-Meuse delta (The Netherlands) and Lower Mississippi Valley (USA). *J. Sed. Res.*, **77**, 124–138.

Goy, A. and **Yébenes, A.** (1977) Características, extensión y edad de la formación Dolomías tableadas de Imón. *Cuadernos de Geología Ibérica*, **4**, 375-384.

Grammer, G. M., Harris, P. M. and **Eberli, G. P.** (2004) Integration of outcrop and modern analogs in reservoir modelling. *American Association of Petroleum Geologists*, *Memoirs*, **80**, 1–22.

Guardiano, F. and **Srivastava, R.** (1993) Multivariate geostatistics: Beyond bivariate moments. In: *Geostatistics Troia '92. Quantitative Geology and Geostadistics* (Ed. A. Soares), **5**, 133-144. Springer, Dordrecht.

Gulliford, A.R., **Flint, S.S.** and **Hodgson, D.M.** (2017) Crevasse splay processes and deposits in an ancient distributive fluvial system: the lower Beaufort Group, South Africa. *Sed. Geol.*, **358**, 1–18.

Gutiérrez-Alonso, G., Fernández-Suárez, J., Jeffries, T.E., Johnston, ST., Pastor-Galán, D., Murphy, J.B., Franco, M.P. and **Gonzalo, J.C.** (2011) Diachronous post-orogenic magmatism within a developing orocline in Iberia, European Variscides. *Tectonics*, **30**(5). DOI: 10.1029/2010TC002845.

Haneberg, W.C. (2008) Using close range terrestrial digital photogrammetry for 3-D rock slope modelling and discontinuity mapping in the United States. *Bulletin of Engineering Geology and the Environment*, **67**, 457–469.

Harris, P. T., Heap, A.D., Bryce, S. M., Porter-Smith, R., Ryan, D.A., and **Heggie, D.T.** (2002) Classification of Australian clastic coastal depositional environments based upon a quantitative analysis of wave, tidal, and river power. *Journal of Sedimentary Research*, **72** (6), 858–870. DOI: 10.1306/040902720858.

Henares, S., **Arribas, J**., **Cultrone, G.** and **Viseras, C.** (2016a) Muddy and dolomitic rip-up clasts in Triassic fluvial sandstones: origin and impact on potential reservoir properties (Argana Basin, Morocco). *Sed. Geol.*, **339**, 218–233.

References

Henares, S., Caracciolo, L., Cultrone, G., Fernández, J. and Viseras, C. (2014) The role of diagenesis and depositional facies on pore system evolution in a Triassic outcrop analogue (SE Spain). *Mar. Petrol. Geol.*, **51**, 136–151.

Henares, S., Caracciolo, L., Viseras, C., Fernández, J. and Yeste, L.M. (2016b) Diagenetic constraints on heterogeneous reservoir quality assessment: a Triassic outcrop analogue of meandering fluvial reservoirs. AAPG Bull., **100** (9), 1377–1398.

Henares, S., Viseras, C., Fernández, J., Pla-Pueyo, S. and Cultrone, G. (2011) Triassic Red Beds in SE Spain: evaluation as potential reservoir rocks based on a preliminary petrological study. *American Association of Petroleum Geologists Search and Discovery Article*, #50541.

Hill, P.R., Meulé, S. and Longuépée, H., (2003) Combined flow processes and sedimentary structures on the shoreface of the wave-dominated Grande-Rivière-de-la-Baleine-delta. J. Sed. Res., **73**, 217–226.

Hodgetts, D. (2013) Laser scanning and digital outcrop geology in the petroleum industry: A review. *Marine and Petroleum Geology*, **46**, 335-354. DOI: 10.1016/j.marpetgeo.2013.02.014.

Holden, L., Hauge, R., Skare, O. and Skorstad A. (1998) Modeling of fluvial reservoirs with object models. *Mathematical Geology,* **30**, 473-496.

Hovadik, J. M. and Larue, D.K. (2007) Static characterizations of reservoirs: Refining the concepts of connectivity and continuity: *Petroleum Geoscience*, **13**, 195–211. DOI: 10.1144/1354-079305-697.

Howell, J.A., Martinius, A.W. and Good, T.R. (2014) The application of outcrop analogues in geological modelling: a review, present status and future outlook. In: *Sediment-Body Geometry and Heterogeneity: Analogue Studies for Modelling the Subsurface* (Eds A.W. Martinius, J.A. Howell and T. R. Good), *Geological Society*, London, *Special Publications*, **387**, 1-25. DOI: 10.1144/SP387.12.

Hubbard, S.M., De Ruig, M.J. and Graham, S.A. (2009) Confined channel-levee complex development in an elongate depo-center: Deep-water Tertiary strata of Austrian Molasse basin. *Marine and Petroleum Geology*, **26**, 85-112.

Hubbard, S.M., Smith, D.G., Nielsen, H., Leckie, D.A., Fustic, M., Spencer, R.J. and Bloom, L. (2011) Seismic geomorphology and sedimentology of a tidally influenced river deposit, Lower Cretaceous Athabasca oil sands, Alberta, Canada. *AAPG Bull*., **95**, 1123–1145.

Hugenholtz, C. H., Paulen, R.C. and Wolfe S.A. (2007) Ground-penetrating-radar investigation of relict channel bars of the Meander River spillway, northern Alberta. *Geological Survey of Canada*, Current Research 2007-A1, 10 p.

Hunter, R.E. and Clifton, H.E. (1982) Cyclic deposits and hummocky cross-stratification of probable storm origin in Upper Cretaceous rocks of the Cape Sebastian area, southwestern Oregon. *J. Sed. Petrol.*, **52**, 0127–0143.

Ichaso, A.A. and Dalrymple, W. (2014) Eustatic, tectonic and climatic controls on an early syn-rift mixed-energy delta, Tilje Formation (Early Jurassic, Smørbukk field, offshore mid-Norway). In: *Depositional Systems to Sedimentary Successions on the Norwegian Continental Margin* (Eds A. W. Martinius, R. Ravnås, J.A. Howell, R. J. Steel and J.P. Wonham), 1st edn. *IAS Special Publications*, **46**, 339-388.

Ielpi, A. and Ghinassi, M. (2014) Planform architecture, stratigraphic signature and morphodynamics of an exhumed Jurassic meander plain (Scalby Formation, Yorkshire, UK). *Sedimentology*, **61**, 1923–1960.

Ielpi, A. and **Ghinassl, M.** (2015) Planview style and palaeodrainage of Torridonian channel belts: Applecross Formation, Stoer Peninsula, Scotland. *Sedimentary Geology*, **325**, 1–16.

Ielpi, A., **Fralick, P.**, **Ventra, D.**, **Ghinassi, M.**, **Lebeau, L.E.**, **Marconato, A.**, **Meek, R.** and **Rainbird, R.** (2018) Fluvial floodplains prior to greening of the continents: stratigraphic record, geodynamic setting and modern analogues. *Sed. Geol.*, **372**, 140–172.

Isaaks, E.H. and **Srivastava, R. M.,** 1989. Applied geostatistics (Vol. 2). New York: Oxford University Press, 561 pp.

Jenson, M.A. and **Pedersen, G.K.** (2010) Architecture of vertically stacked fluvial deposits, Atane formation, Cretaceous, Nuussuaq, centralWest Greenland. *Sedimentology*, **57**, 1280–1314.

Jordan, D.W. and **Pryor, W.A.** (1992) Hierarchical levels of heterogeneity in a Mississippi River meander belt and application to reservoir systems. *AAPG Bull.*, **76**, 1601–1624.

Keeton, G.I., **Pranter, M.J.**, **Cole, R.D.** and **Gustason, E.R.** (2015) Stratigraphic architecture of fluvial deposits from borehole images, spectral-gamma-ray response, and outcrop analogs, Piceance Basin, Colorado. *AAPG Bull.*, **99**, 1929–1956.

King, P. R. (1990) The connectivity and conductivity of overlapping sand bodies, In: *North Sea oil and gas reservoirs—II* (Eds Buller, A.T. et al.), pp. 353-362, Graham and Trotman, London.

Klausen, T.G. and Mork, A. (2014) The Upper Triassic paralic deposits of the De Geerdalen Formation on Hopen: outcrop analog to the subsurface Snadd Formation in the Barents Sea. *AAPG Bull.*, **98**, 1911–1941.

Klein, G. de V. and **Marsaglia, K.M.** (1987) Hummocky cross-stratification, tropical hurricanes and intense winter storms. *Sedimentology*, **34**, 333–359.

Klein, G.D. (1970) Tidal origin of a Precambrian quartzite – the Lower Fine-grained Quartzite (Middle Dalradian) of Islay. Scotland. *Journal of Sedimentary Petrology*, **40**, 973-985.

Klingbeil, R., Kleineidam, S., Asprion, U., Aigner, T. and **Teutsch, G.** (1999) Relating Lithofacies to hydrofacies: outcrop-based hydrogeological characterization of quaternary gravel deposits. *Sediment. Geol.,* **129** (3–4), 299–310. DOI: 10.1016/S0037-0738(99)00067-6.

Kokureck, G., Knight, J. and **Havholm, K.** (1991) Outcrop of semi-regional threedimensional architecture and reconstruction of a portion of the eolian Page Sandstone (Jurassic). In: *The Three-Dimensional Facies Architecture of Terrigenous Clastic Sediments and Its Implications for Hydrocarbon Discovery and Recovery* (Eds A.D. Miall and N. Tyler). *SEPM, Concepts in Sedimentology and Paleontology*, Tulsa, **3**, 25–43.

Koltermann, C.E. and **Gorelick, S.M.** (1996) Heterogeneity in sedimentary deposits: a review of structure-imitating, process-imitating, and descriptive approaches. *Water Resour. Res.*, **32** (9), 2617–2658. DOI: 10.1029/96WR00025.

Kostic B. and **Aigner T.** (2007) Sedimentary architecture and 3D ground-penetrating radar analysis of gravelly meandering river deposits (Neckar Valley, SW Germany). *Sedimentology*, **54**, 789–808.

Kraus, M.J. and **Aslan, A.** (1999) Paleosol sequences in floodplain environments: a hierarchical approach. In: *Palaeoweathering, Palaeosurfaces and Related Continental Deposits* (Ed. M. Thiry), IAS Special Publication, **27**, 303– 321.

Krum, G. L. and **Johnson, C. R.** (1993) A 3-D modelling approach for providing a complex reservoir descriptions for reservoir simulations. In: *The Geological Modelling of Hydrocarbon Reservoirs and Outcrop Analogues* (Eds S. S. Flint and I.D. Bryant). *International Association of Sedimentologists, Special Publications*, **15**, 253–258.

References

Lai, J., **Wang, G.**, **Wang, S.**, **Cao, J.**, **Li, M.**, **Pang, X.**, **Han, C.**, **Fan, X.**, **Yang, L.**, **He, Z.** and **Qin, Z.** (2018) A review on the applications of image logs in structural analysis and sedimentary characterization. *Mar. Petrol. Geol.*, **95**, 139–166.

Larue, D. K. and **Hovadik, J.** (2006) Connectivity of channelized reservoirs; a modelling approach. *Petroleum Geoscience*, **12**, 291–308.

Legarreta, L., **Uliana, M.A.**, **Larotonda, C.A.** and **Meconi, G.R.** (1993) Approaches to nonmarine sequence stratigraphy-theoretical models and examples from Argentine basins. *Collection Colloques et Seminaires –Institut Francais du Petrole*, **51**, 125–144.

Leleu, S., Hartley, A.J. and **Williams, B.P.J.** (2009) Largescale alluvial architecture and correlation in a Triassic pebbly braided river system, Lower Wolfville Formation (Fundy Basin, Nova Scotia, Canada). *Journal of Sedimentary Research*, **79**, 265–286.

Leuven, J.R.F.W., Kleinhans, M.G., Weisscher, S.A.H. and **Van der Vegt, M.** (2016) Tidal sand bar dimensions and shapes in estuaries. *Earth-Science Reviews*, **161**, 204-223. DOI: 10.1016/j.earscirev.2016.08.004.

Li, J. and **Bristow, C.** (2015) Crevasse splay morphodynamics in a dryland river terminus: Río Colorado in Salar de Uyuni Bolivia. *Quatern. Int.*, **377**, 71–82.

Li, J., **Donselaar, M.**, **Enayat Hosseini Aria, S.**, **Koenders, R.** and **Oyen, A.M.** (2014) Landsat imagery-based visualization of the geomorphological development at the terminus of a dryland river system. *Quatern. Int.*, **352**, 100–110.

Long, D.G.F. (2006) Architecture of pre-vegetation sandybraided perennial and ephemeral river deposits in the Paleoproterozoic Athabasca Group, northern Saskatchewan, Canada as indicators of Precambrian fluvial style. *Sedimentary Geology*, **190**, 71–95.

Longhitano, S.G. (2011) The record of tidal cycles in mixed silici-bioclastic deposits: examples from small Plio-Pleistocene peripheral basins of the microtidal Central Mediterranean Sea. *Sedimentology*, **58**, 691-719. DOI: 10.1111/j.1365-3091.2010.01179.x.

Longhitano, S.G., Mellere, D.M., Stell, R.J. and **Ainsworth, R.B.** (2012) Tidal depositional systems in the rock record: A review and new insights. *Sedimentary Geology*, **279**, 2-22. DOI: 10.1016/j.sedgeo.2012.03.024.

López Garrido, A.C. (1971) Geología de la Zona Prebética al NE de la Provincia de Jaén. PhD dissertion, Universidad de Granada, 371 pp.

López-Gómez, J., Alonso-Azcárate, J., Arche, A., Arribas, J., Fernández Barrenechea, J., Borruel-Abadía, V., Bourquin, S., Cadenas, P., Cuevas, J., De la Horra, R., Bienvenido Díez, J., Escudero-Mozo, M.J., Fernández-Viejo, G., Galán-Abellán, B., Galé, C., Gaspar-Escribano, J., Gisbert Aguilar, J., Gómez-Gras, D., Goy, A., Gretter, N., Heredia Carballo, N., Lago, M., Lloret, J., Luque, J., Márquez, L., Márquez-Aliaga, A., Martín-Algarra, M., Martín-Chivelet, J., Martín-González, F., Marzo, M., Mercedes-Martín, R., Ortí, F., Pérez-López, A., Pérez-Valera, F., Pérez-Valera, J.A., Plasencia, P., Ramos, E., Rodríguez-Méndez, L., Ronchi, A., Salas, R., Sánchez-Fernández, D., Sánchez-Moya, Y., Sopeña, A., Suárez-Rodríguez, A., Tubía, J.M., Ubide, T., Valero Garcés, B., Vargas, H., and **Viseras, C.** (2019). Permian-Triassic Rifting Stage. In: *The Geology of Iberia: A Geodynamic Approach* (Eds C., Quesada, and J. Tomás Oliveira). Springer. DOI: 10.1007/978-3-030-11295-0.

Lunt, I.A., Smith, G.H.S., Best, J.L., Ashworth, P.J., Lane, S.N. and **Simpson, C.J.** (2013) Deposits of the sandy braided South Saskatchewan River: implications for the use of modern analogs in reconstructing channel dimensions in reservoir characterization. *American Association of Petroleum Geologists Bulletin*, **97**, 553–576.

Ma, Y.Z. (2019) *Quantitative Geosciences: Data Analytics, Geostatistics, Reservoir Characterization and Modeling*, pp.664. Springer. ISBN 978-3-030-17859-8.

Maino, M., Dallagiovanna, G., Gaggero, L., Seno, S. and **Tiepolo, M.** (2012) U-Pb zircon geo-chronological and petrographic constraints on late to post-collisional Variscan magmatism and metamorphism in the Ligurian Alps, Italy. *Geological Journal*, **47**, 632–652.

Mariethoz, G. and **Caers, J.** (2015) *Multiple-point geostatistics*, pp. 376. Wiley Blackwell. ISBN: 978-1-118-66275-5.

Márquez-Aliaga, A. and **Ros, S.** (2003) Associations of bivalves of Iberian Peninsula (Spain): Ladinian. **Albertiana**, **28**, 85–89.

Martin, Y. and **Church, M.** (1996) Bed-material transport estimated from channel surveys – Vedder River, British Columbia. *Earth Surface Processes and Landforms*, **20**, 247–261.

Martin-Algarra, A. and **Vera, J.A.** (2004) Evolución de la Cordillera Bética. In*: Geología de España* (Ed. J.A. Vera), pp. 347-444, SGE-IGME, Madrid.

McCaffrey, K.J.W., Jones, R.R., Holdsworth, R.E., Wilson, R.W., Clegg, P., Imber, J., Holliman, N. and **Trinks, I.** (2005) Unlocking the spatial dimension: digital technologies and the future of geoscience fieldwork. *Journal of the Geological Society*, **162**, 927-938.

McCann, T., Pascal, C., Timmerman, M.J., Krzywiec, P., López-Gómez, J., Wetzel, A., Krawczyk, C.M., Rieke, H. and **Lamarche, J.** (2006) Post-Variscan (end Carboniferous–Early Permian) basin evolution in Western and Central Europe. In: *European Lithosphere Dynamics* (Eds D.G. Gee and R.A. Stephenson). *Geological Society of London Memoirs,* **32**, 355–388.

McGowen, J.H. and **Garner, L.E.** (1970) Physiographic features and stratification types of coarse-grained point bars: modern and ancient examples. *Sedimentology*, **14**, 77–111.

Miall, A.D. (1985) Architectural-element analysis: a new method of facies analysis applied to fluvial deposits. *Earth-Science Reviews*, **22**, 261–308.

Miall, A.D. (1990) *Principles of Sedimentary Basin analysis*, 2nd edn. Springer Verlag Inc., New York.

Miall, A.D. (1991) Hierarchies of architectural units in terrigenous clastic rocks, and their relationship to sedimentation rate. In: *The Three-Dimensional Facies Architecture of Terrigenous Clastic Sediments and its Implications for Hydrocarbon Discovery and Recovery* (Eds A.D. Miall and N. Tyler). *SEPM, Concepts in Sedimentology and Paleontology*, **3**, 6–12.

Miall, A.D. (1996) *The Geology of Fluvial Deposits. Sedimentary Facies, Basin Analysis, and Petroleum Geology*, pp.582. Springer, Berlin.

Miall, A.D. (2006) Reconstructing the architecture and sequence stratigraphy of the preserved fluvial record as a tool for reservoir development: a reality check. *American Association of Petroleum Geologists Bulletin*, **90**, 989–1002.

Mitten, A.J., Mullins, J., Pringle, J.K., Howell, J., and **Clarke, S.M.** (2020) Depositional conditioning of three dimensional training images: Improving the reproduction and representation of architectural elements in sand dominated fluvial reservoir models. *Marine and Petroleum Geology*, 113, 104156. DOI: 10.1016/j.marpetgeo.2019.104156.

Mjøs, R., **Walderhaug, O.** and **Prestholm, E.** (1993) Crevasse splay sandstone geometries in the Middle Jurassic Ravenscar Group of Yorkshire, UK. In: *Alluvial Sedimentation* (Eds Marzo, M. and Puigdefábregas, C.), IAS Special Publication, **17**, 167–184.

References

Moscariello, A. (2009) Unraveling reservoir architecture of complex low net:gross Red-Bed fluvial sequence using palaeosoils and chemostratigraphy. *AAPG Cape Town, Search and Discovery Article, #50173.*

Mulder, Th., Syvitski, J.P.M., Migeon, S., Faugères, J-C. and **Savoye, B.** (2003) Marine hyperpycnal flows: initiation, behavior and related deposits: A review. *Mar. Petrol. Geol.*, **20**, 861-882. DOI: 10.1016/j.marpetgeo.2003.01.003.

Muñoz, A., Ramos, A., Sánchez-Moya, Y. and **Sopeña, A.** (1992) Evolving fluvial architecture during a marine transgression: Upper Buntsandstein, Triassic, central Spain. *Sedimentary Geology*, **75**, 257–281.

Murphy, J.B., Nance, R.D. and **Cawood, P.A.** (2009) Contrasting modes of supercontinent formation and the conundrum of Pangea. *Gondwana Research*, **15**, 408–420.

Mustapha, H. and **Dimitrakopoulos, R.** (2010) Higher-order stochastic simulation of complex spatially distributed natural phenomena. *Mathematical Geoscience*, **42**, 457–485.

Mutti, E., Rosell, J., Allen, G.P., Fonnesu, F. and **Sgavetti, M.** (1985) The Eocene Baronia tide-dominated delta–shelf system in the Ager Basin. In: *International Association of Sedimentology, 6th European Regional Meetin, Excursion GuideBook* (Eds M. Mila and J. Rosell), pp. 579-600. Lérida.

Muttoni, G., Gaetani, M., Kent, D.V., Sciunnach, D., Angiolini, L., Berra, F., Garzanti, E., Mattei, M. and **Zanchi, A.** (2009) Opening of the Neo-Tethys Ocean and the Pangea B to Pangea A transformation during the Permian. *GeoArabia*, **14**, 17–48.

Myers, K.J. and **Bristow, C.S.** (1989) Detailed sedimentology and gamma-ray log chracateristics of a Namurian deltaic succession II: gamma-ray logging. In: *Deltas Sites and Traps for Fossil Fuels* (Eds Whateley, M.K.G. and Pickering, K.T.*), Geological Society Special Publication*, **41**, 81–88.

Nanson, G.C. and **Page, K.** (1983) Lateral accretion of fine-grained concave benches associated with meandering rivers. In: *Modern and Ancient Fluvial Systems* (Eds J.D. Collinson. and J. Lewin*), IAS Special Publication*, **6**, 133–143.

Nemec, W. and **Postma, G.** (1993) Quaternary alluvial fans in southwestern Crete: sedimentation processes and geomorphic evolution. In: *Alluvial Sedimentation* (Eds M. Marzo and C. Puigdefabregas), *IAS Special Publication*, **17**, 235–276.

Nichols, G. (2017) Challenging orthodoxy: Is the present the key to the past?. *The Sedimentary Record*, **15** (3), 4–9. DOI:10.2110/sedred.2017.3.4.

Nielsen, L., Brockdorff, A. S. V., Bjerager, M. and **Surlyk, F.** (2009). Three-dimensional architecture and development of Danian bryozoan mounds at Limhamn, south-west Sweden, using ground-penetrating radar. *Sedimentology*, **56** (3), 695–708.

Olariu, M. I., Olariu, C., Steel, R. J., Dalrymple, R. W. and **Martinius, A. W.** (2012) Anatomy of a laterally migrating tidal bar in front of a delta system: Esdolomada Member, Roda Formation, Tremp-Graus Basin, Spain. *Sedimentology*, **59**, 356-378.

Ortí-Cabo, F. (1973) El Keuper de Levante español. *Estudios Geológicos*, **30**, 7–46.

Ortí-Cabo, F. (1974) El Keuper del Levante español: litoestratigrafía, petrología y paleogeografía de la cuenca, pp. 174. PhD dissertation, Universidad de Barcelona.

Owen, G. and **Santos, M.G.** (2014) Soft-sediment deformation in a pre-vegetation river system: the Neoproterozoic Torridonian of NWScotland. *Proc. Geol. Assoc.*, **125**, 511–523.

Ozkan, E., Brown, M.L., Raghavan, R. and **Kazemi, H.** (2011) Comparison of fractured horizontal-well performance in tight sand and shale reservoirs. *Society of Petroleum Engineers*, **14**, 1–12.

Pascucci, V., Peter Martini, I. and **Endres, A. L.** (2009) Facies and ground-penetrating radar characteristics of coarse-grained beach deposits of the uppermost Pleistocene glacial Lake Algonquin, Ontario, Canada. Sedimentology, **56**, 529–545.

Pastor-Galán, D., Groenewegen, T., Brouwer, D., Krijgsman, W. and **Dekkers, M.J.** (2015) One or two oroclines in the Variscan orogen of Iberia? Implications for Pangea amalgamation. *Geology*, 43, 527–530. DOI: 10.1130/g36701.1.

Pereira, M.F., Castro, A., Chichorro, M., Fernández, C., Díaz-Alvarado, J., Martí, J. and **Rodríguez, C.** (2014) Chronological link between deep-seated processes in magma chambers and eruptions: Permo-Carboniferous magmatism in the core of Pangaea (Southern Pyrenees). *Gondwana Research*, **25**, 290–308.

Pérez-López A and **Pérez-Valera, F.** (2007) Palaeogeography, facies and nomenclature of the Triassic units in the different domains of the Betic Cordillera (S Spain). *Palaeogeography, Palaeoclimatology, Palaeoecology*, **254**, 606–626.

Pérez-López, A. (1991) El Trías de facies germánica del sector central de la Cordillera Bética. PhD. Thesis, University of Granada, Granada, 400 pp.

Pérez-López, A. (2000) Epicontinental Triassic of the Southern Iberian Continental Margin (Betic Cordillera, Spain). In: *Epicontinental Triassic vol 2. E. Schweizerbart'sche Verlagsbuchhandlung* (Eds G.H. Bachmann and I. Lerche), pp. 1009-1031. Stuttgart.

Pérez-López, A.; Solé de Porta, N.; Márquez, L. and **Márquez Aliaga, A.** (1992) Caracterización y datación de una unidad carbonática de edad Noriense (Formación Zamoranos) en el Trías de la Zona Subbética. *Revista de la Sociedad Geológica de España*, **5**, 113-127.

Pérez-Valera, F. (2005) Estratigrafía y tectónica del Triásico Sudibérico en el sector oriental de la Cordillera Bética. PhD Thesis, University of Granada, Granada, 303 pp.

Pérez-Valera, F. and **Pérez-López, A.** (2008) Stratigraphy and Sedimentology of Muschelkalk carbonates of the Southern Iberian Continental Palaeomargin (Siles and Cehegín Formations, Southern Spain). *Facies*, **54**, 61–8.

Pérez-Valera, F., Solé de Porta, N. and **Pérez-López, A.** (2000) Presencia de facies Buntsandstein (Anisiense–Ladiniense?) en el Triásico de Calasparra (Murcia). *Geotemas*, **1**, 209–211.

Pickel, A., Frechette, J.D., Comunian, A. and **Weissmann, G.S.** (2015) Building a training image with Digital Outcrop Models. *Journal of Hydrology*, **531**, 53–61. DOI: 10.1016/j.jhydrol.2015.08.049.

Pickup, G. E. and **Hern, C. Y.** (2002) The development of appropriate upscaling procedures. *Transport Porous Media*, **46**, 119–138.

Pizzuto, J.E. (1987) Sediment diffusion during overbank flows. *Sedimentology*, **34**, 301–317. DOI: 10.1111/j.1365-3091.1987.tb00779.x.

Pranter, M. J. and **Sommer, N. K.** (2011) Static connectivity of fluvial sandstones in a lower coastalplain setting: An example from the upper cretaceous lower Williams fork formation, Piceance Basin, Colorado. *AAPG Bulletin*, **95**, 899–923. DOI: 10.1306/12091010008.

Pranter, M.J., **Cole, R.D.**, **Panjaitan, H.** and **Sommer, N.K.** (2009) Sandstone-body dimensions in a lower coastalplain depositional setting: Lower Williams fork formation, coal Canyon, Piceance Basin, Colorado. *AAPG Bull.*, **93**, 1379–1401.

Pranter, M.J., **Hewlett, A.C.**, **Cole, R.D.**, **Wang, H.** and **Gilman, J.R.** (2014) Fluvial architecture and connectivity of the Williams Fork Formation: use of outcrop analogues for stratigraphic characterisation and reservoir modelling. In: *Sediment-body Geometry and Heterogeneity:*

Analogue Studies for Modelling the Subsurface (Eds T. Good, J. Howell and A.W. Martinius), *Geological Society*, London, *Special Publications*, **387**, 57–83. DOI: 10.1144/SP387.1.

Pranter, M.J., **Vargas, M.F.** and **Davis, T.L.** (2008) Characterization and 3D reservoir modelling of fluvial sandstones of the Williams Fork Formation, Rulison Field, Piceance Basin, Colorado, USA. *J. Geophys. Eng.*, **5**, 158–172.

Pringle, J. K., Westerman, A. R., Clark, J. D., Drinkwater, N. J. and **Gardiner, A. R.** (2004) 3-D high-resolution digital models of outcrop analog study sites to constrain reservoir model uncertainty: An example from Alport Castles, Derbyshire, UK. *Petroleum Geoscience*, **10**, 343–352. DOI: 10.1144/1354-079303-617.

Pringle, J.K., Howell, J.A., Hodgetts, D., Westerman, A.R. and **Hodgson, D.M.** (2006) Virtual outcrop models of petroleum reservoir analogues: a review of the current state-of-the-art. *First Break*, **24**, 33-42.

Prins, M.A., Postma, G., Cleveringa, J., Cramp, A. and **Kenyon, N.H.** (2000) Controls on terrigenous sediment supply to the Arabian Sea during the late Quaternary, the Indus Fan. *Marine Geology*, **169**, 327–349.

Puig, J.M., Cabello, P., Howell, J. and **Arbués, P.** (2019) Three-dimensional characterisation of sedimentary heterogeneity and its impact on subsurface flow behaviour through the braided-to-meandering fluvial deposits of the Castissent Formation (late Ypresian, Tremp-Graus Basin, Spain). *Marine and Petroleum Geology*, **103**, 661–680. DOI: 10.1016/j.marpetgeo.2019.02.014.

Pyrcz, M. J., Boisvert, J. B. and **Deutsch, C. V.** (2008) A library of training images for fluvial and deepwater reservoirs and associated code. *Computers & Geosciences*, **34** (5), 542–560. DOI: 10.1016/j.cageo.2007.05.015.

Rarity, F., Van Laen, X.M.T., Hodgetts, D., Gawthorpe, R.L., Wilson, P., Fabuel-Perez, I. and **Redfern, J.,** (2014) LiDAR-based digital outcrops for sedimentological analysis: workflows and techniques. In: *Sediment-Body Geometry and Heterogeneity: Analogue Studies for Modelling the Subsurface* (Eds A. W. Martinius, J. A. Howell and T. Good*). Geological Society*, London, *Special Publications*, **387**. DOI: 10.1144/SP387.5.

Ratcliffe, K.T., Martin, J., Pearce, T.J., Hughes, A.D., Lawton, D.E., Wray, D.S. and **Bessa, F.** (2006) A regional chemostratigraphically-defined correlation framework for the late Triassic TAG-I Formation in Blocks 402 and 405a, Algeria. *Petroleum Geosciences*, **12**, 3-12.

Reesink, M., Ashworth, P.J., Sambrook Smith, G.H., Best, L. J., Parsons, D.R., Amsler, M.L., Hardy, R.J., Lane, S.N., Nicholas, A.P., Orfeo, O., Sandbach, S. D., Simpson C.J. and **Szupiany, R.N**. (2014) Scales and causes of heterogeneity in bars in a large multi-channel river: Río Paraná, Argentina. *Sedimentology*, **61**, 1055–1085.

Reineck, H.E. and **Singh, I.B.** (1980) *Depositional Sedimentary Environments*, pp. 551. Springer-Verlag, Berlin.

Renard, P. and **Allard, D.** (2013) Connectivity metrics for subsurface flow and transport. *Adv. Water Resour.*, **51**, 168–196. DOI: /10.1016/j.advwatres.2011.12.001.

Retallack, G.J. (2001) *Soils of the Past: An Introduction to Paleopedology,* 2nd edn, pp. 404. Blackwell Science, Oxford.

Retallack, G.J. and **Dilcher, D.L.** (2012) Outcrop versus core and geophysical log interpretation of mid-Cretaceous palaeosols from the Dakota Formation of Kansas. *Palaeogeogr. Palaeoclimatol. Palaeoecol.*, **329–330,** 47–63.

Reynolds, A.D. (2017) Paralic reservoirs. In: *Sedimentology of Paralic Reservoirs: Recent Advances* (Eds G.J. Hampson, A. D. Reynolds, B. Kostic and M.R. Wells). *Geological Society,* London, *Special Publications*, **444**. DOI: 10.1144/SP444.10.

Rice, S. P., Church, M., Wooldridge, C. L. and **Hickin, E. J.** (2009) Morphology and evolution of bars in a wandering gravel-bed river; lower Fraser river, British Columbia, Canada. *Sedimentology*, **56**, 709–736.

Rider, M. (2000) *The Geological Interpretation of Well Logs*. 2nd edn. Rider-French Consulting Limited.

Rider, M. and **Kennedy, M.** (2011) *The Geological Interpretation of Well Logs*, 3rd edn, pp. 432. Rider-French Consulting, ISBN 978-0-9541906-8-2.

Ringrose, P. and **Bentley, M.** (2015) *Reservoir model design. A practitioner's guide*, pp. 260. Springer.

Ronchi, A., Sarria, E. and **Broutin, J.** (2008) The ''Autuniano Sardo'': basic features for a correlation through the Western Mediterranean and Paleoeurope. *Bollettino Società Geologica Italiana* (Italian Journal of Geosciences), **127**, 655–681.

Rossetti, D.F. and **Santos, A.E.** (2003) Events of sediment deformation and mass failure in Upper Cretaceous estuarine deposits (Cameta´ Basin, northern Brazil) as evidence for seismic activity. *Sed. Geol.*, **161**, 107–130. DOI: 10.1016/S0037-0738(02)00398-6

Rossi, C., Kälin, O., Arribas, J. and **Tortosa, A.** (2002) Diagenesis, provenance and reservoir quality of Triassic TAGI sandstones from Ourhoud field, Berkine (Ghadames) Basin, Algeria. *Marine and Petroleum Geology*, **19**, 117–142.

Rossi, C., **Kälin, O.**, **Arribas, J.** and **Tortosa, A.** (2002) Diagenesis, provenance and reservoir quality of Triassic TAGI sandstones from Ourhoud field, Berkine (Ghadames) Basin, Algeria. *Mar. Petrol. Geol.*, **19**, 117–142.

Sánchez-Moya, Y., Arribas, J., Gómez-Gras, D., Marzo, M., Pérez-Arlucea, M. and **Sopeña, A.** (2004) Inicio del rifting. El comienzo del relleno continental. In: *Geología de España* (Ed. J.A. Vera). Madrid. SGE-IGME. 485–487.

Sánchez-Moya, Y., **Arribas, J.**, **Gómez-Gras, D., Marzo, M.**, **Pérez-Arlucea, M.** and **Sopeña, A.** (2004) Inicio del rifting. El comienzo del relleno continental. In: *Geología de España* (Ed. Vera, J.A.), pp. 485–487. SGE-IGME, Madrid.

Scott, A., **Hurst, A.** and **Vigorito, M.** (2013) Outcrop-based reservoir characterisation of a kilometer-scale sand-injectite complex. *AAPG Bull.*, **97** (2), 309–343.

Selley, R.C. (2004) *Ancient Sedimentary Environments and Their Sub-Surface Diagnosis*, pp. 297. Taylor and Francis Group, London.

Serra, O. and **Surpice, L.** (1975) Sedimentological analysis of sand shale series from well logs. *Society of Petrophysicists and Well-Log Analysts*. SPWLA 16th Annual Logging Symposium 4–7 June 1975, New Orleans, Louisiana.

Shanmugam, G., Poffenberger, M. and **Toro Álava, J.** (2000) Tide-Dominated Estuarine Facies in the Hollin and Napo ("T" and "U") Formations (Cretaceous), Sacha Field, Oriente Basin, Ecuador. *AAPG Bulletin*, **84**, N.5, 652–682.

Sharp, J.M., Mingjuan, S. and **Galloway, W.E.** (2003) Heterogeneity of fluvial systems; control on density-driven flow and transport. *Environmental & Engineering Geoscience*, **9**, 5–17.

Shimer, G.T., McCarthy, P.J. and **Hanks, C.L.** (2014) Sedimentology, stratigraphy and reservoir properties of an unconventional, shallow, frozen petroleum reservoir in the Cretaceous Nanushuk

Formation at Umiat field, North Slope, Alaska. *American Association of Petroleum Geologists Bulletin*, **98**, 631–661.

Sifuentes, W.F., Giddins, M.A. and **Blunt, J.B.** (2009) Modeling CO2 storage in aquifers: assessing the key contributors to uncertainty. In: *SPE Offshore Europe Oil and Gas Conference and* Exhibition, Society of Petroleum Engineers, 8-11 sept., Aberdeen, UK. DOI: 10.2118/123582-MS.

Skelly, R.L., Bristow, C.S. and **Ethridge, F.G.** (2003) Architecture of channel-belt deposits in an aggrading shallow sandbed braided river: the lower Niobrara River, northeast Nebraska. *Sedimentary Geology*, **158**, 249–270.

Slatt, R. M. , Buckner, N., Abousleiman, Y., Sierra, R., Philp, P., Miceli-Romero, A.,Portas, R., O'Brien, N., Tran, M., Davis, R. and **Wawrzyniec, T. (**2011) Outcrop/behind outcrop (quarry), multiscale characterization of the Woodford Gas Shale, Oklahoma. In: *Shale reservoirs—Giant resources for the 21st century* (Ed. J. Breyer), *AAPG Memoir*, **97**, 1–21.

Slatt, R., Buckner, Abousleiman, Y., Sierra, R., Philp, P., Miceli Romero, A., Portas, R., O'Brien, N. R., minh Hue Tran, Davis, R. and **Wawrzyniec, T.** (2012) Outcrop/behind outcrop (quarry), multiscale characterization of the Woodford gas shale, Oklahoma. In: *Shale Reservoirs: Giant Resources for the 21st Century* (Ed J. Breyer), *AAPG Memoirs*, **97**, 1–21.

Slatt, R.M. (2013) Stratigraphic Reservoir characterization for Petroleum Geologists, Geophysicists and Engineers, In: *Developments in Petroleum Science* (Ed J. Cubitt) 2nd edn, pp. 688. Elsevier, Amsterdam, Netherlands. ISBN: 9780444563651.

Sloss, L., Krumbein, W., and **Dapples, E.** (1949) Integrated facies analysis. In: *Sedimentary facies in geologic history* (Ed. C. Longwell), *Geological Society America Memoir*, **39**, 91-124.

Smith, G.H.S., Ashworth, P.J., Best, J.L., Woodward, J. and **Simpson, C.J.** (2006) The sedimentology and alluvial architecture of the sandy braided South Saskatchewan River, Canada. *Sedimentology*, **53**, 413–434.

Snavely, N., Seitz, S. M. and **Szeliski, R.** (2007) Modeling the world from internet photo collections. *International Journal of Computer Vision,* **80**, 189–210.

Soil Survey Staff (1998) *Key to Soil Taxonomy*, 8th edn, pp. 328. United States Department of Agriculture, Natural Resources Conservation Service, Washington, DC.

Sopeña, A., Virgili, C., Arche, A., Ramos, A. and **Hernando, S.** (1983) El Triásico. In: *Geología de España: Libro Jubilar J. M. Ríos* (Ed. J.A. Comba), pp. 47-62. Instituto Geológico y Minero Español. Madrid.

Stampfli, G.M. and **Borel, G.D.** (2002) A plate tectonic model for the Paleozoic and Mesozoic constrained by dynamic plate boundaries and restored synthetic oceanic isochrones. *Earth and Planetary Science Letters*, **196**, 17–33.

Stampfli, G.M., Hochard, C., Vérard, C., Wilhem, C. and **Von Raumer, J.** (2013). The formation of Pangea. *Tectonophysics*, **593**, 1–19. DOI: 10.1016/j.tecto.2013.02.037.

Stephens, M. (1994) Architectural element analysis within the Kayenta Formation (Lower Jurassic) using groundprobing radar and sedimentological proflling, southwestern Colorado. *Sedimentary Geology*, **190**, 179–211.

Strebelle, S. (2002). Conditional simulation of complex geological structures using multiple-point statistics. *Mathematical Geology*, **34**, 1–22.

Sullivan, M.D., Van Wagoner, J.C., Jenette, D.C., Foster, M.E., Stuart, R.M., Lovell, R.W. and **Pemberton, S.G.** (1997) High resolution sequence stratigraphy and architecture of the Shannon Sandstone, Hartzog Draw field, Wyoming: implications for reservoir management. In, *Shallow Marine and Nonmarine Reservoirs, Sequence Stratigraphy, Reservoir Architecture and Production*

Characteristics (Eds K.W. Shanley and B.F. Perkins), pp. 331-344. Gulf Coast Section SEPM Eighteenth Annual Research Conference. Austin, TX, USA.

Surdam, R. C. (2013) *Geological CO2 Storage Characterization. The Key to Deploying Clean Fossil Energy Technology*. Springer Environmental Science and Engineering. ISSN 2194-3222

Szerbiak, R. B., McMechan, G. A., Corbeanu, R., Forster, C. and **Snelgrove, S. H.** (2001) 3-D characterization of a clastic reservoir analog: From 3-D GPR data to a 3-D fluid permeability model. *Geophysics*, **66**, 1026–1037.

Tahmasebi, P. (2018). Multiple point statistics: a review. In: *Handbook of Mathematical Geosciences* (Eds B. Daya Sagar, Q. Cheng and F. Agterberg). Springer, Cham. DOI: <u>10.1007/978-3-319-78999-6_30</u>.

Tessier, B. and **Reynaud, J.** (2016) Contributions to Modern and Ancient Tidal Sedimentology: an introduction to the volume. In: *Contributions to Modern and Ancient Tidal Sedimentology: Proceedings of the Tidalites 2012 Conference* (Eds B. Tessier and J. Reynaud), *International Association of Sedimentologists*. DOI: 10.1002/9781119218395.

Thomas, R.G., **Smith, D.G.**, **Wood, J.M.**, **Visser, J**., **Calverley- Range, E.A.** and **Koster, E.H.** (1987) Inclined heterolithic stratification-terminology, description, interpretation and significance. *Sed. Geol.*, **53**, 123–179.

Tianjian, S., Longxin, M. and **Guoliang, Z.** (2014) Classification and characterization of barrier-intercalation in sandy braided river reservoirs: taking Hegli Oilfield of Muglad Basin in Sudan as an example. *Petroleum Exploration and Development*, **41**, 125–134.

Tinker, S. W. (1996) Building the 3-D jigsaw puzzle: Applications of sequence stratigraphy to 3-D reservoir characterization, Permian Basin. *AAPG Bulletin*, **80**, 460–485.

Trendell, A.M., Atchley, S.C. and **Nordt, L.C.** (2012) Depositional and diagenetic controls on reservoir attributes within a fluvial outcrop analog: Upper Triassic Sonsela Member of the Chinle Formation, Petrified Forest National Park, Arizona. *American Association of Petroleum Geologists Bulletin*, **96**, 679–707.

Turner, P., Pilling, D., Walker, D., Exton, J., Binnie, J. and **Sabaou, N.** (2001) Sequence stratigraphy and sedimentology of the late Triassic TAG-I (Blocks 401/402, Berkine Basin, Algeria). *Marine and Petroleum Geology*, **18**, 959-981.

Tyler, N. and **Finley, R.J.** (1991) Architectural controls on the recovery of hydrocarbons from sandstone reservoirs. In: *The Three-Dimensional Facies Architecture of Terrigenous Clastic Sediments and its Implications for Hydrocarbon Discovery and Recovery* (Eds A.D. Miall and N. Tyler), *SEPM Concepts in Sedimentology and Paleontology,* Tulsa, OK, **3**, 1–5.

Ullman, S. (1979) The interpretation of structure from motion: Proceedings of the Royal Society of London. *Series B, Biological Sciences,* **203**, p. 405–426.

Valle Aguado, B., Azevedo, M.R., Schaltegger, U., Martínez-Catalán, J.R. and **Nolan, J.** (2005) U–Pb zircon and monazite geochronology of Variscan magmatism related to syn-convergence extension in Central Northern Portugal. *Lithos*, **82**, 169–184.

Van Den Bril, K., Gregoire, C., Swennen, R. and **Lambot, S.** (2007) Ground-penetrating radar as a tool to detect rock heterogeneities (channels, cemented layers and fractures) in the Luxembourg Sandstone Formation (Grand-Duchy of Luxembourg). *Sedimentology*, **54**, 949–967.

Van Toorenenburg, K.A., Donselaar, M.E., Noordijk, N.A. and **Weltje, G.J.** (2016). On the origin of crevasse-splay amalgamation in the Huesca fluvial fan (Ebro Basin, Spain): implications for connectivity in low net-to-gross fluvial deposits*. Sed. Geol.*, **343**, 156–164.

References

Varela, A.N., Veiga, G.D. and Poiré, D.G. (2012) Sequence stratigraphic analysis of Cenomanian greenhouse palaeosols: a case study from southern Patagonia, Argentina. *Sed. Geol.*, **271-272**, 67–82.

Varela, A.N., Yeste, L.M., Viseras, C. and García-García, F. (2019) Implications of palaeosols in low net-to-gross fluvial architecture reconstruction: reservoirs analogues from Patagonia and Spain. 34th *IAS Meeting of Sedimentology*, 10–13 Sep 2019, Rome, Italy.

Vasuki, Y., Holden, E., Kovesi, P. and Micklethwaite, S. (2014) Semi-automatic mapping of geological Structures using UAV-based photogrammetric data: An image analysis approach. *Computer & Geosciences*, **69**, 22-32.

Viseras, C. and Fernández, F., (2010) Sistemas aluviales de alta sinuosidad. In: *Sedimentología. Del proceso físico a la cuenca sedimentaria* (Ed. A. Arche), pp. 1290. *Consejo Superior de Investigaciones Científicas.*

Viseras, C. and Fernández, J. (1994) Channel migration patterns and related sequences in some alluvial fan systems. *Sedimentary Geology*, **88**, 201–217.

Viseras, C. and Fernández, J. (2010) Triassic braidplain deposits and their potential as reservoir rocks: examples from Spain and Morocco. In: *Sedimentology at the Foot on the Andes* (Eds E. Schwarz, S. Georgieff and D. Ariztegui), *18th International Sedimentological Congress*. Mendoza, Argentina, **908**.

Viseras, C., Fernández, J. and Henares, S. (2011) Facies architecture in outcropping analogues for the TAGI Reservoir. Exploratory Interest. *AAPG International Conference and Exhibition*, *Search and Discovery Article, #90135*, Milan, Italy.

Viseras, C., Fernández, J., García-García, F., Soria, J.M., Calvache, M.L. and Jáuregui, P. (2009) Dynamics of sedimentary environments in the accelerated siltation of a reservoir: the case of Alhama de Granada, southern Spain. *Environmental Geology*, **56**, 1353–1369.

Viseras, C., Henares, S., Fernández, J. and Jaimez, J. (2013) Outcrop/behind outcrop characterisation in onshore Western Mediterranean basins of Southern Iberia. *American Association of Petroleum Geologists Search and Discovery Article, #41175*.

Viseras, C., Henares, S., Fernández, J., Yeste, L.M., Pla-Pueyo, S. and Calvache, M.L. (2015) Towards 3D reservoir modeling of outcrop analogs through integrated outcrop/behind outcrop characterisation. A Triassic example [abstract]. Presented at the *31th IAS Meeting of Sedimentology*, 22–25 June 2015, Krakow, Poland.

Viseras, C., Henares, S., Yeste, L.M. and García-García, F. (2016) Subsurface VS outcrop key features to reconstruct ancient point bar deposits with examples from Spain and Morocco [abstract]. Presented at the *32nd IAS Meeting of Sedimentology*, 23–25 May 2016, Marrakesh, Morocco.

Viseras, C., Henares, S., Yeste, L.M. and Garcia-Garcia, F. (2018) Reconstructing the architecture of ancient meander belts by compiling outcrop and subsurface data: a Triassic example. In: *Fluvial Meanders and Their Sedimentary Products in the Rock Record* (Eds M. Ghinassi, L. Colombera, N. P., Mountney and A. J. H. Reesink), *IAS Special Publication*, **48**, 419–444. DOI: 10.1002/9781119424437.ch16.

Visser, M.J. (1980) Neap-spring cycles reflected in Holocene subtidal large-scale bedform deposits; a preliminary note. *Geology*, **8**, 543–546.

Von Raumer, J., Bussy, F., Schaltegger, U., Schulz, B. and Stampfli, G.M. (2013) Pre Mesozoic Alpine basements—their place in the European Paleozoic framework. *GSA Bulletin,* **125,** (1/2), 89–108.

Weber, K.J. (1986) How heterogeneity affects oil recovery. In: *Reservoir Characterization* (Eds L. W. Lake and N. B. Jr. Carroll), pp. 545–560. Academy Press, Orlando, FL.

Weissmann, G.S. and **Fogg, G.E.** (1999) Multi-scale alluvial fan heterogeneity modelled with transition probability geostatistics in a sequence stratigraphic framework. *J. Hydrol*, **226** (1–2), 48–65. DOI: 10.1016/S0022-1694(99)00160-2.

Wilkinson, M. W., Jones, R. R., Woods, C. E., Gilment, S. R., McCaffrey, K. J. W., Kokkalas, S. and **Long, J. J.** (2016). A comparison of terrestrial laser scanning and structure-from-motion photogrammetry as methods for digital outcrop acquisition. *Geosphere*, **12** (6), 1865-1880.

Williams, H. and **Soek, H.F.** (1993) Predicting reservoir sandbody orientation from dipmeter data: the use of sedimentary dip profiles from outcrop studies. In: *The Geological Modelling of Hydrocarbon Reservoirs and Outcrop Analogues* (Eds S. S. Flint and I. D. Bryant), *International Association of Sedimentologists, Special Publications*, **115**, 143–156.

Willis, **B.J.** and **Sech**, **R.P.** (2019) Emergent facies patterns within fluvial channel belts. In: Fluvial Meanders and Their Sedimentary Products in the Rock Record (Eds M. Ghinassi, L. Colombera, N.P. Mountney and A. J. H. Reesink*), IAS Special Publication*, **48**, 509–542.

Willis, **B.J.** and **Tang, H.** (2010) Three-dimensional connectivity of point-bar deposits. *Journal of Sedimentary Research*, **80**, 440-454.

Wizevich, M.C. (1991) Photomosaics of outcrops: useful photographic techniques. In: *The Three-Dimensional Facies Architecture of Terrigenous Clastic Sediments and its Implications for Hydrocarbon Discovery and Recovery* (Eds A. D. Miall and N. Tyler), *SEPM Concepts in Sedimentology and Paleontology*, Tulsa, OK, **3**, 22–24.

Wood, L. J. (2004) Predicting tidal sand reservoir architecture using data from modern and ancient depositional systems. In: Integration of outcrop and modern analogs in reservoir modelling. *AAPG Memoir*, **80**, 45-66.

Xu, C., **Cronin, T.P.**, **McGinness, T.E.** and **Steer, B.** (2009) Middle Atokan sediment gravity flows in the Red Oak field, Arkoma Basin, Oklahoma: a sedimentary analysis using electrical borehole images and wireline logs. *AAPG Bull*., **93**, 1–29.

Yang, B. C., Dalrymple, R. W. and **Chun, S. S.** (2005) Sedimentation on a wave-dominated, open-coast tidal flat, south-western Korea: summer tidal flat – winter shoreface. *Sedimentology*, **52**, 235-252. DOI: 10.1111/j.1365-3091.2004.00692.x.

Yang, B.C., Dalrymple, R.W. and **Chun, S.S.** (2006) The significance of hummocky cross-stratification (HCS) wavelenghts: evidence from an open-coast tidal flat, South Korea. *J. Sed. Res*., **76**, 2–8.

Yeste, L.M., García-García, F., McDougall, N.D, Henares, S. and **Viseras, C.** (2017) Tidal vs fluvial point bars: key features which differentiate them in outcrops, core and wireline logs. *33rd IAS Meeting of Sedimentology*, 10-12 Oct 2017, Toulouse, France.

Yeste, L.M., **Henares, S.**, **McDougall, N.**, **García-García, F.** and **Viseras, C.** (2019a) Towards the multi-scale characterization of braided fluvial geobodies from outcrop, core, georradar and well logs data. In: *River to Reservoir: Geoscience to Engineering* (Eds P. Corbett, A. Owen, A. Hartley, S. Pla-Pueyo, D. Barreto, C. Hackney and S. Kape), *GSL Special Publication*, **488**. DOI: 10.1144/sp488.3

Yeste, L.M., **Palomino, R.**, **McDougall, N.**, **Viseras, C.**, **Varela, A.N.** and **García-García, F.** (2019b) Towards Geocellular modelling of highly heterogeneous reservoirs. A Triassic example. *34th IAS Meeting of Sedimentology*, 10–13 Sep 2019, Rome, Italy.

References

Yeste, L.M., Varela, A.N., Viseras, C., Mcdougall, N.D. and García-García, F. (2020) Reservoir architecture and heterogeneity distribution in floodplain sandstones: Key features in outcrop, core and wireline logs. *Sedimentology*. DOI: 10.1111/sed.12747.

Yoshida, S., Jackson, M.D., Johnson, H.D., Muggeridge, A.H. and Martinius, A.W. (2001) Outcrop studies of tidal sandstones for reservoir characterization (Lower Cretaceous Vectis Formation, Isle of Wight, Southern England). In: *Sedimentary Environments Offshore Norway – Palaeozoic to Recent* (Eds O. J. Martinsen and T. Dreyer), *Norwegian Petroleum Society Special Publication*, **10**, 233– 257.

Yu, X., Li, S. and Li, S., (2018) *Clastic hydrocarbon reservoir sedimentology*, pp. 720. Springer.

Zavala, C. and Pan S. X. (2018). Hyperpycnal flows and hyperpycnites: Origin and distinctive characteristics. *Lithologic Reservoir*, **30** (1), 1-27. DOI: 10.3969/j.issn.1673-8926.2018.01.001.

Zeng, H. and Hentz, T.F. (2004) High-frequency sequence stratigraphy from seismic sedimentology: applied to miocene, Vermilion Block 50, Tiger Shoal area, offshore Lousiana. AAPG Bulletin, **88**, 153–174.

Zeng, X., McMechan, G. A., Bhattacharya, J. P., Aiken, C. L.V., Xu, X., Hammon III, W. S. and Corbeanu, R. M. (2004) 3D imaging of a reservoir analogue in point bar deposits in the Ferron Sandstone, Utah, using GPR. Geophysical Prospecting, **52**, 151-163.

Ziegler, P.A. and Stampfli, G.M. (2001) Late Paleozoic-Early Mesozoic plate boundary reorganization: collapse of the Variscan Orogen and opening on the Neotethys. *Mus. Civ Sc Nat Bresc Ann 25*, 17–34.